Fabrication and characterisation of carbon-based devices

Damien Thuau

A thesis submitted for the degree of Doctor of Philosophy.
The University of Edinburgh.
August 30, 2011

Abstract

Thin film material properties and measurement characterisation techniques are crucial for the development of micro-electromechanical systems (MEMS) devices. Furthermore, as the technology scales down from microtechnology towards nanotechnology, nanoscale materials such as carbon nanotubes (CNTs) are required in electronic devices to overcome the limitations encountered by conventional materials at the nanoscale. The integration of CNTs into micro-electronics and material applications is expected to provide a wide range of new applications. The work presented in this thesis has contributed to the development of thin film material characterisation through research on the thermal conductivity measurement and the control of the residual stress of thin film materials used commonly in MEMS devices. In addition, the use of CNTs in micro-electronics and as filler reinforcement in composite materials applications have been investigated, leading to low resistivity CNTs interconnects and CNTs-Polyimide (PI) composites based resistive humidity sensors.

In the first part of this thesis, the thermal conductivity of conductive thin films as well as the control of the residual stress arising from fabrication process in PI micro-cantilevers have been studied. A MEMS device has been developed for the thermal conductivity characterisation of conductive thin films showing good agreement with thermal conductivity of bulk material. Low energy Ar^{+} ion bombardment in a plasma has been used to control the residual stress present in PI cantilevers. Appropriate ion energy and exposure time have led to stress relaxation of the beams resulting in a straight PI cantilever beam.

In the second part of this thesis, low resistivity CNTs interconnects have been developed using both dielectrophoresis (DEP) and Focused Ion Beam (FIB) techniques. An investigation of the effects of CNT concentration, applied voltage and frequency on the CNTs alignment between Al and Ti electrodes has resulted in the lowering of the CNTs' resistance. The deposition of Pt contact using FIB at the CNTs-metal electrodes interface has been found to decrease the high contact resistances of the devices by four and two orders of magnitude for Al and Ti electrodes respectively.

The last part of this thesis focuses on the preparation of CNTs-PI composite materials, its characterisation and its application as resistive humidity sensor. The integration of CNTs inside the PI matrix has resulted in enhancing significantly the electrical and mechanical properties of the composites. In particular, a DEP technique employed to induce CNTs alignment inside the PI matrix during curing has been attributed to play an important role in improving the composite properties and lowering the percolation threshold. In addition, the fabrication and testing of CNTs-PI resistive humidity sensors have been carried out. The sensing performance of the devices have shown to be dependent highly on the CNT concentration. Finally, the alignment of CNTs by DEP has improved the sensing properties of CNTs-PI humidity sensors and confirmed that the change of resistance in response to humidity is governed by the change of the CNTs' resistances due to charge transfer from the water molecules to the CNTs.

Declaration of originality

I hereby declare that the research recorded in this thesis is my own work, unaided except where otherwise acknowledged in the text, and the thesis itself has been written by myself in the School of Engineering and Electronics at the University of Edinburgh. This work has not been submitted for any other degree or professional qualification.

Damien Thuau

Acknowledgements

First and foremost, I would like to express my deep and sincere gratitude to my supervisor, Professor Rebecca Cheung, for her continued encouragement and invaluable suggestions during this work. Her contributions of time, ideas, and funding have been of great value for me in order to make my Ph.D. a productive and stimulating experience. I warmly thank my second supervisor, Dr. Vasileios Koutsos, for his valuable advice. His extensive discussions around my work and interesting explorations in operations have been very helpful for this study.

I also wish to thank many members of the Scottish Microelectronic Centre namely, Dr. Tom Stevenson, Dr. Andrew Bunting, Dr. Camelia Dunare, Dr. John Terry, Dr. Stewart Smith, Alec Ruthven, Ewan McDonald, Kevin Tierney, Hugh Frizell and Richard Blair. I would like to thanks for those who provided the social environment at the SMC and being good friends, namely Enrico, Juanjo, Graham and Issac.

Outside the university and the SMC, I am especially grateful for the moral support of my girlfriend and my friends during the three years of my PhD. Lastly, I am deeply thankful to my parents who supported me in all my studies and to whom I dedicate this thesis.

List of abbreviations

Materials and chemicals	
Carbon nanotube	CNT
Single walled carbon nanotube	SWNT
Multi walled carbon nanotube	MWNT
Argon	Ar
Polyimide	PI
Aluminum	Al
Titanium	Ti
Idium tin oxide	ITO
Platinum	Pt
Silicon	Si
Silicon dioxide	SiO_2
Silicon nitride	Si_3N_4
Xenon difluoride	XeF_2
Ammonium fluoride	NH_4F
Acetic acid	$C_2H_4O_2$
Hydrogen fluoride	HF

Technology	
Micro-electromechanical system	MEMS
Nano-electromechanical systems	NEMS
Field effect transistor	FET
Electrostatic dissipation	ESD
Electromagnetic interference	EMI
Dielectrophoresis	DEP
Focused ion beam	FIB
Scanning electron microscope	SEM
Atomic force microscope	AFM
X-ray photoelectron spectroscopy	XPS
Fourrier transform infra red spectroscopy	FTIR
Dynamic mechanical analysis	DMA
Low pressure chemical vapour deposition	LPCVD
Plasma enhanced chemical vapor deposition	PECVD
Reactive ion etching	RIE
Deep reactive ion etching	DRIE
Inductively coupled plasma	ICP

Nomenclature

Current	I
Alternating current	AC
Voltage	V
Temperature	T
Time	t
Resistance	R
Ultraviolet	UV
Standard Cubic Centimeters per Minute	SCCM
Electric field	E
Dielectrophoresis force	F_{DEP}
Clausius-Mossotti factor	F_{CM}
Complex permittivity	ϵ
Schottcky barrier	SB
Conductance	G
Conductivity	σ
Band gap	E_g
Density	ρ
Electron affinity	χ
Work function	ϕ
Barrier height	ϕ_B
Valence band energy	E_v
Conduction band energy	E_c
Fermi level energy	E_F
Glass transition temperature	T_g

Fundamental Constant	Symbol	Value
Electron charge	e	$1.6\times10^{19}C$
Planck's constant	h	$6.672 \times 10^{-31}Js$
Boltzmann's constant	k_B	$1.38\times10^{-23}JK^{-1}$

Contents

Contents . . . viii
List of figures . . . xii
List of tables . . . xvi

1 Introduction **1**
1.1 Micro-electro-mechanical systems (MEMS) . . . 1
1.1.1 History of MEMS . . . 1
1.1.2 Residual stress in MEMS . . . 2
1.1.3 Thermal conductivity of conductive thin film materials . . . 4
1.2 Nanotechnology . . . 5
1.2.1 CNTs interconnects . . . 6
1.3 Integration of nanotechnology and MEMS . . . 7
1.3.1 Composite material . . . 7
1.3.2 Composite based humidity sensor . . . 9
1.4 Thesis outline . . . 10

2 Materials and applications **14**
2.1 Introduction . . . 14
2.2 Polyimide . . . 15
2.2.1 Structure and synthesis . . . 15
2.2.2 Properties related to applications . . . 20
2.3 Carbon Nanotubes . . . 23
2.3.1 Structure and properties . . . 23
2.3.2 Synthesis . . . 29
2.3.3 Applications . . . 30
2.4 Conclusions . . . 38

3 Assembly, fabrication and characterisation techniques **40**
3.1 Introduction . . . 40
3.2 Dielectrophoresis (DEP) . . . 40
3.2.1 Theory of DEP . . . 41
3.2.2 Application of DEP . . . 44
3.3 Micro-fabrication . . . 45
3.3.1 Thin film deposition . . . 46
3.3.2 Photo-lithography . . . 49
3.3.3 Etching . . . 51
3.4 Characterisation . . . 55
3.4.1 Electrical characterisation . . . 55
3.4.2 Mechanical characterisation . . . 58
3.4.3 Thermal conductivity characterisation . . . 59
3.4.4 Surface characterisation . . . 62
3.4.5 Structure characterisation . . . 65
3.5 Conclusions . . . 68

4 A MEMS for thermal conductivity measurement of conductive thin films 70
4.1 Introduction . . . 70
4.2 Heat transfer mechanisms and heat balance equation . . . 71
4.2.1 Heat transfer mechanisms . . . 71
4.2.2 Heat balance equation . . . 72
4.3 Test micro-structure design . . . 74
4.3.1 The reference and test structure . . . 75
4.3.2 Optimisation of the test microstructures via CoventorWare Finite Element Method (FEM) temperature simulations . . . 77
4.4 Fabrication process . . . 82
4.4.1 Insulating and sacrificial layers . . . 84
4.4.2 Beam and electrodes layers . . . 84
4.4.3 Release of the structure . . . 86
4.5 Measurements . . . 87
4.5.1 Calculation of the linear and quadratic coefficient of temperature 87
4.5.2 I-V characteristics of the reference and test structure . . . 89
4.6 Conclusions . . . 93

5 Stress recovery in Polyimide (PI) MEMS 96
5.1 Introduction . . . 96
5.2 Mechanical deformation due to stress . . . 97
5.3 Fabrication process . . . 100
5.3.1 Polyimide cantilever . . . 100
5.3.2 Polyimide membrane . . . 103
5.4 Ion induced stress release in PI cantilever . . . 104
5.4.1 Mechanical deflection recovery . . . 104
5.4.2 Surface characterisation . . . 111
5.5 Discussion . . . 116
5.6 Conclusion . . . 118

6 Carbon Nanotube interconnect - Improvement of the contact resistance at the SWNTs-metal interface 120
6.1 Introduction . . . 120
6.2 Experimental method . . . 121
6.2.1 SWNT alignment . . . 121
6.2.2 Lowering contact resistance at the SWNT-metal junction . . . 126
6.3 Characterisation . . . 129
6.3.1 SWNT resistance (R_{CNT}) investigation - Optimisation of SWNTs alignment . . . 129
6.3.2 Contact resistances (R_C) investigation . . . 139
6.4 Discussion . . . 143
6.4.1 Wettability - influence of metal electrodes . . . 144
6.4.2 Deposition of Pt contacts on top of the SWNTs-Al and SWNTs-Ti junction . . . 145
6.5 Conclusions . . . 147

7 Preparation and characterisation of Carbon Nanotubes-Polyimide (CNTs-PI)

composite **150**
7.1 Introduction . . . 150
7.2 Randomly orientated CNTs-PI composites . . . 151
7.2.1 Preparation . . . 151
7.2.2 Characterisation . . . 154
7.3 Aligned CNTs-PI composites . . . 160
7.3.1 Dielectrophoresis (DEP) induced CNTs alignment . . . 160
7.3.2 Dielectrophoresis simulations . . . 162
7.3.3 Characterisation . . . 164
7.4 Conclusions . . . 168

8 A resistive CNTs-PI composite humidity sensor **170**
8.1 Introduction . . . 170
8.2 Sample preparation . . . 171
8.2.1 Randomly dispersed CNTs-PI composites . . . 171
8.2.2 Sensor fabrication . . . 172
8.2.3 Aligned CNTs-PI composites . . . 173
8.3 Sensing mechanism . . . 176
8.3.1 At low CNT concentration . . . 176
8.3.2 At CNT concentration around the percolation threshold . . . 177
8.3.3 At high CNT concentration . . . 178
8.4 Characterisation . . . 179
8.4.1 Resistance of the composite . . . 179
8.4.2 Response to humidity . . . 181
8.5 Comparison with other studies . . . 187
8.6 Conclusion . . . 188

9 Conclusions and future work **190**
9.1 Characterisation of MEMS materials . . . 190
9.1.1 A MEMS for thermal conductivity measurements of conductive thin films . . . 191
9.1.2 Stress relief in PI cantilevers . . . 192
9.2 SWNTs interconnects - Improvement of the contact resistance at the SWNTs-metal interface . . . 193
9.3 CNTs-PI composite material . . . 194
9.3.1 Improvement of composite properties . . . 194
9.3.2 CNTs-PI composites resistive humidity sensor . . . 196
9.4 Future work . . . 197
9.4.1 Residual stress control . . . 197
9.4.2 Low resistivity CNTs interconnects . . . 198
9.4.3 CNTs-PI composites . . . 198

A Fabrication process details **200**
A.1 Tools used for the fabrication . . . 200
A.2 Fabrication processing parameters . . . 201

B Mask design **203**

B.1 Design of the MEMS used for thermal conductivity measurement 203
B.2 Design of the electrodes used for SWNTs alignment 204

C Publications **205**

References **206**

List of Figures

1.1 Schematic of the thesis outline 10

2.1 Schematic of the PMDA-ODA Kapton polymeric repeat unit structure . . 15
2.2 Common diamine and dianhydride monomers; adapted from [70] 16
2.3 Polymerization process of Polyimide; adapted from [56] 17
2.4 FTIR spectrum of Polyimide cured at 200°C 19
2.5 Types of hybridisations of carbon 23
2.6 A representation of how a carbon nanotube is formed by joining point 0 to point A; adapted from [103] 24
2.7 Illustrations of three different SWNT structures that are examples of (a) a zig-zag-type nanotube, (b) an armchair-type nanotube, (c) a helical nanotube; adapted from [103] 26
2.8 A first Brillouin zone of graphene; adapted from [107] 27
2.9 1D energy dispersion relations for CNTs adapted from [30] 27
2.10 Schematic of a CNT-FET device 30
2.11 Band diagram of a metal and a semiconductor (a) before contact and (b) after contact 31

3.1 Illustration of the translation and rotation of a CNT (modelled as a single dipole in a prolate ellipsoid) in the electric field between two charged electrodes 41
3.2 Clausius-Mossotti factor for analysis of metallic CNTs in DI water 43
3.3 Schematic of oxidation process via LPCVD 46
3.4 Schematic of a PECVD system 47
3.5 Schematic of a sputtering system 48
3.6 FIB material deposition 49
3.7 Basic photolithography and pattern transfer 50
3.8 Lift-off process 51
3.9 (a) Typical isotropic and (b) anisotropic etch profiles 51
3.10 Schematic of a parellel plate reactor (RIE) 53
3.11 Induced coupled plasma system 54
3.12 Schematic of a conductive material sample 56
3.13 Set-up of four-point probe measurement technique 56
3.14 Schematic of four terminal Greek cross sheet resistance test structure . . 57
3.15 Schematic of a DMA system 59
3.16 Heater on substrate, adapted from [193] 60
3.17 Schematic of an AFM set-up 62
3.18 Schematic diagram of a scanning electron microscope 63
3.19 White light interferometer system 65
3.20 Schematic of an FTIR set-up 66
3.21 Mechanism of photoelectron emission in X-ray Photoelectron Spectroscopy 67

4.1 Schematic of the heat transfer in the metal beam 71
4.2 Schematic of the reference and test structures 75
4.3 CoventorWare simulations of the temperature profile of the test structure with and without Al thin film covering the measuring stripes 79
4.4 Temperature profile of the metal beam of the test structure 79
4.5 CoventorWare simulation of the temperature profile along the test structure for different heating stripe widths of 2, 5, 15 and 25 μm 80
4.6 CoventorWare simulation of the temperature profile along the final reference and test structures 81
4.7 Temperature profile along the structure 82
4.8 Fabrication process flow 82
4.9 Released ITO heating stripe 86
4.10 SEM pictures of the top view of the fabricated ITO reference and test structures 87
4.11 SEM image of a 10 μm wide and 200 μm long Ti bridge 88
4.12 Experimental change of resistance over a range of temperature for Ti bridges 89
4.13 Applied voltage between pads A and D versus measured current between pads B and C for (a) ITO, (b) Ti and (c) Al thin films 90
4.14 Measured voltage between pads B and C versus measured current between pads B and C for (a) ITO, (b) Ti and (c) Al thin films 92

5.1 Schematic of the deflection of a PI cantilever beam due to fabrication process 97
5.2 Schematic drawing of (a) the beam deflection and (b) stress distribution in the PI cantilever 99
5.3 Fabrication process flow of PI cantilever 101
5.4 Optical image of an etch undercut 102
5.5 Fabrication process flow of PI membrane for FTIR spectroscopy measurements 104
5.6 Interference fringes showing that the PI cantilever is less curved after Ar^+ plasma exposure 105
5.7 3D plots and the respective deflection profiles of a 100 μm long, 20 μm wide and 1.9 μm thick of untreated and plasma treated PI cantilever for 1 minute at 100, 150, 200 and 250 eV 106
5.8 Maximum out of plane displacement at the tip end of a PI cantilever beam of 20 μm wide and 1.9 μm thick as a function of beam length exposed to Ar^+ bombardment for 1 min with different Ar^+ ion energies 107
5.9 Out of plane displacement at the tip end of a PI cantilever beam of 200 μm long, 20 μm wide and 1.9 μm thick exposed to Ar^+ bombardment for 1 min as a function of Ar^+ ion energies 108
5.10 Maximum out of plane displacement at the tip end of a PI cantilever beam of 10 μm wide and 1.9 μm thick as a function of beam length for different Ar^+ ion bombardment exposure time at 100 eV Ar^+ ion energy 109
5.11 Scanning electron microscope image of untreated and Ar^+ plasma treated PI cantilever at different energy and exposure time 110
5.12 XPS spectra of C 1s of untreated and plasma-treated PI film 112

5.13 XPS spectra of O 1s of untreated and plasma-treated PI film 112
5.14 XPS spectra of N 1s of untreated and plasma-treated PI film 113
5.15 Deconvolution of C 1s, O 1s and N 1s peaks of untreated and treated PI under Ar^+ plasma at 250 eV for 3 min 114
5.16 FTIR spectra of the PI films exposed to Ar^+ plasma for 3 min at different energies 116

6.1 Fabrication process flow of A) Al and B) Ti electrodes 122
6.2 Clausius-Mossotti factor of SWNTs suspended in DI water 124
6.3 COMSOL simulations of the (a) electric field (E) and (b) dielectrophoresis force (F_{DEP}) induced by a 10 V_{p-p} AC elecric field applied to rectangular electrodes 124
6.4 Dielectrophoresis procedure to align SWNTs between metal electrodes . 125
6.5 Schematic diagram of a CNT bridging two metal electrodes 127
6.6 Side view of a SWNT bridging Al electrodes with Pt leads at the SWNT-Al junction in order to lower R_c 128
6.7 I-V characteristics of SWNTs bridging (a) Al and (b) Ti electrodes separated by a 10 μm gap as a function of SWNT concentration 130
6.8 SEM images of aligned SWNTs as a function of SWNT concentration of (a) 0.1 wt% (b) 0.05 wt% (c) 0.01 wt% (d) 0.005 wt% 131
6.9 I-V characteristics of SWNTs bridging (a) Al and (b) Ti electrodes separated by a 10 μm gap as a function of the electric field magnitude . 132
6.10 Resistances of SWNTs bridging Al and Ti electrodes separated by a 10 μm gap taken at 1 V for different applied voltage 133
6.11 SEM images of aligned SWNTs as a function of the electric field magnitude of (a) 2 V, (b) 4 V (c) 6 V, (d) 8 V, (e) 10 V 134
6.12 Resistances of SWNTs bridging Al and Ti electrodes separated by a 10 μm gap taken at 1V for different applied frequency 135
6.13 I-V characteristics of SWNTs bridging (a) Al and (b) Ti electrodes separated by a 10 μm gap as a function of frequency 136
6.14 SEM images of aligned SWNTs as a function of the applied frequency of (a) 10 kHz, (b) 100 kHz (c) 500 kHz, (d) 1 MHz, (e) 2 MHz, (f) 10 MHz showing that more SWNTs are aligned between the Al electrodes separated by a 10 μm gap at 1 MHz 137
6.15 I-V characteristics of SWNTs bridging Al and Ti electrodes separated by a 10 μm gap 139
6.16 I-V characteristics of SWNTs bridging Al electrodes separated by a 10 μm gap with and without Pt contacts at the SWNTs-Al junctions 141
6.17 I-V characteristics of SWNTs bridging Ti electrodes separated by a 10 μm gap with and without Pt contacts at the SWNTs-Ti junctions 141
6.18 SEM image of SWNTs bridging Ti electrodes separated by a 10 μm gap . 142

7.1 Preparation of CNTs-PI composite via in situ polymerisation procedure . 151
7.2 Preparation of CNTs-PI composite via solution mixing processing 153
7.3 Electrical conductivity of CNTs-PI composite as a function of CNTs concentration 154

7.4 Percolation equation fit to experimental data for the determination of the percolation concentration of CNTs-PI composite 155
7.5 DMA scan of 1 wt% of CNT-PI composite 157
7.6 Storage moduli of PI and CNTs-PI composites with different CNTs concentrations as a function of temperature 157
7.7 Glass transition temperature (T_g) of CNTs-PI composites as a function of CNT concentration 159
7.8 (a) Schematic of the fabrication process flow and (b) the final structure used for CNTs alignment 161
7.9 Aligned CNTs in the direction of the electric field 162
7.10 Clausius-Mossotti factor for CNT into PI 163
7.11 COMSOL simulations of the (a) electric field (E) and (b) dielectrophoresis force (F_{DEP}) induced by a 8 V_{p-p} AC electric field applied to castelled electrodes of 10 μm wide separated by a 10 μm gap 164
7.12 AFM images of CNTs-PI solution subjected to (a) no electric field and (b) an AC electric field of 800 kV/cm at 1 KHz during curing 165
7.13 Influence of DEP on the electrical conductivity of the CNTs-PI composites as a function of CNT concentration 166
7.14 Zoom in the percolation threshold region 167

8.1 Solution mixing processing synthesis of CNTs-PI composites 171
8.2 Fabrication process flow of the CNTs-PI resistive humidity sensor 172
8.3 Optical image and schematic of the CNTs-PI resistive humidity sensor . . 173
8.4 COMSOL simulations of the (a) electric field (E) and (b) dielectrophoresis force (F_{DEP}) induced by a 10 V_{p-p} AC electric field applied to interdigitated electrodes of 20 μm wide separated by a 20 μm gap 175
8.5 (a) Optical image and (b) AFM scan of CNTs aligned inside PI between Al electrodes 176
8.6 Conductive pathways created by tunnelling effect through CNTs-PI composite (a) at low CNT concentration and (b) at high CNT concentration 176
8.7 Resistance of CNTs-PI composite as a function of CNT concentration . . . 180
8.8 The change of resistances of randomly dispersed CNTs-PI composite films as a function of humidity levels for (a) 0.025 wt%, (b) 0.05 wt%, (c) 0.2 wt% and (d) 1 wt% CNTs concentration 181
8.9 The change of resistances of aligned CNTs-PI composite films as a function of humidity levels for (a) 0.025 wt%, (b) 0.05 wt%, (c) 0.2 wt% and (d) 1 wt% CNTs 184

B.1 Schematic of the design of the three masks used for the fabrication of the MEMS device for the measurement of thermal conductivity of conductive thin films 203
B.2 Schematic of the design of the mask used for the SWNTs alignment . . . 204

List of Tables

2.1 Electron affinity and log of the reaction rate constant (log k_r) for different dianhydride reacting with ODA 17
2.2 Acid dissociation constant and log of the reaction rate constant (log k_r) for aromatic diamines reacting with PMDA 17
2.3 Polyimide 2545 cured film properties 18
2.4 Representative properties of SWNT used in Chapter 6 25

4.1 Al properties used in the FEM simulations 78
4.2 Physical dimensions of the reference and test structure 81
4.3 List of thermal conductivity of various materials 85
4.4 Measured linear and quadratic coefficients of temperature for ITO, Ti and Al thin films 89
4.5 Thermal conductivity values of bulk and measured thin film material of ITO, Ti and Al 93

5.1 Mean stress and stress gradient values for a 200 μm long, 20 μm wide and 1.9 μm thick PI cantilever exposed to 100, 150, 200 and 250 eV respectively 108
5.2 Concentration in percentage of carbon, oxygen and nitrogen element at the surface of untreated and Ar^+ plasma-treated PI at 250 eV for 3 min . 111
5.3 The percentage of component ratios of untreated and Ar^+ plasma-treated PI film at 250 eV for 3 min 115

6.1 Dielectrophoresis parameters chosen for an optimised SWNTs alignment 138
6.2 Comparison of the improvement in contact resistance 147

8.1 Sensitivity and linearity characteristics of the humidity response as a function of CNT concentration of randomly dispersed CNTs-PI composites 183
8.2 Table comparing the sensitivity and linearity characteristics of the humidity response as a function of CNT concentration of randomly dispersed and aligned CNTs-PI composites 186
8.3 Table comparing the sensing performances of the results obtained in this experiment with other humidity sensors reported in the literature 188

A.1 PECVD oxide and nitride deposition parameters 201
A.2 Parameters of the DRIE-ICP-RIE process 201
A.3 Parameters of oxide etching recipe using Plasmatherm 202
A.4 Parameters of metal etching recipe using a RIE system 202

Chapter 1
Introduction

The topic of this thesis is composed of two strands, namely, micro-electro-mechanical systems (MEMS) and nanotechnology. This chapter introduces the reader to these two fields, their integration and sets the motivation of the thesis. Furthermore, an outline of the thesis structure is presented chapter by chapter with a short summary of their content.

1.1 Micro-electro-mechanical systems (MEMS)

The microelectronics industry plays a major role in the global economic growth. The growth of the microelectronics industry has a strong impact on the improvement of health, safety, education, entertainment and communication. Its development has led to various advanced micro-electro-mechanical systems (MEMS). MEMS are small integrated devices or systems that combine electrical and mechanical components. The physical dimensions of MEMS range from the sub-micrometer level to the millimetre level. MEMS devices can be made of relatively simple structures having no moving elements, to extremely complex structures composed of several moving elements.

1.1.1 History of MEMS

In 1959, Richard Feynman gave a remarkably insightful lecture, ”There is plenty of room at the bottom”. The talk popularised the growth of micro and nano-technology. Feynman introduced the possibility of manipulating matter on an atomic scale [1]. In 1964, Harvey Nathanson from Westinghouse produced the first batch fabricated MEMS device [2]. In the 1970s, the first silicon accelerometer and the first capacitive pressure sensor using a silicon diaphragm were demonstarted and considered to be one of the earliest commercial successes of microsystems devices. In the 1980s, the potentials of MEMS were established attracting a growing interest from the semiconductor industry.

The role and the importance of Si for MEMS applications were recognised and the review ”Silicon as mechanical material” published by Peterson has become a reference for material properties and etching data for silicon [3]. In the 1990's Analog Devices were the first to produce a surface micromachined accelerometer in high volume. The automotive industry used this accelerometer in automobiles for airbag deployment sensing. In those years, the development of MEMS has led to new applications such as inkjet printers, fuel-injection systems and digital microdisplays. In the last decade, MEMS devices have started to be explored for the development of a variety of sensors and actuators. Today, MEMS are controlling our communications networks and used in biomedical applications. MEMS are even getting smaller moving towards nano electro mechanical systems (NEMS). The global market for MEMS has been estimated at $7.6 billion for 2009 and is expected to reach $13.2 billion by 2014 according to Analysts BCC Research. This increase shows the important role of the MEMS industry in today's society.

1.1.2 Residual stress in MEMS

The fabrication of MEMS consists of bulk micro-machining and surface micro-machining. Surface micro-machining is based on thin film technology including deposition, patterning and etching of different layers as presented in section 3.2 of Chapter 3. Thin film processing often induces high residual stress to one or several thin film layers of the MEMS. The induced stress can be distinguished between intrinsic and extrinsic type. Intrinsic stress known as deposition stress usually comes from the growth process, impurities or lattice mismatch between two materials. Extrinsic stress, known as thermal stress arises from an externally applied force or change in ambient conditions such as mismatch in the coefficient of thermal expansion (CTE) between two materials.

This residual stress can lead to undesired effects such as film layer cracking [4] or buckling of micro-beam [5, 6] in various applications. Therefore, it is desirable to minimize the residual stress built in thin film materials during the fabrication process in order to optimize MEMS' performance and functionality [4–6].

For instance, the case of a thin film deposited on a thick substrate can be considered. When the thin film is attached to the substrate, it undergoes either compressive

(negative) or tensile (positive) stress, in other words the thin film experiences compressive or tensile (stretched) forces in order to match the substrate area. In the case of a cantilever, once the sacrificial layer (layer underneath or substrate) is removed, the stress existing in the beam can then redistribute resulting in a bending deformation influencing the dynamics characteristics and functionality of the devices such as RF MEMS switches and micro-accelerator [5]. Furthermore, the presence of residual stress can result in the mechanical behaviour of the MEMS deviating from the designed values.

The above undesirable effects are some examples of why it is important not to neglect the existence of residual stress in MEMS devices. As a consequence, the characterisation of the residual stress as well as the control of its evolution in thin film material have become a large area of research in the MEMS industry. Long-past, the MEMS industry had been based only on metal and semiconductor thin film materials, therefore the stress evolution on these materials are well studied and understood. However, in the 1970's, polymers were introduced in the MEMS industry as photoresists for patterning. From that time, the place of polymers in the microelectronics industry has grown fast for different reasons explained later in section 1.3. Today, polymer thin films are used also as materials in several MEMS devices. However, the study of stress on polymer thin film lags far behind those of conventional materials.

While some studies have been reported on the evolution of stress within materials such as SiC [7], Pt [8], or Cu [9]; SU8 is the only polymer material in which the evolution and control of stress during and after the fabrication process has been investigated [10–12]. On the other hand, ion bombardment has been reported as an interesting approach to modify polymers' properties [13]. The ability to modify polymers' properties permits polymer thin films to be used in a large range of MEMS applications.

Polyimide (PI) is a polymer widely used in microelectronics as an insulating, interlayer dielectric thanks to its excellent electrical, thermal and mechanical properties. Possible ameliorations to adhesion properties have been reported due to surface changes of PI after ion bombardment exposure. Firstly, it has been reported that the formation of a cross-linked layer can increase the mechanical strength of the surface of the layer. Secondly, the increase in surface area of the PI due to higher roughness of the surface after ion bombardment has been identified as another reason for surface adhesion

enhancement. Thirdly, the removal of contaminants that could hamper a good bonding interface between PI and metal has been achieved by ion bombardment.

Likewise, the electrical properties of PI have been reported to change significantly after exposure to different ionic plasma. The dielectric constant of PI has been found to decrease after exposure to fluorinated plasma resulting in an excellent candidate for dielectrics and insulating materials while, exposure to boron ion bombardment created amorphous carbon islands at the surface of the PI films enhancing their electrical conductivity by several orders of magnitude changing the material state from insulating to semiconductor. Hydrogen (H), Helium (He) and Carbon (C) ions irradiation on PI thin films have been shown to increase the hardness and elastic modulus and decrease the tensile strength of the PI [14].

To our knowledge the change of stress in PI thin film related to the exposure of low ion energy bombardment has not been reported so far. In Chapter 5, low energy Ar^+ ion bombardment in a plasma has been employed to relieve the residual stress present in PI cantilever arising from fabrication processing. It has resulted in the recovery of the mechanical bending deformation leading to straight horizontal PI cantilever beams.

1.1.3 Thermal conductivity of conductive thin film materials

Thermal conductivity of thin film materials is another important parameter for many new MEMS applications such as pressure and gas sensors [15], micro-valves [16] and micro-actuators [17]. At thicknesses lower than 1 μm, thin film properties can change drastically from the values of bulk materials. The difference in thermal conductivity between bulk materials and thin film materials is due to the fact that for material with small thicknesses, the thermal transport is lowered by phonon scattering at lattice imperfections and boundaries [16]. This difference increases as the size of electronic devices shrinks and therefore, thermal conductivity can influence the performance and reliability of electronic devices as they enter the nanoscale. Thin film material properties and measurement techniques have attracted engineers' attention in the last few years. The electrical, optical and magnetic properties of thin film materials have been reported widely in the literature. However, there is very little reported on the mechanical and thermal properties of thin films [18].

Different electrical and optical [19–21] methods have been used previously to measure the thermal conductivity of thin film materials using test micro-structures. These test micro-structures based mostly on electrical techniques (such as the well-known 3 ω method that exploits the temperature dependent electrical resistivity for the measurement of thermal properties of a material) are employed generally by injecting a current through a metal heater line patterned on the layer to be characterised and measuring the temperature rise, either by using a separate temperature sensor or by using the heater itself as a thermometer. The thermal conductivity value is then extracted by using appropriate thermal model depending on the structures. Such a technique has been employed largely in cantilever [22], membrane [23, 24], and bridges more especially, for the thermal conductivity characterisation of polysilicon [22, 25–27]. However, most of the techniques mentioned above involve complicated measurement procedures and additional processing fabrication steps that may influence the heat conductivity of the thin film material to be measured.

In Chapter 4, a MEMS test structure has been fabricated based on the model described by [28] for the thermal conductivity measurement of poly-Si. In this work, a similar technique has been developed for the thermal conductivity measurement of ITO, Ti and Al thin films of thickness 500 nm. The main advantage of the test structure presented here is its simplicity and straightforwardness. The measurements can be made in air, they are carried out by applying current and voltage and the analysis considers the heat loss due to convection and radiation. Therefore, no extra measurements need to be taken to compensate for heat loss which could potentially affect the characteristics of the material being tested or lead to the use of complicated fabrication methods followed by intricate measurements and calculations.

1.2 Nanotechnology

The microelectronics industry growth follows Moore's law, made by Gordon Moore in 1965, which predicted that the number of transistors on a chip doubles every 1.5 to 2 years resulting in a continuous improvement of integrated circuits performance every year. As the industry tries to follow this prediction, new materials have been introduced in the fabrication of MEMS. Nanoscale materials have been reported to possess unique properties resulting in higher performance devices. Among the potential promising

materials are carbon nanotubes (CNTs).

CNTs were discovered by Iijima *et al* in 1991 while investigating the soot of an arc-discharge experiment used to create C60 buckyballs [29]. Iijima investigated the periodic structures in the soot by transmission electron microscope (TEM) and concluded that graphene based tubes had been created in the discharge area. Single walled nanotubes (SWNTs) can be described as a rolled up one-atom-thick layer of graphite (called graphene) into a seamless cylinder. By changing the degree of twist of the wrapping graphene sheet different chiralities are obtained resulting in metallic or semiconducting nanotubes [30]. Furthermore, tubes with different diameters fitted into each other, like a Russian doll, make a multi-walled CNT (MWNT) [29]. CNTs are nanoscale materials having excellent intrinsic electrical properties and outstanding mechanical and thermal properties. CNTs are considered as the future new building block of nano-electronics. The structure and properties of CNTs will be presented in more detail in Chapter 2.

1.2.1 CNTs interconnects

As technology scales down, the size of the transistors and interconnects shrinks. The replacement of Al/SiO_2 by $Cu/low-\kappa$ materials has led to a reduction in interconnect delays. However, the resistivity of metals at the nanoscale increases sharply leading to the limitations of copper at such small dimensions. Electron scattering is limited in CNTs due to their 1 dimensional (1D) nature. The electron mean free paths is in the micron range for CNTs, while it is 40 nm for bulk copper [31]. Moreover, the sp^2 hybridisation nature of CNT is responsible for high mechanical strength material capable of conducting current up to $10^9 A/cm^2$ in contrast to $10^6 A/cm^2$ for copper [32]. Nevertheless, in reality, the contact resistance present at the CNT-metal junction can lower the current density in CNT interconnects.

Depending on their electrical nature, CNTs could replace conventional materials in the fabrication of transistors and interconnects. Semiconducting CNTs are used as electron channel for nano-transistors [33,34] and metallic CNTs are used as wires for microchip interconnects [35–37].

The most promising forms of CNTs that can replace Cu interconnects potentially have

been reported to be SWNTs bundles [38, 39] and large diameter MWNTs [40, 41]. In theory, the use of SWNTs as interconnects can solve the size effect problem as well as lower the interconnect resistances resulting in an improvement of interconnect delays [42].

Although CNT interconnects are seen to be promising for low resistivity interconnects, numerous technical challenges remain for CNTs to be integrated in realistic circuits. The main concerns of scientists are the preparation of high density CNTs bundles, the selective growth of metallic SWNTs [43], the ability to control the growth direction of the SWNTs, the reduction of the contact resistances [41], the fabrication of defect free SWNTs [44] and the growth of SWNTs at lower temperatures [41].

In Chapter 6, low resistivity SWNTs interconnects have been developed by placing SWNTs between Al and Ti electrodes by dielectrophoresis (DEP). Then, Focussed ion beam (FIB) induced Pt contact deposition at the SWNTs-metal junction has been employed to improve the contact between SWNTs and the metal (Al and Ti) electrodes and therefore reduce the resistances of the devices further.

1.3 Integration of nanotechnology and MEMS

After looking at the characterisation of MEMS materials and the possible uses of CNTs into micro-electronics interconnects applications, interest has been devoted to the integration of CNTs and PI as composite materials and their possible applications.

1.3.1 Composite material

For the new fast-growing market applications such as transparent electrodes, flat-panel displays or window glass, materials having good thermal and electrical stability and high mechanical properties are required. This is also the case for the aerospace and automotive industries where mechanical strength and conductivity are important parameters needed in the development of innovative equipment. CNTs-polymer based composite materials are seen as an excellent candidate material to satisfy the new aspects required in such micro-electronics applications. The excellent thermal and electrical conducting properties and the high mechanical strength of CNTs make them

a promising filler material for composite properties enhancement. The reason for the huge interest in CNTs-polymer composites is due to the fact that CNTs-polymer composites are often preferred over heavy weight, rigid metals for such applications due to their superior flexibility, light weight, better durability, and tunable properties. CNTs have been integrated into most of the common polymers such as epoxy resins, PMMA, PI and many others. In particular, the integration of CNTs into a non-conductive polymer has been found to form an excellent material for electrostatic dissipation (ESD), and electromagnetic interferences (EMI) shielding application [45–48]. Two interesting reviews reporting the properties of CNTs-polymer composites summarise the large amount of papers published in the field [49, 50]. Although this research area seems very promising, some challenges still remain to achieve CNTs-polymer composites with high performances.

One of the most important parameters in the preparation of a strong and electrically conducting polymer composite is the homogeneity of the filler dispersion within the polymer matrix. CNTs tend to agglomerate with each other due to van der Waals forces, leading to difficulties in separating and dispersing them evenly into the polymer matrix resulting in a weak interface between polymers and nanotubes [51]. A good dispersion increases the interaction surface between the nanotubes and the polymer and limits the CNTs aggregating with each other [52]. Various dispersion methods exist to prepare CNTs-polymer composites leading to composite materials with different physical properties [49, 50]. In addition, it has been reported that an alignment of the CNTs within the polymer matrix prevents significantly the CNTs to agglomerate with each other and therefore improve the quality of the dispersion. Several techniques have been proposed to align CNTs into polymer matrices [53].

Another key parameter for an efficient load transfer of the CNTs properties to the composite material is the strength of the interface between the CNTs and the polymer matrix [51, 54, 55]. In order to improve the interfacial bonding between CNTs and the polymer matrix, the surface of the CNTs can be modified chemically by attaching molecules at the nanotube sidewalls [56–58]. This process is called functionalisation. Nevertheless, some drawbacks of functionalisation have been identified where mechanical improvement has been achieved at the expense of degradation of the electrical properties of the composite [59].

In Chapter 7, the improvement of the electrical and mechanical properties of CNTs-PI composites as a function of CNT concentration has been investigated. PI has been used largely as polymer matrix due to its interesting transparent and flexible material characteristics. Electrically, PI by itself is an insulator and its use in application areas that need electrically conductive polymers has been limited. Mechanically, it is desirable to increase the mechanical strength of the PI for many practical uses. By integrating CNTs into an insulating matrix, one can produce highly conductive thin film at low CNT's loading and reach a level of electrical conductivity high enough for electromagnetic interference shielding and to prevent electrostatic charge. The integration of CNTs into PI has been reported by several authors to lead to high performance CNTs-PI composites [60–64]. The difference between this work and previous studies on CNTs-PI composites is the use of dielectrophoresis (DEP) technique to induce a CNTs alignment within the PI matrix in order to improve the composite properties. The mechanical and electrical properties of aligned composite are better than those of random composite, however alignment is not easy to implement in CNTs-polymer composite in traditional ways. The use of DEP has been reported recently improving significantly the electrical and mechanical properties of an epoxy resin [65] and a high density polyester (HDPE) [66].

1.3.2 Composite based humidity sensor

The main advantages of polymers over inorganic materials lie in the fact that they are easy to shape and process, they can be tailored to give a wide range of properties while requiring low temperature processing and having relatively low cost compared to Si [67]. These characteristics provide lighter, more flexible and less expensive micro-electronics devices. Therefore, polymers are a credible alternative to replace inorganic materials in many MEMS applications and among others, humidity sensors. In addition, polymer and polymer composite materials are expected to provide a new range of MEMS applications where conventional inorganic material would be inappropriate.

Humidity has become a critical parameter in numerous applications such as the automotive industry, living environment, agriculture or medical fields [68]. Over the years, humidity sensors have gained much attention from researchers. There

are several types of humidity sensors including optical, hygrometric, capacitive and resistive humidity sensors [69–73]. In the case of capacitive and resistive type humidity sensors, the absorption of water molecules by the sensing layer causes a change of dielectric constant or a change of conductivity of the material respectively.

PI has been reported as a very good sensing material for humidity detection due to its ability to be integrated with CMOS process, its resistance to chemical, bi-directional water transport (absorption and evaporation) and high sensitivity [73, 74]. PI has been used first as the key sensing material for a capacitive humidity sensor [75–77]. In general, capacitive type sensors have been reported as better devices compared to resistive-type sensors. Their principal asset comes from their linear response while resistive type humidity sensors present a logarithmic response and thus a non-linear sensitivity to humidity. In contrast, resistive type humidity sensors show difficulties detecting relative humidity below 40%. Nevertheless, besides these drawbacks, PI resistive humidity sensors have also been reported to have a large sensitivity to humidity involving simple and straightforward measurements [78, 79].

Due to their large surface area and hollow cores, CNTs are excellent material for physical absorption and chemical interaction [80]. In particular, CNTs are promising materials for humidity sensing due to a large and linear change of resistance in the presence of water molecules [80, 81]. As a result, the fabrication of CNTs-PI based composite humidity sensors has been seen recently as a potential solution to overcome the non-linear response and the too high threshold of humidity level detection of PI.

In Chapter 8, CNTs-PI composites with randomly dispersed and aligned CNTs have been used to fabricate resistive type humidity sensors, respectively. The sensing performance of the devices have been found to depend on the CNT concentration and the degree of CNTs alignment inside the PI matrix.

1.4 Thesis outline

An overview of the structure of the thesis is illustrated in Figure 1.1 and a brief summary of each chapter is found below.

This thesis deals with two main strands, MEMS and nanotechnology and their

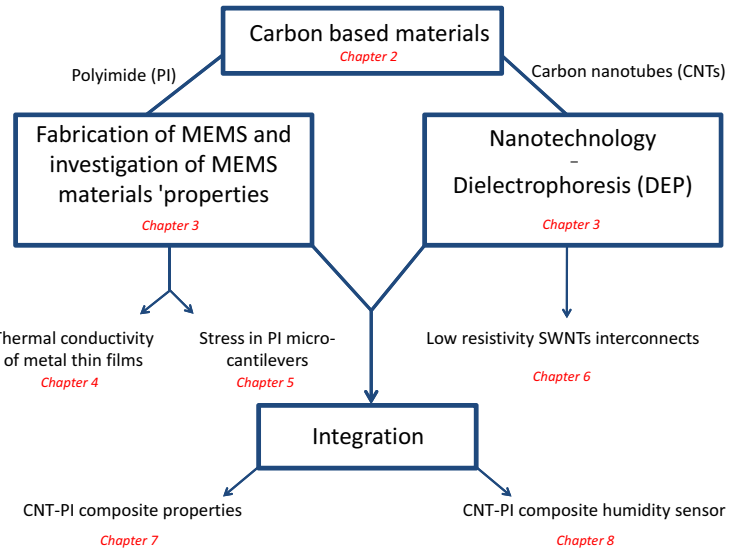

Figure 1.1: *Schematic of the thesis outline*

integration. Chapters 2 and 3 are background chapters. Chapter 2 presents the materials' properties and the applications in which they have been employed in this thesis. The different technologies utilised within this work are described in detail in Chapter 3. The following chapters (Chapters 4 to 8) present the results obtained in this work. The characterisation of MEMS materials and more specifically an investigation on the thermal conductivity and residual stress in thin film materials have been investigated in Chapters 4 and 5 respectively. The development of CNTs as low resistivity inteconnects for micro-electronic applications is presented in Chapter 6. The last part of this thesis has been focused on the integration of the CNTs with the PI. In Chapter 7, the preparation of CNTs-PI composite material and its electrical and mechanical characterisation are discussed. Finally, the as-fabricated CNTs-PI composite film has been used as resistive type humidity sensors in Chapter 8.

Chapter 2: Materials and applications. A descriptive introduction to PI and CNTs, the two main materials used in this work, has been made. The first part of this chapter refers to PI. The structure of PI and the diverse applications of PI based on their properties are discussed. The second part is focused on the structure and properties of CNTs. Finally, a brief review of the possible application of carbon nanotubes in electronics and as fillers for composite applications is presented.

Chapter 3: Assembly, fabrication and characterisation techniques. The first part of this chapter is devoted to dielectrophoresis (DEP). Initially, the theory behind DEP is explained alongside the Clausius Mossotti factor, the electric field and the dielectrophoresis forces acting on the CNTs. Then, the recent applications of DEP on CNTs are discussed. In the second part, a description of the various processes used to fabricate the different electronic devices presented in this thesis is made. It includes thin film deposition, patterning and etching techniques. Finally, in the last part of this chapter, the characterisation techniques employed to check the structures fabricated and their performances are explained.

Chapter 4: A MEMS for thermal conductivity measurement of conductive thin films. In this chapter, the fabrication of a MEMS for thermal conductivity measurement of conductive thin films is presented. The heat transfer model of the fabricated MEMS is explained including the role of the different heat transfer mechanisms by conduction, convection and radiation on the final heat balance equation. CoventorWare FEM simulations have been performed to optimize the design of the MEMS devices in order to achieve reliable and accurate measurements. Finally, the thermal conductivity of Al, ITO and Ti thin film metals has been calculated.

Chapter 5: Stress recovery in Polyimide (PI) MEMS. In this chapter, low energy Ar^+ ion bombardment approach has been used to relieve the residual stress arising from fabrication processing present in a PI cantilever. An appropriate control of the ion energy and exposure duration has led to the recovery of the mechanical bending deformation of the beam resulting in straight horizontal PI cantilever beams. XPS and FTIR non destructive surface and structural characterization techniques have shown that low ion energy bombardment lead to chemical bonds breaking and re-arrangement. The reduction of C=O groups and the increase in C-O and C-N-C groups correlate with the reduction of the mechanical deflection present in the PI cantilever beams. The process of bond re-arrangement and/or the new bond re-arrangement may induce the stress relaxation of the PI cantilevers.

Chapter 6: Carbon Nanotube interconnects - Improvement of the contact resistance at the SWNTs-metal interface. SWNTs interconnects have been fabricated by placing SWNTs between Al and Ti electrodes using DEP. The resistance of the subsequent SWNTs interconnects have been measured showing the important role

contact resistance plays at the SWNTs-metal interface. FIB technique has been employed to reduce the high contact resistance leading to low resistivity interconnects.

Chapter 7: Preparation and characterisation of Carbon Nanotube-Polyimide (CNTs-PI) composite. This chapter presents the integration of CNTs within PI. CNTs have been integrated into the PI matrix by solution mixing in order to enhance the electrical and mechanical properties of the composite. Once again, DEP has been employed to align CNTs within the PI resulting in a high mechanical strength and highly conductive material at low CNT concentration.

Chapter 8: A resistive CNTs-PI composite humidity sensor. The last chapter presents the fabrication of a resistive type humidity sensor based on the previous CNTs-PI composite material. The high electrical conductivity obtained by integrating CNTs into PI has shown to be sufficient enough to overcome detection problem at very low relative humidity. Furthermore, the increase of CNTs concentration and their alignment induced by DEP into the PI matrix has led to a better sensitivity and linearity of the devices' responses to relative humidity.

Chapter 9: Conclusions and Future Work. An overall summary of the work done and a review of the main results are presented. Possible improvements and future work are suggested from the obtained results.

Chapter 2
Materials and applications

2.1 Introduction

The high demand for thin, lightweight, flexible and low cost electronics has led to the integration of polymer material into MEMS devices. One of the main advantages of polymers over inorganic materials lie in the fact that their properties can be tailored by post-processing treatment to give a wide range of properties while requiring low temperature processing. Therefore, polymers are a credible alternative to replace inorganic materials in MEMS and are also expected to provide a new range of applications where conventional inorganic material would be inappropriate. In addition, the downscaling of the technology from micro-technology towards nano-technology requires the use of new materials instead of conventional materials such as Si in the fabrication of electronic devices. Nanoscale materials have been reported to possess unique properties resulting in higher performance devices. Carbon nanotubes (CNTs) are among the potential promising materials.

The aim of this chapter is to introduce Polyimide (PI) and carbon nanotubes (CNTs), the two main materials involved in this work. The structures information of each material is provided. The possible applications of each materials are also reviewed.

Section 2.2 of this chapter is devoted to PI. Initially, the various types of monomers available to synthesize PI at different molecular weight are presented. The synthesis methods employed later in this work to prepare PI thin film are then described. Moreover, PI applications in recent years due to the properties improvement is discussed.

Section 2.3 is focussed on CNTs. First, CNT structures and associated properties is reviewed. Then, the several existing synthesis methods to produce CNTs are listed and briefly described. Finally, the use of CNTs in electronic applications and filler reinforcement into composite materials is reviewed in the last section.

2.2 Polyimide

2.2.1 Structure and synthesis

Polyimides (PI) belong to a class of thermally stable organic materials often used in micro-electronics applications. Polyimides are a chemical family by themselves with numerous possible variant forms due to the different monomers available for their synthesis. Most of the PI are aromatic and consist of a large series of carbon atoms alongside nitrogen and oxygen atoms that usually form five aromatic rings such as the Kapton PI2545 used in this thesis (Figure 2.1).

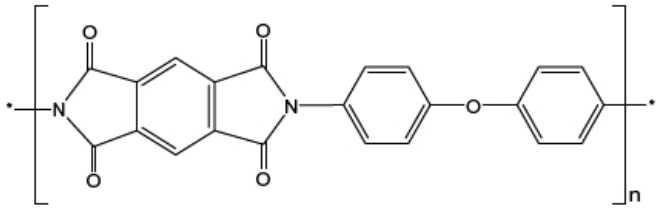

Figure 2.1: *Schematic of the PMDA-ODA Kapton polymeric repeat unit structure*

In the 1950s, researchers at Dupont developed a standard process known as the two step poly(amic acid) method to synthesise PI. This synthesis method consists of the addition of a dianhydride and diamine at ambient conditions in a dipolar aprotic solvent such as N,N-dimethylacetamide (DMAc) or N- methylpyrrolidinone (NMP) to yield the formation of an intermediate poly(amic acid) via a nucleophilic attack on the carbon atom of the carbonyl group from a dianhydride by the free electron pair of the nitrogen from the aromatic diamine. The chemical bond formation between the nitrogen of the diamine and the carbon of the dianhydride results in the cyclic intermediate poly(amic acid). Figure 2.2 lists the common diamine and dianhydride monomers used for the synthesis of poly(amic acid) [82].

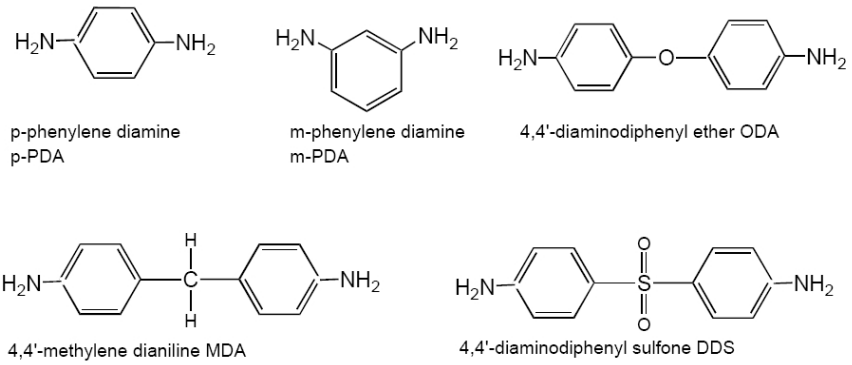

(a) Diamine monomers

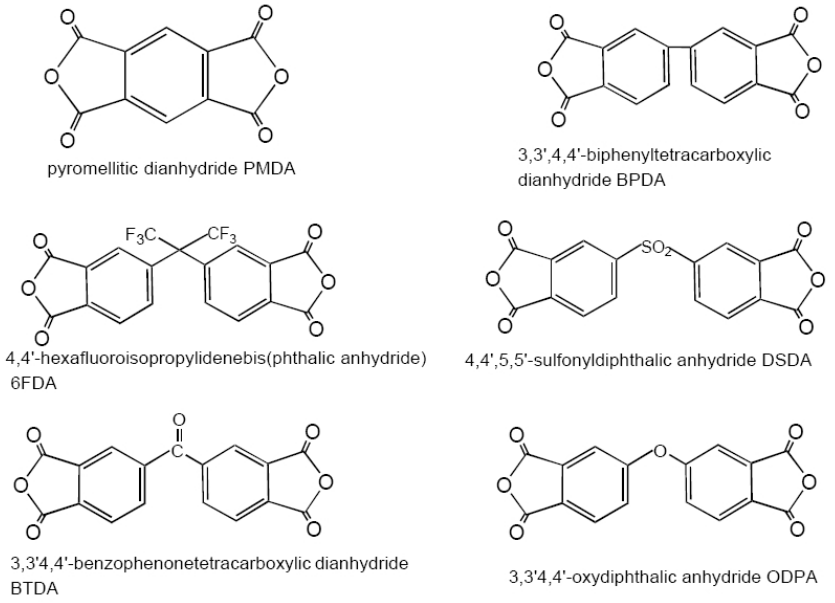

(b) Dianhydride monomers

Figure 2.2: *Common diamine and dianhydride monomers; adapted from [70]*

Besides this main reaction, the synthesis process induces other undesirable side reactions that can affect the final product. Among them, a reversible reaction takes place where the anhydride ring opens to form an amic acid group. The former main reaction being much faster than the latter, it results in an irreversible reaction yielding high molecular weight product when high purity monomers are used. In order to produce high molecular weight poly(amic acid), a high reactivity between the two monomers is also required. The monomer reactivity is defined by the capability of

a nucleophilic group to accept an electron pair and it has been found to depend on the electron affinity, E_A, of the dianhydride and the acid dissociation constant of the diamine as shown in Tables 2.1 and 2.2 [83] [84].

Dianhydride	E_A (eV)	log k_r
PMDA	0.85	0.78
DSDA	0.52	1.05
BTDA	0.48	0.49
BPDA	0.21	0.13
ODPA	0.18	-0.06

Table 2.1: *Electron affinity and log of the reaction rate constant (log k_r) for different dianhydride reacting with ODA*

Diamine	pK_a	log k_r
p-PDA	6.08	2.12
ODA	5.20	0.78
m-PDA	4.80	0
DAPB	3.10	-2.15

Table 2.2: *Acid dissociation constant and log of the reaction rate constant (log k_r) for aromatic diamines reacting with PMDA*

The classic two-step poly(amic acid) process to synthesise PI is illustrated in Figure 2.3. The approach consists of the addition of a dianhydride and diamine at ambient conditions in a dipolar aprotic solvent such as N,N-dimethylacetamide (DMAc) or N-methylpyrrolidinone (NMP) to form an intermediate poly(amic acid). In this study, the intermediate PMDA-ODA poly(amic acid) PI2545 has been imidized by thermal heating to obtain the final PI thin layer. This thermal processing is also called ”curing”, but actually it consists of cyclodehydration of the poly(amic acid) to form ordered and stiff polyimide chains [62].

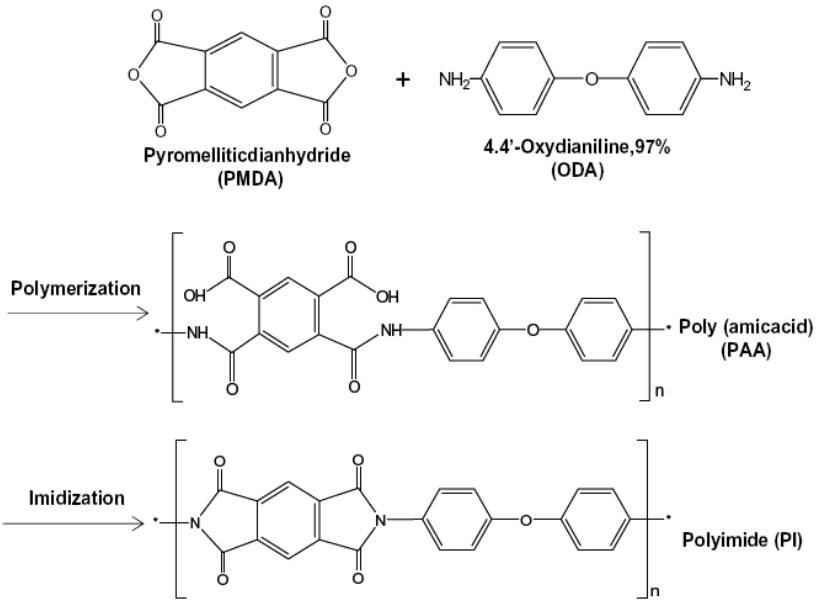

Figure 2.3: *Polymerization process of Polyimide; adapted from [56]*

PI is widely used in microelectronics as an insulating, interlayer dielectric due to its excellent electrical, thermal and mechanical properties [82]. Table 2.3 lists the main properties of the PI2545 PI used within this work.

Properties	Values
Tensile strength (MPa)	260
Elongation (%)	100
Modulus (GPa)	2.3
Dielectric constant	3.5
Dissipation factor	0.002
Coefficient of thermal expansion 1μm film (ppm)	13
Glass transition temperature	$\geq$ 400°C
Decomposition temperature	580°C
Weight loss (% at 500°C , 60 min)	1.86
Refractive index	1.78

Table 2.3: *Polyimide 2545 cured film properties*

For these applications, poly(amic acid) is used generally and imidized to PI by thermal

curing at temperatures above 300°C. However, recently, PI has been introduced into the fabrication of new electronic devices where a 300°C thermal treatment can critically affect the devices' performance. For instance, PI has been used as gate dielectric layers in organic field-effect transistors [85] and as insulation layer in organic light emitting diodes [86]. These devices require temperatures lower than 300°C to achieve high performance.

The physical properties of PI are dependent on the degree of imidization of the product. Infrared spectroscopy (FTIR) is the most commonly used technique to determine the degree of imidization of PI. The principle of FTIR will be discussed in more detail in Chapter 3, section 3.4.4. The FTIR spectrum of PI is presented in Figure 2.4, providing important insight about the quality of the PI film produced. According to HD Microsystems, the company which provides us with the poly(amic acid), "a 200°C cure temperature cycle will result in 95% of imidization". A FTIR spectrum of the as-prepared sample has shown no significant differences between the 200°C cured PI used in this work (can be seen in Figure 2.4) and a 300°C cured Polyimide [87] showing a good imidized product. Therefore, it has been concluded that the imidization of PI at 200°C is sufficient enough to achieve low stiffness PI structures having the main structural characteristics of a 300°C cured PI film. Likewise, this procedure could broaden their industrial applications.

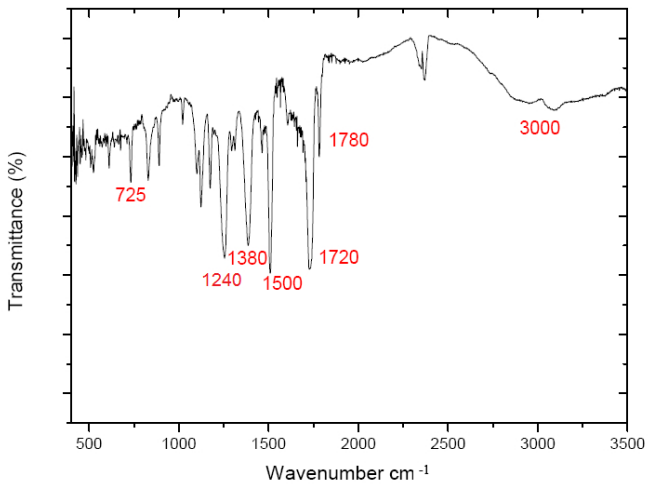

Figure 2.4: *FTIR spectrum of Polyimide cured at* 200°*C*

The main characteristic bands of PI are the imide absorption bands around 1780

cm^{-1}(C=O asymmetrical stretching), 1720 cm^{-1} (C=O symmetrical stretching), 1380 cm^{-1} (C-N stretching) and 725 cm^{-1} (C=O bending) [87]. The total absence of a C=C vibrational peak at 1635 cm^{-1} indicates the complete formation of crosslinks [87]. Moreover, the absence of peaks at 3320 cm^{-1} and 1540 cm^{-1} confirms the breaking of N-H bonds and the formation of N-C bonds to form the imide ring [87]. The peak at 1240 cm^{-1} corresponds to the C-O-C vibration between the two aromatic rings [87]. These peaks are characteristics of a full imidization process resulting in a successful cyclodehydration of the poly(amic acid) to form ordered and stiff polyimide chains.

2.2.2 Properties related to applications

The nature or general behaviour of PI is determined by two key characteristics: its chemical structure and its molar mass distribution. The chemical structure and the molar mass distribution define the cohesive forces, the density and the molecular mobility of the PI. The chemical structure refers to the nature of the repeating units, the nature of the end groups, the composition of possible branches and cross links and the nature of defects in the structural sequence. The molar mass distribution corresponds to the average molecular size and its regularity of PI chains [88].

Originally, PI, having a low dielectric constant $\epsilon^{'}$ has been used as dielectric material for packaging applications [82]. Due to the shrinkage of the microchips size, the electrical connections are made closer to each other which may increase the presence of electromagnetically induced noise into the signal. To avoid noise and increase the speed at which the signal passes through the electrical connection, a dielectric material with a low dielectric constant needs to be placed in between the electrical connections [89]. Another property required for dielectric materials in packaging is a low dissipation factor which refers to the power loss in the dielectric. When an electric signal passes through the electrical connections, the dielectric material is polarised and absorbs some electrical energy resulting in heating of the material which corresponds to the dielectric loss, $\epsilon^{"}$ [90]. The dissipation factor is defined as the ratio between the loss and the real components of the dielectric constant of a material. The dissipation factor value for PI has been reported to be as low as 0.002 [91, 92]. In addition, PI has a dielectric strength of 10^5 to 10^6 $V.mm^{-1}$ enabling it to withstand high voltages without breakdown [91, 93].

Furthermore, the fact that the physical and chemical properties of PI and of most polymer materials can be adjusted to almost any specific characteristics desired, has made PI a very promising material for composite and electronic sensors applications as investigated in Chapter 5, 7 and 8. The properties of PI are defined by the monomers and the processing techniques used for their preparation. However, it has been shown in this work that the mechanical and electrical properties of PI can be modified extensively by two different approaches.

Firstly, low energy Ar^+ ion bombardment in a plasma has been employed as a post-fabrication treatment to control the stress present in PI micro-cantilevers. The coefficient of thermal expansion (CTE) of PI is usually higher than that of other typical inorganic materials used in microelectronics fabrication [92, 93]. The mismatch of CTE between the two materials can lead to a consequent stress built in the PI layer during micro-fabrication processing. The elevated temperatures required in plasma etching or metal deposition, result in a faster expansion of the PI layer compared to its surrounding layer [93–95]. In Chapter 5, a tensile stress of ≈ 55.2 MPa has been calculated in a 1.9 μm thick PI cantilever beam released from a silicon substrate causing an out of plane deflection of the PI cantilever beams. The calculated stress value has been found to be in agreement with the 30-55 MPa typical tensile stress of PI thin film on silicon substrate reported by other studies [6, 95, 96]. In this experiment, the residual stress present in PI micro-cantilevers after fabrication processing has been controlled by low energy Ar^+ ions bombardment in a plasma in order to reduce the out of plane deflection of the cantilever beams. The recovery of the out of plane deflection of the cantilever beam has been controlled by both ion energy and bombardment duration resulting in a straight PI cantilever beam.

Secondly, CNTs (conductive and high strength fillers) have been integrated into the PI matrix during its preparation in order to improve the electrical and mechanical properties of the pure PI. In Chapter 7, the use of CNTs as electrical and mechanical reinforcement has drastically enhanced the physical properties of PI. By adding 5 wt% of CNTs to the PI, the electrical conductivity of the composite has been increased by 12 orders of magnitude, changing the electrical state of the composite from insulator to conductor. By integrating 2 wt% CNTs in the PI, the storage modulus of the PI has been improved by about 440% below the glass transition temperature. The T_g of the

composite has been increased from $61.4°$C to $98.6°$C as the CNT concentration increased from 0 to 2 wt%. A more detailed discussion on the benefits of CNTs as conductive and high-strength fillers into polymer composites is made in section 2.2.3.2 of this chapter.

Finally, PI has great potential as a substrate or sensing layer in various MEMS applications as seen in Chapter 8. Over the last decade, polymers have attracted great interest in the fabrication of artificial sensors in the biomedical area. The use of polymer as a sensing element instead of common sensor materials has led to better selectivity and faster sensing devices.

In particular, PI has been widely used as a capacitive humidity sensor [75–77]. The absorption of molecules with high dipole moments or the PI swelling due to the interaction with non-polar particles, changes the permittivity of the PI causing changes of the material capacitance. However, capacitive type humidity sensors have been reported to require more complex and costly measurement setups compared to that of resistive type devices. In the last few years, PI has been studied as a resistive humidity sensor [78]. PI based resistive humidity sensors have been reported showing a large resistance change (up to 6 orders of magnitude) at high humidity levels (detection $\geq$ 50%) [78]. Nevertheless, the nonlinear response to humidity levels and the humidity detection threshold for resistive type humidity sensors are two important drawbacks [78]. These two issues will be amplified when coupled with an external circuitry resulting in poor device performance.

Therefore, PI has been substituted by CNTs-PI composite recently showing a large improvement in the sensing properties of the devices [97, 98]. On the one hand, the humidity detection limit has been improved due to the high conductivity of the CNT integrated to the PI matrix. On the other hand, a higher and more linear change of composite resistance as the humidity level increases has been attributed to the charge transfer that occurs between H_2O molecules and CNTs in the presence of water [97]. In Chapter 8, CNTs have been integrated into PI as shown in Chapter 7 and aligned using DEP, resulting in substantial improvements of the sensing properties of the composite.

2.3 Carbon Nanotubes

Since their discovery in 1991, carbon nanotubes (CNTs) have received tremendous research interest. CNTs are extremely small objects that are expected to be the new building blocks of technology in the near future. They are often seen as the solution to overcome the limitations encountered with current techniques for the miniaturization of microchips [99]. They are inert and versatile, have a high aspect ratio, a large surface area, high electrical and thermal conductivities and possess high tensile strength. Due to their unique properties, they are deemed the promising candidate for a large number of applications provided that their cost is sufficiently low.

2.3.1 Structure and properties

A carbon atom has six electrons which occupy the different energy level shells. Two strongly bound electrons fill the $1s$ atomic orbital which is the case for all carbon hybridisation and four weakly bound electrons fill the $2s$ and $2p_x$, $2p_y$ and $2p_z$ orbitals (Figure 2.5 (a)). However, carbon exists under various forms having different hybridisations as shown in Figure 2.5.

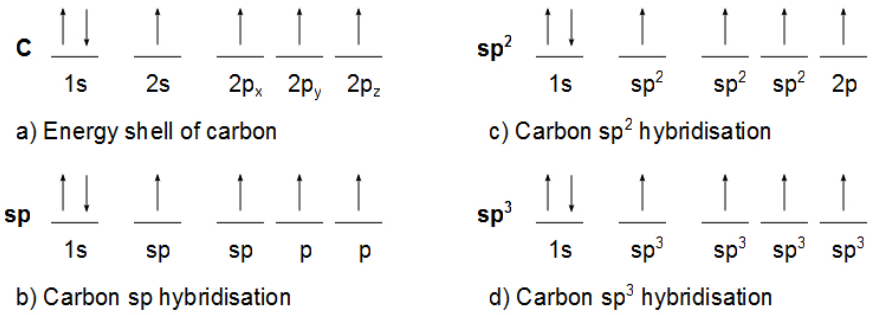

Figure 2.5: *Types of hybridisations of carbon*

In sp hyrbidisation, one of the three 2p orbitals is mixed with the 2s orbitals resulting in two sp orbitals and two remaining unchanged p orbitals (Figure 2.5 (b)). In sp^2 hybridisation, which is the configuration found in graphite and CNTs, two of the three 2p orbitals are mixed with the 2s orbitals as shown in Figure 2.5 (c). In this configuration, a carbon atom forms up to 3 σ bonds between adjacent carbon atoms and one π bond perpendicular to the plane of graphene. Although very strong and

considered as a covalent bond, σ orbitals are not responsible for the electric transport of graphene. The conduction of graphene is determined by the electrons near the Fermi level, since they can easily occupy the unoccupied states. Therefore, it is the π orbitals, which lie near the Fermi level, that contribute to the electrical transport. Finally in sp^3 hybridisation, which is the configuration found in diamond, all the 4 electrons form sp^3 hybrids. The 2s orbitals are mixed with the three 2p orbitals resulting in four σ bonds (Figure 2.5 (d)).

2.3.1.1 Chirality of carbon nanotube

Carbon nanotubes can be considered as a sheet of graphene rolled up to form a hollow cylinder of nanometre scale diameter. The lattice structure of graphene consists of a hexagonal arrangement of sp^2 hybridized carbon atoms as shown in Figure 2.6.

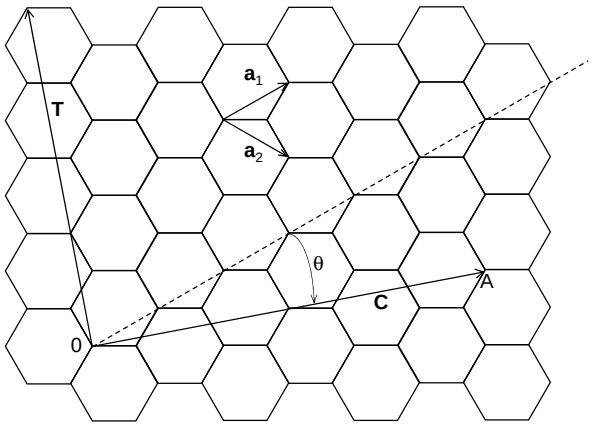

Figure 2.6: *A representation of how a carbon nanotube is formed by joining point 0 to point A; adapted from [103]*

Depending on the direction the tubes are rolled in (called chirality), the electronic behaviour of the carbon nanotubes can change from metallic with no band gap to semiconductor with a distinct band gap. The physical and electronic behaviour of CNTs can be understood and calculated using the tight binding model [100]. Due to the graphitic sp^2 bond between the neighbouring carbon of the rolled graphene sheet, CNTs are expected to be the ultimate high-strength fibres. The sp^2 bond is 33 times

stronger than the sp^3 bond of diamond, the hardest substance in nature [101, 102]. The cylindrical shape of the CNTs along with the very short C-C bond lengths (0.124 vs 0.154 nm for graphene and diamond respectively) give CNTs an extraordinary structural stability under deformation [101, 102]. The mechanical properties of CNTs have been widely reported with Young's modulus and tensile strength values of 1 TPa and 50 GPa respectively [101, 102]. Table 2.4 lists the physical properties of the SWNT used in Chapter 6.

Properties	Values
SWNT diameter(nm)	0.8-1.2
SWNT length (nm)	100-1000
Molecular weight (Amu)	$3.4\times10^5 - 5.2 \times 10^6$
Color	Black
Morphology	Dry powder of nanotube bundled in ropes
Maximum density (g.cm^{-3})	1.6
Bulk density (g.cm^{-3})	0.1
TGA residue as Fe (super pure)	$\leq$5 wt%
Maximum surface area (m^2.g)	1315
Buckypaper resistance (Ω)	0.2-2
Moisture content	$\leq$5 wt%

Table 2.4: *Representative properties of SWNT used in Chapter 6*

The different ways to roll a graphene sheet into tubes are described by the (n,m) indices defined by the chiral vector C, as follows [103]:

$$C = a_1 n + a_2 m \equiv (n, m) \tag{2.1}$$

where a_1 and a_2 are the unit vectors and n and m are the integers of the vector OA.

The diameter of the nanotube can be closely deduced from the chiral vector of the tubes by the following equation [103]:

$$d = \frac{C_h}{\pi} = \frac{a\sqrt{n^2 + nm + m^2}}{\pi} \tag{2.2}$$

Nanotubes can be ordered into three main categories: arm chair tubes (n,n) where $\theta = 30°$, zig-zag tubes (n,0) where $\theta = 0°$ and chiral tubes (n,m) where $0° \leq \theta \leq 30°$ as shown in Figure 2.7. Some tubes show planes of symmetry such as in Figure 2.7 (a) and (b) and others do not, as the one in Figure 2.7 (c). The electronic behaviour of a nanotube can be defined as follows: if $(2n + m)$ is a multiple of 3, the nanotube is metallic; otherwise it is a semiconductor. Consequently, arm chair tubes $(n = m)$ are always metallic, zig-zag tubes are either metallic or semiconductor depending on m (i.e. (9,0) is metallic and (10,0) is semiconducting) and finally chiral tubes can be either metallic or semiconducting. Generally, $1/3$ of the nanotubes are metallic and $2/3$ of nanotubes are semiconducting.

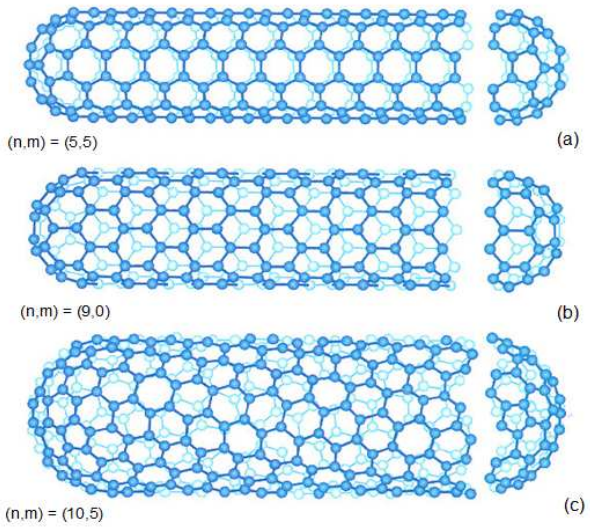

Figure 2.7: *Illustrations of three different SWNT structures that are examples of (a) a zig-zag-type nanotube, (b) an armchair-type nanotube, (c) a helical nanotube; adapted from [103]*

Nanotubes can be categorised as single-walled nanotubes (SWNTs) or multi-walled nanotubes (MWNTs). SWNTs can be described by wrapping a one-atom-thick layer of graphite called graphene into a seamless cylinder. MWNTs consist of multiple rolled layers of graphite. SWNTs can be either metallic or semiconductor, but all MWNTs

are metallic in their behaviour [104, 105]. Metallic CNTs are considered as ballistic conductors due to the low defect density and the limited electron scattering along the tubes, which allow CNTs to withstand high current density ($10^{10} A/cm^2$) that is about 1000 times higher than copper with essentially no heating [106].

2.3.1.2 Unit cell, band structure and 1D energy dispersion

CNTs are a very attractive material due to their one-dimensional (1D) periodic structure along the tube axis. The electronic properties of CNTs are deduced from the electronic structure of graphene. The difference between the electronic properties of graphene and those of CNTs is due to the confinement of the electrons around the circumference of the tubes. The production of a carbon nanotube by rolling up a sheet of graphene, implies new periodic boundary conditions, namely $C \cdot k = 2\pi m$ where C is the chiral vector, k is the wavevector and m an integer. By applying these periodic boundary conditions, the electronic band structure of CNTs can be deduced from the electronic band structure of graphene by cancelling the two-dimensional (2D) energy dispersion relations of the π bond of graphene.

The conduction and the valence bands of graphene meet at the six Fermi points (K points) of the Brillouin zone as shown in Figure 2.8. If the wavevector k passes through the K points, the electrons are free and the nanotube is metallic; otherwise in the $(\Gamma - M)$ direction, the nanotube is semiconducting. In other words, the electrical behaviour of the CNTs can change depending of the orientation of the graphene lattice with respect to the tube axis [107].

Figure 2.9 shows the 1D energy dispersion relations for metallic and semiconducting CNTs. The crossover of the 1D energy dispersion relations at the Fermi level (E_F) indicates a metallic behaviour, whereas the presence of a gap refers to a semiconducting behaviour. The 1D energy dispersion of metallic CNTs such as arm chair (5,5) and zig-zag (9,0) tubes are shown in Figure 2.9 (a) and 2.9 (b) respectively, whilst the 1D energy dispersion of a semiconductor CNT (10,0) is shown in Figure 2.9 (c). It has been found that the band gap of a semiconducting nanotube can vary between zero and 2 eV and is inversely proportional to the tube diameter [30].

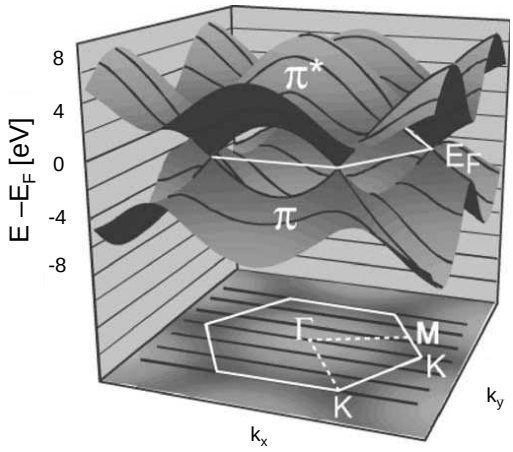

Figure 2.8: *A first Brillouin zone of graphene; adapted from [107]*

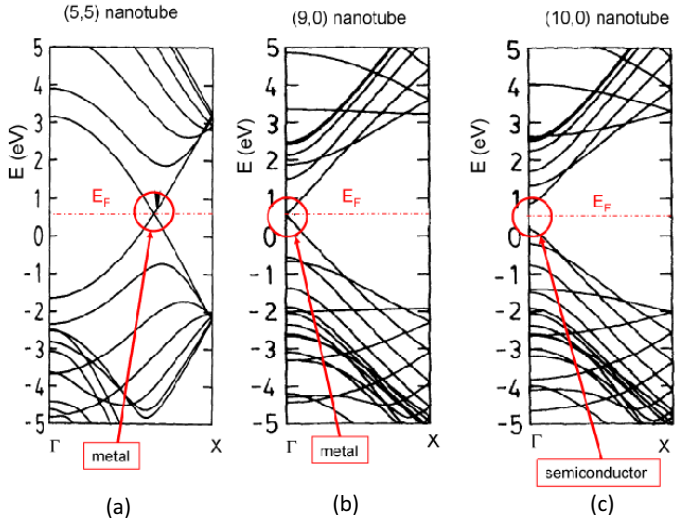

Figure 2.9: *1D energy dispersion relations for CNTs adapted from [30]*

2.3.2 Synthesis

Several methods exist for the bulk production of CNTs such as arc-discharge, laser ablation and chemical vapour deposition (CVD). All these methods involve high temperature processing and produce both metallic and semiconducting nanotubes with different chirality.

The arc discharge method is the one by which CNTs were first produced. A very high current is applied between the anode (a movable carbon rod) and the cathode (the electrode where the carbon is collected) to generate a high energy plasma [43]. The carbon from the anode rod is consumed and deposited on the cathode where it recondenses in the form of nanotubes under the electric arc. By adding metal catalysts to the anode and changing the temperature, either SWNTs or MWNTs can be produced. A yield of 30% by weight is obtained generally.

Laser ablation techniques like arc discharge are based on the condensation of hot gaseous carbon atoms coming from the evaporation of solid carbon. The laser ablation method consists of focussing a laser beam onto a graphite pellet containing the catalyst in a quartz tube filled with Argon gas at a temperature of $1200°$C. The resulting vaporised carbons move along the Argon flow and lie on a water cooled copper collector as the vaporised carbon recondenses [43]. Although very expensive, the laser ablation technique yields CNT concentration of 70%; moreover, the production of more pure CNTs (containing less impurities and defects) with controllable diameters can be achieved under specific synthesis conditions.

The chemical vapour deposition (CVD) technique consists of placing a substrate in a $700°$C to $900°$C reaction chamber with inert gas. The substrate surface is covered with metal catalysts. Then, carbon-containing gas (acetylene, ethylene, ethanol or methane) is introduced in the chamber at a controlled flow rate and enters into contact with the catalysts on the surface of the substrate. At the contact area with the catalyst the gaseous carbon breaks apart, resulting in the growth of CNTs on substrate [43]. CVD method presents the advantage of a lower synthesis temperature and a capacity of growing the tubes directly on a desired substrate.

2.3.3 Applications

The following section presents the current applications of CNTs. CNTs are the ideal material for many applications such as energy storage [108, 109], field emission displays [110, 111], nano-transistors [33, 34], interconnects [35–37] and conductive or high-strength composite.

This section is divided into two parts. In the first part, the applications of CNTs in micro-electronics devices are reviewed focussing on CNT-FET used in many sensor devices and CNTs interconnects. The second part of the section discusses the progress in CNTs based composites.

2.3.3.1 Carbon nanotube in electronics

The actual 32 nm technology node, which refers to the expected average half-pitch of a memory cell at this technology level, is predicted to reach a 22 nm node within 2011 and an 11 nm node by 2015. This prediction is conceivable on the condition that nanotechnology can be controlled on a large scale. As discussed in Chapter 1, the downscaling of the technology will introduce new materials incorporated into nanoscale structures [112]. CNTs are seen as a very promising material for microelectronics due to their nanoscale dimension and exceptional electrical properties [31, 113, 114]. Progress in the separation of metallic and semiconducting CNTs, generally achieved using DEP has led to the commercialisation of field-effect CNT transistors (CNT-FET) [33, 34] and CNT interconnects [35–37].

However, some challenging tasks remain to integrate CNTs into realistic circuits. Among them, the high contact resistance at the CNT-metal interface has been one of the principal issues that scientists have tried to overcome [115, 116].

CNT-field-effect transistors (CNT-FETs)

The operating characteristics of p-type semiconducting SWNTs-FET are comparable to those of a MOSFET. A FET consists of two metal electrodes named source and drain connected by a semiconducting channel. Figure 2.10 illustrates a CNT-FET device.

The semiconducting channel is made of Si in a MOSFET and replaced by a

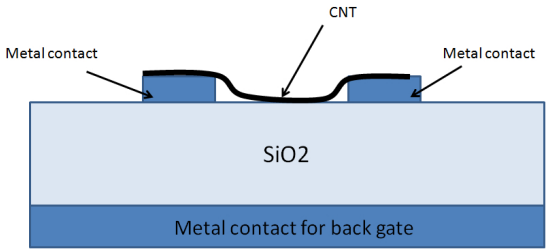

Figure 2.10: *Schematic of a CNT-FET device*

semiconducting CNT in a CNT-FET. A third electrode, designed as the gate, is separated from the channel by an insulating layer. In the case of a p-type FET, where the dominant carriers are holes, a negative charge is introduced on the gate and the applied voltage V_{GS} exceeds a certain threshold, thus a hole current flows through it. In a similar manner, in the case of an n-type FET, an electron current flows throughout the channel when a positive charge is placed on the gate and the applied voltage exceeds the threshold.

In 1998, the first work on CNT-FETs were reported by both Delft and IBM groups [117, 118]. The fabricated CNT-FETs devices behaved as p-type FETs and the ON/OFF current ratio was reported to be around $\approx 10^5$. Their devices showed a high parasitic contact resistance ($\geq 1M\Omega$), low drive current and a low conductance ($10^{-9}A/V = nS$).

The performance of a CNT-FET has been generally characterised by its Schottky barrier (SB) which determines the contact resistance at the CNT-metal interface.

The SB comes from the difference of Fermi levels between the CNT and the metal at their junction and therefore is mainly dependent on the semiconductor band gap and the metal work function. Figure 2.11 shows the band diagrams of (a) a metal and p-type semiconductor SWNT before contact and (b) at the SWNT-metal interface. In that case, the barrier can be defined as, $\phi_B = E_g - (\phi_M - \chi_s)$, where E_g is the bandgap of the semiconductor. However, in the case of an n-type semiconductor SWNT, the barrier is defined as, $\phi_B = \phi_M - \chi_s$ where ϕ_M is the work function of the metal and χ_s is the semiconductor electron affinity, which is the difference between the vacuum E_{vac} and the bottom of the conduction band E_c levels.

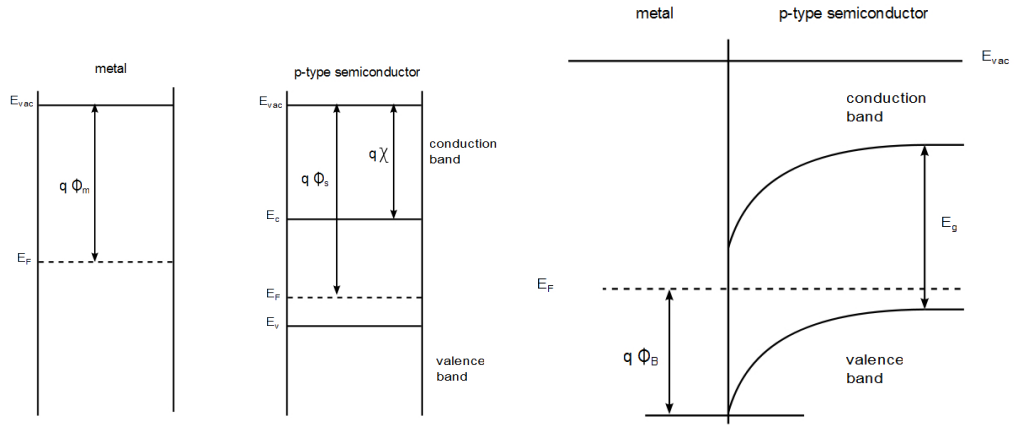

(a) A metal and a semiconductor before contact (b) A Schottky barrier formed after contact of the metal and the semiconductor

Figure 2.11: *Band diagram of a metal and a semiconductor (a) before contact and (b) after contact*

The presence of a SB at the CNT-metal junction increases the contact resistance and therefore tends to be a problem for the device performance. Since the fabrication of the first CNT-FET, important progress has been made towards reducing the contact resistance and improving the characteristics of the CNT-FETs and integrating them into integrated circuits. Bachtold *et al* reported the fabrication of nanotube integrated circuits based on the arrangement of CNT-FETs into logic NOT and NOR gates [119]. Klinke et al functionalised CNT with hydroxamic acid molecules improving the contact resistance between the nanotubes and the metal electrodes resulting in CNT-FETs with excellent electrical characteristics [120]. More recently, the fabrication of an ambipolar CNT-FET that exhibits two logic gate functions in a single logic circuit enables more functions to be implemented with fewer physical resources leading to new opportunities for designing logic circuits for the next generation applications [121, 122]. Moreover, the ability to handle currents 200 times higher than the conventional MOSFET along with their extremely low switching resistance makes CNT-FETs very attractive in many micro-electronics applications. Based on these CNT-FETs, numerous CNT flow sensors [123], strain sensors, chemical sensors [124–127], gas sensors [128, 129] and pH sensors [130, 131] have been fabricated in the last decade.

CNT as interconnects

Besides, CNTs' applications in FETs, CNTs have shown promising characteristics for interconnects due to their large current conduction capability, large electron mean free path, high mechanical strength and stability. As integrated circuits enter the nanoscale regime, the interconnect feature sizes shrink approaching the mean free path (MFP) of electrons in bulk copper resulting in an increase of copper resistivity due to surface and grain boundary scatterings [132, 133]. CNTs have been reported to withstand current densities of up to $10^{10} A/cm^2$ [134]. H. Cho *et al* studied the performances of CNTs and optical interconnects in comparison with the scaled Cu interconnects for high performance integrated circuits. CNTs seem to be a promising material due to their low power density [135]. The use of CNTs as interconnects has led to significant improvements in power dissipation, delay, crosstalk and bandwidth density [136].

In addition, CNTs which are long concentric graphene tubes can be considered as quantum wires where electrons can travel only in one dimension limiting the scattering effect. The transport of electrons is then described as ballistic ($G = h/4e^2$) where e is the electron charge and h is Planck's constant. Thus, the resistance of a SWNT has been calculated as $R = 1/G$ and reported to be approximately 12.9 kΩ. However, experimental values of SWNT resistance integrated into devices have been found to be much higher, hindering the electron transport throughout the external circuit. The reason for the divergence in the resistance values is mainly due to the high additional contact resistance between the SWNTs and the metal, caused by imperfections at the contact. Several studies have been devoted to the reduction of the contact resistance between CNTs and the metal electrodes [115, 116]. The choice of the metal electrodes has been reported to have a strong influence on the devices' resistance where Au and Pd metal electrodes seem to result in the lowest contact resistances [116]. A few post-synthesis techniques have been reported to lower the contact resistance at the SWNTs-metal junction including the use of an ultrasonic bonding technique [137], thermal annealing [138] and electron beam induced deposition of amorphous carbon [139].

2.3.3.2 Carbon nanotube as reinforcement in composite materials

Due to their exceptionally high tensile strength and stiffness, CNTs are a promising candidate as reinforcement for composite materials. CNTs have shown better

mechanical properties than carbon fibres which are already much stronger than steel [140]. In addition, due to their high aspect ratio (length/diameter$\approx$ 1000), CNTs have a large surface area to volume ratio resulting in a larger interfacial contact area with the polymer matrix. The integration of CNTs into a polymer matrix aims to modify the neat polymer properties by adapting the CNTs' exceptional electrical, mechanical and thermal properties into the original polymer's properties. Therefore, many groups such as NASA for aerospace or Zyvex and Mistui Corporations for sport goods and packaging applications invest in the development of CNTs reinforcing polymer composites. The increasing number of CNTs-polymer composite applications range from packaging, automotive, aerospace, sports goods, to energy and many others.

Dispersion

CNT dispersion plays an important factor to the mechanical and electrical properties of the composite [49, 50]. The preparation of a strong and electrically conducting composite is related to the quality of the filler dispersion within the polymer. CNTs tend to agglomerate with each other due to van der Waals forces leading to difficulties in separating them and dispersing them evenly into the polymer matrix. A homogeneous dispersion increases the interaction surface between the nanotubes and the polymer and limits the CNTs to aggregate with each other [52]. Several dispersion methods have been reported to fabricate CNTs-polymer composite including solution mixing, melt spinning, melt processing, in situ polymerization, processing of composites based on thermosets, electrospinning and swelling [49, 50].

Besides the method employed to disperse the CNTs, an alignment of the CNTs into the polymer matrix can have a strong influence on the final properties of the composite [53]. The alignment of the CNTs prevents the agglomeration of the CNTs and thus, improves the quality of the dispersion [53]. The mechanical properties such as stiffness and strength, and electrical properties of a composite material are linked directly to the alignment of CNTs in the polymer matrix [53]. CNTs can be aligned either vertically on a substrate during growth by chemical vapour deposition (CVD) or by post synthesis methods such as electro-spinning, mechanical stretching, magnetic field and electric field into a polymer matrix.

However, a simple mixing of CNTs into a polymer matrix does not always lead to a good load transfer [54]. Therefore, chemical modifying methods, known as functionalisation, to modify the surface of the nanotubes and therefore improve the interfacial bonding with the polymer matrix have been reported [56–58]. There are two conventional attachment methods known as non-covalent and covalent functionalisation. Non-covalent functionalisation is based on van der Waals forces, where functional groups are wrapped around the surface of the nanotube. These functional groups are chosen to be more compatible with the polymer matrix where the tubes are to be integrated in, resulting in a better dispersion. Non-covalent functionalisation has the advantage of not damaging the original structure of the CNTs. However, the weak forces between the wrapping functional groups and the CNT have been reported to lead to a low load transfer [141–143]. On the other hand, covalent functionalisation has been found to improve significantly the load transfer of CNTs-polymer composite. Nevertheless, the covalent attachments modify the surface of the CNTs introducing defects on their walls that can damage their electrical properties, resulting in integrating low strength filler to the polymer [144, 145].

It is noteworthy that functionalisation is not necessary for all composite formation. Furthermore, contrary to the case of mechanical reinforcement, it has been found that functionalisation of the tubes does not always enhance the electrical conductivity properties of the composite [146]. The improvement in mechanical and thermal properties of a composite has been achieved sometimes at the expense of the composite electrical conductivity [59]. This can be explained by the fact that the attachment of molecules at the nanotube sidewalls can alter the sp^2 configuration of the CNTs degrading their electrical properties.

In Chapter 7, solution mixing and in situ polymerisation approaches have been employed to prepare CNTs-PI composite. Solution mixing processing consists of mixing the nanotube and a soluble polymer in a suitable solvent before evaporating the solvent to yield the final composite material. It has been reported as a good technique for debundling and dispersing the CNTs homogeneously [53]. The preparation of CNTs-polymer composite by in situ polymerization technique has led to the higest enhancement of the composite properties [147, 148]. The main advantage of this method is that the reinforcement is obtained at a molecular level. A strong interfacial

bonding between the CNTs and the polymer matrix has been reported via in situ polymerization due to covalent interactions where polymer macromolecules graft onto the walls of the nanotubes [49, 50]. The final properties of the composites are therefore a function of the processing methods. In this work, attention has been dedicated particularly to the enhancement of the electrical and mechanical properties of the CNTs-PI composites by inducing CNT alignment into the PI matrix. Thereby, an electric field has been used with the intention to induce dipole moments in the CNTs, creating translational and rotational forces due to re-distribution of free electrons on the CNTs. These forces served to align the CNTs in the direction of the electric field line as well as prevented agglomeration of the CNTs, improving further the electrical properties of the CNTs-PI composites [149].

Mechanical reinforcement

There are hundreds of reports on the improvement of mechanical properties and possible application of CNTs integrated into various polymer matrices in the literature. Most of these publications have been devoted to the enhancement of two mechanical aspects, the Young's modulus and the tensile strength of the composite [150]. The final composite properties are strongly dependent on the CNT type, growth method, functionalisation as well as the polymer type and the processing method. Although very promising, some challenging requirements exist in order to prepare high performance CNTs-polymer composite materials. In general, the improvement of mechanical properties at low CNT loading concentration depends on the interfacial bonding between the CNTs and the polymer matrix. The highest enhancement of mechanical properties of a composite has been achieved via in situ polymerisation technique where strong interactions between the CNTs and the polymer matrix occur during the growth stage [150]. The advances made in this field have been reviewed widely [151–153].

Thermal reinforcement

It was reported [154, 155] that addition of 1 wt% of SWNTs can led to a 110% increase in the thermal conductivity of the composite. This increase was attributed to the formation of a percolation network of SWNTs. In addition, the coefficient of thermal expansion (CTE) was found to decrease with the addition of SWNTs limiting the curing

shrinkage and offering a better thermal stability of the composite. The improvement in thermal stability of polymers such as PMMA and PVOH [156] with the introduction of SWNTs was also reported. The increase of the glass transition temperature of composites limits the damages caused by temperature effects on their structures and properties and enables the application of these composites at high temperatures [157].

Electrical reinforcement

Beside the fact that CNTs attract strong attention as mechanical or thermal reinforcement in composites, it is worth noting that using CNTs as electrical conductive fillers is also an area of high interest for potential applications in lithium batteries, supercapacitor, polyactuator, biosensor, flexible transparent electrodes, electrostatic dissipation (ESD) and electromagnetic interference (EMI)-shielding application [45–48, 158–160].

Many electrical conductive polymers including polyaniline (PANI), polypyrrole, poly(p-phenylene), polythiophene, poly(p-phenylenevinylene) and Poly(3,4-ethylenedioxythiophene) - poly(styrenesulfonate) (PEDOT-PSS) have shown great performances for applications ranging from microelectronics, to high performance chemical sensors, light-emitting and photovoltaic devices, and displays [161–163]. However, conductive polymers possess some drawbacks, namely, limited thermal stability and low stiffness and strength. Therefore, conductive composites fabricated by integrating conductive fillers within insulating polymer matrices have been proposed recently to overcome the above limitations. Generally, CNT-polymer composites are lighter; possess a higher flexibility, better durability, and capability to tailor thermal and electrical conductivity in comparison to most conventional materials.

The conduction of CNTs-polymer composite is based on a percolation theory where the electric state of the composite changes from insulator to conductor at a critical CNT concentration (sufficient to form conductive pathways) [164]. In the same manner as in mechanical reinforcement, the processing techniques play an important role in the final electrical properties of the composites. The main focus in most research papers based on conductive composites has been to lower the percolation threshold as reported by the interesting review of Bauhofer *et al* [164]. It has been reported that while percolation

thresholds ranging from 1.0 wt% to 3.0 wt% of CNT concentration have been obtained with MWNTs, percolation thresholds as low as 0.025 wt% of CNT concentration have been reached with SWNTs [164]. In Chapter 7, the integration of nanotube into a non-conductive PI has been found to improve drastically the electrical and mechanical properties of the pure PI resulting in an excellent material for electrostatic dissipation (ESD), and EMI-shielding application [45–48]. In addition, the application of an AC electric field to the CNTs-PI composites during curing has lowered the percolation threshold of the PI from 0.15 wt% to 0.036 wt% CNT probably due to the better connection in the percolating network. Below the percolation threshold (without field) at 0.15 wt%, the electrical conductivity values of the CNTs-PI composites (with field applied) have been 100 times higher than the electrical conductivity value of the CNTs-PI composites (without field applied).

Conducting composites can be described as multifunctional materials whose combination of tuneable electrical, thermal and mechanical properties make them unique [165].

2.4 Conclusions

The uses of PI and CNTs materials in electronic applications have been developed widely in the last decade. In order to provide a theoretical framework for the work undertaken in this thesis, the principal structure-properties relationship and the main applications of PI, CNTs and CNTs-PI composite materials have been reviewed.

The physical properties of PI have been found to largely depend on the synthesis method and the structure of the material. Many of these properties can be modified by post-synthesis treatments or by integration of conductive and high strength CNTs which can potentially broadened their applications.

As technology scales down, the size of the transistors and interconnects shrinks. However, the resistivity of metals at the nanoscale increases sharply leading to their limitations at such small scales. Therefore, there is a requirement for novel nanoscale material for future. CNTs are often seen as one of such promising nano-material due to their nanoscale dimension and exceptional electrical properties. Electron scattering is limited in CNTs due to their 1 dimensional (1D) nature. The electron mean free

path is in the micron range for CNTs, while it is 40 nm for bulk copper. Moreover, the sp^2 hybridisation nature of CNT is responsible for high mechanical strength capable of conducting current up to $10^9 A/cm^2$ in contrast to $10^6 A/cm^2$ for copper. However, some challenging tasks remain to integrate CNTs into realistic circuits. One of the aims of this thesis has been to reduce the high contact resistance at the CNT-metal interface in order to fabricate low resistivity SWNTs interconnects.

Finally, the preparation of PI and other polymer based CNTs composites by dispersing CNTs within the polymer matrix has been regarded with great interest as new electronics materials. The combination of the CNTs and polymer properties can lead to composite material having unique properties, appropriate for numerous applications ranging from packaging to electronic sensing. Although this research area seems very promising, some challenging requirements exist in order to fabricate high performance CNTs reinforced polymer composites. The two main parameters for an efficient load transfer of the CNTs properties to the composite material are the quality of the filler dispersion and the strength of the interface between the CNTs and the polymer matrix. The different dispersion methods and the main achievements in CNTs-polymer composite materials reported in the literature have been discussed. A part of the work carried out in this thesis has contributed to develop a method to improve the CNTs-PI composite electrical and mechanical properties by inducing CNTs alignment within the composite via dielectrophoresis. Subsequently, the fabricated composite material has been used as sensing layer in a resistive humidity sensor, demonstrating good sensing properties which are attributed to the improvement of the CNT concentration and the degree of CNTs alignment in the composite.

Chapter 3
Assembly, fabrication and characterisation techniques

3.1 Introduction

Micro-electro-mechanical systems (MEMS) are small integrated devices offering attractive characteristics such as reduced size, weight and power dissipation compared to their macroscopic counterparts. As micro-fabrication technology continues to scale down towards molecular level, new types of applications and rapid advances in the technologies and techniques have been achieved to fabricate recent MEMS or nano-electro-mechanical systems (NEMS).

Chapter 3 presents the technology employed in this work. This chapter is divided into three main parts: dielectrophoresis (DEP), micro-fabrication technology and characterisation techniques.

In section 3.2, the theory behind DEP and the recent applications of DEP on CNTs such as the manipulation and separation of the nanotubes are presented.

In section 3.3, the different surface micromachining processes used to fabricate the various devices presented in this work are described.

In section 3.4, attention is focussed on the characterisation techniques used to investigate the structure of the devices fabricated and their final performance.

3.2 Dielectrophoresis (DEP)

This section is devoted to DEP. In section 3.2.1, a definition of DEP is given along with an explanation of the DEP theory describing the mechanism behind CNTs manipulation and alignment. In section 3.2.2, the several current applications of DEP on CNTs are discussed.

3.2.1 Theory of DEP

The word dielectrophoresis comes from the Greek word phoresis, which means carrying. Dielectrophoresis describes the motion of a particle induced by a dipole moment in response to an applied electric field [166]. The force generated by the electric field producing the motion of a particle is called the dielectrophoresis force.

If the electric field is uniform, the forces on each of the two poles of the dipole are balanced (equal and opposite), therefore the net force is zero and there is no movement. On the other hand, if the electric field is non-uniform, the forces on each of the two poles of the dipole are out of balance and there is movement of the particle. Depending on the polarisability of the particle with respect to the surrounding medium, the particle is attracted either towards the high-electric-field region (positive DEP) or towards low electric field region (negative DEP) [167, 168].

In this thesis, CNTs have been manipulated and more specifically, aligned via DEP in various experiments. In Chapter 6, DEP has been employed to align CNTs between metal electrodes to fabricate low resistivity CNTs interconnects. In Chapters 7 and 8, CNTs have been aligned inside a PI matrix resulting in a high performance composite material. Since CNTs have been the only type of particle manipulated using DEP, in this work, the following DEP calculations and applications are addressed to CNTs specifically. However, it is noteworthy that DEP can be applied to other particles.

The dielectrophoresis force, F_{DEP}, and torque, T_{DEP}, experience by the CNT shown in Figure 3.1 are defined by [166]:

$$F_{DEP} = (p \cdot \nabla)E \tag{3.1}$$

$$T_{DEP} = p \times E \tag{3.2}$$

where p is the induced dipole moment of the particle and E is the electric field.

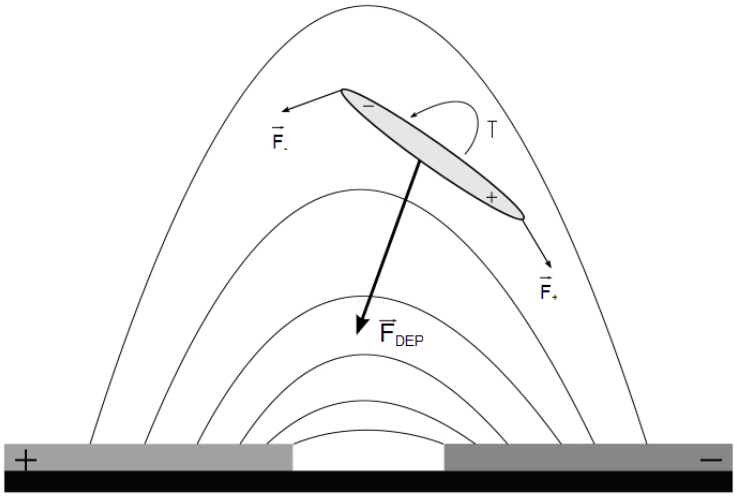

Figure 3.1: *Illustration of the translation and rotation of a CNT (modelled as a single dipole in a prolate ellipsoid) in the electric field between two charged electrodes*

The effective dipole moment of a polarized particle is expressed as [166]:

$$p = \nu\tilde{\alpha}E \tag{3.3}$$

where ν is the particle volume and $\tilde{\alpha}$ the complex effective polarisability. The dielectrophoresis forces acting on a particle suspended in a medium of permittivity ϵ_m is given by:

$$F_{DEP} = \Gamma\epsilon_m Re[F_{CM}]\nabla\left|E\right|^2 \tag{3.4}$$

where Γ is the geometrical factor and in the case of a cylindrical shape such as CNT of radius r and length l, is defined as [169]:

$$\Gamma = \frac{\pi r^2 l}{6} \tag{3.5}$$

$|E|$ is the magnitude of the applied electric field, and $Re[F_{CM}]$ is the real part of the Clausius-Mossotti factor defined as:

$$F_{CM} = \frac{\epsilon_p^* - \epsilon_m^*}{\epsilon_m^*} \tag{3.6}$$

where ϵ_p^* and ϵ_m^* are the complex permittivity of the particle and the medium and are defined by:

$$\epsilon^* = \epsilon - j\frac{\sigma}{\omega} \tag{3.7}$$

where ϵ is the permittivity, σ is the conductivity, $j = \sqrt{-1}$ is the imaginary vector and $\omega = 2\pi f$ is the angular frequency of the electric field.

In the low and high frequency limits, equation (3.5) can be written as:

At low frequency : $\omega \to 0$

$$Re[F_{CM}] = \frac{\sigma_p - \sigma_m}{\sigma_m} \tag{3.8}$$

At high frequency : $\omega \to \infty$

$$Re[F_{CM}] = \frac{\epsilon_p - \epsilon_m}{\epsilon_m} \tag{3.9}$$

At low frequency, F_{DEP} is governed by the conductivity of the particle and the medium while at high frequency, F_{DEP} is a function of the permittivities of the particle and the medium. In the intermediate frequency regime, the magnitude and the polarity of the F_{DEP} are influenced strongly by both dielectric and conductive properties of the particle and medium, which is the principle behind DEP sorting.

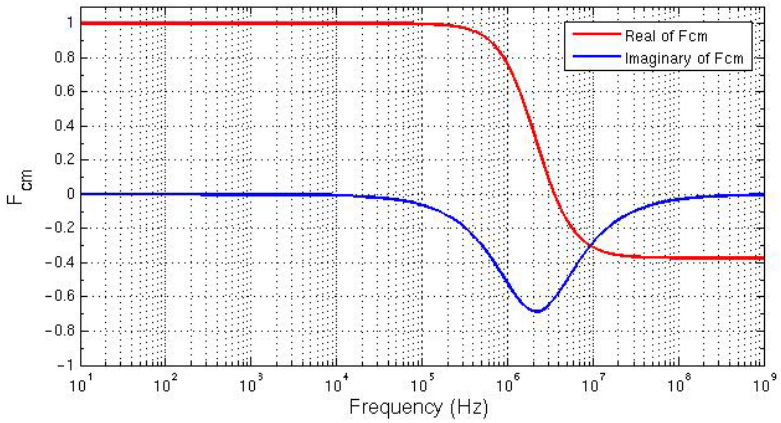

Figure 3.2: *Clausius-Mossotti factor for analysis of metallic CNTs in DI water*

The Clausius-Mossotti factor, F_{CM}, governs the movement of a particle in a medium toward the highest or lowest electric field regions. If F_{CM} is positive, then particles move toward the regions of high field strength (positive dielectrophoresis), whereas if F_{CM} is negative, the particles are repelled from these regions. The real part of

the Clausius-Mossotti factor, $Re[F_{CM}]$ determines the F_{DEP} while its imaginary part, $Im[F_{CM}]$ defines the electro-rotation (torque) on the CNT. Figure 3.2 represents the calculated real and imaginary part of the Clausius-Mossotti factor of a metallic CNT in DI water using MATLAB. In this case, the CNTs will experience positive dielectrophoresis for frequencies lower than 2 MHz and negative dielectrophoresis for higher frequencies.

3.2.2 Application of DEP

3.2.2.1 Manipulation of CNTs

DEP has been used to direct, align and separate CNTs and other particles based on their differences of polarisation arising from their dielectric constant, their conductivity and their sizes [166, 170–177]. The assembly of CNTs can be achieved by various methods such as chemical modification of the substrate [178], direct growth on substrate by chemical vapour deposition (CVD) [179], mechanical transfer process such as stamping of nanotubes onto a substrate [180], and post synthesis techniques such as DEP offering more freedom in the manipulation of CNTs. CNTs forests grown by CVD are often vertical, perpendicular to the substrate and have limited length resulting in very thin film thickness. On the other hand, manipulation of CNTs via DEP can lead to a CNT alignment to any angle desired. As presented in Chapter 6, 7 and 8 of this thesis, the electrical conductivity and the apparent number of aligned CNTs can be monitored by controlling the CNT solution concentration, the geometry of the electrodes and the electric field magnitude.

The first CNT alignment reported dates from 1996 when Yamamoto *et al* applied a non-uniform electric field to a MWNT-isopropyl alcohol (IPA) suspension between electrodes [181]. It has been reported that the CNTs move toward the negative electrode and align along the electric field lines. Later, they reported the influence of frequency on the alignment of CNTs where the number of aligned CNTs had been found to increase with the increase of the frequency. Their explanation was based on the motion of an electric dipole in an electric field [182]. More importantly, dielectrophoresis can be incorporated easily in device fabrication and has the potential to be used in wafer-level deposition for mass production of SWNT-based sensors. Recently, DEP was employed as a mass production and reproducible assembly technique for the alignment of a single bundle of SWNTs between gold electrodes separated by a

10 μm gap [183].

3.2.2.2 Separation of CNTs

Separation of semiconductor (s-SWCNTs) and metallic (m-SWCNTs) is an even greater challenge. The fact that metallic and semiconducting nanotubes possess very different polarisability drew scientific attention on the possible use of dielectrophoresis to separate them [184, 185]. Metallic and semiconductors SWNTs have a larger and smaller dielectric constant than water respectively; therefore the Clausius-Mossotti factor is positive for metallic and negative for semiconductors SWNTs-water solution [186]. As a result, metallic SWNTs will be attracted toward the electrodes and bridge them whereas semiconductors will remain in suspension. Krupke *et al* separated metallic from semiconducting CNTs by applying AC electric field to a CNT-SDS-DI water suspension. They reported a ratio of metallic CNTs up to 80% [187]. Wei *et al* reported the separation of very conductive and less conductive MWNTs using either positive or negative dielectrophoresis via a micro-fluidic chamber [186]. They used the ratio of intensity of the D band over the G band (I_D/I_G) from the Raman spectra to characterise the separation or the result of purification of the MWNTs.

3.3 Micro-fabrication

This section presents the micro-fabrication technology including thin film deposition, patterning and etching used in this work. The fabrication of MEMS is based on surface micromachining including the deposition, patterning and etching of the different thin film layers composing the MEMS devices. As discussed in Chapter 1, high stress can arise from fabrication processing to the several thin film layers of the MEMS. Therefore, it is important to understand the different processes that exist for each step of the fabrication process in order to optimise the devices.

Moreover, several electronic devices have been fabricated in this thesis based on micro-fabrication technology.

3.3.1 Thin film deposition

Fabrication of MEMS generally requires the deposition of extra layers. The four deposition methods to deposit thin film material in this work have been low pressure chemical vapour deposition (LPCVD) techniques for oxide (SiO_2), nitride (Si_3N_4) and polysilicon ($PolySi$) deposition, plasma-enhanced chemical vapour deposition (PECVD) for SiO_2 and Si_3N_4 deposition, sputtering for aluminium (Al), titanium (Ti) and indium tin oxide (ITO) deposition and Focused Ion Beam (FIB) for platinum (Pt) deposition.

3.3.1.1 LPCVD

LPCVD material deposition has been carried out by a chemical reaction in the gas phase. The pressure of the chamber has been kept very low (0.1 to 1.0 Torr) and the substrate temperature has been raised to high temperatures ($900°$C) in order to create enough energy for the chemical reaction to occur. Figure 3.3 describes the oxidation process of Si wafer using a LPCVD furnace.

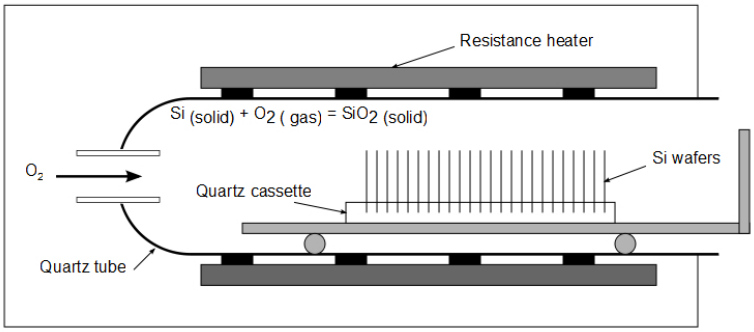

Figure 3.3: *Schematic of oxidation process via LPCVD*

LPCVD produced thin film with good thickness uniformity as well as good mechanical properties. Typical stress values have been reported to be around 100-300 MPa for oxide, 1GPa for nitride and 200-300 MPa for polysilicon.

3.3.1.2 PECVD

Figure 3.4 represents a PECVD system. The PECVD technique is based on a RF generated plasma where a radio-frequency voltage applied between the two electrodes induces free electron oscillation and collision with gas molecules resulting in a sustainable plasma. Within an RF field, electrons gather enough energy to cause ionisation at low pressure. In addition, it enables the process temperature to be reduced to $250°$C. PECVD allows the deposition of oxide, nitride, amorphous silicon, etc. The main characteristics of PECVD material deposited are good adhesion, conformal step coverage, and adequate electrical properties however; PECVD produces materials with higher pin-hole density than LPCVD.

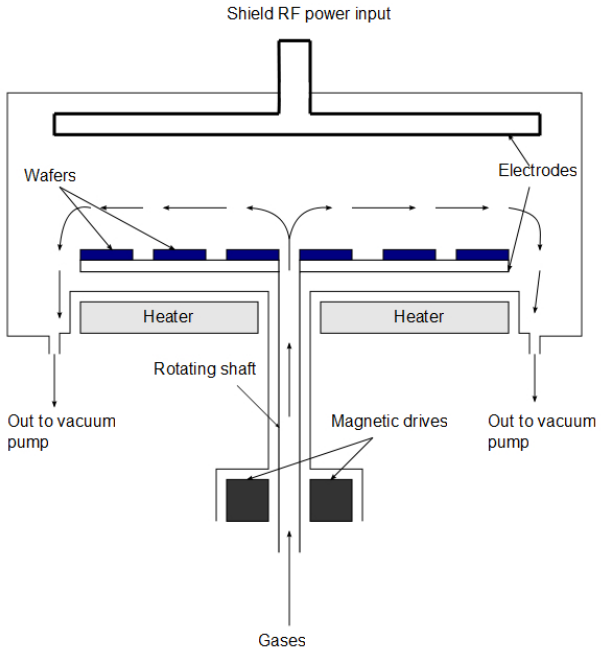

Figure 3.4: *Schematic of a PECVD system*

The parameters used for the deposition of PECVD oxide and nitride in this work are listed in Appendix A.

3.3.1.3 Sputtering

In a sputtering deposition system such as the Balzers, the material to be deposited is transported from a source target to the wafers inside a chamber. During sputtering, the

target material which is at a negative potential is bombarded with positive inert argon ions creating a plasma.

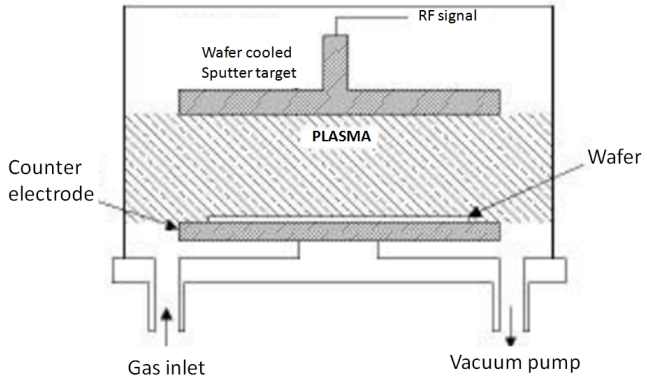

Figure 3.5: *Schematic of a sputtering system*

The system consists of a parallel-plate where the top electrode is the target material and where the wafer sits on top of the bottom electrode as shown in Figure 3.5. The target material is sputtered under argon bombardment and ejected towards the wafer. The inert ions used during bombardment are produced via a DC or RF plasma. Many metals and alloys can be deposited at very good step coverage with an excellent adhesion using the sputtering technique making it a favourable deposition technique in micro-fabrication.

3.3.1.4 Focused Ion Beam (FIB)

Finally, FIB has been the last technique employed to deposit material in this work. FIB is widely used in fundamental materials studies and technological applications such as transmission electron microscope (TEM) sample preparation [188], IC repair [189], resistless lithography [190] and in the fabrication of various MEMS [191].

FIB systems operate in a similar manner as scanning electron microscope (SEM) but instead of a beam of electrons, FIB systems use a focused beam of gallium ions (Ga^+) that can be operated at low beam currents for imaging or high beam currents for site specific sputtering or milling. The typical ion source used in most of the FIB is a liquid metal ion source (LMIS). The source consists of a needle connected to a reservoir of liquid metal such as gallium (Ga^+). A Ga^+ ion beam is produced via an electric field from the source and hits the sample surface and sputter a certain amount of material

depending on the primary current used.

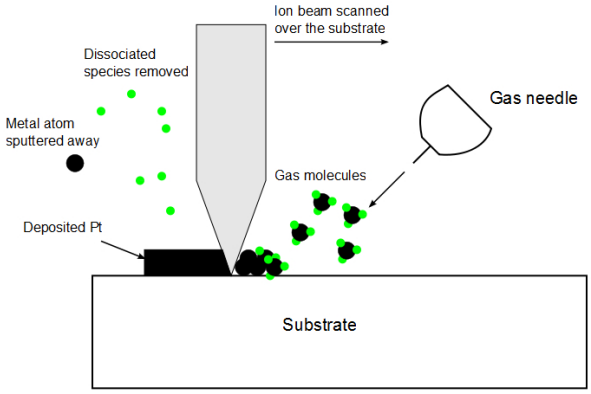

Figure 3.6: *FIB material deposition*

FIB can be used for material etching or metal deposition. In this work, FIB has been used for both purposes. In Chapter 4, FIB has been used to cut the beam of the MEMS fabricated in order to investigate the release state of the suspended beam while, in Chapter 6, FIB has been employed to deposit Pt contact on top of the SWNTs-metal electrode interface in order to reduce the contact resistances of the fabricated devices. Pt has been deposited locally under the presence of a precursor gas, which has been injected into the vacuum chamber through a gas needle located 100 μm above the substrate surface. As the ion beam scans the sample, it breaks some chemical bonds from the substrate surface and creates new bonds at the surface. Thus, the gas is absorbed at the surface resulting in film growth as shown in Figure 3.6.

3.3.2 Photo-lithography

3.3.2.1 Traditional process

Lithography is a technique used to define a pattern on a substrate. There are several lithography techniques such as photo-lithography, electron beam (e-beam) lithography and X-ray lithography. Photo-lithography is the most commonly used lithography technique in IC industry and the one used within this thesis. Photo-lithography consists of defining a pattern from a photomask onto thin film materials. First, a mask layout has to be designed via a computer. A photomask is a flat glass plate with a metal pattern designed on it, resulting in a light or dark field known as mask polarity. The dark metal

pattern is opaque to UV light while the glass region is transparent. Some of the masks designed in this work are presented in Appendix B.

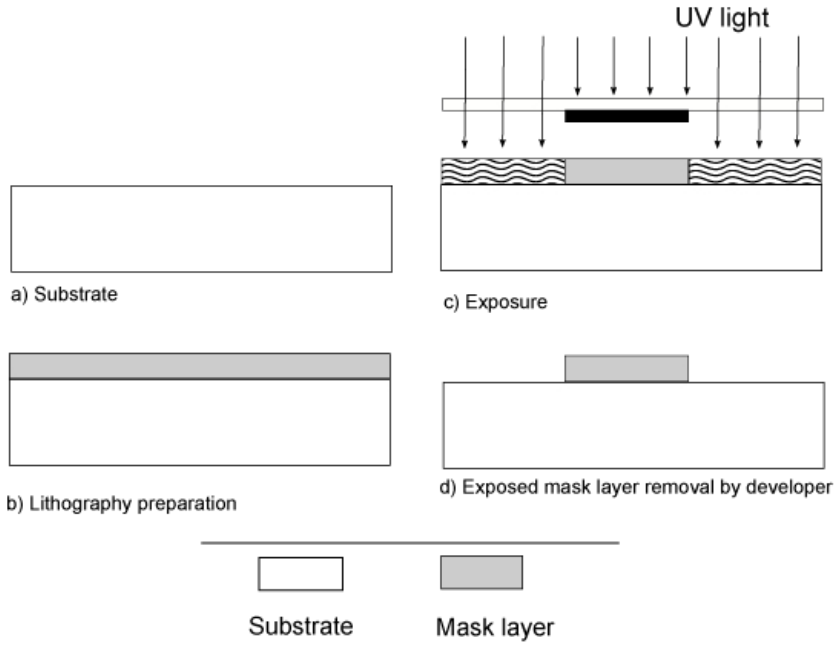

Figure 3.7: *Basic photolithography and pattern transfer*

The principle of photo-lithography and pattern definition of a thin film of silicon dioxide (SiO_2) on a silicon (Si) substrate is illustrated in Figure 3.7. First, a mask layer (thin layer of photoresist) is spun coated on top of the structural layer (substrate) (Figure 3.7 (b)). Then, the mask is aligned with the structural layer and the mask layer is exposed to UV light (Figure 3.7 (c)). After exposure, the mask layer is developed and hard-baked leaving the desired pattern on the substrate (Figure 3.7 (d)).

3.3.2.2 Lift-off process

An alternative to the traditional patterning process described above is the lift-off process presented in Figure 3.8. Lift-off process is called an additive process in contrast to the traditional photo-lithography process followed by etching called subtracting method. The difference between lift-off process and the traditional patterning is that in the lift-off process, the photoresist is deposited and patterned first onto the substrate (Figure 3.8 (b)-(d)). Subsequently, the metal layer is sputtered onto the patterned photoresist (Figure 3.8 (e)). Thus, the photoresist is removed with a specific solvent,

starting at the edge of the photoresist and lifting off the metal (Figure 3.8 (f)). Evaporation techniques to deposit metal are preferred during the lift-off process as no metal will be deposited on the inward sloping wall of the pattern. This will result in a gap in the metal deposited, enabling the solvent to react with the uncoated photoresist walls.

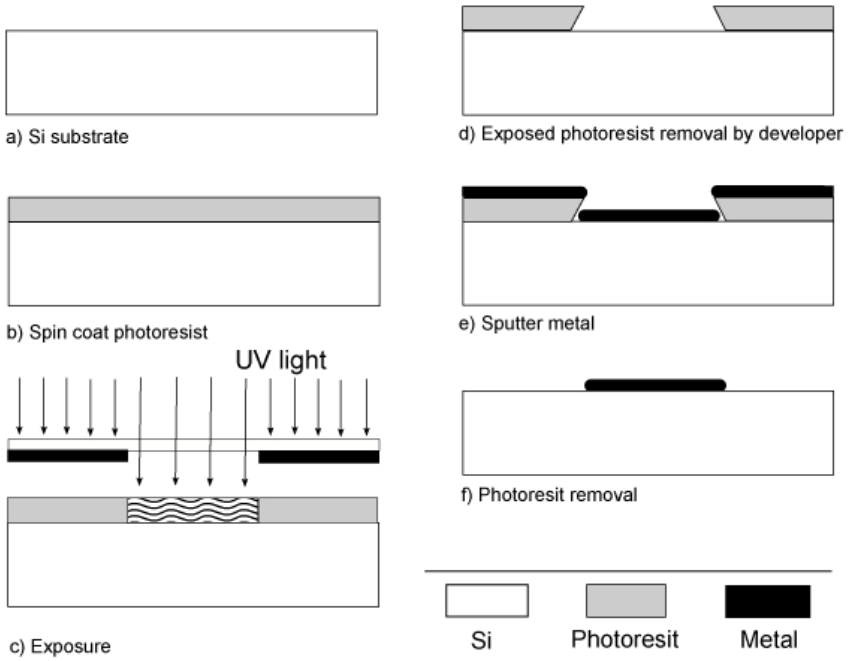

Figure 3.8: *Lift-off process*

3.3.3 Etching

The etch and release processes are critical steps in MEMS micro-fabrication. The key characteristics of an etching process are selectivity and directionality. The etching selectivity refers to the ratio of the etching rates between the mask layer and the underneath material layer to be etched. Directionality defines the etched profile as seen in Figure 3.9. In an isotropic etching, the material is etched in all directions at the same etch rate while in anisotropic etching the etch rate varies depending on the direction in the material. As a result, isotropic etching leads to a semicircular profile and anisotropic etching can result in straight sidewalls, although it is not always the case (Si etching by KOH).

A good selectivity is essential for removal of sacrificial layer in MEMS fabrication.

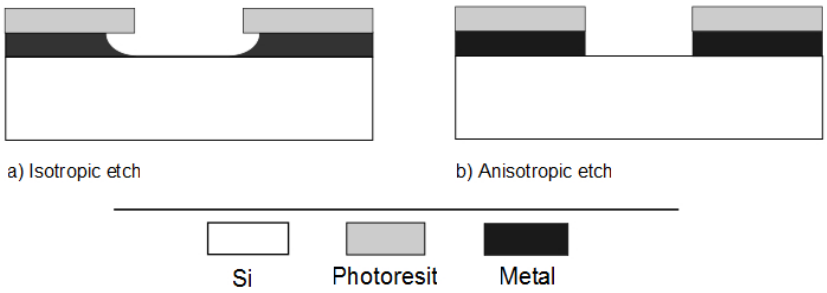

Figure 3.9: *(a) Typical isotropic and (b) anisotropic etch profiles*

Depending on the material to be used, an appropriate sacrificial layer has to be used. In this work, polyimide (PI) and various metals, titanium (Ti), indium tin oxide (ITO) and aluminium (Al) have been used for MEMS. Poly-Silicon has been chosen as sacrificial layer due to their good selectivity with the above listed materials.

There are two types of etching processes: wet etching and dry etching. Wet etching consists of immersing the material to be etched in a liquid chemical solution that will dissolve it. For example SiO_2, Si_3N_4, metals and silicon can be etched with an appropriate combination of acid and base solutions. The drawback using wet etching is the isotropic etching profile that can cause undercutting of the mask layer by the same distance as the etch depth changing the original dimensions of the designed strutures. In the case of a cantilever, the final beam could become longer than the first designed one. These dimensional changes could result in collapsed beams For those reasons, dry etching has overcome wet etching in the micro-fabrication industry.

In this study, wet etching has been employed in one specific case, in Chapter 5, where a solution of 50% ammonium fluoride, NH_4F, and 50% acetic acid, $C_2H_4O_2$, has been employed to etch the SiO_2. A double reaction occurs where the SiO_2 reacts with the aqueous solution such as:

$$NH_4F + C_2H_4O_2 \rightarrow HF + NH_4C_2H_4O_2(\text{dissolved in water})$$

$$HF + SiO_2 \rightarrow SF_4(\text{volatile}) + H_2O \tag{3.10}$$

3.3.3.1 Reactive ion etching (RIE)

RIE is based on a plasma etching mechanism. A plasma can be described as a highly ionised gas formed by ions and neutrals with high energy electrons causing excitation and ionisation within the plasma and being electrically neutral. An RF power source is used to generate a plasma. The RF power source electrically drives the plasma by introducing enough energy to break the gas molecules into ions within its chamber as shown in Figure 3.10.

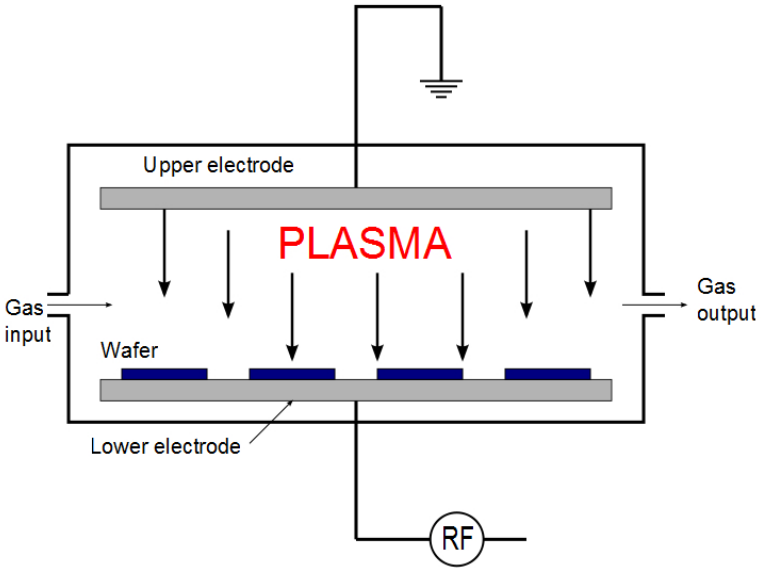

Figure 3.10: *Schematic of a parellel plate reactor (RIE)*

The reactive species are accelerated towards the wafer where they are absorbed at the surface of the material. At this point, a chemical reaction (equation 3.11) occurs between the etchants and the atoms of the material to be etched. The reaction products are removed from the surface of the material by desorption and diffusion.

$$CF_x + SiO_2 \rightarrow SiF_y + (CO, CO_2) \tag{3.11}$$

The parameters used to etch SiO_2 and various metals in a RIE system are listed in Appendix A.

3.3.3.2 ICP-RIE

An extension of the RIE process is the deep reactive ion etching (DRIE) using an inductively coupled plasma (ICP) able to achieve very deep etch patterns through the substrate as shown in Figure 3.11. In contrast to the RIE system, where the increase of plasma density is closely related to the DC bias of the cathode, an ICP system offers the possibility of creating higher plasma density at low DC bias limiting radiation damage caused to the wafer. ICP system includes an additional RF powered magnetic field to generate the plasma. Therefore, the plasma density can be controlled independently by this additional RF magnetic field while the DC bias in the cathode is responsible only for the attraction of positive ions (e.g. Ar^{+}) to target the wafer and etch in the presence of reactant radicals (e.g. Cl^{-}).

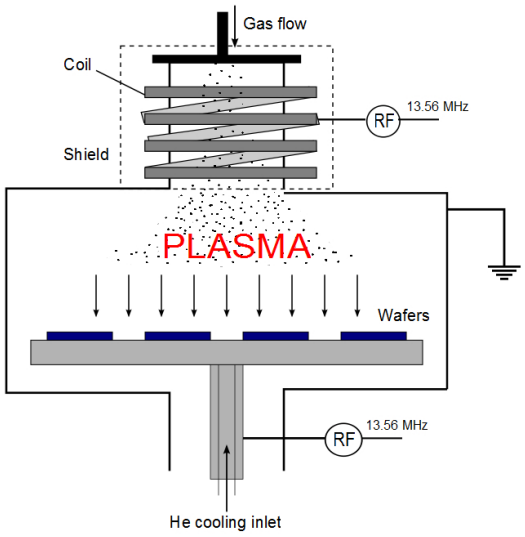

Figure 3.11: *Induced coupled plasma system*

High aspect ratio features are fabricated using an advanced etching process in an ICP-RIE known as the Bosch process. It consists of two separate cycles, a passivation deposition and an etching step that last several seconds. The passivation cycle deposits a polymer thin film on the surface of the substrate using C_4F_8 gas preventing further etching. Then, the following etching step removes the polymer away on the horizontal surfaces but not on the sidewalls using SF_6/Ar. Therefore, the polymer that remains on the sidewalls will protect the sidewalls from the etching. Aspect ratios of the order of 30:1 can be achieved using DRIE. The parameters of the process used to etch Si are

listed in Appendix A.

3.3.3.3 Vapour phase

The last dry etching process employed in this work is the so-called vapour-phase etching. Vapour-phase etching does not require a plasma to produce reactive species. XeF_2 is a white solid with a room temperature vapour pressure of 4 Torr that reacts with Si. The vapour-phase etching technique involves a chemical reaction at the surface of the material to be etched with the gas molecules within a chamber at room temperature and pressure between 1 and 9 Torr. The etch rate is a function of the pressure and the aperture size. The two most common vapour phase etching technologies are silicon dioxide (SiO_2) etching using hydrogen fluoride (HF) and silicon (Si) etching using xenon difluoride (XeF_2). Both processes are isotropic and mainly used for etching sacrificial layers and released structures avoiding the striction problems encountered with wet etching. In this work, Si has been etched with XeF_2 in order to release PI cantilever beams and to release Ti, ITO and Al bridge beams due to its advantages over ICP-RIE with SF_6/O_2. The release etch has been performed under a pressure of 9 Torr and a flow rate of 50 SCCM. The exothermic etch reaction is given by:

$$2XeF_2 + Si \rightarrow 2Xe + SiF_4 \tag{3.12}$$

3.4 Characterisation

The last section of this chapter focuses on the characterisation techniques that have been employed to analyse material properties and MEMS performances. This section is divided in five parts as electrical, mechanical, thermal, surface and structural characterisation.

3.4.1 Electrical characterisation

Resistance measurement and I-V characteristics are often performed using a two-point electrical measurement technique. However, when the resistance of the contacts or the probes are high, four-point measurement is generally chosen giving more accurate

results.

3.4.1.1 Two-point probe

Resistance is usually measured using ohm's law, R=V/I. A current is applied to a conducting slab of material (Figure 3.12) and the voltage across the material is measured. Then, the resistance is calculated by dividing the measured voltage by the source current.

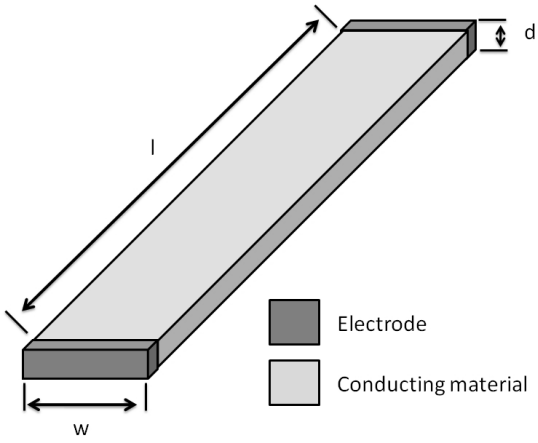

Figure 3.12: *Schematic of a conductive material sample*

In a two-point probe measurement, the measured value includes the resistance of the probes and the contacts, and the bulk resistance of the material. While in a four-point probes measurement both contact resistances are eliminated so that only the bulk resistivity can be obtained.

3.4.1.2 Four-point probe

The four-point probe measurement technique consists of applying four electrically conducting pins in contact with the surface of the material to be measured (Figure 3.13). The four probe tips have been arranged originally in-line with equal spacing between them. However, the four point probe technique has been adapted to different designs and other configurations are possible such as the Greek cross technique, the Van der Pauw technique or the MEMS devices developed in Chapter 4.

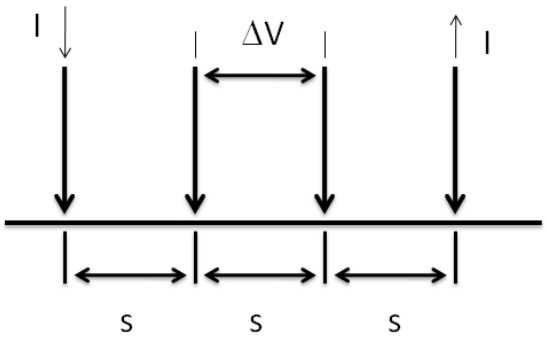

Figure 3.13: *Set-up of four-point probe measurement technique*

A current (I) is forced between the two outer probes and the potential difference (ΔV) between the two inner probes is measured. If the length, width and thickness of the sample being measured, are much greater than the probe spacing, then the resistivity of the semi-infinite sample can be calculated as [192]:

$$\rho = 2\pi s(\frac{\Delta V}{I}) \tag{3.13}$$

In the case of a not semi-infinite sample, a correction factor that depends on the sample geometry has to be added [193]. If the sample is too small to be measured with the four-point probes techniques, van der Pauw test structure or other Greek cross structures, as shown in Figure 3.14, can be used to extract the sheet resistance of the material.

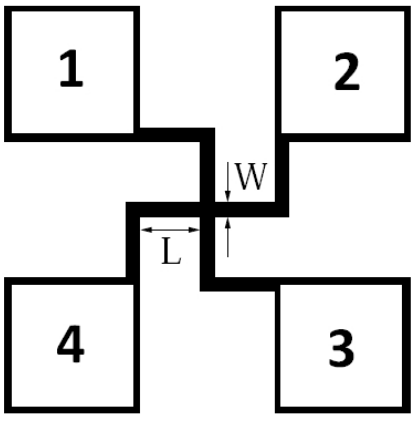

Figure 3.14: *Schematic of four terminal Greek cross sheet resistance test structure*

In the case of an ideal structure, a single should be sufficient to obtain an accurate value of the sheet resistance, however, in general four measurements are needed. Two are measured at a static zero degree orientation [194]:

$$R_0(+I) = (\frac{V_4 - V_3}{I_{12}}) \tag{3.14}$$

$$R_0(-I) = (\frac{V_3 - V_4}{I_{21}}) \tag{3.15}$$

and two at a ninety degree orientation [194]:

$$R_{90}(+I) = (\frac{V_3 - V_2}{I_{41}}) \tag{3.16}$$

$$R_{90}(-I) = (\frac{V_2 - V_3}{I_{14}}) \tag{3.17}$$

The four measurements are then averaged. A single resistance value is then defined as [194]:

$$R(\pm I) = (\frac{R_0(\pm I) + R_{90}(\pm I)}{2}) \tag{3.18}$$

which is used to calculate the sheet resistance with [194]:

$$Rs = f(\frac{\pi R(\pm I)}{ln(2)}) \tag{3.19}$$

where f is a correction factor which accounts for asymmetry in the structure.

3.4.2 Mechanical characterisation

3.4.2.1 Dynamic mechanical analysis (DMA)

Figure 3.15 represents the schematic diagram of the Dynamic Mechanical Analyser (DMA) system used in this work. DMA is a technique used to measure the stiffness and damping characteristics of a structural material. The measurement consists of applying a sinusoidal controlled force (stress or strain) to the material resulting in a material's displacement or deformation. The deformation of the material is related to its stiffness. Modulus is calculated from the amplitudes of motion and force, while damping is measured from the time delay (phase lag) from the applied force to the resulting motion. The storage modulus can be defined as the measure of the material's

elastic response to deformation while the loss modulus can be defined as the material's viscous behaviour to deformation. The ratio of loss to storage modulus is referred as tan delta (tan δ) and represents the measure of the energy dissipation of a material. Tan δ is a key parameter in dynamic mechanical testing as it is known to vary according to material deformations. The properties of a material can be recorded from temperature as low as $-150°C$ up to temperature around $400°C$.

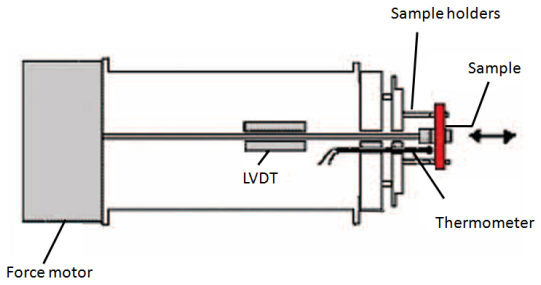

Figure 3.15: *Schematic of a DMA system*

It is worth noting that the transition between glassy and rubbery behaviour in polymers, called the glass transition temperature, T_g is due to the increased ability of polymer molecules to slide and rotate relative to each other as temperature increase through a certain range [195]. From the mechanical point of view, this transition manifests in a reduction of stiffness and in the ability to deform reversibly without fracture.

3.4.3 Thermal conductivity characterisation

One of the aims of this thesis is to develop a MEMS device for the thermal conductivity measurement of thin films (see Chapter 4). This section discusses existing methods for thermal conductivity measurement which are compared with the MEMS developed in this work.

Many methods have been reported to measure the thermal conductivity of thin film materials. Most methods are based on electrical heating phenomenon using a steady state or transient heating model. Nevertheless, a few optical techniques based on the reflectance and photo-acoustic principle have also been developed.

3.4.3.1 3ω method

Electrical transient methods consist of measuring the time response of a material to a heating power or the thermal response to a sinusoidal heating current. Up to now, the most commonly used electrical transient method is the 3ω method that exploits the temperature dependent electrical resistivity for the measurement of thermal properties of different materials.

The 3 omega method comes from Corbino [196] who discovered the small third-harmonic voltage component while applying an alternating current through a heater. The experimental device to measure the thermal conductivity of the substrate consists of a metal heater on a semi-infinite substrate as shown in Figure 3.16.

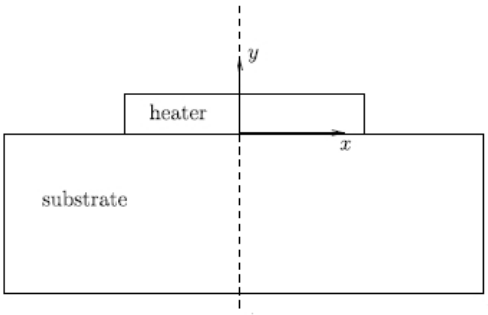

Figure 3.16: *Heater on substrate, adapted from [193]*

Initially, an alternating current, $I_0 cos\omega^* t^*$, flows through the heater, where I_0 is the magnitude, ω^* is the frequency of the current, and t^* is time. Therefore, the instantaneous Joule heat generated in the heater per unit time per unit length is $Pcos^2\omega^* t^* = P(1 + cos^2\omega^* t^*)/2$, where $P = I_0^2 R$ is the power per unit length, and R is the heater resistance per unit length. The voltage drop across the heater is measured and from that, by resistance thermometry, the spatial average of the oscillatory temperature of the heater is deduced. The relation between the amplitude of the heater spatially-averaged temperature oscillation and the frequency of the alternating current depends on the thermal conductivity and diffusivity of the substrate material, and so their values can be deduced [197].

3.4.3.2 Test structure

Several test structures have been designed to characterise thermal properties of thin film layer under steady state conditions, where the temperature does not change with time. In principle, a current is applied to these test structures through a metal heater line patterned on the layer to be characterised. Subsequently, the temperature rise is measured by using a separate temperature sensor or the heater itself as a thermometer. The thermal conductivity value is then extracted by using appropriate thermal model depending of the structures. Such technique has been employed largely in cantilever [22], membrane [23, 24], and bridges, particularly for the thermal conductivity characterisation of polysilicon [25–27]. Based on this principle, numerous MEMS devices and measurement procedures have been developed to determine the thermal properties of thin film layers [26, 198, 199].

Other test microstructures used for the characterisation of thermal properties have been developed from the well-known existing test structures. Van der Pauw's method can be applied to thermally conducting slabs which are singly connected [200], with flat, homogeneous surfaces that do not have heat sources or sinks. The analogy between electrical and thermal conduction can then be done by controlling precisely the generated heat power and temperature at the contacts and by ignoring heat radiation effect in the structure. In van der Pauw's thermal analysis, the electrostatic potential is analogous to the temperature, the electrical conductivity to thermal conductivity and the electrical current density to heat flux. Thus, thermal resistance can be calculated in the same way sheet resistance is calculated.

Most of the techniques mentioned above involve complicated measurement procedures and additional processing fabrication steps that may influence the heat conductivity of the thin film material to be measured. In Chapter 4, a MEMS test structure for thermal conductivity measurement has been fabricated based on the model develop by [28] to characterise ITO, Ti and Al 500 nm thick thin films. The main advantage of the test structure presented in this study is its simplicity. The measurements can be made in free air, they are carried out by applying current and voltage. Heat loss due to convection and radiation has been included in the analysis. Therefore, no further measurements are needed to compensate heat loss which could potentially affect the results. More details on the principle of the MEMS devices are given in the next chapter.

3.4.4 Surface characterisation

3.4.4.1 Atomic force microscopy (AFM)

Atomic force microscope (AFM) is a technique for imaging the topography of surfaces to a high resolution of 0.1 nm [201]. AFM has been developed as an alternative technique to the scanning tunnelling microscope (STM) which has been able to image conductive samples in vacuum only. AFM has been used widely in the study of surface science, such as imaging and surface characterisation, and more recently as a new tool for probing interaction forces between surface or molecules.

An AFM consists of a sharp probe mounted at the tip of a flexible micro-cantilever as shown in Figure 3.17. When the tip approaches the sample surface, the forces between the tip and the sample result in a deflection of the cantilever. Depending on the mode of operation, several forces can be measured with an AFM including mechanical contact force, van der Waals forces, capillary forces, chemical bonding, electrostatic forces. A beam of laser light is reflected from the top surface of the cantilever onto a position sensitive photo-detector. As the probe scans the surface of the sample to be studied, the deflection of the cantilever can be monitored as a function of the change in the position of the laser spot on the photo-detector. A three dimensional (3D) image of the sample surface can be drawn to a high resolution.

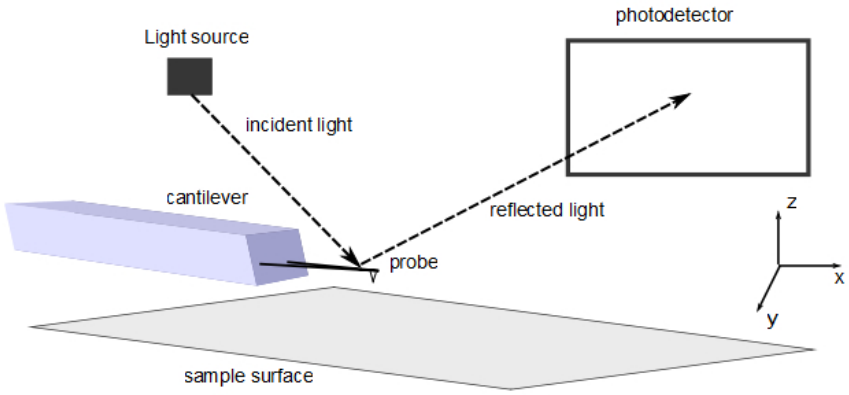

Figure 3.17: *Schematic of an AFM set-up*

An AFM can operate in several imaging modes. In contact mode, which is the most common mode of operation when imaging a hard and relatively flat surface due to its simplicity, the probe remains in contact with the sample at all times. As the probe scans

across the surface and meets different features in depth, the cantilever is deflected; the z height is altered to cause a return to the original position. The change in z-position is monitored as a function of the x, y plane and a topographical image of the sample surface is created. In tapping mode or intermediate mode, the cantilever oscillates up and down at a frequency close to its resonance frequency and the tip is tapped across the sample surface. By maintaining a constant oscillation amplitude across the surface' scan, a constant tip-sample interaction is maintained and a topographic image of the surface is obtained in the same manner as in the contact mode. In non contact mode the tip does not touch the surface. The tip oscillates as in tapping mode but at a much smaller amplitude. Using a feedback loop to monitor changes in the amplitude due to attractive Van der Waals and electrostatic forces that occur between the probe and the surface, the surface topography can be measured.

Tapping mode appears less likely to damage the sample surface than contact mode because it eliminates the lateral forces between the tip and the sample. Moreover, it is more efficient than non contact mode when imaging surfaces with greater variation in sample topography [202]. AFM has been used in contact mode to characterise the degree of CNTs alignment in Chapter 7 and 8.

3.4.4.2 Scanning electron microscopy (SEM)

Electron microscopes appeared in the 1930s as an alternative to the optical microscopes providing enhanced magnification and resolution (in the nanometer range). SEM is a commonly used tool for the study of micro-structure materials. The principle of a SEM is based on a focussed electron beam (e-beam) interacting with a solid specimen to produce an image of its surface [203]. A SEM is composed of an electron column, a detection system and a viewing system. The electron column consists of an electron gun which is made of an electrode source (cathode) and two electrodes (grid and anode) that extract and accelerate the electrons as shown in Figure 3.18.

The beam then goes through lens and apertures that condense the beam and control the incident beam current. Scan coils generate a magnetic field which deflects the beam and an objective lens focuses the point at different points on the sample. Thus, the electron beam hits the sample surface producing secondary electrons and

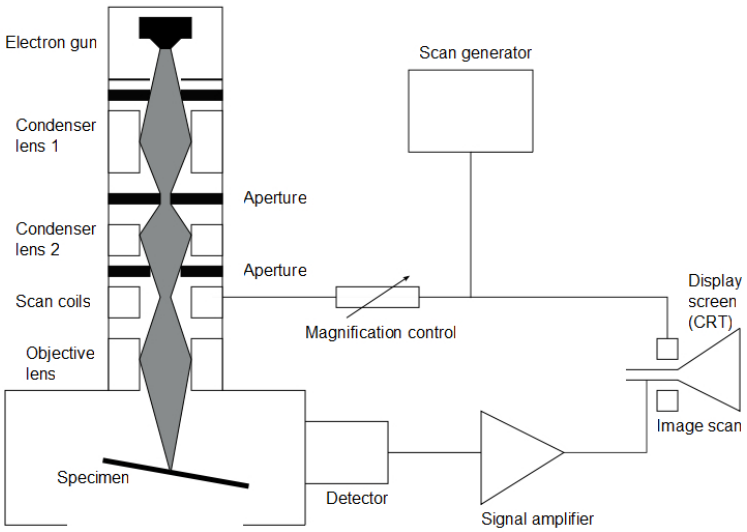

Figure 3.18: *Schematic diagram of a scanning electron microscope*

backscattered electrons. Those electrons are collected, detected and amplified creating a map of intensity of secondary electron emission from the scanned area of the sample that will appear on the CRT screen as variations in brightness, reflecting the surface morphologies of the specimen. The SEM system employed in this work was a Philips SEM XL 40 FEG.

3.4.4.3 White light interferometry

White-light interferometry is an extremely powerful tool for non-contact optical profiling, step heights and surface roughness measurements. It is a traditional technique in which a pattern of bright and dark lines (fringes) result from an optical path difference between a reference and a sample beam. Incoming light is collimated from a white light source and split into two separate beams, one beam goes to a reference surface which is known as the constant optical path whilst the other passes through or is reflected from the sample. The reflected light from each beam is captured and recombined at the beam splitter, undergoing constructive and destructive interference and producing the light and dark fringe pattern. The resulting interference pattern is imaged onto the CCD array. It is worth focussing at the point where maximum constructive interferences occur which corresponds to the brightest image. At that point, changes of the vertical movement of the lens can be tracked

precisely, creating a 3D image of the sample surface by measuring the position of the lens required to produce the brightest image at each point on the CCD array, as shown in Figure 3.19.

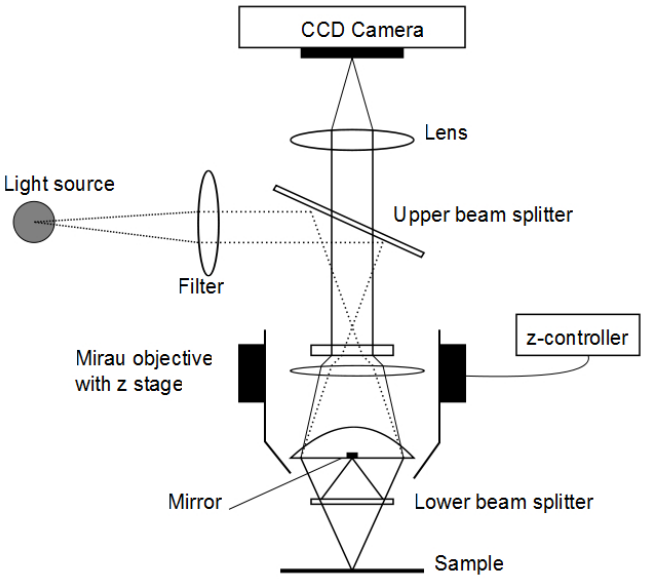

Figure 3.19: *White light interferometer system*

Although most of the white light interferometers have an extremely good vertical resolution of the order of 0.01 nm, their poor lateral resolution (0.35 μm) make them less attractive than an AFM for some applications. In this work, a Zygo white light interferometer has been used as a practical tool for the measurement of the out of plane deflection of a PI cantilever beam due to residual stress arising from the micro-fabrication process.

3.4.5 Structure characterisation

3.4.5.1 Fourier transform infra red spectroscopy (FTIR)

Fourier Transform Infrared (FTIR) spectroscopy is a technique used to determine spectrum of absorption of organic or inorganic solid, liquid or gas samples. FTIR spectroscopy consists of focussing a broadband beam at the sample containing several frequencies simultaneously. Different scans are recorded by varying the wave interference of the beam after passing through the sample. The final spectrum of

the sample is obtained by analysing the raw measurement from the different moving mirror positions using the Fourier Transform.

An appropriate choice of the source, beam splitter and detector is required to achieve accurate IR spectra of the studied sample. It is worth knowing approximately the wavenumber region of the main absorption peaks of the sample before starting any measurements. These regions are defined using wavelengths (λ) in (μm) or wavenumber in reciprocal centimetres (cm^{-1}). The wavenumber in infrared region of the electromagnetic spectrum ranges from 14,000 cm^{-1} to 10 cm^{-1}. The region of most interest for chemical analysis is the mid-infrared region (4000 cm^{-1} to 400 cm^{-1}) which corresponds to changes in vibrational energies within molecules. Infrared spectroscopy (IR) is useful for identifying certain functional groups in molecules and an IR spectrum of a given compound is unique and can therefore serve as a fingerprint for the compound [204].

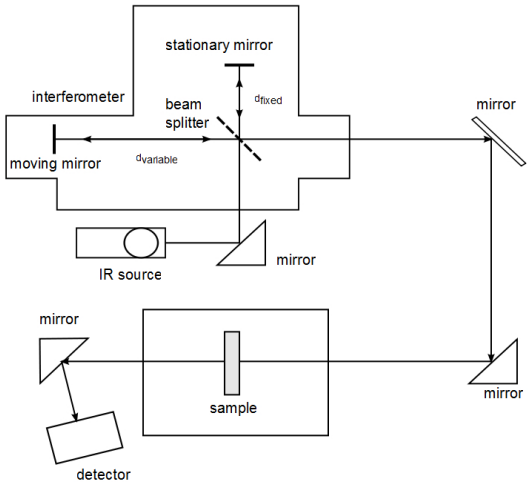

Figure 3.20: *Schematic of an FTIR set-up*

Figure 3.20 illustrates the principle of operation of an FTIR. Light from an infrared source is directed to a beam-splitter, which ideally reflects and transmit 50 % of the incoming light. The reflected light hits a stationary mirror located at a distance, d_{fixed}, while the transmitted light is directed to a moving mirror located at a variable distance, $d_{variable}$. The light beams from both mirrors are then directed back to the beam-splitter which transmits both beams interference to the sample. After passing through the sample, the detector collects the interference of the beams. The same

process is repeated for a different distance $d_{variable}$ of the moving mirror. The number of scans determines the resolution of the measurement.

In this work, the degree of imidisation of PI thin film cured at 200°C has been characterised by FTIR. Moreover, the structural changes of PI exposed to low energy Ar^+ ion bombardment have been investigated using an FTIR spectroscopy.

3.4.5.2 X-ray photon electron spectroscopy (XPS)

X-ray photon electron spectroscopy is a powerful technique that measures the elemental composition and the chemical state on the surface of a material down to 1-10 nanometer by X-ray source irradiation.

When X-rays irradiate the sample surface with sufficient energy, electrons are ejected from the core levels of the surface atoms [205]. Electrons will only be removed from the surface atoms if the energy of the incident photon is higher than the binding energy. The energy of the emitted electron is related to the chemical bond of the atom hence electrons located at lower energy levels will result in emitted electrons with reduced kinetic energy due to higher binding energy to be overcome [206]. The principle of operation of a XPS is illustrated in Figure 3.21.

The relationship between the kinetic energy of an ejected electron, the incident X-rays energy, the binding energy of the electrons and the work function is defined as follow:

$$E_B = h\upsilon - \varphi - E_K \tag{3.20}$$

where E_B is the binding energy, h is the Planck's constant, υ is the frequency of the incident X-rays, φ is the surface work function, which is the energy required for an electron to go from the valence to the continuum and E_K is the kinetic energy.

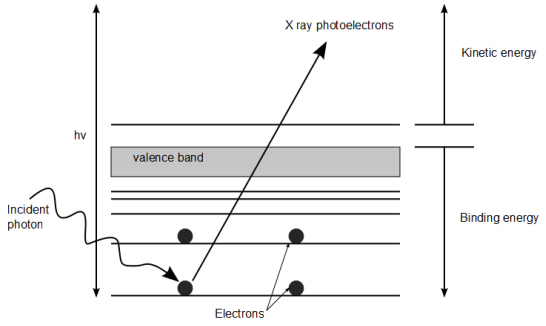

Figure 3.21: *Mechanism of photoelectron emission in X-ray Photoelectron Spectroscopy*

The kinetic energy of the emitted photoelectrons depends on the bond formed within the atoms. The deconvolution of an elemental peak gives information about the chemical state of the atoms. It is important to know what type of core electron is being analysed. In the case of PI as presented in Chapter 5, XPS has been employed to characterise PI films. The peaks have been deconvoluted using Gaussian distribution using OriginLab 8.0.

In this study, XPS measurements were carried out using a VG Sigma Probe using an Aluminium Kalpha $Al - K_a$ monochromated source, for which $h\upsilon = 1486.6eV$. The flood gun was used under a pressure of Argon gas at 3.10^{-8} Torr. An 800 micron diameter spot was used.

3.5 Conclusions

In this chapter, the technology employed for the fabrication of MEMS devices, the development of CNTs interconnects and the preparation of CNTs-PI composites based humidity sensor has been described.

Initially, the theory of dielectrophoresis (DEP) technique has been explained where it has been shown that a CNT subject to a non-uniform electric field experiences both dielectric force and torque that govern its movement. In addition, the use of DEP to align CNTs for CNT-FETs and CNTs interconnects devices have been reviewed.

Secondly, the micro-fabrication steps required for the fabrication of the electronic

devices made in this thesis have been presented. The thin film deposition techniques used within this work are low pressure physical vapour deposition (LPCVD) technique for oxide (SiO_2), nitride (Si_3N_4) and Polysilicon ($PolySi$), plasma-enhanced physical vapour deposition (PECVD) for SiO_2 and Si_3N_4, sputtering for Al, Ti and ITO and FIB for Pt. To pattern the deposited layers, photolithography has been employed. Lift-off processes have also been used to form patterns. The next fabrication step consisted of etching the subsequent patterned layer. To do so, three methods have been used for the etching or the release of sacrificial or substrate material namely, RIE, ICP-RIE and vapour etching. The principles of these techniques as well as their main advantages and drawbacks have been reviewed.

Finally, materials characterisation is important for MEMS designs and performances. In this work, two-probe and four-probe measurement techniques have been used for electrical and thermal characterisation. Two-probe measurement has been used to determine the electrical conductivity of CNTs and CNTs-PI composite material, while the four-probe configuration has been adapted to obtain the thermal conductivity of ITO, Ti and Al thin films. DMA is a useful tool for the calculation of the elastic modulus and the glass transition temperature of CNTs-PI composites. AFM, SEM and white light interferometry have been used to study the alignment of CNTs and the structure and morphology of MEMS devices. Finally, FTIR and XPS have been used to characterise the surface of PI. Working principles of all these characterisation techniques has been briefly described.

Chapter 4
A MEMS for thermal conductivity measurement of conductive thin films

4.1 Introduction

The thermal conductivity of thin film materials is an important parameter to be considered in the design of MEMS sensors and actuators [15–17]. The performance and reliability of many microdevices, such as microscale thermometers, pressure sensors, gas flow detectors, and fluid valve actuators, are strongly influenced by heat conduction [16]. Heat transfer can also adversely affect the operation of IC interconnects and high voltage and high-power transistors [20]. To design and operate such devices effectively, it is critical to quantify the thermal conductivities for thin films material, which differ substantially from their bulk counterpart. The difference in thermal conductivity between bulk materials and thin film materials is due to the fact that for material with small thicknesses, the thermal transport is lowered by phonon scattering at lattice imperfections and boundaries [16]. Therefore, new techniques are needed for a precise characterisation of thermal conductivity of thin film materials.

In this chapter, a simple and straightforward technique has been developed for the measurement of the thermal conductivity of ITO, Ti and Al thin films based on a MEMS device described by [28]. The measurements of thermal conductivity are made in air and the heat transfer by convection, radiation and conduction is considered in the analysis.

In section 4.2, the theory of heat transfer is presented including the role of the different heat transfer mechanisms by conduction, convection and radiation on the final heat balance equation of the fabricated MEMS.

In section 4.3, the structure design and the fabrication process are presented. The

optimisation of the structure is developed using CoventorWare Finite Element Method (FEM) simulations.

In section 4.4, the fabrication process is explained.

In section 4.5, the electrical measurements of the devices for the three different metals studied and the final calculation of thermal conductivity are presented.

4.2 Heat transfer mechanisms and heat balance equation

In this section, the several different forms of heat transfer occurring in the suspended beam of the MEMS fabricated in this experiment are described. The heat balance equation of the MEMS device is developed from the first law of thermodynamics, the law of conservation of mass and Newton's second law.

4.2.1 Heat transfer mechanisms

Heat transfer is the transport of thermal energy in a single medium or within its surroundings when the temperature within the medium or between the medium and its surrounding is different. Heat transfer occurs in three different ways, by conduction, convection and radiation. Conduction is the transfer of thermal energy from a region of higher temperature to a region of lower temperature by direct contact interaction between two neighbouring molecules and acts to equalize temperature difference. Convection is the transfer of thermal energy due to the movement of mass between a fluid and its surrounding. Radiation is the transfer of energy due to electromagnetic waves. Thermal radiation depends on emissivity, temperature and surface area and reflectivity. Figure 4.1 illustrates the schematic of the heat transfer mechanisms by conduction, convection and radiation occurring in the suspended metal beam of the test structure presented in the next section.

The heat transfer is based on physical laws and mainly governed by the first law of thermodynamics. The law of conservation of mass and the Newton's second law have to be used for specific situations such as convection problems in order to obtain a complete heat transfer equation. James R. Welty develops in detail the heat transfer equation of a thin film material considering the different lumped, integral and differential

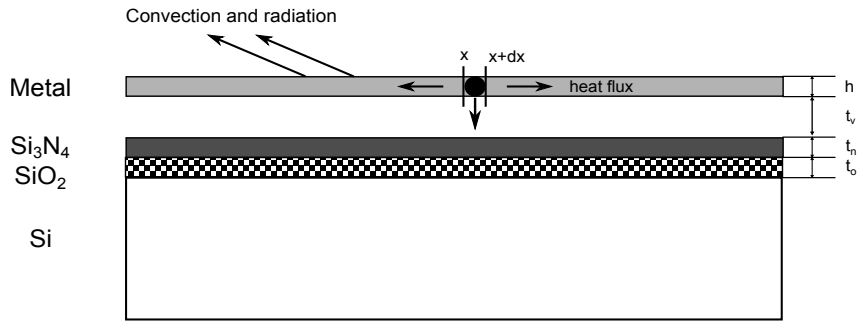

Figure 4.1: *Schematic of the heat transfer in the metal beam*

formulations [207]. Here, the heat transfer equation of the metal thin film has been developed based on the model described in [207].

4.2.2 Heat balance equation

Heat flows in the direction of decreasing temperature. The heat flux vector, q defines the magnitude and the direction of the heat transfer rate per unit area and can be expressed as the sum of the conduction (q_k), convection (q_u), and radiation (q_r) heat flux vectors [207]:

$$q = q_k + q_u + q_r \tag{4.1}$$

The conduction heat flux defined by Fourier's law can be written as [207]:

$$q_k = -k\nabla T \tag{4.2}$$

The convection heat flux can be defined as [207]:

$$q_u = \rho c_p u \tag{4.3}$$

Using equations (4.1), (4.2) and (4.3), the heat flux vector becomes [207]:

$$q = -k\nabla T + \rho c_p u + q_r \tag{4.4}$$

where k is the thermal conductivity, ρ is the density, c_p is the specific heat, u is the velocity vector of the heat transfer medium, q_r is the radiation heat flux vector and ∇T

is the gradient of temperature defined as:

$$\nabla T = \frac{\partial T}{\partial x} + \frac{\partial T}{\partial y} + \frac{\partial T}{\partial z} \tag{4.5}$$

The differential volume thermal energy equation is defined as [208]:

$$\nabla q = \nabla \cdot (q_k + q_u + q_r) \tag{4.6}$$

$$\nabla q = \nabla \cdot (-k\nabla T + \rho c_p u T + q_r) \tag{4.7}$$

$$\nabla \cdot (-k\nabla T + \rho c_p u T + q_r) = -\rho c_p \frac{\partial T}{\partial t} + s^{\cdot} \tag{4.8}$$

where $\rho c_p \frac{\partial T}{\partial t}$ is the time rate of heat storage and $s^{\cdot}$ is the heat generated. Expressing into Cartesian coordinates, equation (4.8) becomes:

$$-k\frac{\partial^2 T}{\partial x^2} - k\frac{\partial^2 T}{\partial y^2} - k\frac{\partial^2 T}{\partial z^2} + \rho c_p \frac{\partial T}{\partial x} + \rho c_p \frac{\partial T}{\partial y} + \rho c_p \frac{\partial T}{\partial z} + \frac{\partial q_r}{\partial x} + \frac{\partial q_r}{\partial y} + \frac{\partial q_r}{\partial z} = \rho c_p \frac{\partial T}{\partial t} + s^{\cdot} \tag{4.9}$$

Equation (4.9) can be simplified by assuming one dimensional (1D) system equation. In fact, this approximation is valid for the structure presented since the length of the beam is much larger than its width and thickness and where a correction number, the shape factor, S, is added for the missed dimensions. In the case of 1D system, the electro-thermal response of the metal beam is written as:

$$-k\frac{\partial^2 T}{\partial x^2} + \rho c_p \frac{\partial T}{\partial x} + \frac{\partial q_r}{\partial x} = \rho c_p \frac{\partial T}{\partial t} + s^{\cdot} \tag{4.10}$$

In our case, the heat generated ($s^{\cdot}$) comes from Joule heating, J, via an applied voltage. According to Ohm's law, the heat generated (J) can be expressed as:

$$J = \frac{j^2}{\sigma} \tag{4.11}$$

where j is the current density and σ the electrical conductivity (equal to $1/\rho$ with ρ the electrical resistivity). In addition, the heat transfer coefficient of the metal thin film per unit length, G_f, due to convection and radiation has to be taken into consideration in the final heat balance equation. The heat transfer coefficient, G_f, is defined as:

$$G_f = (2h + w)\beta + 4(2h + w)\epsilon\sigma T_0^3 + \frac{S}{R_t} w \tag{4.12}$$

where w and h are the width and the thickness of the film, β is the air convection coefficient, ϵ is the effective emissivity, σ is the Stefan-Boltzman constant, S is the shape factor equal to:

$$S = \frac{h}{w}\left(\frac{2t_v}{h} + 1\right) + 1; \tag{4.13}$$

and R_T is the equivalent thermal resistance of the SiO_2, Si_3N_4 and the air layer: (see Figure 4.1)

$$R_T = \frac{t_v}{k_v} + \frac{t_n}{k_n} + \frac{t_o}{k_o} \tag{4.14}$$

with t_o, t_n, t_v and k_o, k_n, k_v the thicknesses and thermal conductivities of the three SiO_2, Si_3N_4 and air layers respectively.

Under steady state conditions, the temperature is unchanged with time and therefore the heat balance equation of a beam of width w and thickness h can be simplified to:

$$j^2wh + k_pwh\frac{\partial^2T(x,t)}{\partial x^2} - G_f\left[T_x - T_0\right] = 0 \tag{4.15}$$

In the next section, the heat balance equation developed for a suspended beam of width w and thickness h as shown by equation (4.15) will be adapted to the reference and test structures fabricated in this experiment.

4.3 Test micro-structure design

In this section, the development of the design and the final layout of the MEMS devices for thermal conductivity measurement are presented. The design includes a pair of micro-structures: one is used as a reference and the other one as a test structure.

In the first part of this section, the layout of the reference and test structures is presented. In addition, the principle of the thermal conductivity measurement is explained. In the second part, CoventorWare simulations have been performed to obtain constant temperature along the heating stripe. The influence of the deposition conditions of Al thin films and the heating stripe dimensions have been investigated.

4.3.1 The reference and test structure

The design comprises a reference structure and a test structure as shown in Figure 4.2 for the measurement of theral conductivities.

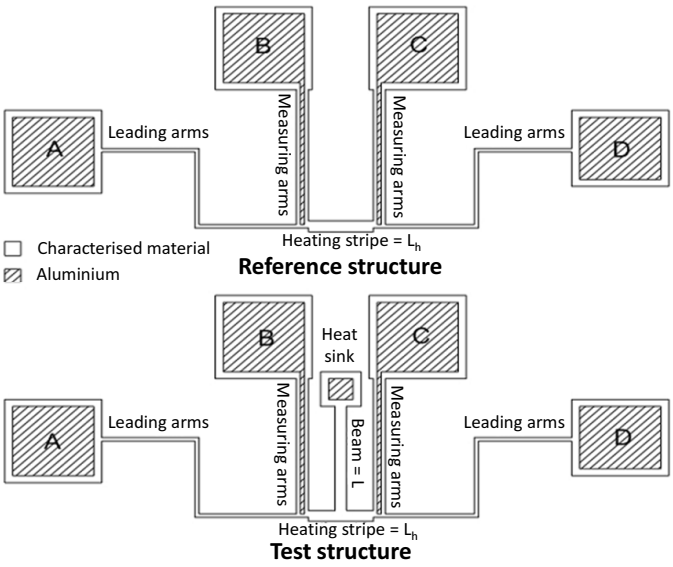

Figure 4.2: *Schematic of the reference and test structures*

The geometries of the two structures are very similar. For each structures, it consists of four Al pads A, B, C and D, two leading arms connecting the A and D pads to the heating stripe (heater) and two measuring arms (voltage probes) connecting the heating stripe to pads B and C. During the test, a voltage is applied between pads A and D inducing a current flow creating Joule heating into the structures. The corresponding flowing current and the voltage drop across the heating stripes of the reference and the test structures are recorded between pads B and C. The only difference between the test and the reference structure is that there is a suspended beam connected to a heat sink in the test structure as shown in Figure 4.2. Due to this difference, each structure has different heat balance conditions. Therefore, the heating powers P_R and P_t for the reference and test structures respectively, can be expressed as:

$$P_R = G_R \Delta T_R \tag{4.16}$$

and as:

$$P_t = G_R \Delta T_t + P_B \tag{4.17}$$

where G_R is the total heat transfer coefficient of the reference structure and ΔT is the difference of temperature between the heating stripe and the substrate (T_0). P_B is the heat dissipation power of the metal beam.

Both structures have been designed to obtain a constant temperature along the heating stripe. Under this condition, there is no temperature gradient along the heating stripe of the reference structure therefore, no thermal current flows through it and the heat balance condition for the heating stripe can be written as:

$$P_{Rh} = V_R I_R = G_f L_h \Delta T_R \tag{4.18}$$

where P_{Rh} is the heating power applied to the heating stripe, V_R and I_R are the measured voltage and current along the heating stripe and L_h is the length of the heating stripe.

However, along the metal beam of the test structure, a thermal current flows from the heating stripe to the heat sink. Therefore, the heat dissipation power P_B of the metal beam can be defined as:

$$P_B = G_f L \left(\frac{\Delta T_t}{2} \right) + whk_p \left(\frac{\Delta T_t}{L} \right) \tag{4.19}$$

where L is the beam length. In the right hand side of equation 4.19, the first term represents the heat dissipation by convection, radiation and heat transfer through the air gap and the substrate while the second term represents the heat dissipation by conduction through the anchor. Solving for k_p, equation (4.19) becomes:

$$k_p = \frac{L}{wh\Delta T_t} \left[P_B - GL \left(\frac{\Delta T_t}{2} \right) \right] \tag{4.20}$$

The thermal conductivity of the metal thin film can be determined by combining equations (4.16-4.20):

$$k_p = \frac{L}{wh\Delta T_t} \left(P_t - G_R \Delta T_t - \frac{GL\Delta T_t}{2} \right) \tag{4.21}$$

$$k_p = \left[\left(\frac{P_t}{\Delta T_t} - \frac{P_R}{\Delta T_R}\right) - \frac{P_{Rh}}{2\Delta T_R}\frac{L}{L_h}\right] \times \frac{L}{wh} \tag{4.22}$$

where ΔT_R and ΔT_t are the difference of temperature between the heating stripe of each structure and the substrate and are equal ($\Delta T_R = \Delta T_t$), see section 4.5. As a result, the difference between the heating powers of the test and the reference structures ($P_t - P_R$) can be assumed to correspond only to the heat dissipation of the beam P_B.

Therefore, as described in section 4.5, the thermal conductivity of the metal beam, k_p, can be deduced from equation (4.22) by calculating the change of temperature between the heating stripe of each structure and the substrate, (ΔT_R and ΔT_t), the heating powers of the heating stripe (P_{Rh}) and of each structures (P_t and P_R) from their recorded I-V characteristics.

4.3.2 Optimisation of the test microstructures via CoventorWare Finite Element Method (FEM) temperature simulations

The method presented above works successfully only under certain conditions. The conditions that render the measurements valid are:

1) the temperature of the structure should not exceed 800 K, so that the effects of heat dissipation by radiation can be ignored in the thermal conductivity calculations [209]. This observations has also been reported by [210] who found that radiation only contributes at high input powers, or material surface temperatures above 800 K.

2) the temperature along the heating stripe of both structure has to be constant to ensure no thermal current flows through it. This conditions is required to cancel out the air-free convection coefficient, the effective emissivity, the Stefan-Boltzman constant, the shape factor of the beam, and the equivalence thermal resistance of the air layer, Si_3N_4 layer, and SiO_2 layer between the beam and substrate in the final equation used to determine the thermal conductivity of the material [211].

3) the temperature along the metal beam is assumed to decrease linearly from the heating stripe to the heat sink if the temperature difference between the heating stripe and the heat sink is not high, ensuring that a thermal current flows through the metal beam [28].

4) the changes of temperature between the reference structure and the substrate, ΔT_R, and between the test structure and the substrate, ΔT_t, have to be equal ($\Delta T_R = \Delta T_t$) in order to assume that the difference in heating power between the reference structure and test structure ($P_t - P_R$) is due to the heat dissipation of the metal beam of the test structure, P_B [28].

The design of both structures has been optimised in order to match the above required conditions. To do so, the influence of the deposition of a thin Al layer on top of the measuring wires as well as the effect of the physical dimensions of the structures on the temperature profile have been investigated by CoventorWare FEM Simulations. The thin film structure and the metal electrodes have been fixed together and, in order to decrease the computational time, the substrate has been excluded from the analysis. The mesh elements are bricks of dimensions in (X,Y,Z) coordinates of (2,2,0.5) μm (2 μm^3 corresponding to 15200 elements) in the simulations presented in Figure 4.3, 4.4 and 4.5. As boundray conditions, the temperature of the four Al pads electrodes and the heat sink has been set at (300 K) for all simulations. The heat sink has been designed to be big enough (a 50 μm^2 squared pad) in order to assume that its temperature is 300 K, leading to the observed change of temperature along the metal beam. A voltage of 1 V has been applied between the A and D electrodes to generate heat through the structure. Table 4.1 lists the Aluminum's properties used in this study.

Parameter	Value
Young's Modulus [GPa]	70
Poisson ratio	0.35
Thermal exp. coef. [10^{-6}/ °C]	23.1
Thermal conductivity [W/m°C]	237
Electrical resistivity[nΩ/m]	28.2

Table 4.1: *Al properties used in the FEM simulations*

Figure 4.3 shows the temperature profile of the test structure along its 15 μm wide heating stripe (a) without and (b) with a thin 500 nm thickness Al film on top of the measuring wires (voltage probes).

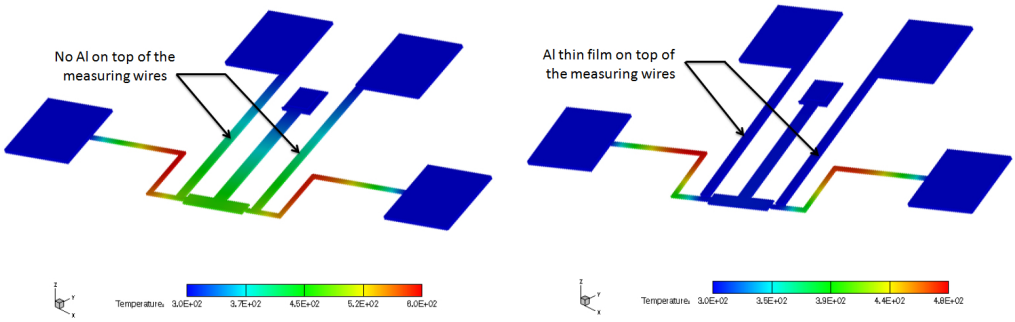

(a) without Al layer on the measuring wires (b) with Al layer on the measuring wires

Figure 4.3: *CoventorWare simulations of the temperature profile of the test structure with and without Al thin film covering the measuring stripes*

From Figure 4.3 (a), when the voltage is applied, the temperature of the heating stripe in the structure without Al thin film rises up to 460 K in the measuring arms and 600 K in the leading arms respectively. However, when Al thin film is deposited on the measuring arms the temperature of the heating stripe is kept low (320 K) and the maximum temperature that the structure undergoes is 480 K in the leading arms. The deposition of a thin Al layer on the measuring arms has resulted in increasing the measurement accuracy as well as limiting the thermal heating of the structure. In addition, a linear change of temperature along the beam due to a thermal current flowing towards the heat sink is observed. Figure 4.4 shows the temperature profile along the metal beam of the test structure with Al layer on the measuring arms.

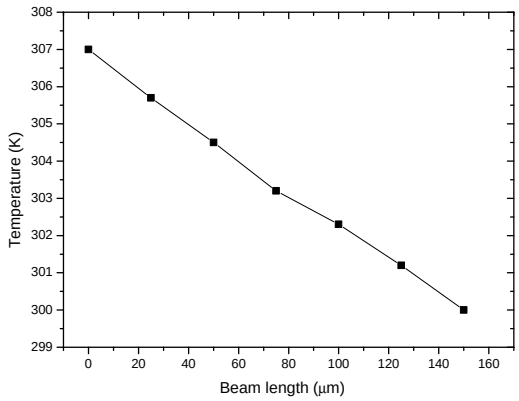

Figure 4.4: *Temperature profile of the metal beam of the test structure*

The second condition to match is to obtain a constant temperature along the heating stripe. To do so, an examination of the effects of different width and length dimensions of the heating stripe on its temperature profile has been performed. Figure 4.5 shows the temperature profile along the test structures with different heating stripe widths of 2, 5, 15 and 25 μm.

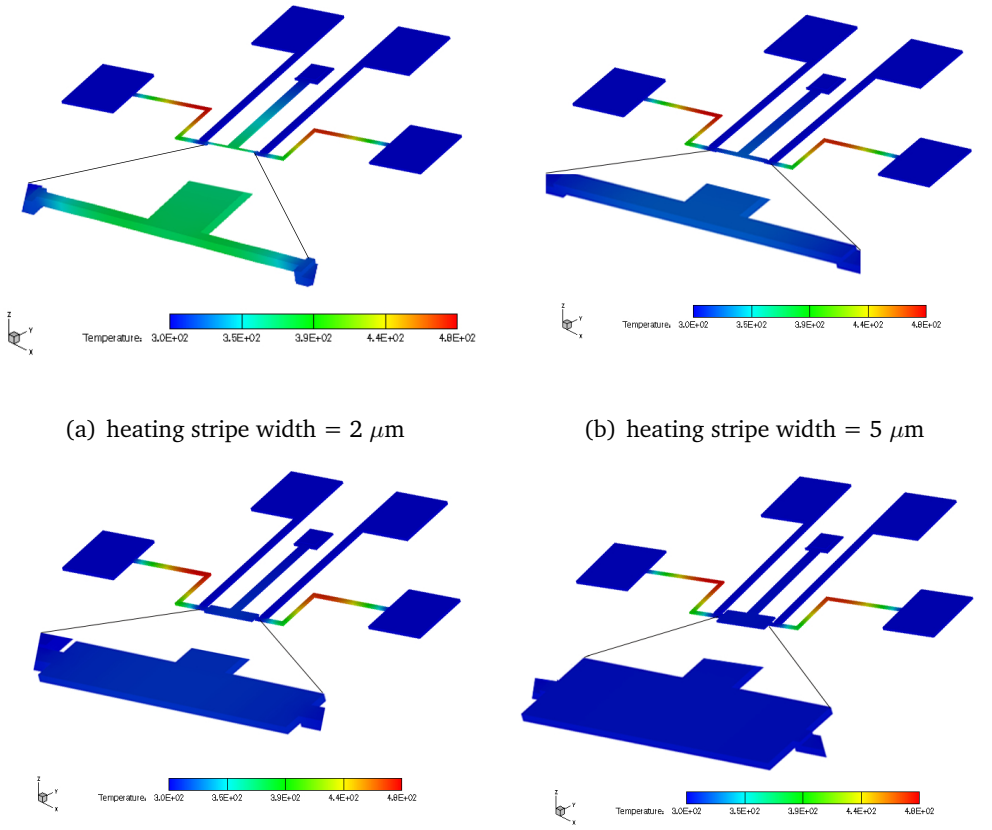

(a) heating stripe width = 2 μm

(b) heating stripe width = 5 μm

(c) heating stripe width = 15 μm

(d) heating stripe width = 25 μm

Figure 4.5: *CoventorWare simulation of the temperature profile along the test structure for different heating stripe widths of 2, 5, 15 and 25 μm*

It has been found that when the heating stripe is narrow (i.e. 2 μm and 5 μm), the temperature along the stripe is not uniform. However, for stripes wider than 15 μm, the temperature has been seen to be uniform along the heating stripe. Therefore, 15 μm has been defined as the critical width of the heating stripe for the MEMS devices. On the other hand, the length of the heating stripe appears not to have significant

influence on its temperature. The temperature profiles of test structures with heating stripe lengths of 20, 80 and 150 μm have been found to be identical. For the ease of fabrication process and measurement procedure, the length of the heating stripe has been defined as 80 μm long.

Finally, it is required that the changes of temperature between the reference structure and the substrate, ΔT_R, and between the test structure and the substrate, ΔT_t, are equal ($\Delta T_R = \Delta T_t$) in order to cancel out the heat dissipation by radiation and conduction through the substrate and the Al pads while subtracting the heating powers of the two structures in equation (4.22). From Figure 4.6, when the voltage is applied, the same change of temperature ($\Delta T_R = \Delta T_t$) has been observed. These observations are valid for Al, Ti and ITO metal beam.

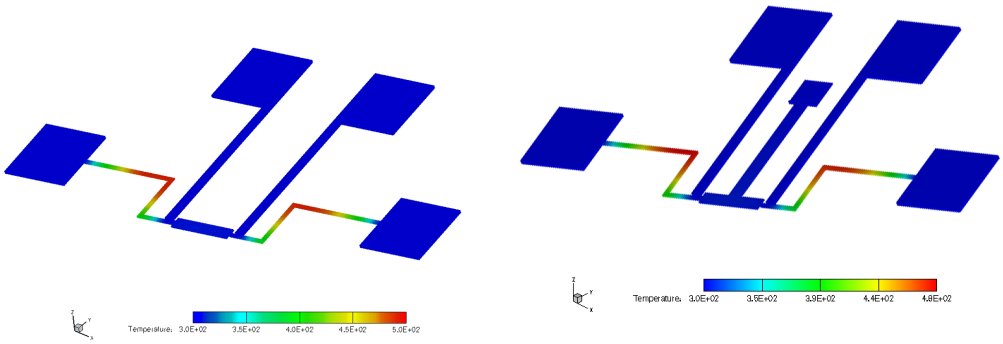

(a) Reference structure (b) Test structure

Figure 4.6: *CoventorWare simulation of the temperature profile along the final reference and test structures*

Table 4.2 shows the final dimensions for the test and reference structures (leading wire, measuring wire, heating stripe and the beam) satisfying the above conditions.

Dimension	Length (μm)	Width (μm)	Thickness (μm)
Leading wire	250	5	0.5
Heating stripe	80	15	0.5
Measuring stripe	200	10	0.5
Beam	150	15	0.5

Table 4.2: *Physical dimensions of the reference and test structure*

The temperature profile of the test structure taken from Figure 4.6 (b) has been plotted in Figure 4.7 showing that the temperature along the heating stripe (250 μm $\leq x \leq$ 330 μm) is constant and the maximum temperature reached in the leading arms is kept low enough (420 K) to ignore radiation effects. It is worth noting that the temperature of the four Al pads electrodes and the heat sink has been set at (300 K) for all simulations and a voltage of 1 V has been applied between the A and D electrodes to generate heat through the structure.

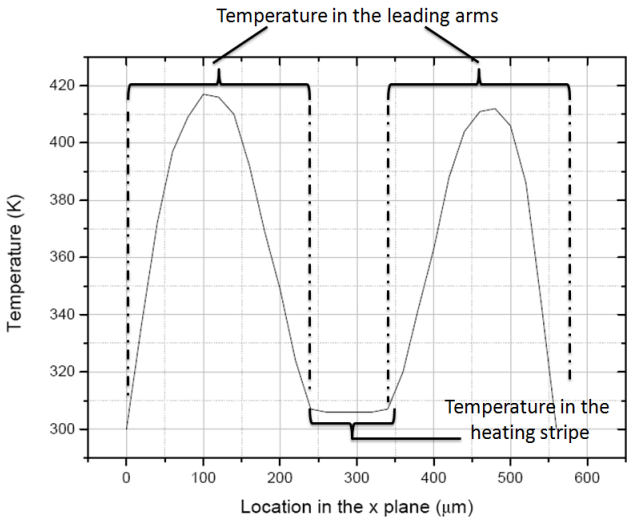

Figure 4.7: *Temperature profile along the structure*

4.4 Fabrication process

This section presents the fabrication process of the test structure developed for the measurement of thermal conductivity of ITO, Ti and Al thin film. The fabrication process flow is based on the surface micromachining techniques described in Chapter 3, section 3.2. In this experiment, three masks have been designed for the pattern of the sacrificial, beam and electrodes pads layers (see Appendix B). Figure 4.8 shows the schematic of the fabrication process.

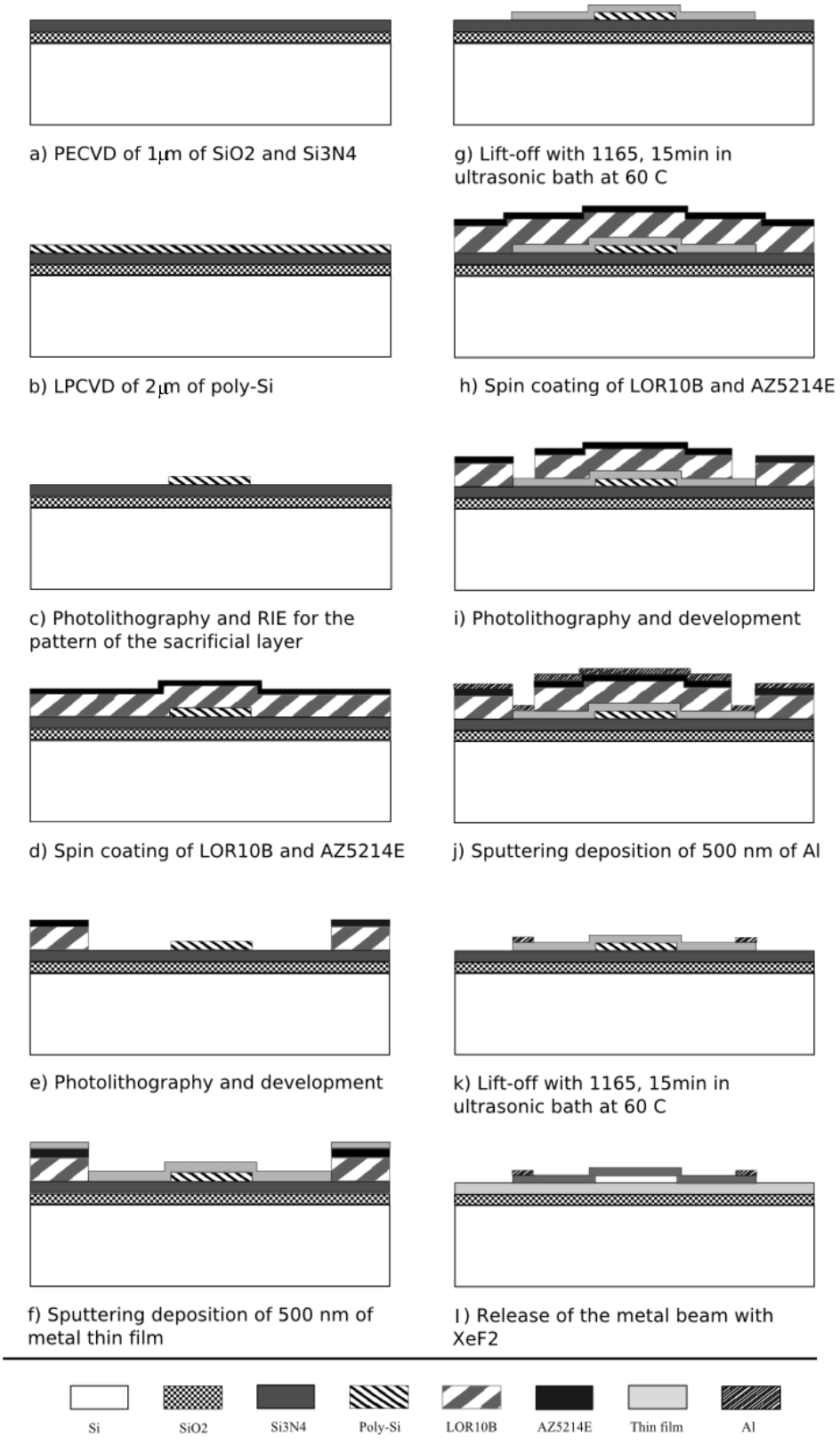

Figure 4.8: *Fabrication process flow*

4.4.1 Insulating and sacrificial layers

The process begins with the deposition of a SiO_2 (1 μm thick) and Si_3N_4 (1 μm thick) by plasma enhanced chemical vapour deposition (PECVD) for electrical and thermal insulation on a 3-inch Silicon wafer, respectively (Figure 4.8 (a)). Then, a 2 μm thick layer of polysilicon (poly-Si) has been deposited by low pressure chemical vapour deposition (LPCVD) to be used as sacrificial material on top of the insulation layers (Figure 4.8 (b)).

The poly-Si sacrificial layer has been photolithographically patterned using 1:1 contact printing in Karl Suss MA8/BA6 mask aligner. For this process, the poly-Si has been masked with a 7 μm thick SPR2207 photoresist and etched in RIE using a $SiCl_4/Ar$ plasma. The remaining photoresist has been completely removed in a O_2 plasma after 60 minute process (Figure 4.8 (c)).

4.4.2 Beam and electrodes layers

Titanium (Ti), Indium Tin Oxide (ITO) and Aluminium (Al) have been chosen as metal for the beam fabrication due to a combination of reasons. These three materials are commonly used in MEMS devices, where the characterisation of the thermal properties of these thin films is often required. Ti has a low density and remains resistant to corrosion in various conditions because a the thin layer of oxide can form on its surface which makes it a desirable material for MEMS devices such as infrared and pressure sensors in hars environment [212]. ITO has been used widely as conductive transparent coating in MEMS devices such as photovoltaic applications [213] and Al is commonly used as thin film metal layer in MEMS devices.

The structure can only work if the beam material is electrically conductive since the thermal conductivity is calculated using I-V measurements. Also, it was decided that if the resistivity of the beam is too low, it might be difficult to carry out the necessary calculations. The material whose thermal conductivity is being investigated, must heat up in order for this method to yield satisfactory results. If the sample is a highly conductive metal, joule heating is not very significant, which make the results from the experiment difficult to analyse. Table 4.3 lists the thermal conductivity of different materials. In principle, the thermal conductivity of thin film material within the range

of thermal conductivity from ITO to Al could be calculated from the fabricated devices. However, the method presnted may not be suitable for materials having lower or higher thermal conductivity than the 10 to 237 $W.m^{-1}.K^{-1}$ range.

Material	Thermal conductivity ($W.m^{-1}.K^{-1}$)
Silver	429
Copper	401
Gold	310
Aluminum	237
Zinc	116
Nickel	91
Iron	80
Platinum	70
Tin	67
Steel, Carbon 1%	43
Lead	35
Titanium	22
ITO	10
Pyrex Glass	1
PVC	0.2
Polypropylene	0.1

Table 4.3: *List of thermal conductivity of various materials*

As discussed in Chapter 3, section 3.2, etching and lift-off process are two common ways for patterning metals in the micro-fabrication industry. Lift-off process has been preferred over etching process to pattern the beam and the electrodes pads of the structures in order not to etch the polysilicon sacrificial layer while patterning the beam and not to damage the beam while patterning the electrodes pads. The procedure used in this experiment has been a bi-layer lift-off process. First, a LOR5B layer has been spin coated onto the substrate at 4000 rpm for 60 seconds and baked at $190°$C for 60 seconds. LOR5B is not photosensitive but it is soluble in conventional developers. Then, an AZ5214E photoresist layer has been spin coated on top of the LOR5B layer (Figure 4.8 (d)). The photoresist has been exposed to UV lithography followed by reversal bake step for 2 minutes at $120°C$. The cross-linking agent in the resist has turned to be active due to the high temperature. Once the exposed area has cross-linked, it has become insensitive to light and almost insoluble in developer. However, the unexposed area has continued to act like regular photoresist. Thus, a flood exposure step has been carried out and the unexposed areas have been dissolved in developer (AZ 726 MIF) (Figure

4.8 (e)).

Then, the metal material has been sputtered (Figure 4.8 (f)). Initially, the thickness of the beam has been chosen to be 2 μm. The fabrication of a thick beam requires a very thick layer of lift-off resist which has to be 2 to 3 times thicker. The use of thick photoresist can lead to problems during patterning and depositing the metal layers. It has been observed while using a thick LOR layer that the metal layer peeled off the wafer after deposition. Moreover, the pattern of the structures has not been well defined. Therefore, the thickness of the metal beam has been reduced to 500 nm resulting in a significant improvement in the quality of the structures. The final pattern of the metal beam has been created by washing away the sacrificial LOR5B layer using an 1165 developer for 15 minutes in an ultrasonic bath at $60°C$ (Figure 4.8 (g)). The exact same lift-off process has been repeated to pattern the Al electrodes pads (Figure 4.8(h)-(k)).

4.4.3 Release of the structure

XeF_2 has been used to etch the polysilicon used as sacrificial layer using a MEMSSTAR XeF_2/HF tool. The recipe used for etching the sacrificial layer had to have selectivity to Si_3N_4, the insulation layer. XeF_2 etching has been performed under a pressure of 9 Torr and a flow rate of 50 SCCM. The beam and heating stripe have been released while the insulation layers, ITO, Ti and Al layers have not been damaged (Figure 4.8 (l)). Figure 4.9 is a SEM image of a released ITO heating stripe of a reference structure.

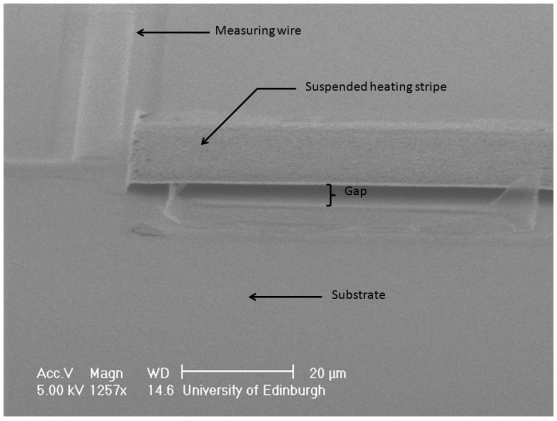

Figure 4.9: *Released ITO heating stripe*

Figure 4.10 shows SEM images of the top view of the fabricated ITO (a) reference and (b) test structures.

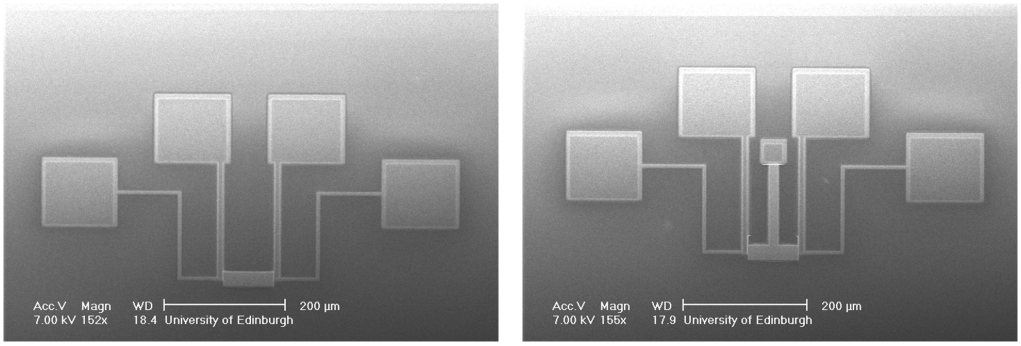

(a) Reference structure (b) Test structure

Figure 4.10: *SEM pictures of the top view of the fabricated ITO reference and test structures*

4.5 Measurements

This section presents the procedure employed to deduce the thermal conductivity of ITO, Ti and Al thin films. Firstly, the linear and quadratic coefficients of temperature of the three materials have been determined. Secondly, the I-V characteristics of the reference and test structures required for the calculation of the heating powers of the reference and the test structures have been recorded and presented.

4.5.1 Calculation of the linear and quadratic coefficient of temperature

Equation 4.22 in section 4.3 expresses the thermal conductivity, k_p of a thin film deduced from the analogy of the electro-thermal models of the reference and test structures such as:

$$k_p = \left[\left(\frac{P_t}{\Delta T_t} - \frac{P_R}{\Delta T_R}\right) - \frac{P_{Rh}}{2\Delta T_R}\frac{L}{L_h}\right] \times \frac{L}{wh}$$

where ΔT_R and ΔT_t are the difference of temperature between the heating stripe of the reference and test structure and the substrate respectively. P_R and P_t are the heating powers of the reference and test structure respectively and P_{Rh} is the heating power of

the heating stripe.

In order to calculate the thermal conductivity of a metal, ΔT_R, ΔT_t, P_R, P_t and P_{Rh} have to be determined, knowing the dimension of the structure, L, L_h, w and h. All these parameters can be calculated from the recorded I-V characteristics of both structures.

To determine the change of temperature ΔT_R and ΔT_t in equation (4.22), the linear (a_1) and quadratic (a_2) coefficients of temperature of the material have been determined by measuring the change of resistance across ITO, Ti and Al bridges such as the one shown in Figure 4.11 at regular temperature intervals.

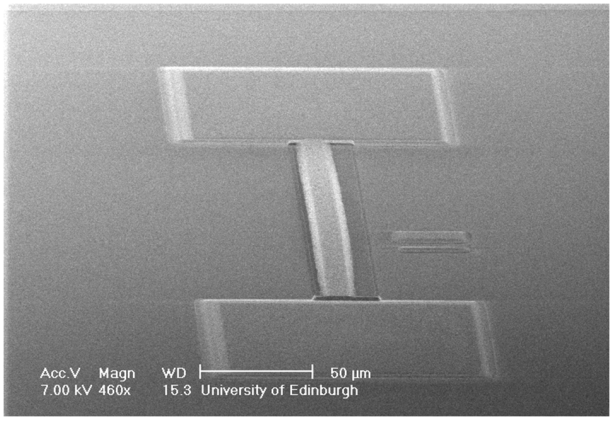

Figure 4.11: *SEM image of a 10 μm wide and 200 μm long Ti bridge*

The linear (a_1) and quadratic (a_2) coefficients of temperature of each material have been deduced from the change of material resistance over a range of temperature. The relationship between resistance and temperature can be defined as:

$$R_i = R_0[1 + a_1\Delta T_i + a_2(\Delta T_i)^2] \tag{4.23}$$

where R_i is the resistance of the metal at the temperature T_i, R_0 is the resistance at the temperature T_0 and $\Delta T_i = T_i - T_0$ is the change of temperature. In order to calculate (a_1) and (a_2), two different values of T have been chosen and values have been inserted into equation (4.23) and solved as simultaneous equations. Figure 4.12 shows the change of resistance of two Ti bridges of (a) 10 μm by 200 μm and (b) 5 μm by 300 μm. The linear and quadratic coefficients of temperature of ITO and Al thin films have been determined in the same way. Table 4.4 summarises the coefficients of

temperature for the three films studied.

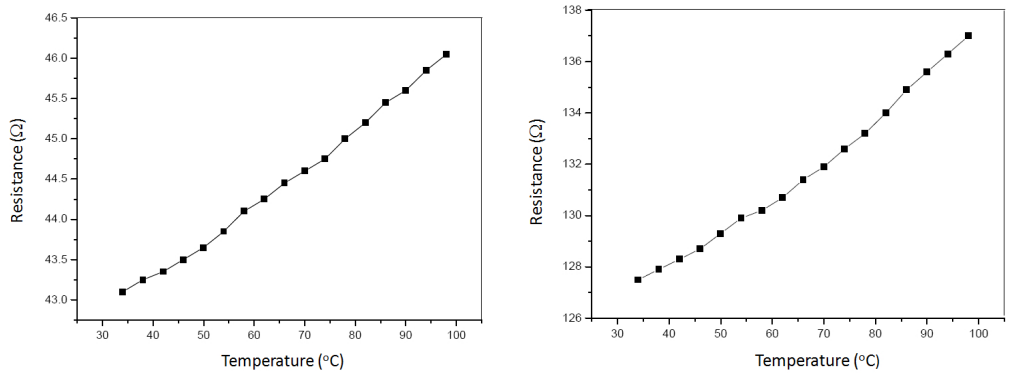

(a) Ti bridge (width = 10 μm length = 200 μm) (b) Ti bridge (width = 5 μm length = 300μm)

Figure 4.12: *Experimental change of resistance over a range of temperature for Ti bridges*

	ITO	Ti	Al
Linear coefficient of temperature $a_1(K^{-1})$	$2.35.10^{-3}$	$6.59.10^{-4}$	$4.25.10^{-3}$
Quadratic coefficient of temperature $a_2(K^{-2})$	$4.79.10^{-6}$	$6.62.10^{-6}$	$2.68.10^{-7}$

Table 4.4: *Measured linear and quadratic coefficients of temperature for ITO, Ti and Al thin films*

4.5.2 I-V characteristics of the reference and test structure

Figure 4.13 shows the applied voltage versus measured current for (a) ITO, (b) Ti and (c) Al thin films. The design of the reference and test structures has been optimised in order to obtain the same electrical power for each structure. First, a voltage of 1 V has been applied between pads A and D inducing a current flow creating Joule heating into the structures. The corresponding flowing current has been measured between pads B and C and the same change of resistance has been observed in the heating stripe of both structures, $\Delta R_R = \Delta R_t$. Therefore, it can be assumed that no electrical current flows through the metal beam.

By fitting the resistances of each structures obtained from Figure 4.13 into equation (4.23) ($R_{i1} = R_R$ and $R_{i2} = R_t$), the change of temperature in the reference structure, $\Delta T_{i1} = \Delta T_R$, and in the test structure, $\Delta T_{i2} = \Delta T_t$, can be calculated. Assuming that R_0, a_1 and a_2 are constant, if $\Delta R_R = \Delta R_t$, then $\Delta T_R = \Delta T_t$. This condition supports the results obtained from the electro-thermal simulations as shown in Figure 4.6, where both structures have been developed so that the temperature along their heating stripe is constant and the difference of temperature between their heating stripes and the substrate are equal, $\Delta T_R = \Delta T_t$. Under this condition, there is no temperature gradient along the heating stripe. Therefore, there is no thermal current flowing through it. Accordingly, the heat transfer through the substrate and the Al electrodes is then identical for both structure and cancel out in equation (4.22) by analogy. Furthermore, the temperature during the measurement has been kept low ($T = 420K$) so that radiation effect can be ignored.

In the same way, the previously measured current has been sourced for both structures between pads A and D and the measured voltages (V_R) between pads B and C have been recorded. Figure 4.14 shows the measured voltages (V_R) between pads B and C versus measured currents (I_R) between pads B and C for the reference and the test structures for (a) ITO, (b) Ti and (c) Al thin film. The difference in the measured power ($P_t - P_R$) between the two structures seen by the mismatch between the two curves in Figure 4.14 can be assumed to be due to the thermal current flowing along the beam towards the heat sink in the test structure and corresponds to the heat dissipation of the metal beam (P_B).

The heating powers of the test structure, P_t, of the reference structure, P_R, and of the heating stripe, P_{Rh}, can be calculated using the I-V characteristics plotted in Figure 4.14, where $P_{Rh} = P_R$. The dimensions of the structure are $L = 200$ μm, $L_h = 80$ μm, $w = 15$ μm and $h = 500$ nm in order to ensure the resistances of both structures to be equal (Figure 4.13). Using equation (4.22), the thermal conductivity of the Ti, ITO and Al thin films have been calculated and found to be slightly lower than the thermal conductivity value of bulk materials.

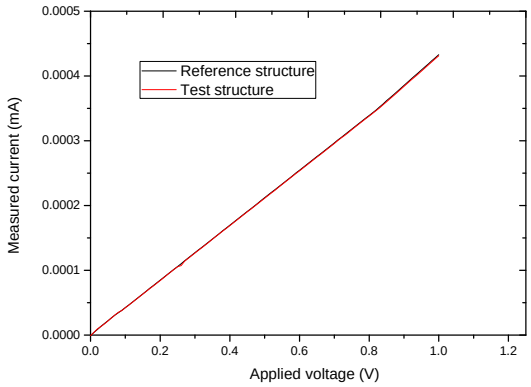

(a) ITO

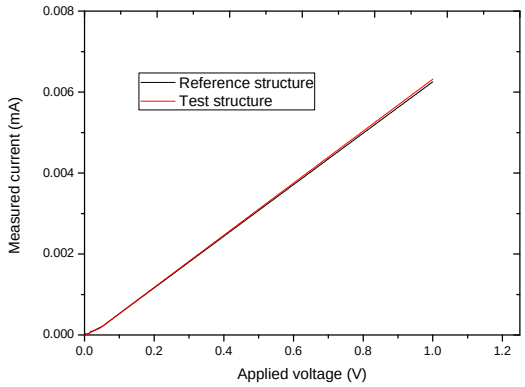

(b) Titanium

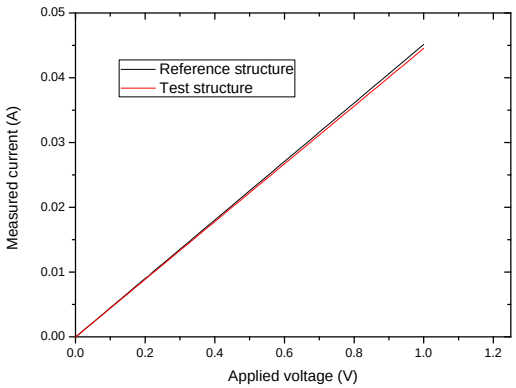

(c) Aluminum

Figure 4.13: *Applied voltage between pads A and D versus measured current between pads B and C for (a) ITO, (b) Ti and (c) Al thin films*

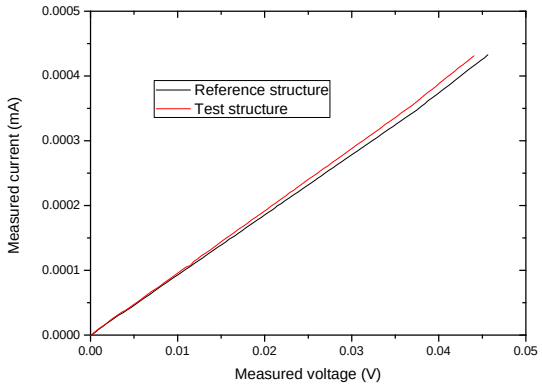

(a) ITO

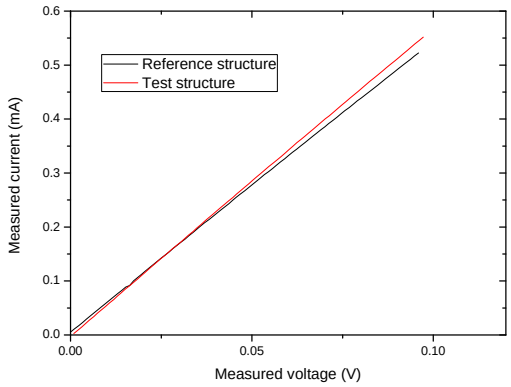

(b) Titanium

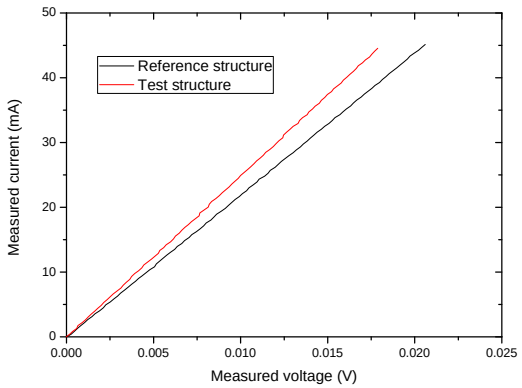

(c) Aluminum

Figure 4.14: *Measured voltage between pads B and C versus measured current between pads B and C for (a) ITO, (b) Ti and (c) Al thin films*

Table 4.5 lists the different thermal conductivity values for thin films and bulk material for ITO, Ti and Al [214].

	ITO	Ti	Al
Bulk (W.m^{-1}.K^{-1})[199]	12	21.9	237
Thin film (W.m^{-1}.K^{-1})	10.2	16.8	200

Table 4.5: *Thermal conductivity values of bulk and measured thin film material of ITO, Ti and Al*

The thermal conductivity of 500 nm thick ITO, Ti and Al thin films have been found to be 10.2 $W.m^{-1}.K^{-1}$, 16.8 $W.m^{-1}.K^{-1}$ and 200 $W.m^{-1}.K^{-1}$ respectively. These values are similar to the values of bulk material (Table 4.5) but slightly lower due to the fact that for material with small thicknesses, the thermal transport is lowered by phonon scattering at lattice imperfections and boundaries [16]. The thermal conductivity of a 950 nm and 1.4 μm thick Al thin film has been reported by be 201 $W.m^{-1}.K^{-1}$ and 180 $W.m^{-1}.K^{-1}$ respectively [25, 198]. Here, the thermal conductivity of a 500 nm thick Al film has been calculated as 200 $W.m^{-1}.K^{-1}$. Although the thermal conductivity of 1.4 μm thick Al film should be closer to the bulk value, the value obtained in this experiment for a 500 nm thick Al film is higher than the one reported by [198]. The difference observed could be due to the different MEMS devices and the thermal model proposed to characterise the thermal conductivity of the material. For instance, the heat lost by conduction through the Al interconnections, as well as the effect of the heat spreading through the SiO_2 layer have not been taken into consideration in the calculations reported by [198], which could be the reason for the low thermal conductivity value obtained for Al. In addition, the different quality of the deposited material and the low resistivity of Al can be an explanation for the divergent calculated values. On the other hand, our results are in reasonable agreement with values reported by [25].

4.6 Conclusions

The work presented in this chapter has consisted in the design and the fabrication of a MEMS structure for the measurement of the thermal conductivity of metal thin films. The main advantage of the method presented in this study is its simplicity and straightforwardness. The measurements can be made in air and the analysis considers

the heat loss due to convection and radiation. Therefore, no extra measurements need to be taken to compensate heat loss which could potentially affect the characteristics of the material being tested or lead to the use of complicated fabrication methods followed by intricate measurements and calculations.

The MEMS devices are composed of a pair of micro structures: one used as a reference and the other one as a test structure. The two structures have identical geometry and consist of four Al pads A, B, C and D, two leading arms connecting the A and D pads to the heating stripe (heater) and two measuring arms (voltage probes) connecting the heating stripe to pads B and C. During the test, a voltage applied between pads A and D, induces a current that heats up the structures by Joule heating and the corresponding passing current and the voltage drop across the heating stripes of the reference and the test structures have been recorded between pads B and C. The only difference between the two structures is that in the test structure a beam is used to connect the heating stripe to a heat sink.

The heat balance equation of the MEMS has been developed including the role of the different heat transfer mechanisms by convection, conduction through the substrate and radiation from all the surfaces of the beam. FEM simulations have been performed in order to study the temperature profile of the structure. The design geometry of the reference and test structures has been optimized so that the temperature along their heating stripe is constant, the temperature along the metal beam decreases linearly from the heating stripe to the heat sink and that the changes of temperature between the reference structure and the substrate, ΔT_R, and the test structure and the substrate, ΔT_t, are equal ($\Delta T_R = \Delta T_t$). Under these conditions, there is no temperature gradient along the heating stripe. Therefore, there is no thermal current passing through it. Thus, by subtracting the heating powers of the two structures, the heat dissipation by radiation and conduction through the substrate and the Al pads are cancelled out.

However, along the metal beam of the test structure, a thermal current flows from the heating stripe to the heat sink. Therefore, it has been deduced that the difference between the heating powers ($P_t - P_R$) calculated from the measured I-V characteristics of both structures is due to the thermal current flowing through the beam towards the heat sink in the test structure and corresponds to the heat dissipation of the metal beam P_B. As a result, only the heat dissipation of the metal beam enters into consideration

in the final thermal conductivity calculation.

In order to calculate the change of temperature in both structures, the linear and quadratic coefficients of temperature have been determined by measuring the change of resistance across the metal bridges. Then, the heating powers of each structure have been calculated from the measured I-V characteristics. The thermal conductivity of ITO, Ti and Al thin films have been measured to be 10.2 $W.m^{-1}.K^{-1}$, 16.8 $W.m^{-1}.K^{-1}$ and 200 $W.m^{-1}.K^{-1}$, respectively. Overall, the thermal conductivity values of of ITO, Ti and Al thin films show good agreement with the thermal conductivity of bulk material. The calculated values in this study are close to but lower than the values of bulk materials as expected. These results demonstrate the capability of the developed MEMS structure for thermal conductivity measurement of conductive thin film.

Chapter 5
Stress recovery in Polyimide (PI) MEMS

5.1 Introduction

Polymer thin film materials attract great interest as functional layers for novel micro-electronics sensors due to their excellent mechanical, dielectric and chemical properties. However, the use of polymer in the micro-fabrication industry remains challenging since most polymer thin films experience a form of residual stress after micro-fabrication process. For many sensor applications, it is desirable to minimize the residual stress built in polymer thin films during the fabrication process in order to optimize MEMS' performance and functionality.

This chapter presents an approach to relieve the residual stress induced during fabrication processing of Polyimide (PI) micro-cantilevers leading to stress free PI cantilever resonators.

In section 5.2, the different forms of stress present in PI cantilevers resulting in an out of plane beam deflection after the release process are calculated and presented.

In section 5.3, the fabrication process of PI cantilevers as well as PI membranes used for the spectroscopy characterisation are described.

In section 5.4, low energy Ar^+ ion bombardment in a plasma has been employed to eliminate the stress present in PI cantilevers. The mechanical deflection recovery of the cantilever beam and the surface characterisation of the film using XPS and FTIR are presented. The effects of low energy Ar^+ ion bombardment on the PI structure along with the mechanism responsible for deflection relaxation are discussed.

5.2 Mechanical deformation due to stress

This section presents the different types of stress present in the PI cantilever beams fabricated in this experiment as well as the mechanical bending deformation as a result of the stress.

Micro-fabrication processing often induces stress in the different film layers of a device. PI processing involves thermal cycling, and mean stress arises from mismatch of the coefficient of thermal expansion (CTE) between two materials. Non-uniform processing conditions throughout the beam thickness lead to the presence of stress gradient in the PI. One issue related to the use of polymer material in released structures such as cantilevers is the bending of the beam as a result of the presence of stress. The residual stress causes the cantilever to bend either, upwards or downwards, depending on the type of stress created within the material (tensile or compressive) [6].

Before the release of a cantilever, the cantilever beam experiences intrinsic tensile stress (σ) composed of a uniform stress (σ_0) causing an in-plane extension and a stress gradient (σ_1) leading to an out of plane displacement.

The total intrinsic stress can be expressed as [215]:

$$\sigma(z) = \sigma_0 + \sigma_1 \frac{z}{t/2} \tag{5.1}$$

where $z \in (-t/2, t/2)$ is the coordinate normal to the surface of the beam with the origin at the film's mid plane, t is the thickness of the film, (σ_0) is the uniform stress and (σ_1) is the stress gradient obtained by calculation as shown later in this section. However, before the release, the attractive force between the PI film and Si substrate prevents stress relief. Once released, the mean stress and the stress gradient redistributes along and through the beam resulting in an in-plane extension and a non-linear deflection causing an upward bending of the beam [215] (Figure 5.1).

A cantilever bending away from the substrate after release is the result of a positive stress gradient within the beam. In such case, before release, the cantilever beam experiences a compressive stress (material has the desire to expand, but the expansion is prevented) on the bottom layer and a tensile stress (material has the desire to

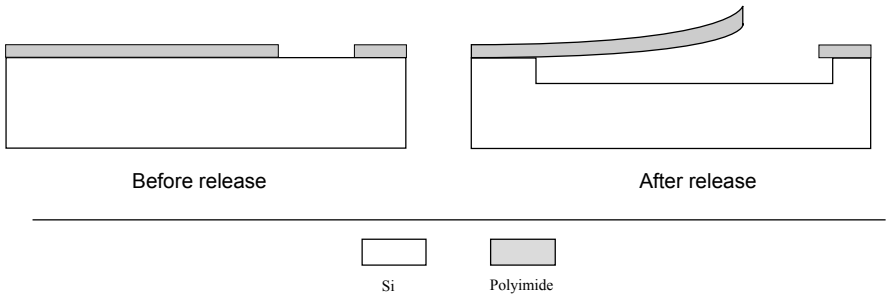

Figure 5.1: *Schematic of the deflection of a PI cantilever beam due to fabrication process*

contract, but the contraction is prevented) on the top layer. Thus, once the beam is released the upper tensile part can contract and the compressive bottom part can expand leading to an upward deformation. On the other hand, a cantilever bending towards the substrate is associated with a negative stress gradient. In such case, the bottom layer is tensile and the top layer is compressive before release. The non-uniform stress in the beam thickness creates a bending moment M_0 [215]:

$$M_0 = \int_{-t/2}^{t/2} \sigma(z) w z dz = \frac{wt^2}{6}\sigma_1 \tag{5.2}$$

which results in a constant curvature and a non-linear deflection of the cantilever beam. The radius of curvature, R can be defined as:

$$R = \frac{E}{d\sigma(z)/dz} = \frac{EI}{M_0} = \frac{Et}{2\sigma_1} \tag{5.3}$$

The deflection profile and the length of the PI cantilever beam after elongation can be determined from the radius of curvature using simple trigonometry mathematics [215]. Figure 5.2 shows the geometrical model of the cantilever beam bending due to stress used for the calculations.

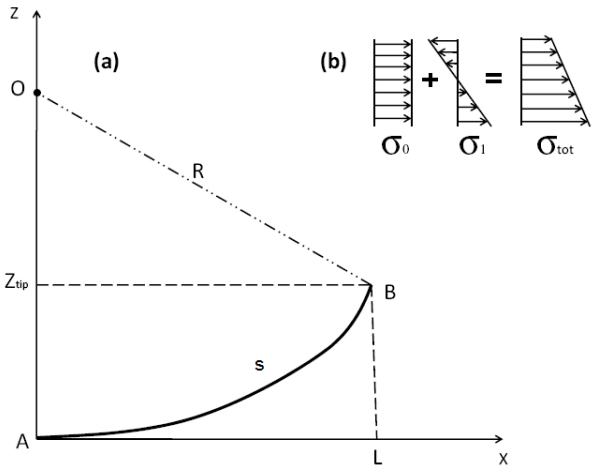

Figure 5.2: *Schematic drawing of (a) the beam deflection and (b) stress distribution in the PI cantilever*

The cantilever profile described here as the arc of circle of centre O is defined as [215]:

$$sin\left(arctan\frac{Z_{tip}}{L}\right) = \frac{\sqrt{L^2 + z_{tip}^2}}{2R} \tag{5.4}$$

The length of the cantilever after elongation is calculated to be [215]:

$$s = R \cdot 2\frac{\pi \arcsin\left(\frac{\sqrt{L^2+z_{tip}^2}}{2R}\right)}{180} \tag{5.5}$$

where M_0 is the bending moment, E is the Young's modulus and I is the moment of inertia of the cross-sectional area of the cantilever beam, z_{tip} is the deflection of the tip of the cantilever, L is the length of the bent cantilever projected on the x-axis, s is the length of the cantilever after elongation and l is the original length. Combining equations 5.3 and 5.4, the stress gradient can be determined by [215]:

$$\sigma_1 = \frac{2Etsin(arctan\frac{Z_{tip}}{L})}{\sqrt{L^2 + z_{tip}^2}} \tag{5.6}$$

Then, the mean stress can be calculated by [215]:

$$\sigma_0 = E\epsilon = E\frac{s-l}{l} \tag{5.7}$$

where ϵ is the strain of the cantilever. According to equations 5.6 and 5.7, the mean stress σ_0 and the stress gradient σ_1 for a released cantilever beam of 200 μm long, 20 μm wide and 1.9 μm thick, unexposed to ion bombardment, has been calculated to be 55.2 MPa and 2.25 MPa respectively.

5.3 Fabrication process

This section presents the fabrication processes of PI cantilevers and PI membranes for the purpose of investigating the relief of the residual stress by low energy Ar^+ bombardment into PI film. Initially, one mask has been used to define arrays of PI cantilevers of 1.9 μm thick, 5 μm to 20 μm wide and 25 μm to 400 μm long. The lengths of the cantilevers have been designed to vary from 25 μm to 400 μm long in order to examine the influence of the cantilever geometry on the amount of stress generated during fabrication process. Secondly, free-standing PI membranes have been fabricated in order to characterise the effects of low energy Ar^+ bombardment on the surface structure of PI by FTIR spectroscopy.

5.3.1 Polyimide cantilever

As mentioned in Chapter 2, poly(amic acid) is imidized generally to PI by thermal curing at temperature above 300°C. However, recently, PI has been introduced into the fabrication of new electronic devices where a 300°C thermal treatment can affect critically the devices' performances [85, 86]. These devices require temperature lower than 300°C to achieve high performance. Therefore, in this work, the processing of PI has been limited to temperature $\leq$ 300°C. Here, the stress relaxation study has been performed on PI treated at 200°C, a temperature compatible with the fabrication processes of electronic devices. The FTIR spectrum of the as-fabricated PI thin film presents all the characteristics peaks of a good imidized product as shown in Figure 2.4. The elastic modulus of a macroscopic sample of 10×5.5×0.25 mm^3 of PI has been measured to be 400 MPa using a Dynamic Mechanical Analyser (DMA) at 1Hz. The low

elastic modulus value obtained compared to the value quoted (2.3 GPa) in the datasheet (see Table 2.3) can be explained by the low curing temperature employed to imidize the poly(amic acid) into PI. It could be that due to the large size of the sample there is less crosslinking than in the 1.9 μm thick samples but we believe that this should be closer to the modulus of the 1.9 μm samples rather than the value quoted in the datasheet as we have used low baking temperature, and the value given in the datasheet of HD Microsystems is for higher temperatures.

The fabrication of PI cantilevers started by spun-coated Polyimide PI 2545 on a 3 inch Silicon wafers at 700 rpm for 30 s followed by 4000 rpm for 1 min (Figure 5.3 (a)). Then, the PI was cured in an air-circulating oven to obtain a uniform PI thin film. The temperature has been increased from room temperature to $200°C$ by a heating rate of $4°C/min$ and kept constant at $200°C$ for 30 min and slowly cooled down to room temperature. The resulting PI film has a thickness of approximately 1.9 μm. The PI cantilevers have been patterned using standard UV lithography (Figure 5.3 (b) and (c)). Afterwards, the PI cantilevers have been etched using O_2 plasma in a RIE system (Figure 5.3 (d)). The remaining photoresist has been removed completely using acetone (which does not attack cured PI) as an alternative approach to the usual O_2 plasma step which would have etched the PI film further (Figure 5.3 (e)). The cantilevers have been released from the silicon substrate using a dry release etch process consisting of vapour phase XeF_2 continuous etching (Figure 5.3 (f)). Dry release technique has been preferred rather than a wet release process because of its accurate control of release rate. Release rates are in the range of 3 to 10 μm/min depending on the aperture size of the exposed sacrificial layer and on the release conditions [216]. Here, the release etch has been performed under a pressure of 9 Torr and a gas flow rate of 50 SCCM.

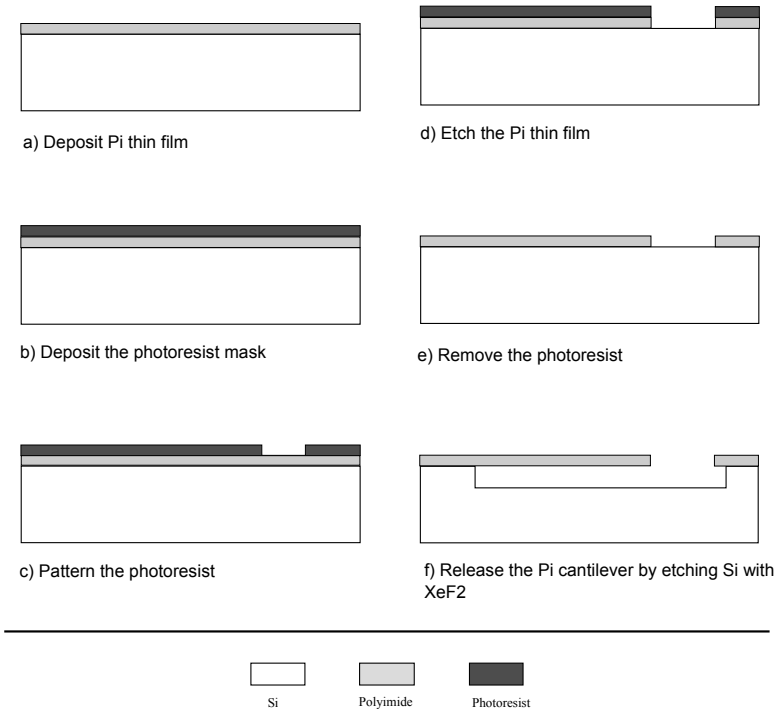

Figure 5.3: *Fabrication process flow of PI cantilever*

Although the dimensions of the PI cantilevers structures are defined during the design process, the final XeF_2 etch release process can alter the dimensions of the structures. In this experiment, Si substrate has been used as sacrificial layer and has not been patterned due to the very good selectivity between PI and Si under XeF_2, thus there is a need to control the release rate in order to minimise the undercut at the anchors as shown in Figure 5.4.

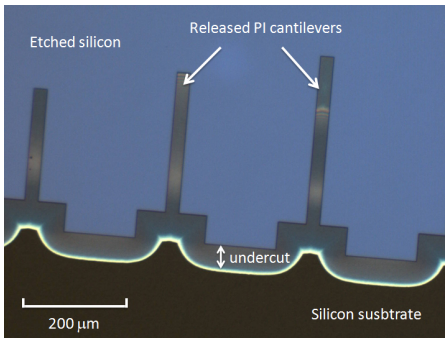

Figure 5.4: *Optical image of an etch undercut*

An over-release can cause unwanted variations to the design dimensions and in the case

of cantilevers; the final beam could become longer than the first designed one. These dimensional changes could result in collapsed beams.

5.3.2 Polyimide membrane

In order to characterise the PI films treated with Ar^+ plasma, PI free standing membranes have been fabricated. The fabrication process is illustrated in Figure 5.5. First, a 1 μm thick oxide has been grown thermally on both sides of a 3 inch silicon wafer in a furnace at $900°C$ (Figure 5.5 (a)). On the front side of the wafer, the thermal oxide has been used as a stop layer during the deep etching step for the purpose of protecting the PI layer from being damaged. Thermal oxide has been chosen over PECVD oxide due to its better flatness. Then, on the back side of the wafer, an additional 2 μm of SiO_2 layer has been deposited by plasma enhanced chemical vapour deposition (PECVD) to be used as a mask during the deep Si etching step (Figure 5.5 (b)).

Afterwards, PI thin film has been spin coated and cured in the exact same way as the one described in the fabrication process of the PI cantilever (Figure 5.5 (c)). The resulting thickness of the PI layer is therefore 1.9 μm. Next, the back side SiO_2 has been patterned by standard UV lithography and etched with CF_4/H_2 in a Plasmatherm RIE etcher (Figure 5.5 (d)). Si etching has been performed using a Deep Reactive Ion Etching (DRIE) process (Bosch process) in an Inductively Coupled Plasma process (ICP), which consists of alternative etch and passivation steps. During the passivation step, C_4F_8-based plasma has been employed to deposit conformally a thin polymer layer. During the etch step, the plasma has been switched to SF_6/O_2 and the plate has been DC biased giving rise to ion bombardment onto the surface of the wafer. The polymer parallel to the surface of the wafer is removed much faster than the polymer deposited on the walls yielding to a directional etching of the silicon (see Chapter 3, section 3.3.3.2 for the principle of operation and Table A2 of Appendix A for the parameters of the procedure employed).

Once the Si has been etched away, a free-standing $SiO_2 - PI$ membrane remained (Figure 5.5 (e)). Since SiO_2 exhibits low transparency at far/mid-IR and the $SiO_2 - PI$ layer exhibits undesired roughness due to mechanical stress between both materials, both effects of which are undesirable for transmissive FTIR measurements. Therefore,

a solution of 50% ammonium fluoride, NH_4F, and 50% acetic acid, $C_2H_4O_2$, has been employed to etch the SiO_2, resulting in the final freestanding PI layer (Figure 5.5 (f)).

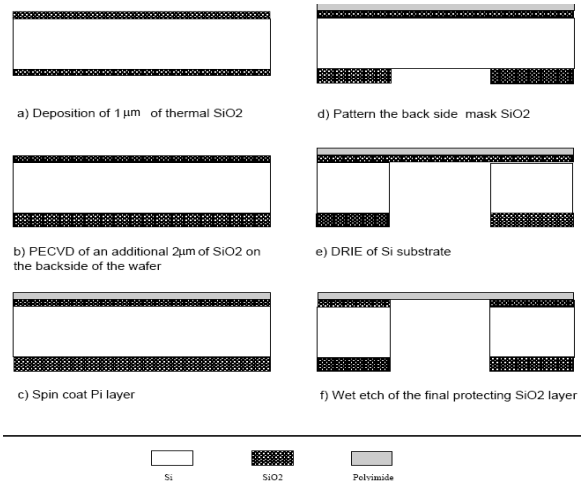

Figure 5.5: *Fabrication process flow of PI membrane for FTIR spectroscopy measurements*

5.4 Ion induced stress release in PI cantilever

This section presents the approach used to relieve the residual tensile stress present in the PI cantilevers. The effects of Ar^+ ion energy and exposure duration on the recovery of the mechanical deformation of the PI cantilever beams are investigated. Surface characterisation using XPS and FTIR techniques highlights the surface structural change of the PI material due to ion bombardment.

5.4.1 Mechanical deflection recovery

5.4.1.1 Effects of ion energy

The as-fabricated PI cantilevers have been bombarded with Ar^+ ions in an ICP reactor with Ar^+ ion energies ranging from 100 to 250 eV. The ICP reactor offers the separate control of the ion flux and the incoming ion energy by monitoring the coil power and the substrate power respectively [217]. In this experiment, the platen power has been changed from 11 to 38 W to obtain a DC bias of 100, 150, 200 and 250 V respectively whereas all the other parameters have been kept constant. A coil power of 500 W, a work pressure of 10 mT, an argon gas flow of 40 SCCM and a frequency of 13.56 MHz

have been used. PI cantilevers of length ranging from 25 to 400 μm and width ranging from 1 to 20 μm have been exposed to the above different conditions for 1, 2 and 3 minutes.

The deflection profiles of the untreated and plasma-treated PI cantilevers have been measured using white light interferometry. Figure 5.6 consists of three microscope images from a white light interferometer showing the cantilever beam deflection before and after exposure to Ar^+ bombardment for a minute at 150 and 250 eV. The cantilever dimensions were 150 μm long, 10 μm wide and 1.9 μm thick. The image on the left hand side shows an untreated cantilever where approximately 2/3 of the beam is out of focus revealing a large tip deflection. After exposure to Ar^+ plasma for a minute at 150 eV, only half of the cantilever beam is out of focus while fringes appear on the other half corresponding to a decrease of the deflection. The full recovery of the original beam deflection has been achieved after further treating the sample under Ar^+ plasma for a minute at 250 eV. It is clear that the curvature of the beam has been minimised as the ion energy increases. Therefore, it has been assumed that the original mean stress and stress gradient present within the cantilever beam are relaxed under Ar^+ plasma exposure.

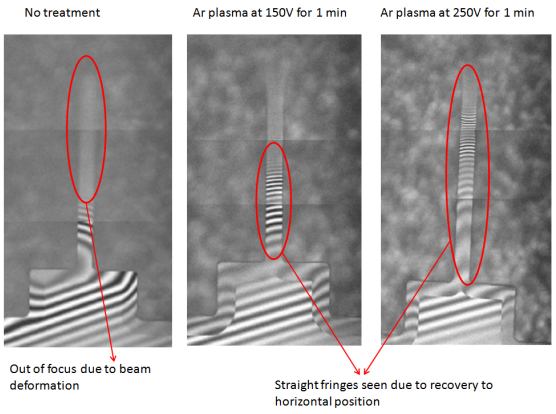

Figure 5.6: *Interference fringes showing that the PI cantilever is less curved after Ar^+ plasma exposure*

The 3 dimensional (3D) profile of a 100 μm long, 20 μm wide and 1.9 μm thick cantilever beam subject to different Ar^+ ion energies along with their surface deflection profiles have been recorded with a white light interferomter and plotted in Figure 5.7.

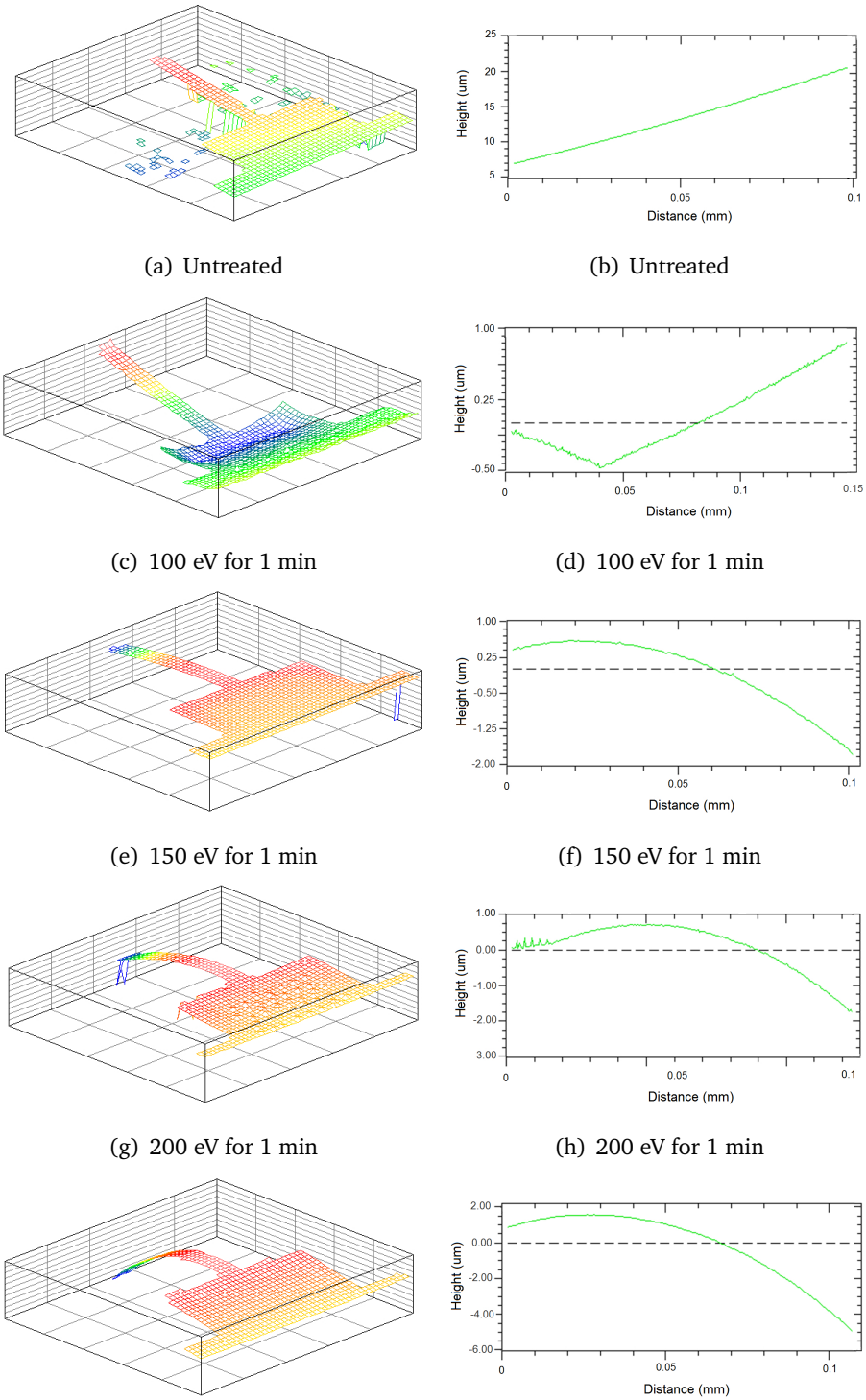

(a) Untreated (b) Untreated

(c) 100 eV for 1 min (d) 100 eV for 1 min

(e) 150 eV for 1 min (f) 150 eV for 1 min

(g) 200 eV for 1 min (h) 200 eV for 1 min

(i) 250 eV for 1 min (j) 250 eV for 1 min

Figure 5.7: *3D plots and the respective deflection profiles of a 100 μm long, 20 μm wide and 1.9 μm thick of untreated and plasma treated PI cantilever for 1 minute at 100, 150, 200 and 250 eV*

Before treatment, the 100μm long cantilever beam presents a maximum tip deflection of 22 μm (Figure 5.7 (a) and (b)). The mechanical deflection due to the tensile stress experienced by the cantilever beam is reduced by increasing incoming Ar^+ ion energy. Cantilevers exposed to Ar^+ ion plasma of 100, 150 and 200 eV for a minute respectively and on different samples, have a maximum tip deflection that varies between +1 and -1.75 μm (Figure 5.7 (c)-(h)). In this case, the cantilever beam deflection is assumed to be negligible and the cantilever is considered free of stress. The stress state of the material can also be inverted from tensile to compressive by increasing the incoming ion energy as seen in Figure 5.7 (i) and (j) where the cantilever beam deflection reach -5 μm.

Figure 5.8 shows the maximum out of plane displacement at the tip end of PI micro-cantilever beams as a function of beam length exposed to Ar^+ bombardment for 1 min with different Ar^+ ion energies.

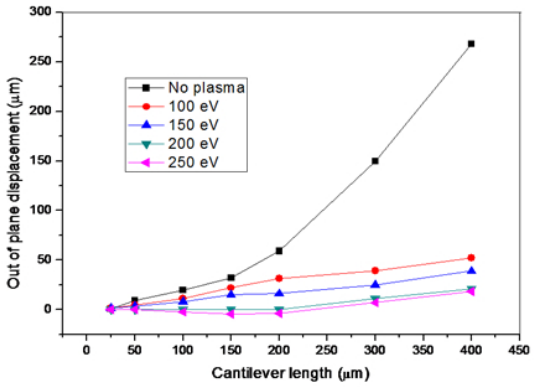

Figure 5.8: *Maximum out of plane displacement at the tip end of a PI cantilever beam of 20 μm wide and 1.9 μm thick as a function of beam length exposed to Ar^+ bombardment for 1 min with different Ar^+ ion energies*

It can be seen that the curved beam returns to its horizontal position progressively as the ion energy increases. A 200 μm long cantilever shows an out of plane maximum displacement of 66 μm once released. After exposure for a minute in Ar^+ plasma at 100 eV, the cantilever beam shows an out of plane maximum displacement of 33 μm while the beam treated with 250 eV shows an out of plane maximum displacement of 2 μm. The deflection recovery corresponds to 76 % and 99 % for a beam exposed to 100 eV and 250 eV respectively. It is believed that the recovery of the beam deflection indicates

the possibility of stress relief, as a result of ion bombardment. The recovery of the out of plane displacement of the PI cantilever beams as a function of ion energy is shown clearly in Figure 5.9. Figure 5.9 represents the out of plane displacement recovery of the PI cantilever of 200 μm long, 20 μm wide and 1.9 μm thick beams exposed to Ar^+ plasma for 1 minute as a function of ion energy.

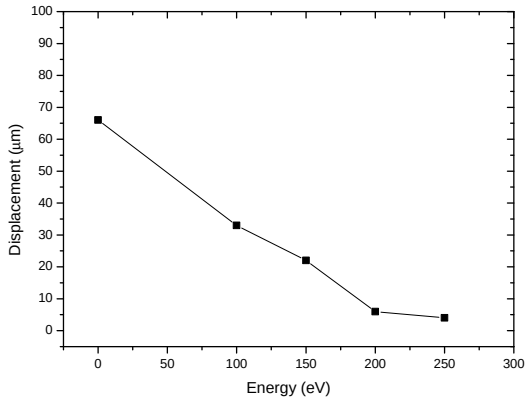

Figure 5.9: *Out of plane displacement at the tip end of a PI cantilever beam of 200 μm long, 20 μm wide and 1.9 μm thick exposed to Ar^+ bombardment for 1 min as a function of Ar^+ ion energies*

Table 5.1 lists the different values of mean stress and stress gradient calculated from equations 5.6 and 5.7 for a cantilever beam of 200 μm long, 20 μm wide and 1.9 μm thick exposed to different ion energies. It can be seen that as the Ar^+ ion energy increases, both the mean stress and stress gradient present in the beam decrease.

ion energy (eV)	Mean stress σ_0(MPa)	Stress gradient σ_1(MPa)
0	55.2	2.25
100	13	1.23
150	6.8	0.89
200	0.76	0.31
250	0.05	0.07

Table 5.1: *Mean stress and stress gradient values for a 200 μm long, 20 μm wide and 1.9 μm thick PI cantilever exposed to 100, 150, 200 and 250 eV respectively*

5.4.1.2 Effects of exposure duration

Figure 5.10 illustrates the maximum out of plane displacement at the tip end of a PI cantilever beam 10 μm wide and 1.9 μm thick as a function of beam length for different Ar^+ ion bombardment exposure time at 100 eV Ar^+ ion energy.

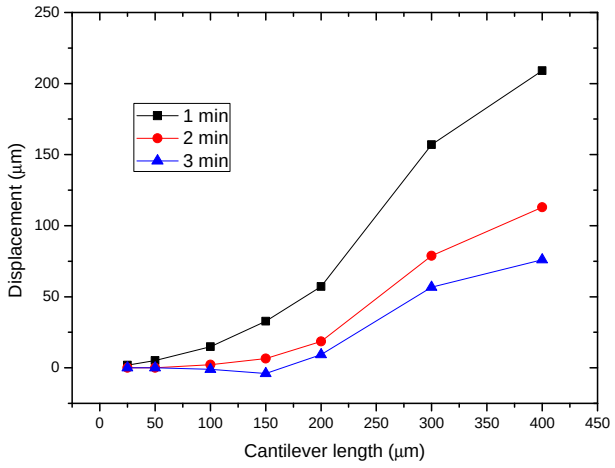

Figure 5.10: *Maximum out of plane displacement at the tip end of a PI cantilever beam of 10 μm wide and 1.9 μm thick as a function of beam length for different Ar^+ ion bombardment exposure time at 100 eV Ar^+ ion energy*

It is clear that the out of plane deflection of the PI cantilevers is reduced by the increase of Ar^+ plasma bombardment time. It is possible that as exposure duration increases, more ions will knock on the sample surface resulting in further relaxation of the tensile stress present.

Figure 5.11 (a-d) shows SEM images of PI cantilevers beam (a) before and (b) after Ar^+ plasma treatment at 100 eV for 2 min, (c) 200 eV for 2 min and at (d) 250 eV for 3 min.

In Figure 5.11 (a), untreated cantilevers tend to curl and show an upward out of plane bending. On the other hand, as the energy of the ions increases, cantilevers become progressively straighter (Figure 5.11 (b) and (c)). In Figure 5.11 (c), the PI cantilevers subjected to Ar^+ plasma at 200 eV for 2 min appear to be the straightest. In Figure 5.11 (d), PI cantilevers exposed to Ar^+ plasma at 250 eV for 3 min bend downwards and

touch the substrate due to a higher Ar^+ energy and longer exposure time treatment. The parameters of the ion bombardment treatment appear to be critical as too high ion energy and/or too long exposure time will result in the beam bending the opposite way. Thus, these experiments indicate that it is possible to tailor the stress gradient of PI cantilever beams of micron-scale dimensions using appropriate ion bombardment process.

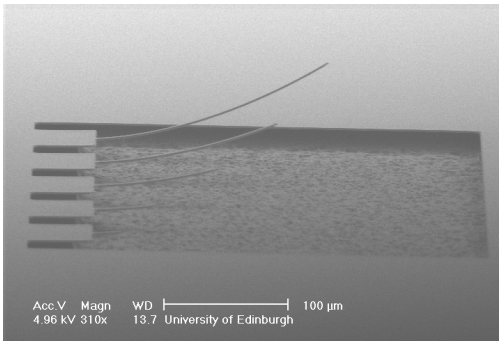

(a) No plasma

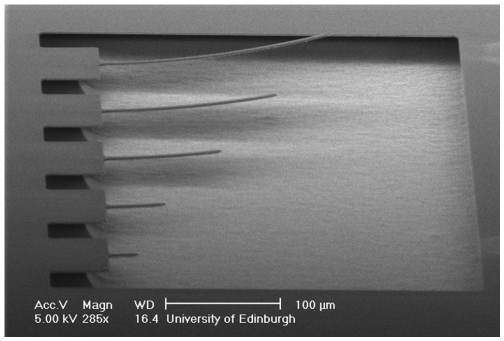

(b) Ar^+ plasma of 100 eV for 2 min

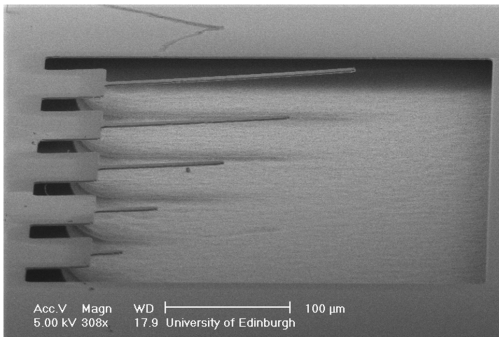

(c) Ar^+ plasma of 200 eV for 2 min

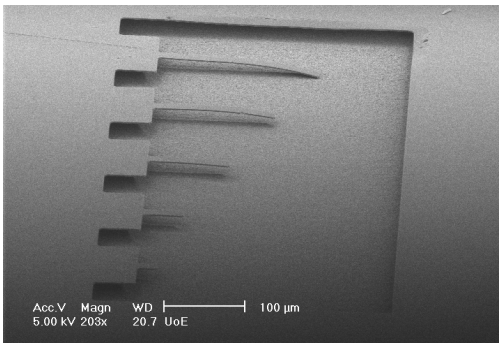

(d) Ar^+ plasma of 250 eV for 3 min

Figure 5.11: *Scanning electron microscope image of untreated and Ar^+ plasma treated PI cantilever at different energy and exposure time*

The results presented in this chapter are in agreement with the study of Bureau *et al* reporting the evolution of stress within SU8 polymer [12]. A $SF_6/N_2/O_2$ plasma was used as post fabrication technique to induce compressive stress within SU8 cantilever beams. The amount of stress existing in the beams was controlled by the plasma parameters.

5.4.2 Surface characterisation

In order to gain further insight into the effect of Ar^+ plasma bombardment on the structure of PI, X-ray photoelectron spectroscopy (XPS) and Fourier transform infrared (FTIR) spectroscopy have been performed.

5.4.2.1 X-ray photon spectroscopy (XPS)

X-ray photoelectron spectroscopy (XPS) has been performed on PI thin films exposed to different incoming ion energies. Figures 5.11-5.13 shows the XPS analysis of C 1s, O 1s and N 1s elemental peaks of reference pristine PI and Ar^+ plasma-treated PI at 100, 150, 200 and 250 eV. As the energy of Ar^+ plasma exposure increases, the intensity of the C 1s peak appears to broaden (Figure 5.12), the oxygen peak decreases quickly (Figure 5.13), while the nitrogen peak has been found to become broader and shifted towards lower energy (Figure 5.14).

The concentration of each element at the surface of untreated and Ar^+ plasma-treated PI are presented in Table 5.2.

	Carbon	Oxygen	Nitrogen
Untreated PI	68.4	24	7.6
Plasma-treated PI	70.9	22.2	6.9

Table 5.2: *Concentration in percentage of carbon, oxygen and nitrogen element at the surface of untreated and Ar^+ plasma-treated PI at 250 eV for 3 min*

After exposure to Ar^+ plasma at 250 eV for 3 min, the concentration of carbon increases by 3.6 % whereas the concentration of oxygen and nitrogen reduces by 7.6 and 9.2 % respectively. The fitting error has been evaluated to range between 1 and 5 % for the different elemental peaks.

For a better understanding of the chemical changes on the PI structure due to Ar^+ plasma bombardment, the C 1s, O 1s and N 1s peaks have been decomposed into chemical bonding peaks corresponding to their chemical groups as seen in Figure 5.15. The percentage amount of chemical groups of each element of untreated and Ar^+

plasma-treated PI at 250 eV for 3 min are presented in Table 5.3. The reference sample is in good agreement with the value obtained from literature [218]. The slight of the elemental peaks of this study and [218] is assumed to be due to the charging of the PI material. It is worth noting that our samples have been exposed to air. However, our calculations do not take into account the effects of contamination of the sample, which could lead to a change of C1s and O1s peak intensity. In addition, the deconvolution of the C1s, O1s and N1s spectra are presented without a background substraction due to the fact that the peaks are relatively well levelled.

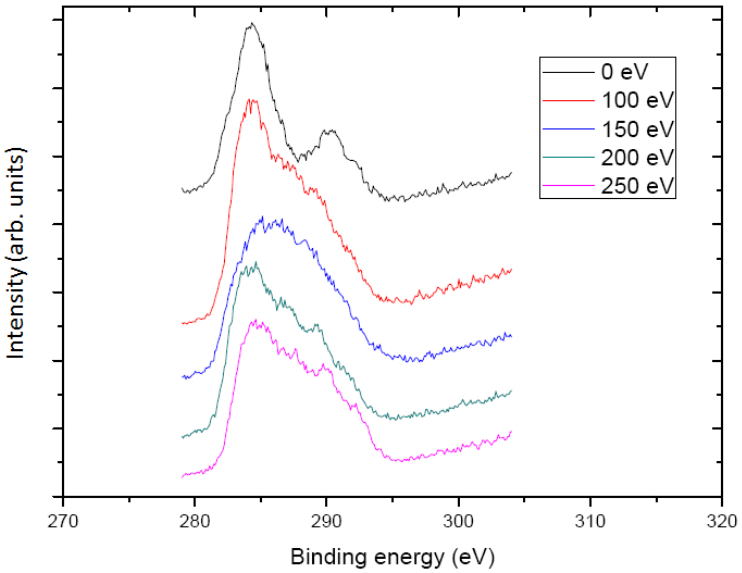

Figure 5.12: *XPS spectra of C 1s of untreated and plasma-treated PI film*

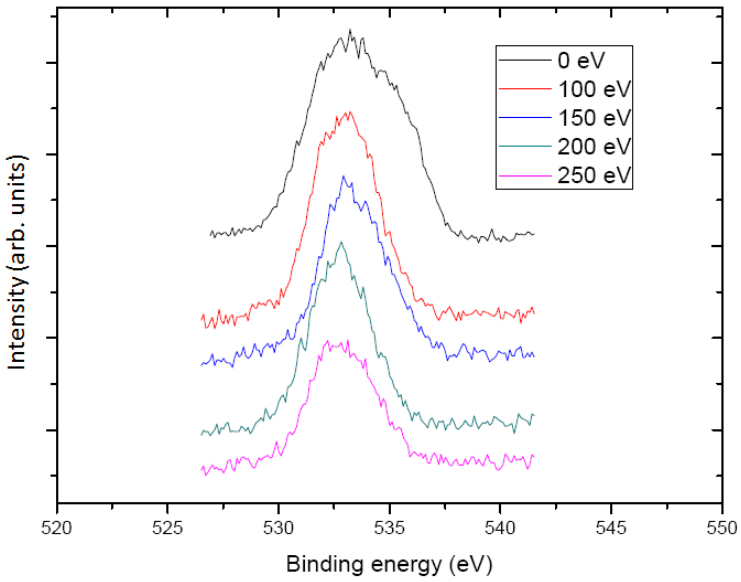

Figure 5.13: *XPS spectra of O 1s of untreated and plasma-treated PI film*

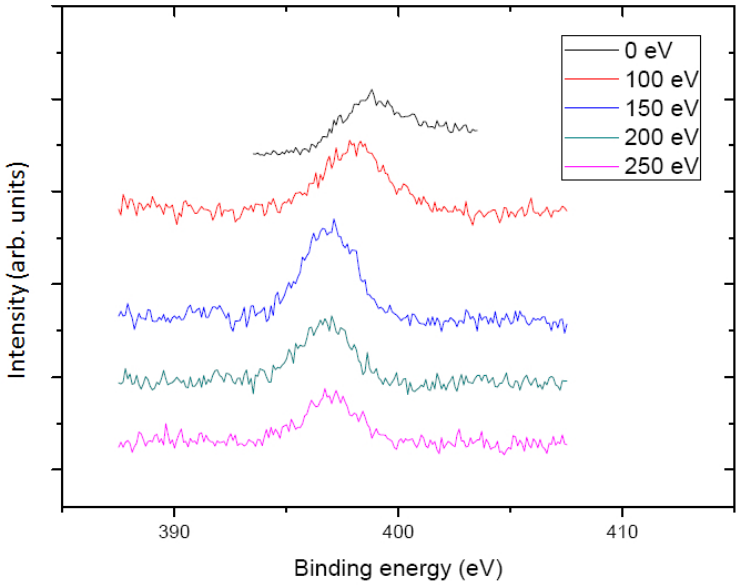

Figure 5.14: *XPS spectra of N 1s of untreated and plasma-treated PI film*

The carbon 1s peak can be resolved into four chemical group peaks. The first peak at 283.4 eV corresponds to the C=C bonds; the second peak at 285.0 eV to the C-C bonds; the third peak at 286.9 to C-N-C and C-O bonds; and the fourth peak at 290.8 eV to the C=O bonds.

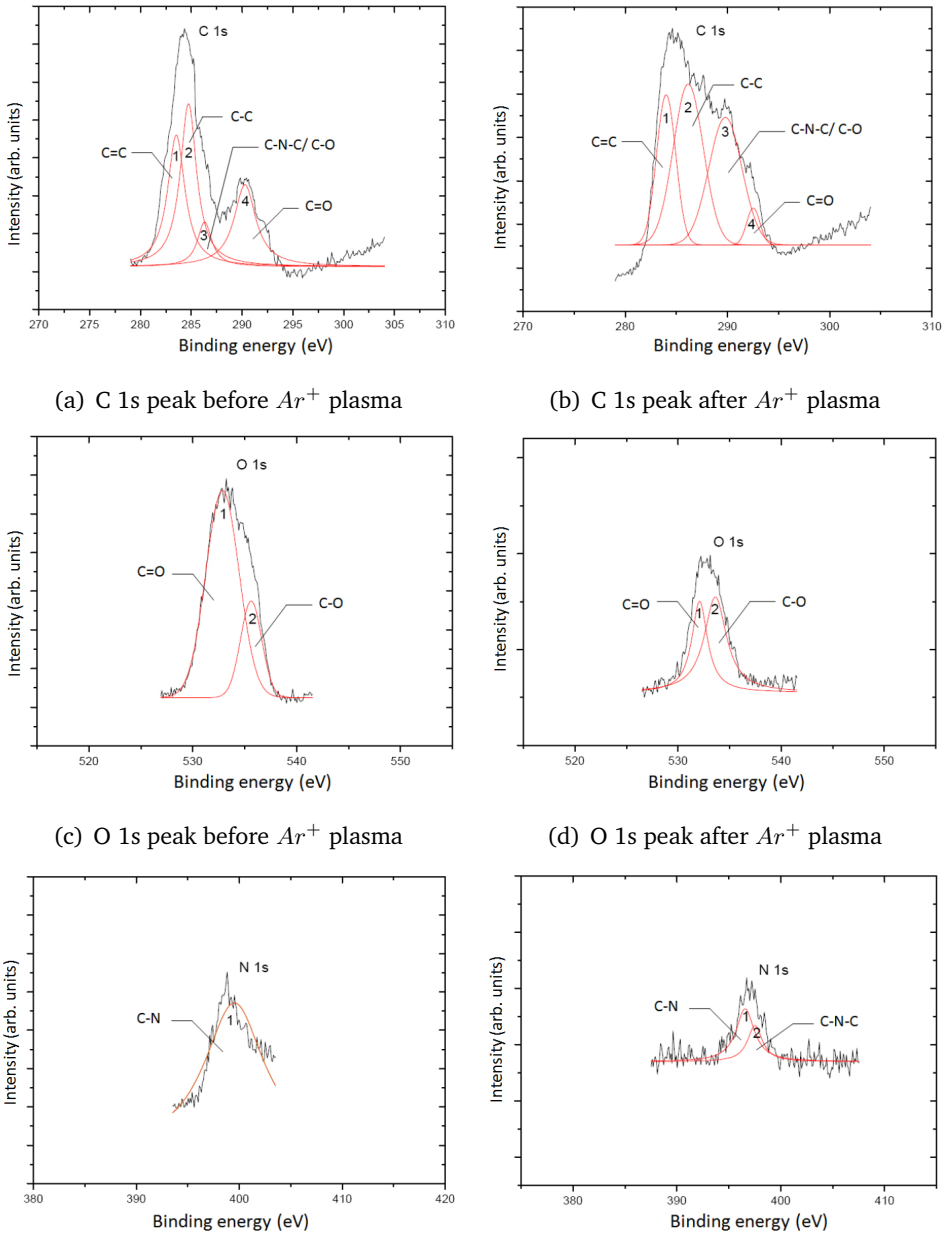

(a) C 1s peak before Ar^+ plasma

(b) C 1s peak after Ar^+ plasma

(c) O 1s peak before Ar^+ plasma

(d) O 1s peak after Ar^+ plasma

(e) N 1s peak before Ar^+ plasma

(f) N 1s peak after Ar^+ plasma

Figure 5.15: *Deconvolution of C 1s, O 1s and N 1s peaks of untreated and treated PI under Ar^+ plasma at 250 eV for 3 min*

In the carbon peak, the amount of C=C and C-C chemical groups (peaks 1 and 2) do not show significant changes after Ar^+ ion plasma exposure compared to the amount of C-N-C/C-O and C=O groups (peaks 3 and 4) (Figure 5.15 (a) and (b)). The amount of C=O groups (peak 4) has been seen to reduce quickly under Ar^+ plasma exposure,

and an increase in C-N-C/C-O groups (peak 3) is evident (Figure 5.15 (a) and (b)). The decrease in the amount of C=O groups from 24.2 % to 3.9 % after exposure to Ar^+ plasma at 250 eV for 3 min is accompanied by an increase of amount of C-O groups from 8.7 % to 31.9 %, as shown in Table 5.3. It is highly possible that the C=O bonds in the PI structure are broken as a result of ion bombardment and some broken C=O bonds may re-oxidize to form C-O bonds after exposure to air and others may re-arrange to form C-N-C bonds.

The oxygen 1s peak (Figure 5.15 (c) and (d)) found at 532.6 eV can be deconvolved into two main chemical groups; the C=O component peak at 531.8 eV and the C-O component peak at 535.9 eV. It can be seen that after Ar^+ plasma exposure at 250 eV for 3 min, the amount of C-O chemical groups of the oxygen peak increases by more than a factor two, while the amount of C=O groups decreases by about 39.7 % (Table 5.3). This observation reinforces the possibility of C=O bonds breaking that re-arrange to form C-O group as previously observed in the carbon peak.

The nitrogen 1s peak is located at 399.6 eV and corresponds to the nitrogen contained in the pristine PI. A new chemical group (C-N-C) appears at 397.2 eV in the N 1s peak after Ar^+ bombardment and supports the observed increase of the amount of (C-N-C/C-O) chemical bonds in the C 1s peak after Ar^+ ion bombardment (Figure 5.15 (e) and (f)).

	Carbon				Oxygen		Nitrogen	
	C=C	C-C	C-N-C/C-O	C=O	C=O	C-O	C-N	C-N-C
Theoretical	36.4	36.4	9.1	18.2	80	20	100	0
Untreated	30.9	36.2	8.7	24.2	77.1	22.9	100	0
Treated	25.2	39	31.9	3.9	46.5	53.5	64.5	35.5

Table 5.3: *The percentage of component ratios of untreated and Ar^+ plasma-treated PI film at 250 eV for 3 min*

5.4.2.2 Fourier Transform Infrared spectroscopy (FTIR)

Figure 5.16 shows the FTIR spectra in transmission mode of the untreated and plasma-treated PI recorded in the range 400-3000 cm^{-1}. The measurement have been performed on the PI membranes described in section 5.3.2 in order to avoid

undesirable effects of underlayers in the measurements. All the samples present similar peaks characteristics. The peaks appearing at around 1780 and 1720 cm^{-1} have been assigned to be stretching vibrations of the asymmetrical and symmetrical (C=O) carbonyl group respectively. The peak at 1500 cm^{-1} has been ascribed to the C=C stretching vibrations of the aromatic amine. The peak at 1380 and 1240 cm^{-1} have been attributed to the N-C-N and C-O stretching respectively. It can be seen that as the Ar^{+} ion bombardment energy increases, the intensity of the peaks decreases. This reduction in peak intensity is assumed to be due to the partial chemical bond breaking of the imides and aromatic structures and chemical bond rearrangement. Moreover, the slight shift of the peaks is assumed to be due to a change of residual stress of the material.

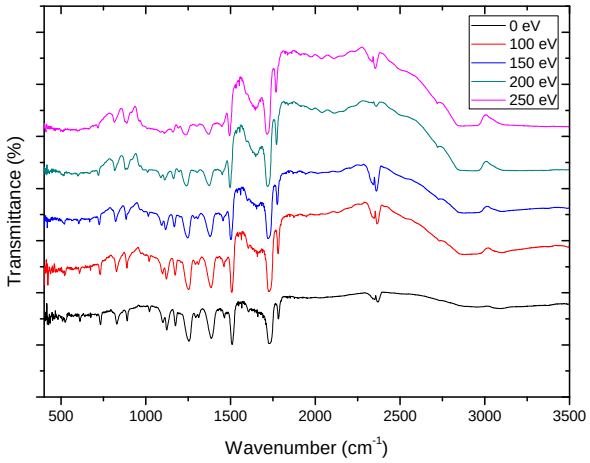

Figure 5.16: *FTIR spectra of the PI films exposed to Ar^{+} plasma for 3 min at different energies*

5.5 Discussion

The presence of tensile stress in thin film often stems from fabrication processing. However, it has been possible to release the tensile stress or even to invert the stress state of the film by ion bombardment treatment [219]. Experimental study of stress relaxation induced by high energy (keV to MeV) Si^{+} ion implantation have been achieved in HfN thin films [220]. The stress gradient present in gold films has been

relaxed by 500 keV He^+ and N^+ ion implantation [221]. Ions having sufficiently high energies to overcome the potential barrier of the surface penetrate within the target material and create collision with the target material. The energy of the incoming ion decreases as it goes through the material due to energy transfer by electronic excitation and chemical bond breaking and reformation with the neighbouring atoms. The penetration of the incoming ion stops when its energy is dissipated in the affected volume of material. These interactions result in an increase of density in a local region and create defects in the film reducing or even changing the stress state of the material.

Many authors have suggested that incoming ion with extremely low energies (below 100 eV) cannot pass the potential barrier of the surface and are reflected without penetrating the material. However, N. A. Marks *et al* proposed an explanation based on molecular dynamics (MD) simulations to describe the generation of compressive stress due to 30 to 100 eV ions bombardment during the growth of carbon films [222]. They stated that stress relaxation can occur at such low ion energy where the impacting ion does not penetrate at all the target material. When an incoming ion with a certain kinetic energy knocks on the surface it distorts and compresses small region at the surface layer by energy transfer due to the conversion of ion's kinetic energy into potential energy for the film. The compressed area expands after a fraction of a pico-second, transforming the potential energy resulting from the compression into kinetic energy. The kinetic energy is then released creating a thermal spike. The diffusion of the kinetic energy within the target material causes weak chemical bonds breaking and chemical rearranging into stronger bonds. The same observation has been confirmed later by Koster *et al* showing that stress modification can be induced with ion energies of 150 eV or less [223]. Experimentally, low energy Ar^+ ions have been employed to relax the stress gradient in polysilicon thin film and silicon substrate [224].

In agreement with [222–225], the results presented in this experiment suggest that stoichiometric re-arrangement of PI films can lead to stress relaxation of mechanical cantilevers. While low energy inert ions do not penetrate deep into the target material, their energy could serve to cause chemical bond breaking and bond re-arrangement, possibly giving rise to stress relaxation. The new chemical bond rearrangement of the PI structure after Ar^+ plasma bombardment observed in the XPS analysis shows that the reduction of C=O bonds and the increase of C-O and C-N-C bonds exists. The

process of bond re-arrangement and/or the new bond re-arrangement may induce the stress relaxation of the PI cantilevers.

5.6 Conclusion

In this chapter, an approach to relieve the residual stress built during fabrication processing of Polyimide (PI) micro-cantilever leading to straight PI cantilever resonators has been presented.

After the release of the PI cantilever, a stress induced out of plane deflection has been observed resulting in a non-linear deflection along the cantilever. The residual mean stress and stress gradient present within the beam have been analysed and calculated.

Low energy Ar^+ ion bombardment plasma technique has been used as post-fabrication technique to reduce the out of plane deflection of the cantilever beam. The recovery of the out of plane deflection of the cantilever beam has been controlled by both ion energy and bombardment duration. As exposure time and ion energy increase, stress relaxation in the material increases. The mean stress and stress gradient present within a PI cantilever beam of 200 μm long, 20 μm wide and 1.9 μm thick after release have been calculated to be 55.2 MPa and 2.25 MPa respectively. An exposure to Ar^+ ions of 250 eV for three minutes has been shown to relieve almost the total amount of stress present in the beam; the mean stress and stress gradient being calculated to be then 50 kPa and 70 kPa respectively.

XPS and FTIR non destructive surface and structural characterization techniques have shown that low ion energy bombardment lead to chemical bonds breaking and re-arrangement. The interpretations of XPS and FTIR measurements support the recovery of mechanical deflection of the PI cantilever beam exposed to Ar^+ plasma bombardment. The deconvolution of the C 1s, O 1s and N 1s peaks has shown that chemical bonds breaking and re-arrangement after exposure to Ar^+ plasma occurs. The reduction of C=O groups and the increase in C-O and C-N-C groups correlate with the reduction of the mechanical deflection present in the PI cantilever beams. The process of bond re-arrangement and/or the new bond re-arrangement may induce the stress relaxation of the PI cantilevers.

By choosing appropriate ion energy and ion exposure duration, it is possible to relieve the stress gradient present in PI cantilever beams resulting in straight PI cantilevers. The method presented enables the fabrication of straight PI canitlever beams for possible sensing applications. In addition, the low energy Ar^+ ions bombardment plasma technique presented could be used for performance optimisation for MEMS structures using other polymer materials.

Chapter 6
Carbon Nanotube interconnect - Improvement of the contact resistance at the SWNTs-metal interface

6.1 Introduction

Due to their large current conduction capability, CNTs can withstand higher current density compared to copper [32]. Moreover, their high aspect ratio and large electron mean free path allow a better electron flow within the tubes without scattering as in copper [40, 226]. As a result, CNTs are great candidates for low resistivity interconnects as they address the problems faced by copper wires. However, one of the recurrent problems in SWNT-metal devices is the high contact resistance present at the SWNT-metal junction which significantly influences the electrical conductivity of the device. To obtain low resistivity interconnects, it is necessary to lower the high contact resistance present at the SWNTs-metal interface.

This chapter presents the development of low resistivity SWNTs interconnects. Dielectrophoresis (DEP) and Focused Ion Beam (FIB) techniques have been used in order to align the SWNTs and reduce the contact resistances respectively.

In section 6.2, the preparation of SWNTs-de-ionized (DI) water suspensions and the fabrication process of the Al and Ti electrodes used to induce the alignment of the SWNTs are described. Then, the DEP procedure employed to align the SWNTs and the deposition of Pt contacts at the SWNTs-metal interface using FIB in order to improve the contact interface between the SWNTs and the metal (Al or Ti) electrodes are presented.

In section 6.3, the influence of SWNTs concentration, voltage and frequency has been investigated in order to find the ideal conditions for an optimum SWNTs alignment

leading to low SWNTs resistances. Then, the effects of Pt metal deposition at the junction between the SWNTs and the metal (Al and Ti) electrodes on the contact resistance of the devices are presented.

In section 6.4, the reasons for the reduction of resistance due to FIB induced Pt contacts deposition are explained. Finally, the results obtained are compared with other methods used to reduce the contact resistance of CNTs interconnects.

6.2 Experimental method

In the first part of this section, the experimental procedure to induce SWNTs alignment using DEP between metal electrodes is presented. The preparation of SWNTs suspension and the fabrication of the metal (Al or Ti) electrodes are described. Afterwards, the DEP technique used to induce SWNTs alignment is explained. COMSOL simulations of the electric field, E, and dielectrophoresis force, F_{DEP} are presented showing the movement of the nanotubes in response to the F_{DEP}. Finally, the experimental set-up used in this work is described also.

In the second part of this section, the FIB technique developed to reduce the high contact resistance which exists at the SWNT-metal interface is presented.

6.2.1 SWNT alignment

6.2.1.1 SWNT suspension

The CNTs used in this chapter have been HiPco SWNTs obtained from UNIDYM Inc. SWNTs suspensions have been prepared by dispersing the SWNTs into DI water containing 1.0 wt% of sodium dodecyl sulfonate (SDS). These SWNTs are in the form of bundles due to the van der Waals forces present among them. In order to separate the nanotubes, a commercial surfactant, sodium dodecyl sulfate (SDS), has been added to the SWNT-DI water suspension to stabilize the hydrophobic surface of the SWNTs. Four different concentrations of SWNT suspensions (0.1, 0.05, 0.01 and 0.005 wt% of SWNTs) have been prepared by adding various amounts of SWNTs into the SDS-DI solution. The dispersion of tangled SWNTs has been facilitated by using an ultrasonic bath for 30 minutes. The principle of sonication is based on sound waves that create

ripples in water which are transferred to the SWNTs suspension throughout the glass beaker.

6.2.1.2 Electrode fabrication

In order to induce dielectrophoresis forces (F_{DEP}) on the SWNT suspension, metal electrodes have been designed (see Appendix B) and fabricated on a Si/SiO_2 substrate. The electrode design consists in a pair of rectangular Al and Ti electrodes of 0.5 μm thick, 1 to 10 μm wide and separated by a gap of 1 to 20 μm. The influence of the type of metal electrodes (Al or Ti) on the I-V characteristics and the apparent number of the aligned CNTs has been studied. The fabrication process flows of both metal electrodes are slightly different and illustrated in Figure 6.1.

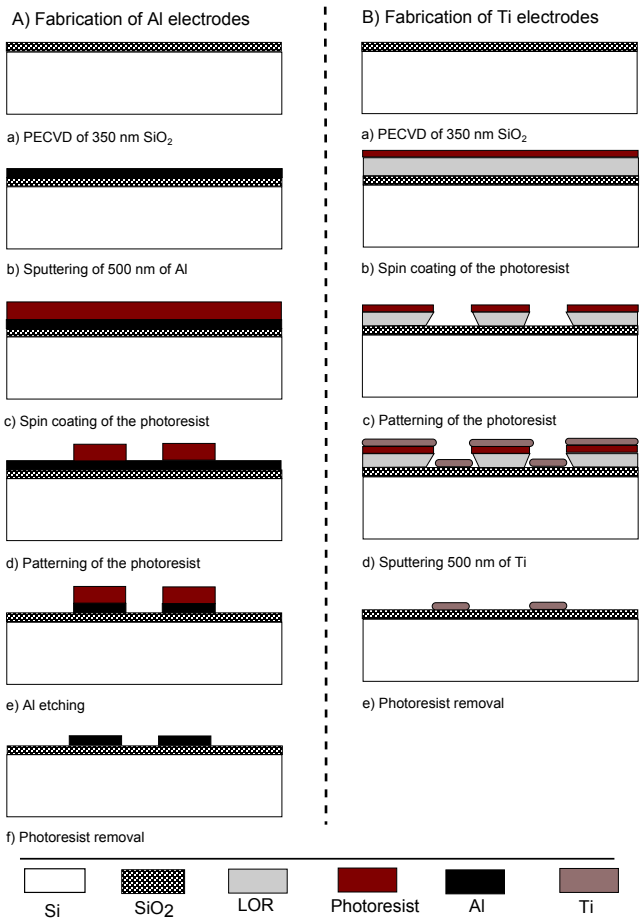

Figure 6.1: *Fabrication process flow of A) Al and B) Ti electrodes*

The first step for both processes has been to deposit a 350 nm thick PECVD SiO_2 layer onto a silicon wafer as an insulation layer between the metal electrodes and the wafer. Afterwards, processes differ from one another. Al electrodes have been fabricated by sputtering a 0.5 μm thick Al layer and patterned photolithographically. The exposed Al areas have been etched using an RIE technique in a $SiCl_4/Ar$ plasma as described in Chapter 3, section 3.3.3. Then, the remaining photoresist has been completely removed in a O_2 plasma after 60 minute process.

In contrast, lift-off process has been preferred to pattern Ti due to the slow dry etch rate of Ti. First, a LOR5B layer has been spun coated onto the substrate at 4000 rpm for 60 seconds and baked at $190°$C for 60 seconds. LOR5B is not photosensitive but it is soluble in conventional developers. Then, an SPR 220.7 photoresist layer has been spun coated on top of the LOR5B layer. The photoresist has been exposed to UV lithography followed by reversal bake step for 2 minutes at $120°$C. The cross-linking agent in the resist has been activated due to the high temperature. Once the exposed area has cross-linked, it has become insensitive to light and almost insoluble in developer. The unexposed area however, has continued to act like regular photoresist. Thus, a flood exposure step has been carried out and the unexposed areas could be dissolved in a MF26A developer. Then, a 0.5 μm Ti layer has been sputtered. Finally, the electrodes have been patterned by washing away the sacrificial LOR5B layer using an 1165 developer for 15 minutes in an ultrasonic bath at $60°$C.

6.2.1.3 Dielectrophoresis

Dielectrophoresis simulations

In this experiment, SWNTs have been aligned between rectangular electrodes. The determination of the real and imaginary part of the Clausius-Mossotti factor, F_{CM}, using MATLAB and the COMSOL simulations of the electric field, E, and dielectrophoresis force, F_{DEP}, resulting from a 10 V_{p-p} AC electric field applied between two 10 μm wide Al electrodes separated by a 5 μm gap are presented in Figure 6.2, 6.3 (a) and (b) respectively. For both calculations and simulations, electrical conductivities of $1.10^8 S.m^{-1}$ and $1.10^{-4} S.m^{-1}$ and permittivities of 3.9 and 79 have been assumed for SWNT and the DI water respectively.

Before analysing the F_{DEP} acting on the SWNTs, it is worthwhile to understand the Clausius-Mossotti factor, F_{CM}, that governs the movement of the SWNTs toward the highest or lowest electric field regions. F_{CM} is dependent on the conductivity and permittivity of both SWNTs and medium and the angular frequency of the applied electric field.

If F_{CM} is positive, then particles move towards the regions of the highest field strength (positive dielectrophoresis), whereas if F_{CM} is negative, the particles are repelled from these regions. Figure 6.2 represents the calculated real and imaginary part of the Clausius-Mossotti factor of a SWNTs suspended in DI water using MATLAB. The red curve represents the real part of the F_{CM} which defines the magnitude and the sign of the F_{DEP}, whereas the blue curves represents the imaginary part of the F_{CM} which refers to the torque applied to the SWNTs. At frequencies below 2MHz, SWNTs suspended into DI water will experience positive dielectrophoresis while at higher frequencies the SWNTs will be subjected to negative dielectrophoresis.

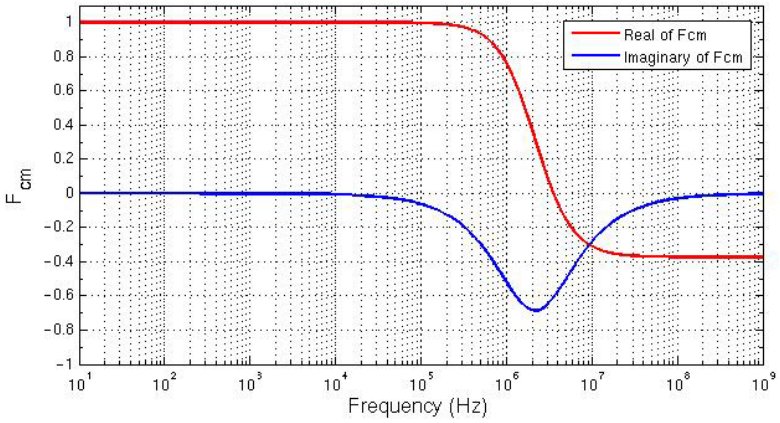

Figure 6.2: *Clausius-Mossotti factor of SWNTs suspended in DI water*

In Figure 6.3 (a), the strength of the electric field is maximum in the red regions and minimum in the dark blue regions. The magnitude of the electric field can be seen to be higher at the edges of the electrodes. The high electric field regions are located between the electrodes.

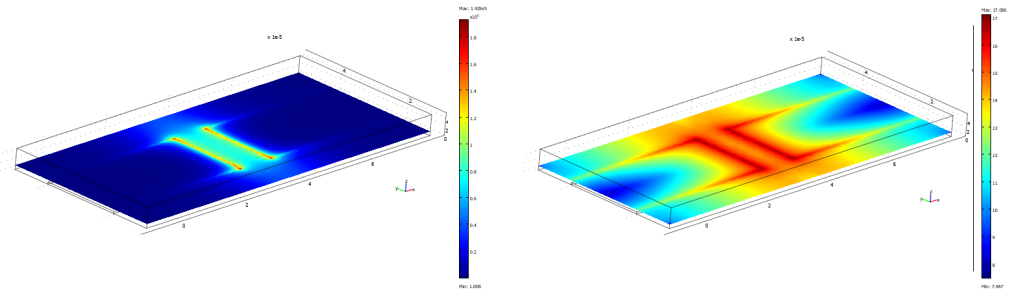

(a) Electric field (b) Dielectrophoresis forces, F_{DEP}

Figure 6.3: *COMSOL simulations of the (a) electric field (E) and (b) dielectrophoresis force (F_{DEP}) induced by a 10 V_{p-p} AC elecric field applied to rectangular electrodes*

Similarly, the magnitude of the F_{DEP} has been simulated (Figure 6.3 (b)). The strength of the F_{DEP} is defined by the same colour scale, where red regions represent high F_{DEP} and blue regions represent low F_{DEP}. The F_{DEP} appears to be higher in the area between the electrodes, where the SWNTs should be attracted.

Dielectrophoresis procedure

The different steps to induce SWNT alignment are illustrated in Figure 6.4. First, a 25 μL drop of SWNTs-DI water suspension has been deposited on the different Al and Ti electrodes configuration patterned on top of the Si/SiO_2 chip with a pipette (Figure 6.4 (a)). Care has been taken to ensure that no air bubbles have been trapped in the solution. A different pipette tip has been used for each different concentration to avoid contaminations. Afterwards, a sin wave AC voltage of 10 V_{p-p} has been applied across the electrodes at different frequencies in order to induce SWNTs alignment (Figure 6.4 (b)). Finally, the SWNTs suspension has been rinsed with DI water and dried with a nitrogen gun in order to keep only the SWNTs bridging the electrodes (Figure 6.4 (c)).

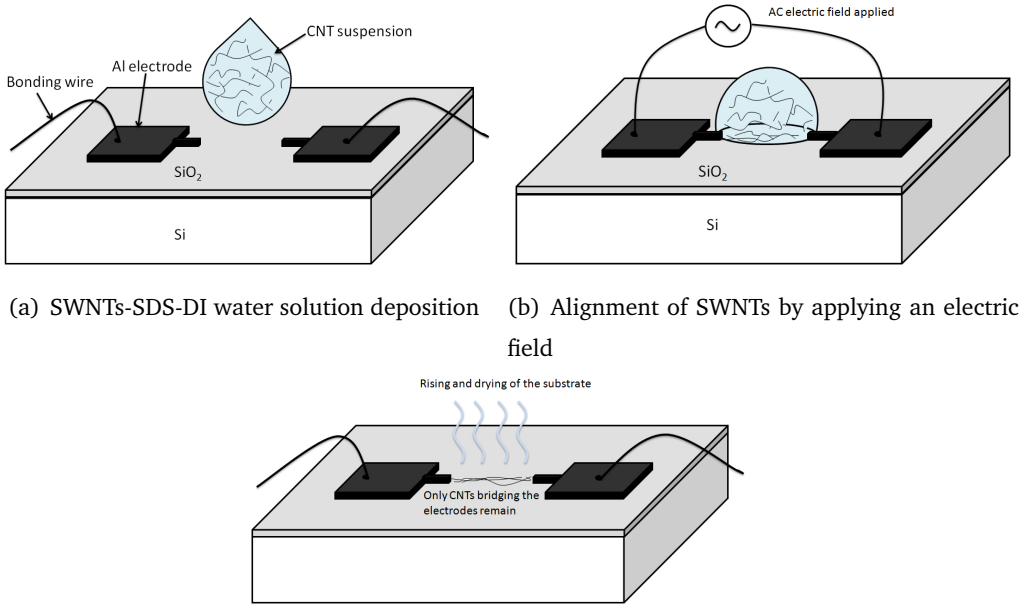

(a) SWNTs-SDS-DI water solution deposition

(b) Alignment of SWNTs by applying an electric field

(c) Evaporation of the SDS-DI water resulting in SWNTs bridging the electrodes

Figure 6.4: *Dielectrophoresis procedure to align SWNTs between metal electrodes*

The results and characterisation of aligned SWNTs between Al and Ti electrodes under different conditions will be presented in section 6.3.

6.2.2 Lowering contact resistance at the SWNT-metal junction

6.2.2.1 Contact resistance at CNT-metal interface

In Chapter 2, section 2.3.1, SWNTs have been described as a perfect, very thin and straight wire where electrons are allowed to move only along the axis of the wire. This assumed there are no defects along the tube, in which the transport of electrons (without scattering) can be described as ballistic ($G = h/4e^2$) where e is the electron charge and h is the Planck's constant. The resistance of a SWNT can be divided into two parts: the intrinsic resistance which arises from the scattering of electrons by the defects or imperfections in the tube that is assumed to be zero in a perfect SWNT and the two contact resistances that are calculated as ($R = 1/G$) and reported to be approximately 12.9 kΩ. However, experimental resistance values of SWNT aligned between metal electrodes have been found to be much higher, hindering the

electron transport throughout the external circuit [107]. In fact, the metal electrode contact with the CNTs may cause reflection effects resulting in contact resistance at the CNT-metal interface. These reflections occur due to inefficient coupling of the electron wavefunction from the electrode into the CNT.

Figure 6.5 shows the total measured resistance defined as the sum of the nanotube resistance and the two contact resistances at each SWNT-metal interfaces.

$$R_{TOT} = R_{C1} + R_{CNT} + R_{C2} \tag{6.1}$$

where R_{C1} and R_{C2} are the two contact resistances at the SWNT-metal junctions and are equal, $R_{C1} = R_{C2}$ and R_{CNT} is the intrinsic resistance of the carbon nanotube.

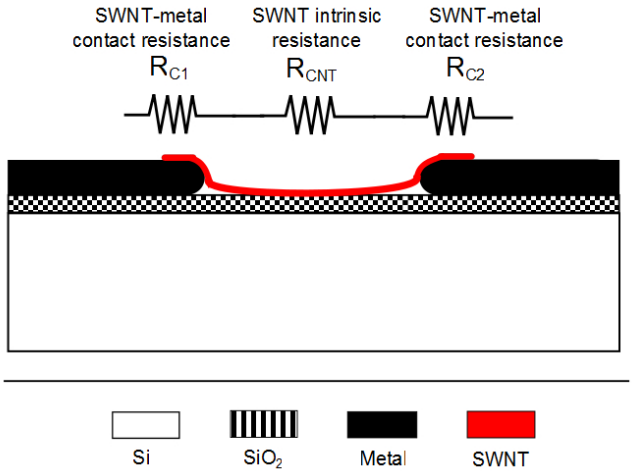

Figure 6.5: *Schematic diagram of a CNT bridging two metal electrodes*

In addition, the carbon nanotube resistance changes according to the number of SWNTs bridging the metal electrodes. Therefore, the SWNTs alignment has been optimised by varying the electric field, the applied frequency and the SWNT concentration in order to minimize R_{CNT}. The two contacts resistances R_{C1} and R_{C2} at the SWNTs-metal electrodes that dominate the devices' resistances have been reduced by depositing a thin layer of Pt at the SWNTs-metal electrodes (Al and Ti) interface using FIB.

It is noteworthy that in this experiment, all the I-V characteristics used to determine the resistances have been recorded using a two-point probes measurement technique. Therefore, the resistance measurements may include additional resistance parameters

due to the probes and their contacts with the electrodes pads.

6.2.2.2 FIB induced Pt contacts deposition

As mentioned in Chapter 2, high contact resistance can degrade device performance. Therefore, the reduction of contact resistance in interconnects has attracted a huge amount of attention. Few techniques have been reported to lower the contact resistance at the SWNTs-metal junction [137–139]. These methods include the use of an ultrasonic bonding technique [137], thermal annealing [138] and electron beam induced deposition of amorphous carbon [139] and will be discussed in more detail in section 6.4.

Recently, FIB has been used to measure the contact resistance at the CNT-metal interface, where the deposition of tungsten (W) via FIB enables electrical contact between the CNTs and the electrodes [227]. Similarly, in this experiment, a technique based on FIB has been developed for the purpose of decreasing the contact resistance present at the SWNT-metal junction. FIB has been employed to deposit a thin layer of Pt at the SWNTs-metal contact (Figure 6.6). The approach consists of reduced contact resistances that are beneficial for SWNTs based electronics applications.

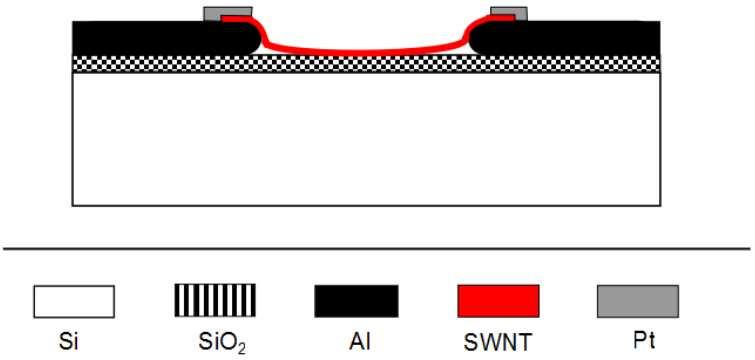

Figure 6.6: *Side view of a SWNT bridging Al electrodes with Pt leads at the SWNT-Al junction in order to lower* R_c

The influence of Pt deposited contacts at the SWNTs-metal junction is presented and discussed in the following sections of this chapter.

6.3 Characterisation

In this section, the influence of SWNT concentration, applied voltage and applied frequency on the SWNTs alignment between Al and Ti electrodes have been investigated by measuring the I-V characteristics of the devices and observing the SWNTs alignment using SEM imaging.

In addition, the influence of the deposition of Pt contact at the SWNTs-metal junction by FIB has been studied. It has been found that FIB induced Pt contact deposition lowers the resistances of the Al-SWNTs-Al and Ti-SWNTs-Ti devices.

6.3.1 SWNT resistance (R_{CNT}) investigation - Optimisation of SWNTs alignment

The current flow across the metal electrodes through aligned SWNTs has been analyzed using current - voltage (I-V) characteristics. I-V characteristic measurements have been repeated for a series of electrode pairs. The fact that the SWNTs used in this experiment have been both metallic and semiconductor in nature will contribute to differing electronic conductivity characteristics. The following measurements presented in this section are the average value from three measurements.

Once the I-V characteristics have been recorded, the nature of the SWNTs alignment has been investigated using an SEM. A thin gold layer approximately 5 nm thick has been then evaporated onto the samples in order to avoid charging during SEM imaging.

The influence of the SWNTs concentration, the applied voltage and the frequency on the alignment of SWNTs between Al and Ti electrodes has been investigated. The amplitude of the AC voltage has been varied between 2 and 10 V_{p-p} and applied to the metal electrodes for 3 minutes. The SWNTs concentration of the SWNTs-DI water suspension ranges from 0.1 wt% to 0.005 wt%. The frequency has been changed from 10 kHz to 10 MHz. In order to study the effects of these parameters on the SWNT alignment and therefore, on R_{CNT}, two assumptions had to be taken into consideration: (1) both contact resistances, R_{C1} and R_{C2} are identical for each metal such as ($R_{C1Al} = R_{C2Al}$ and $R_{C1Ti} = R_{C2Ti}$) and (2) the number of aligned SWNTs at a certain concentration is the same between Al and Ti electrodes.

6.3.1.1 CNT concentration dependence investigation

Figure 6.7 represents the I-V characteristics of the four suspensions containing different SWNTs concentrations bridging (a) Al and (b) Ti electrodes where an AC electric field of 10 V_{p-p} has been applied to the metal electrodes for 3 minutes.

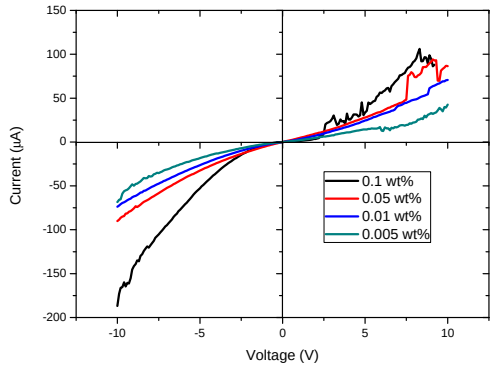

(a) Al electrodes

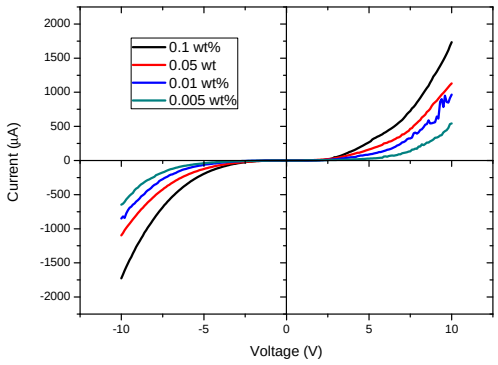

(b) Ti electrodes

Figure 6.7: *I-V characteristics of SWNTs bridging (a) Al and (b) Ti electrodes separated by a 10 μm gap as a function of SWNT concentration*

From Figure 6.7 (a), the resistances of the aligned SWNTs between Al electrodes decrease (represented by the higher slope in the I-V curves) as the SWNT concentration in the suspension increases. The decrease of resistance can be explained by the fact that at higher SWNT concentration, the probability that a SWNT bridges the electrodes becomes higher. A higher number of aligned SWNTs between the electrodes are

expected to conduct more current. Similarly, from Figure 6.7 (b), the resistances of the aligned SWNTs between Ti electrodes decrease with the increase of SWNT concentration. Therefore, by comparing the I-V characteristics of SWNTs bridging Al (Figure 6.7 (a)) and Ti (Figure 6.7 (b)) electrodes, it is noteworthy that for the same CNT concentration, Ti-SWNTs-Ti have lower resistance than Al-SWNTs-Al. The difference of resistances could be due to the different chemical bonding interfaces between the metal (Al or Ti) electrodes and the carbon atoms of the SWNTs. A more detailed explanation is given in section 6.3.2.

Figure 6.8 shows the SEM images of SWNTs bridging Al electrodes separated by a 5 μm gap for (a) 0.1 wt% (b) 0.05 wt% (c) 0.01 wt% (d) 0.005 wt% SWNT concentrations.

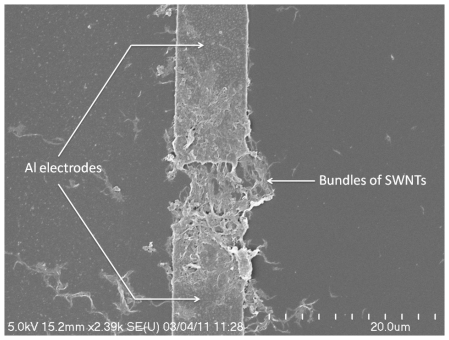

(a) SWNT concentration of 0.1 wt%

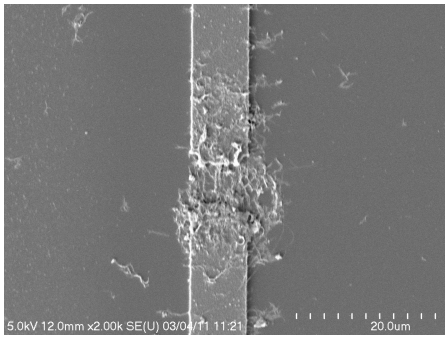

(b) SWNT concentration of 0.05 wt%

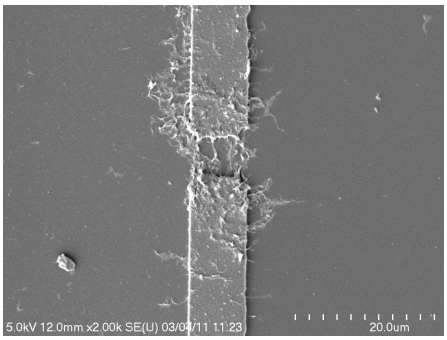

(c) SWNT concentration of 0.01 wt%

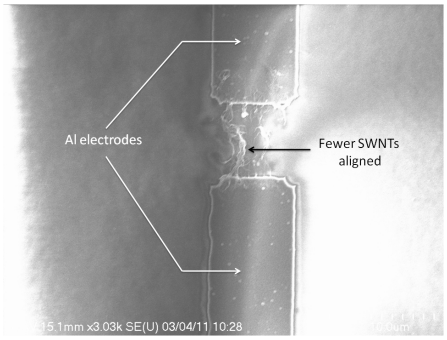

(d) SWNT concentration of 0.005 wt%

Figure 6.8: *SEM images of aligned SWNTs as a function of SWNT concentration of (a) 0.1 wt% (b) 0.05 wt% (c) 0.01 wt% (d) 0.005 wt%*

The increase in the number of SWNTs bridging the Al and Ti electrodes as the SWNTs concentration increase has been confirmed by the SEM images. At 0.1 wt% (Figure 6.8 (a)), a large number of SWNTs have been attracted towards the high electric field

region, resulting in the formation of a dense random network of SWNTs between the electrodes. As the SWNT concentration decreases from 0.05 to 0.005 wt% (Figure 6.8 (b) to (d)), less SWNTs have been aligned between the metal electrodes. Although the SEM image of 0.005 wt% shows charging of the sample, it can be observed that only few SWNTs bridge the electrodes at such a low concentration.

0.005 wt% SWNTs-DI water suspension has been chosen for the rest of the experiment in order to limit the size of the CNTs bundles as shown in Figure 6.8.

6.3.1.2 Electric field dependence investigation

The influence of the electric field on the SWNTs alignment has been investigated in order to minimise R_{CNT}. Figure 6.9 shows the I-V curves for SWNTs assembled between (a) Al and (b) Ti electrodes for various magnitude of the electric field, from 2 to 10 V at a constant frequency of 1 MHz. The concentration of SWNTs has been 0.005 wt% and the electric field has been applied for 3 minutes. The non-linearity nature in both I-V characteristics recorded denotes the semiconducting nature of the aligned SWNTs. This results in the presence of a Schottky barrier (SB) at the SWNT-metal contact.

Figure 6.10 represents the resistances of the Al-SWNTs-Al and Ti-SWNTs-Ti devices at 1 V for different applied voltage. A decrease of the resistance has been observed as the magnitude of the applied AC electric field increases. SWNTs aligned using a 2 V_{p-p} AC electric field amplitude shows the highest resistance, whereas SWNTs aligned with a 10 V_{p-p} AC electric field amplitude shows the lowest resistance (19 MΩ/μm and 83 kΩ/μm for Al and Ti metal electrodes respectively). As defined by equation 3.4, in Chapter 3, the higher the electric field magnitude, $|E|$, the higher is the F_{DEP} resulting in more SWNTs bridging the electrodes.

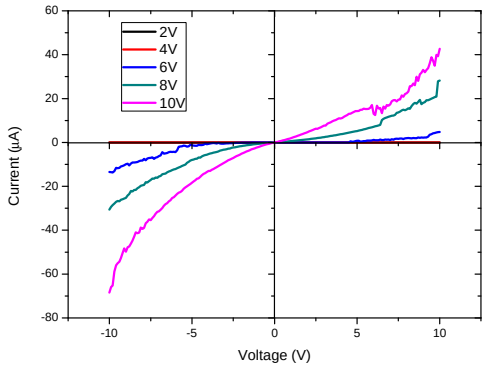

(a) Al electrodes

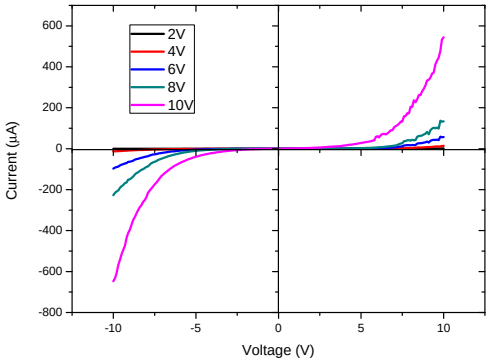

(b) Ti electrodes

Figure 6.9: *I-V characteristics of SWNTs bridging (a) Al and (b) Ti electrodes separated by a 10 μm gap as a function of the electric field magnitude*

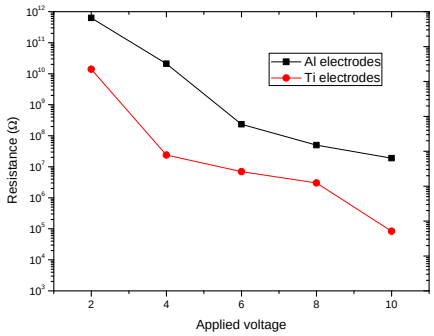

Figure 6.10: *Resistances of SWNTs bridging Al and Ti electrodes separated by a 10 μm gap taken at 1 V for different applied voltage*

Figure 6.11 represents the SEM images showing the number of aligned SWNTs between Al electrodes separated by a 10 μm gap for different electric field magnitudes.

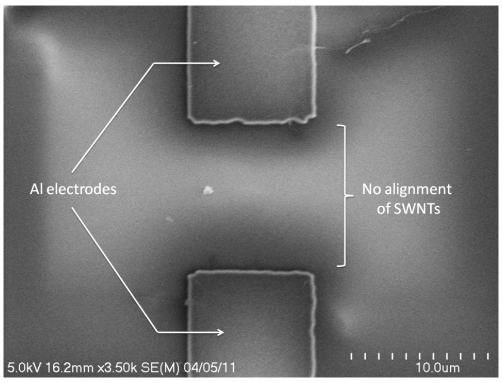

(a) Electric field = 2V

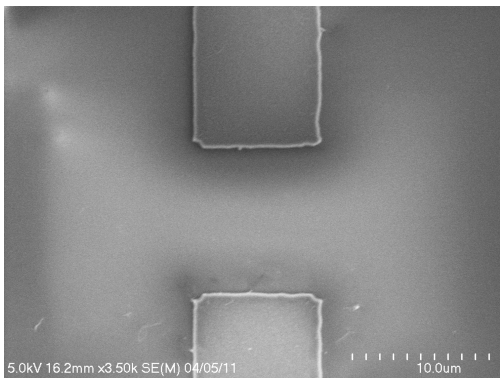

(b) Electric field = 4V

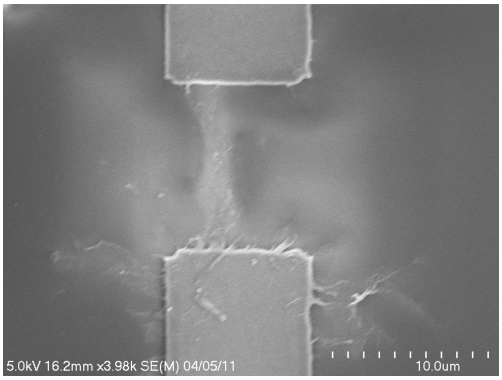

(c) Electric field = 6V

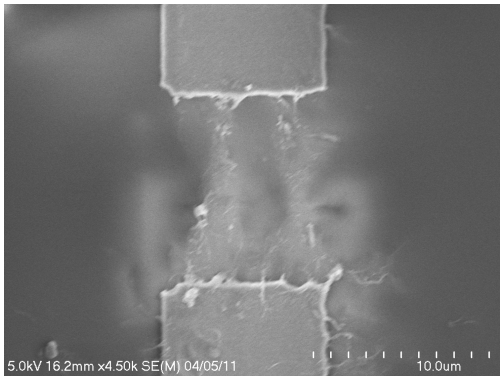

(d) Electric field = 8V

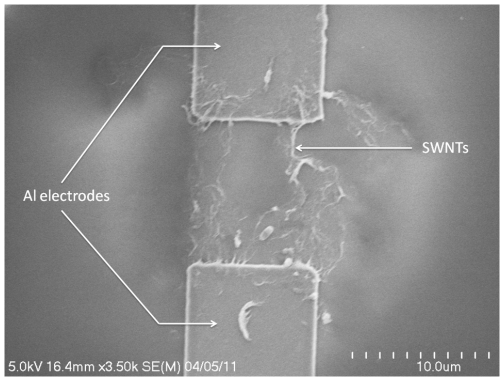

(e) Electric field = 10V

Figure 6.11: *SEM images of aligned SWNTs as a function of the electric field magnitude of (a) 2 V, (b) 4 V (c) 6 V, (d) 8 V, (e) 10 V*

It can be seen from Figure 6.11 (a) and (b) that at low electric field (2 to 4 V) no

significant SWNTs alignment is achieved. As the applied voltage increases from 6 to 10 V (Figure 6.11 (c)-(e)), the number of SWNTs attracted between the electrodes increases. From these measurements, an AC electric field of 10 V_{p-p} has been chosen as the voltage for the alignment of SWNTs leading to more SWNTs aligned resulting in a lower resistance.

6.3.1.3 Frequency dependence investigation

Figure 6.12 shows the I-V characteristics of SWNTs aligned between (a) Al and (b) Ti electrodes for a range of electric field frequency. Low resistances have been found in the frequency range of 500 kHz to 2 MHz. Figure 6.13 shows the devices resistances taken at 1 V for different applied frequency. The lowest sample's resistances have been obtained using a frequency of 1 MHz which has been defined as the optimum frequency. As the applied frequency deviates from this optimum frequency, the number of SWNTs aligned between the electrodes deceases. As a consequence, the sample's resistance increases. It is worth noting that the same behaviour has been observed for both devices.

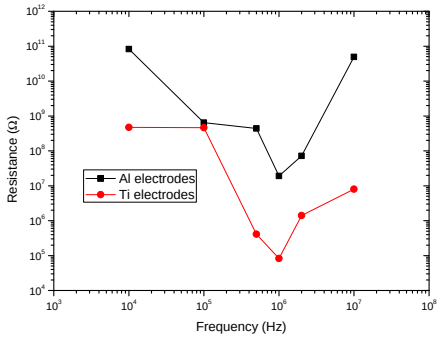

Figure 6.12: *Resistances of SWNTs bridging Al and Ti electrodes separated by a 10 μm gap taken at 1V for different applied frequency*

The degree of SWNTs alignment between Al and Ti electrodes as a function of the applied frequency has been investigated using an SEM (Figure 6.14 (a)-(f)). As explained in section 6.2.1.3, the degree of SWNTs alignment is determined by the F_{DEP}, which depends on the frequency of the applied electric field. From the Clausius-Mossotti factor simulation, one expects SWNTs to align between the

electrodes at frequencies below 2 MHz and to be repelled from the electrodes at higher frequencies.

In this experiment, SWNTs alignment has been observed at frequencies ranging from 100 kHz to 2 MHz with the higher number of SWNTs bridging the electrodes at a frequency of 1 MHz. As shown in Figure 6.2, the Clausius-Mossotti factor becomes negative at frequencies higher then 2 MHz. Therefore, it is natural to obtain the lowest resistances before the threshold (1 MHz) and to observe an important increase of the resistances at higher frequencies (10 MHz), where the SWNTs have been repelled from the electrodes and no significant alignment has been observed.

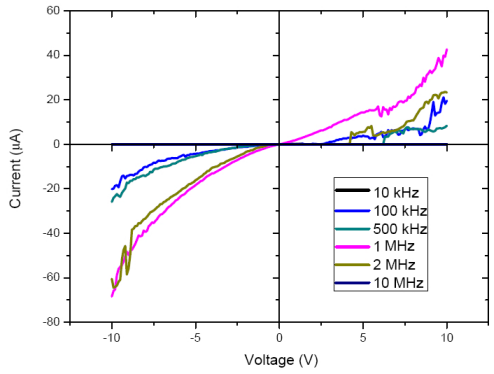

(a) Al electrodes

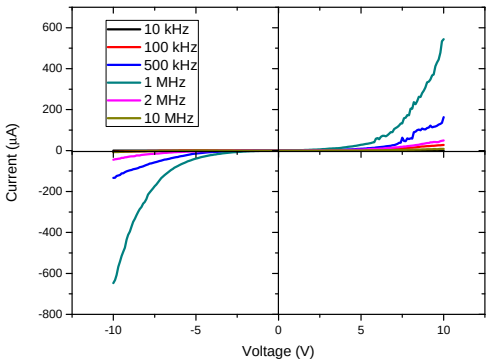

(b) Ti electrodes

Figure 6.13: *I-V characteristics of SWNTs bridging (a) Al and (b) Ti electrodes separated by a 10 μm gap as a function of frequency*

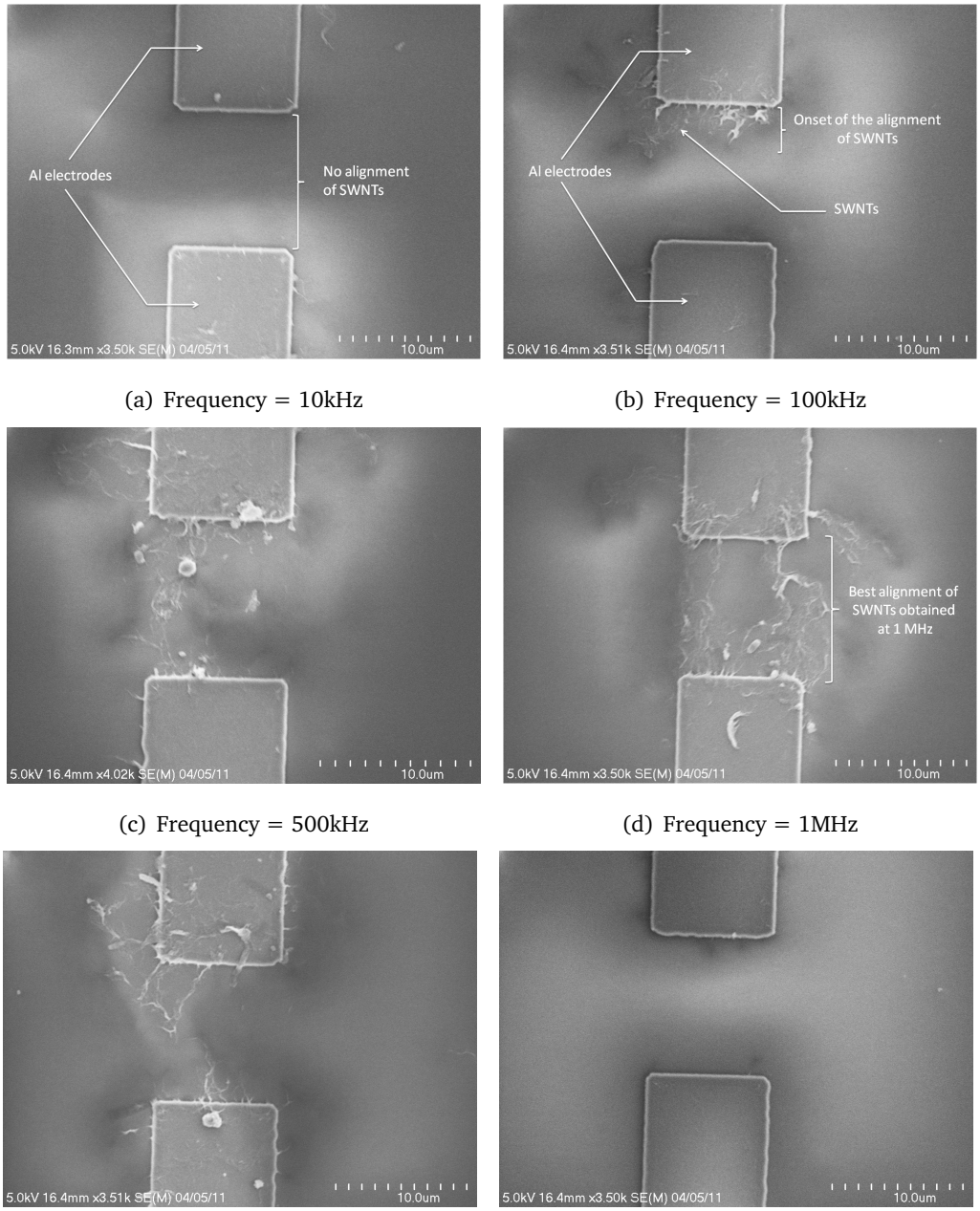

(a) Frequency = 10kHz

(b) Frequency = 100kHz

(c) Frequency = 500kHz

(d) Frequency = 1MHz

(e) Frequency = 2MHz

(f) Frequency = 10MHz

Figure 6.14: *SEM images of aligned SWNTs as a function of the applied frequency of (a) 10 kHz, (b) 100 kHz (c) 500 kHz, (d) 1 MHz, (e) 2 MHz, (f) 10 MHz showing that more SWNTs are aligned between the Al electrodes separated by a 10 μm gap at 1 MHz*

6.3.1.4 Influence of the SWNTs alignment optimisation on R_{CNT} - A summary

The optimum conditions have been defined in order to obtain the lowest R_{CNT}, assuming that the two contact resistances R_{C1} and R_{C2} are equal for each metal and that the number of aligned SWNTs at a certain SWNT concentration in the suspension is the same for both metal electrodes. The effects of the SWNTs concentration, applied voltage and frequency on the alignment of SWNTs and therefore on R_{CNT} have been investigated and summarises below.

A high SWNT concentration has led to the formation of a random network of SWNTs between the electrodes, while a low SWNT concentration has resulted in fewer SWNTs bridging the electrodes. Therefore, 0.005 wt% SWNT concentration has been chosen as the critical concentration in order to reduce the size of the SWNTs bundle aggregates.

Then, it has been demonstrated that a higher voltage leads to a higher number of SWNTs bridging the electrodes, reducing the sample resistances. Therefore, 10 V_{p-p} has been chosen as the optimum electric field amplitude to obtain low R_{CNT}.

Finally, the SWNTs alignment has been shown to depend strongly on the applied frequency. The SWNTs alignment is closely related to the Clausius-Mossotti factor that governs the dielectrophoresis force acting on the SWNTs. A higher degree of SWNTs alignment has been observed at a frequency of 1 MHz.

The optimum parameters used to align SWNTs and to obtain the lowest SWNTs resistance (R_{CNT}) in this experiment are listed in Table 6.1.

Parameters	Values
AC voltage (V_{p-p})	10
CNT concentration (wt%)	0.005
Frequency (MHz)	1
Exposure time (minutes)	3
Drop size (μL)	25
Solvent	SDS-DI-water

Table 6.1: *Dielectrophoresis parameters chosen for an optimised SWNTs alignment*

6.3.2 Contact resistances (R_C) investigation

In this section, the influence of two parameters on the R_C of SWNTs-metal electrodes have been investigated. Initially, the influence of the types of metal (Al and Ti) electrodes on the R_C is presented. Although, Ti electrodes has led to lower R_C compared to Al electrodes, the use of Ti as metal electrode has not been enough to achieve low resistivity SWNTs interconnects. Therefore, a technique has been developed to decrease the R_C further. The deposition of Pt thin film at the SWNTs-metal electrodes junction by FIB has been employed to improve the contact interface between the CNTs and the metals decreasing the R_C. For the calculation of R_C, it has been assumed that at a given SWNT concentration, the number of SWNTs aligned between the Al and Ti electrodes is the same and thus, the SWNT resistance (R_{CNT}) is the same.

6.3.2.1 Types of metal electrodes

The effects of Al and Ti material as metal electrodes have been evaluated by calculating the devices resistance from their I-V characteristics. Although the best SWNTs alignment between both, Al and Ti electrodes has been achieved using the same DEP parameters, namely, an AC electric field of 10 V_{p-p} applied for 3 minutes at 1 MHz, a difference in resistances has been observed between the SWNTs aligned between Al and Ti electrodes as shown in Figure 6.15.

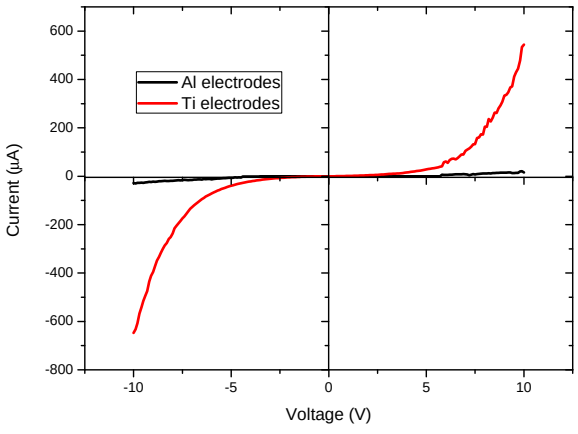

Figure 6.15: *I-V characteristics of SWNTs bridging Al and Ti electrodes separated by a 10 μm gap*

The lowest resistance (higher slope of the I-V) corresponds to the best contact between the nanotube and the metals. At 1 V, the resistances of Al-SWNTs-Al and Ti-SWNTs-Ti have been found to be 19 MΩ/μm and 83 kΩ/μm respectively. Therefore, Ti produces a lower R_C value when used at the SWNTs-metal interface with SWNTs than Al, resulting in a better contact with the carbon atoms of the SWNTs. The contact between a SWNT and a metal can be either an ohmic contact or a Schottky contact. From Figure 6.15, the non linearity in the I-V characteristics recorded denotes the presence of a Schottky contact rather than an ohmic contact. A Schottky contact results in a Schottky barrier (SB) formed at the SWNTs-metal junction due to the difference of Fermi levels between the SWNTs and the metal. The presence of a SB at the SWNT-metal junction increases the R_C and therefore tends to be a problem for the device performances. As discussed in Chapter 2, the performances of CNT-FETs or CNT interconnects are generally characterised by their SB which determines the R_C at the SWNT-metal interface.

The contact resistance of a device is expected to increase as the work function of the metal electrodes deviates from the CNTs' one. The work function of CNTs is in the range 4.6 to 5.1 eV, while both Ti and Al have slightly lower work functions, respectively 4.28 eV and 4.33 eV. Although the work functions of Al and Ti are similar, Ti has shown lower (more than 2 orders of magnitude) contact resistance compared to Al (see Figure 6.15). Therefore, it has been considered the hypothesis that besides the influence of the metal work function, the resistance of SWNTs-metal devices is dependent also on the wettability between SWNTs and metal. Wettability defines how good the contact between the two materials is and therefore refers to the chemical interaction or the chemical bonding strength between the metal and the SWNTs.

In this study, it has been assumed that Al has a weak chemical bonding to carbon while Ti forms a stronger chemical bonding to carbon. The weaker chemical bonding interface between Al-SWNTs compared to Ti-SWNTs has been attributed as the reason for the observed difference of resistances between the two devices. The influence of the nature of the chemical bonding between the metal and the CNT on the R_C is discussed in detail in section 6.4.

6.3.2.2 Effects of FIB induced Pt contact deposition

Although the choice of Ti as metal electrode has led to a relatively low R_C compared to Al, a technique based on FIB has been developed to reduce the R_C further. Platinum (Pt) contacts have been deposited by FIB at the SWNT-metal interface with the intention of improving the contact interface between both materials and therefore lower the R_C.

The I-V characteristics of aligned SWNTs between two Al and Ti electrodes separated by a 10 μm gap with and without Pt contacts at the SWNT-metal junction have been recorded and plotted in Figure 6.16 and 6.17.

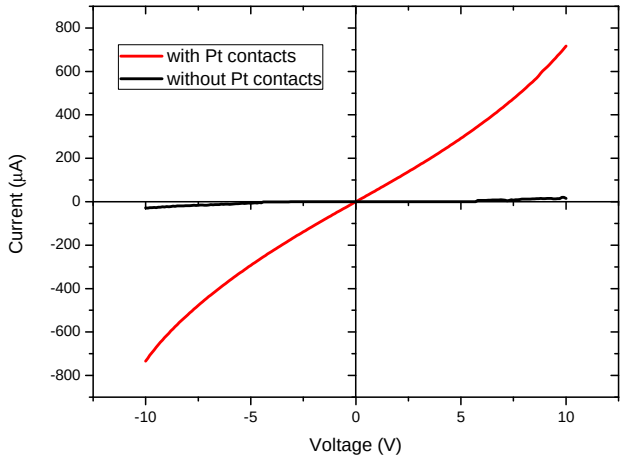

Figure 6.16: *I-V characteristics of SWNTs bridging Al electrodes separated by a 10 μm gap with and without Pt contacts at the SWNTs-Al junctions*

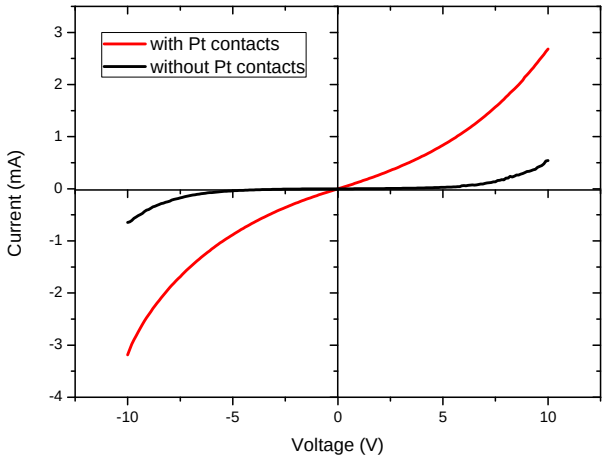

Figure 6.17: *I-V characteristics of SWNTs bridging Ti electrodes separated by a 10 μm gap with and without Pt contacts at the SWNTs-Ti junctions*

From Figures 6.16 and 6.17, it can be seen that the deposition of Pt using an FIB system has the principal consequence of lowering significantly the resistance of the samples for both metals electrodes. After the deposition of Pt contacts, samples show almost linear I-V characteristics. As a result, the nature of the SWNT-metal contact seems to have switched from Schottky to ohmic. In addition, the resistances of SWNTs-Al and SWNTs-Ti devices have been reduced by four orders of magnitude (from 19 MΩ/μm to 1.8 kΩ/μm), and two orders of magnitude (from 83 kΩ/μm to 780 Ω/μm) respectively. The larger decrease of contact resistance observed for Al-SWNTs-Al compared to Ti-SWNTs-Ti is due to the poor wettability of Al with the SWNTs. Ti has a better bonding interface with the SWNTs than Al, therefore the deposition of Pt contacts on top of the SWNTs-metal junction has less influence on Ti-SWNTs junction than on Al-SWNTs junction.

Figure 6.18 is a SEM image of 0.005 wt% SWNTs bridging Ti electrodes separated by a 10 μm electrode gaps with Pt contacts deposited at the SWNTs-metal interface. The dimensions of the top Pt contact layer are $4 \times 1 \times 0.5\mu$m.

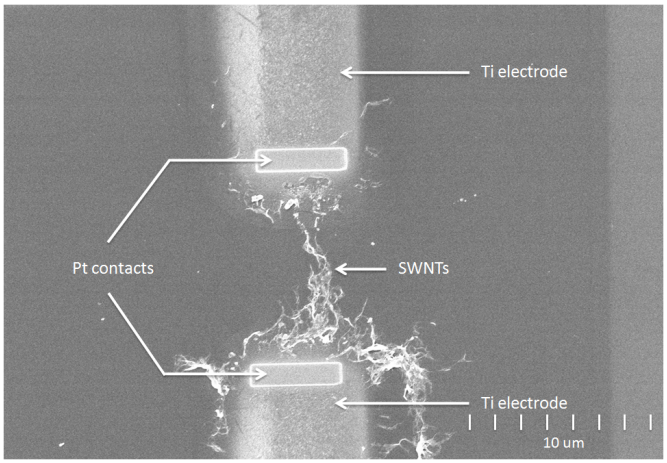

Figure 6.18: *SEM image of SWNTs bridging Ti electrodes separated by a 10 μm gap*

As mentioned previously, the resistances have been obtained from two-point probe measurements including the total resistance of the devices and the resistances of the probes and their contacts with the electrodes pads. Nevertheless, from Figure 6.18 it can be seen that Pt has been deposited only around the SWNTs-metal electrodes interface regions. Therefore, the deposition of Pt by FIB provides supporting evidence of the change in contact resistances of the devices.

6.4 Discussion

In this section, the effects of two parameters on the R_C of SWNTs-metal electrodes are discussed. Initially, the influence of wettability between the SWNTs and the metal (Al and Ti) electrodes is discussed. The reasons why Ti electrodes have led to lower R_C compared to Al electrodes are explained. However, the use of Ti as metal electrode was not enough to achieve low resistivity SWNTs interconnects. Therefore, a technique has been developed to decrease the R_C further. FIB has been employed to improve the contact interface between the CNTs and the metals. The effects of the deposition of an additional Pt thin layer on top of the SWNTs-metal electrodes junction on the R_C are discussed and compared with the existing methods reported in the literature. The aim is to fabricate devices with a resistivity lower than the one of Cu which is 17 $n\Omega.m^{-1}$. Although, the resistivity of our devices was higher than Cu, the FIB technique has shown a significant reduction of the contact resistance present at the CNT-metal

junction.

6.4.1 Wettability - influence of metal electrodes

In the last decade, a huge amount of attention has been addressed theoretically and experimentally to the R_C at the CNT-metal interface. Numerous theoretical studies can be found in the literature reporting the influence of the metal material, the type of CNT, the chemical structure of the CNT-metal contact for the use of CNTs as interconnects or in CNT-FETs applications. The R_C between CNT and various metals such as Al [228], Ni [229], Au [229], Co [230], Pd [231], Fe [71], Ti [232], Cu [233] and Ta [233] have been analysed widely.

For a long period of time, the R_C at the CNT-metal interface has been defined only by the SB and tunnelling barrier heights present at the interface between CNTs and the metal electrodes [234].

In section 6.3.2.1, it has been seen that although Al and Ti have similar work functions (4.28 and 4.33 eV), the resistance of both devices differ from one another. Assuming that the number of SWNTs is the same between both metal electrodes and therefore that the SWNT resistance is the same for both device, it can be deduced that the R_C at the SWNTs-Al and SWNTs-Ti interface are different. From the measurements presented, it is clear that besides the influence of the metal work function, the R_C is dependent also on the wettability between the SWNTs and the metals. This observation is in agreement with previous works reporting on the R_C between CNTs and different metals [231, 232, 235, 236]. Lim *et al* studied the effect of work function and wettability between CNTs and various metals [235]. The chemical bonding between CNTs and metals has been reported as the key parameter in controlling the SB height. More specifically, for metals having good wettability with the CNTs, the R_C does not correlate with the work function. However, metal having poor wettability with the CNTs, the shifting of work functions increases the R_C of the device.

Good wettability reduces the R_C by enhancing the surface contact area and the bonding strength between the CNTs and the metal. The chemical bonding strength between graphene and metal has been reported to be dependent on the number of metal unfilled d-orbitals. Al does not have d vacancies while Ti has 8 resulting in a good affinity

with the CNTs [235]. As a consequence, a strong interaction between Ti and the sp^2 configuration of CNTs exists with strong covalent bonds between the two components [229, 232, 236].

Most of the reported experimental values for CNT-metal contact resistance agree with theoretical studies. However, a disagreement between theoretical and experimental values has been cited in some publications. Ke *et al* suggested that the disagreement between theoretical and experimental values of contact resistance can be attributed to the difficulty of determining the accurate contact area and contact bonds between the CNT and the metal [237]. The influence of CNT-metal contact area on the contact resistances has been emphasised by Lan *et al* [238].

Finally, the experimental values of R_C reported in the literature are scattered. The scattering of R_C values can be attributed to the number of CNTs, different quality of materials used and the several configurations employed such as tube on metal, metal on tube, tube embedded in the metal. In this experiment, SWNTs have been placed between Al and Ti electrodes using DEP. In this configuration, the SWNTs are laid on top of the electrodes and the contact between the SWNTs and the metal electrodes is due mainly to Van der Waals forces resulting in a weak bonding interface between both materials leading to high contact resistances. Furthermore, SWNTs deposited on the top of the metal electrodes can result in high tunnelling barrier hampering the electron transfer [239]. Therefore, thin Pt layers have been deposited by FIB at the interface between the SWNTs and the metal (Al or Ti) electrodes in order to lower the contact resistances of the devices.

6.4.2 Deposition of Pt contacts on top of the SWNTs-Al and SWNTs-Ti junction

Few techniques have been employed to lower the R_C at the SWNTs-metal junction [137–139]. Chen *et al* [137] used an ultrasonic bonding technique to embed the SWNTs into the metal electrodes. An ultrasonic bonding of power 0.19 W has been observed to decrease the resistances of the devices by more than three orders of magnitude; the resistances have dropped from 45 MΩ/μm to 8 kΩ/μm. The ultrasonic bonding has created defects at the ends of the SWNTs increasing the electron scatter at the junction breaking the Bloch symmetry of the electrons between the SWNTs and the metal as

described by Tresoff *et al* [239].

In 2009, Kane *et al* [138] investigated the influence of thermal annealing on the R_C of SWNTs and Pt electrodes. They found that at temperature below 880 K, thermal annealing leads to high R_C, while at temperatures higher than 880 K, thermal annealing results in very low R_C. They stated that annealing is not the main factor in the lowering of the R_C since there is no clear explanation for the reduction of the resistance in the range 440 K to 880 K and moreover because Pt anneals at temperatures higher than 1300 K. The change of resistance has been assumed to be due to the Pt carbidization at $T \leq 800K$ and graphitization at $T \geq 800K$. The nanocrystalline graphite is assumed to strengthen the interface between the SWNTs and the metal. Graphitic contacts are assumed to enhance the chemical bonding, increasing the contact surface area and avoiding atomic separation between the metal and the SWNTs.

Similar explanations have been concluded by Rykaczewski *et al* [139] in their study on the properties of carbon material deposited at the MWNTs-metal junction. Electron beam induced deposition of amorphous carbon at the MWNTs-metal interface has led to the decrease of the R_C of the devices from 200 kΩ/μm to 5 kΩ/μm. The deposition process has been assumed to induce heating at the SWNTs-metal contact resulting in a partial graphitization of the amorphous carbon improving the electrical contact between the materials.

In this experiment, the deposition of a thin Pt layer at the interface between the SWNTs and the metal has been found to lower significantly the resistances of the devices. The resistance of a 10 μm long SWNTs interconnect bridging Al electrodes has been found to decrease from 19 MΩ/μm to 1.8 kΩ/μm. The resistance of a 10 μm long SWNTs interconnect bridging Ti electrodes has been reduced from 83 kΩ/μm to 780 Ω/μm. The deposition of Pt contacts by FIB on the top of the SWNTs-metal junction has embedded the SWNTs into the metal (Al or Ti) electrodes, limiting the possible separation that can exists when SWNTs are laid on top of the electrodes. The deposition of a top Pt layer creates top and side contacts with the SWNTs, increasing the contact surface area between the SWNTs and the Al and Ti electrodes. In addition, an improvement of the chemical bonding may be achieved due to the possible modifications of SWNTs walls during Pt deposition.

Pt has a higher work function (5.65 eV) than CNTs (4.6 to 5.1 eV) and forms non-ohmic contacts with CNTs [240]. Moreover, the wettability between CNTs and Pt has been reported to be weaker than Ti but better than Al (Ti $\geq$ Pt $\geq$ Al) [235]. Therefore, the decrease of the resistances of the Ti-SWNTs-Ti devices is essentially due to the increase of contact area between SWNTs and Ti via Pt deposition. While in the case of Al-SWNTs-Al devices, the reduction of contact resistance is assumed to be due to the increase of contact area between SWNTs and Al and to the better wettability of Pt with SWNTs, favouring the electron flow.

Table 6.2 lists the improvement of R_C between CNTs and metal electrodes using the different various methods mentioned above.

	Before treatment	After treatment
Ultrasonic bonding [137]	45 MΩ/μm	8 kΩ/μm
Thermal annealing [138]	5 MΩ/μm	480 kΩ/μm
e-beam induced carbon deposition [139]	200 kΩ/μm	5 kΩ/μm
FIB induced Pt deposition (this work)	(Al) 19 MΩ/μm	(Al) 1.8 kΩ/μm
	(Ti) 83 kΩ/μm	(Ti) 780 Ω/μm

Table 6.2: *Comparison of the improvement in contact resistance*

The relatively low resistances obtained in this experiment come from the fact that bundles of SWNTs have been aligned between the metal electrodes while, in the other studies, one single CNT has been aligned. Nevertheless, the reduction of resistances for all these studies [137–139] and the one presented in this work ranges between two and four orders of magnitude.

6.5 Conclusions

The work presented in this chapter has consisted of developing a method to reduce the contact resistance existing at the SWNTs-metal interface for interconnect applications.

Initially, a model representing the different resistance components of the total resistance of the device has been described. The total measured resistance has been defined as

the sum of the nanotube resistance R_{CNT} and the two contact resistances R_C at each SWNTs-metal interfaces.

SWNTs have been aligned between Al and Ti electrodes. SWNTs suspensions have been prepared by dispersing the SWNTs into DI water containing 1.0 wt% of sodium dodecyl sulfonate (SDS) under ultrasonication. The alignment of SWNTs between Al and Ti electrodes has been done using a DEP technique. An investigation of the effects of the SWNTs concentration, the applied voltage and the frequency on the alignment of SWNTs between Al and Ti electrodes have resulted in lowering the R_{CNT}. The amplitude of the AC voltage has been varied between 2 and 10 V_{p-p} and applied to the metal electrodes for 3 minutes. The SWNTs concentration of the SWNTs-DI water suspension ranges from 0.1 wt% to 0.005 wt%. The frequency has been changed from 1 kHz to 10 MHz. The lowest SWNT resistance, R_{CNT} has been obtained for the optimum conditions; an AC voltage of 10 V_{p-p} at 1 MHz for 3 minutes. Samples have been characterised by measuring the current flow across the metal electrodes through aligned SWNTs recording their (I-V) characteristics. In addition, the nature of the SWNTs alignment has been investigated using SEM imaging.

The total resistance of the CNT-metal device is mainly dominated by the contact resistances R_C at the SWNTs-metal junction. The influence of two parameters on the R_C of SWNTs-metal electrodes have been investigated. The effects of wettability between the SWNTs and the metal (Al and Ti) electrodes and the deposition of Pt contact at the SWNT-metal electrodes interface using FIB have been discussed. Assuming that the number of SWNTs bridging the metal electrodes at a certain SWNT concentration is the same for both metal electrodes, and thus the SWNT resistance is identical in both devices, it can be deduced that Ti-SWNTs-Ti devices have lower resistances than the Al-SWNTs-Al devices (83 kΩ/μm versus 19 MΩ/μm). Since both metals have similar work functions, the difference in resistances has been attributed to the different strength of the chemical bond between the carbon atoms of the CNTs and the Al and Ti. The chemical bonding strength between graphene and metal has been reported to depend on the number of metal unfilled d-orbitals. Al does not have d vacancies while Ti has 8 resulting in a good affinity with the CNTs. As a consequence, a strong interaction between Ti and the sp^2 configuration of CNTs exists with strong covalent bonds between the two components.

In order to further lower R_C, FIB has been employed to improve the contact interface between the CNTs and the metals. It has been observed that R_C has been significantly lowered by depositing an Pt thin layer on top of the SWNTs-metal electrodes. The resistance of Al-SWNTs-Al devices have been reduced from 19 MΩ/μm to 1.8 kΩ/μm, while the resistances of Ti-SWNTs-Ti devices have been reduced from 83 kΩ/μm to 780 Ω/μm respectively. The deposition of Pt contacts by FIB on top of the SWNTs-metal junction has embedded the SWNTs into the metal (Al or Ti) electrodes, limiting the possible separation that can exist when SWNTs are laid on top of the electrodes. The deposition of a top Pt layer creates top and side contacts with the SWNTs, increasing the contact surface area between the SWNTs and the Al and Ti electrodes. Since the wettability between CNTs and Pt is weaker than Ti but better than Al (Ti $\geq$ Pt $\geq$ Al), it has been suggested that the decrease of the resistances of the Ti-SWNTs-Ti devices is essentially due to the increase in surface contact area between the SWNTs and Ti via Pt deposition. In the case of Al-SWNTs-Al devices, the reduction of contact resistance has been assumed to be due to the increase of contact area between the SWNTs and Al as well as the relatively good wettability of Pt (compared to Al) with SWNTs, favouring the electron flow.

Furthermore, comparison between the results presented in this thesis and several other different methods reported in the literature have shown similar improvements with a reduction of resistances ranging between two and four orders of magnitude. Nevertheless, it is noteworthy that the resistances of the devices fabricated in this study are relatively low. The low resistances obtained have been attributed to the fact that bundles of SWNTs have been aligned between the metal electrodes while some of the other studies have reported the alignment of a single CNT between metal electrodes.

Chapter 7
Preparation and characterisation of Carbon Nanotubes-Polyimide (CNTs-PI) composite

7.1 Introduction

CNTs possess a wide range of tremendous properties. Although the combination of all these properties makes CNTs the perfect filler material for composite applications, some challenging requirements exist in order to integrate CNTs into a polymer matrix. One of the main challenges is to achieve a good interfacial bonding connection between the nanotube and the polymer matrix [51, 54, 55]. If the interfacial bonding between the nanotube and the polymer matrix is not strong enough, then the advantageous mechanical properties of the CNTs will not be transferred to the final composite. Another key parameter in composite preparation remains the ability to disperse the nanotubes uniformly throughout the polymer matrix without damaging their structures. This is essential to achieve efficient load transfer across the CNTs-polymer interface.

After the study of stress control in PI MEMS in Chapter 5 and the reduction of contact resistance in CNTs interconnects electronics applications in Chapter 6, Chapter 7 presents the integration of both materials. The preparation of randomly dispersed CNTs-PI composite and aligned CNTs-PI composites using dielectrophoresis along with their characterisation are presented. The effects of CNT concentration and CNTs alignment on the electrical and mechanical properties of the composite are discussed.

In section 7.2, the preparation and characterisation of randomly dispersed CNTs-PI composite is presented. The enhancement of the electrical and mechanical properties of the composite as a function of the CNTs concentration has been investigated. The electrical conductivity of the composite has been described to follow a percolation theory, where the electrical state of the composite has been found to change from

insulator to conductor at a critical CNT concentration. The evolution of the storage modulus E' and glass transition temperature T_g of composites as a function of CNT concentration have been determined.

In section 7.3, the preparation of aligned CNTs-PI composite using dielectrophoresis (DEP) is presented. The alignment of CNTs inside the PI matrix has resulted in a further enhancement of the composite properties. In addition, aligned CNTs have been found to lower significantly the percolation threshold.

7.2 Randomly orientated CNTs-PI composites

7.2.1 Preparation

A batch of special polymer grade XD ESD carbon nanotubes obtained from Unidym consisting of a mixture of single (SWNTs) and multiwalled carbon nanotubes (MWNTs) have been used in both processing methods. The size of these nanotubes ranges in length from 1 to 5 μm and $1-6$ nm in diameter. Since this product is a mixture of different types of nanotubes, it has been considered to be both semiconductor and metallic in type.

In this study, two approaches have been used for integrating CNTs into PI matrix: in situ polymerisation and solution mixing. The main difference between the two techniques is how the CNTs have been integrated to the PI. In the case of in situ polymerisation, the CNTs have been added during the poly(amic acid) preparation while in the case of solution mixing, the CNTs have been mixed with the as-purchased poly(amic acid). The two procedures are explained in more detail in the following section.

7.2.1.1 In situ polymerisation

In the case of in situ polymerisation process, 4,4-diaminodiphenyl ether (ODA) and pyromellitic dianhydride (PMDA) monomers have been chosen due to the good electron affinity of the ODA and the good acid dissociation constant of the PMDA as shown in Chapter 2, section 2.1. A N,N-dimethylacetamide (DMAc) solvent has been used for the poly(amic acid) synthesis. The in situ polymerisation synthesis method used in this work is illustrated in Figure 7.1.

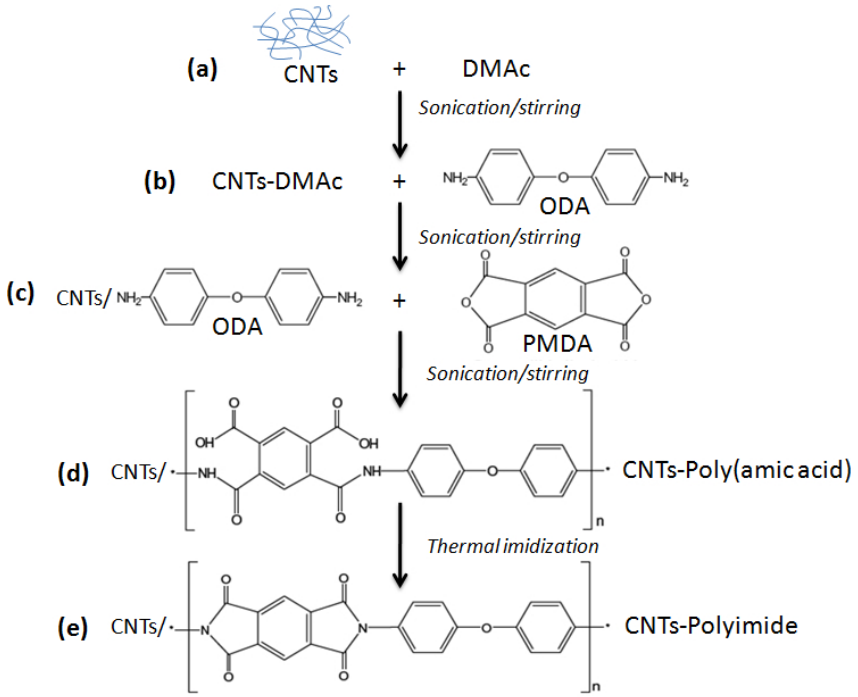

Figure 7.1: *Preparation of CNTs-PI composite via in situ polymerisation procedure*

A certain amount of CNTs has been diluted into DMAc and dispersed using an ultrasonic bath for 15 min (Figure 7.1 (a)). Then, the diamine has been added to the CNTs-DMAc solution (Figure 7.1 (b)). The CNTs-DMAc-ODA solution has been stirred for 1h before adding the dianyhdride (Figure 7.1 (c)). The resulting solution has been stirred overnight until the viscosity of the solution increases to a certain level and stabilises resulting in a CNTs-poly(amic acid) solution (Figure 7.1 (d)). Afterwards, the CNTs-poly(amic acid) solution has been spun coated on a 3 in. Si wafer covered with 350 nm thick SiO_2 at 700 rpm for 30 s and 4000 rpm for 1 min. The resulting solution has been cured in an air-circulating oven to obtain solvent-free CNTs-PI film (Figure 7.1 (e)). The curing temperature has been increased from room temperature to $200°$C by a heating rate of $4°$C/min and kept constant at $200°$C for 30 min and slowly cooled down to room temperature. The resulting CNTs-PI film had a thickness of approximately 1.9 μm.

Although in situ polymerisation has been used widely to prepare CNT-PI composite and is expected to lead to a better final product [60, 61], in this study a white precipitate appeared during the polymerisation step resulting in extremely low molecular weight

poly(amic acid). Possible explanations responsible for the unsuccessful synthesis of a good product could be due to environmental parameters. While the reaction synthesis has been performed at room temperature and in air ambient, some reports have suggested than a reaction that takes place at lower temperature under nitrogen will lead to a better product.

7.2.1.2 Solution mixing processing

As a consequence, solution processing mixing method has been employed as an alternative option to the in situ polymerisation procedure. Figure 7.2 represents the different step of solution processing mixing method.

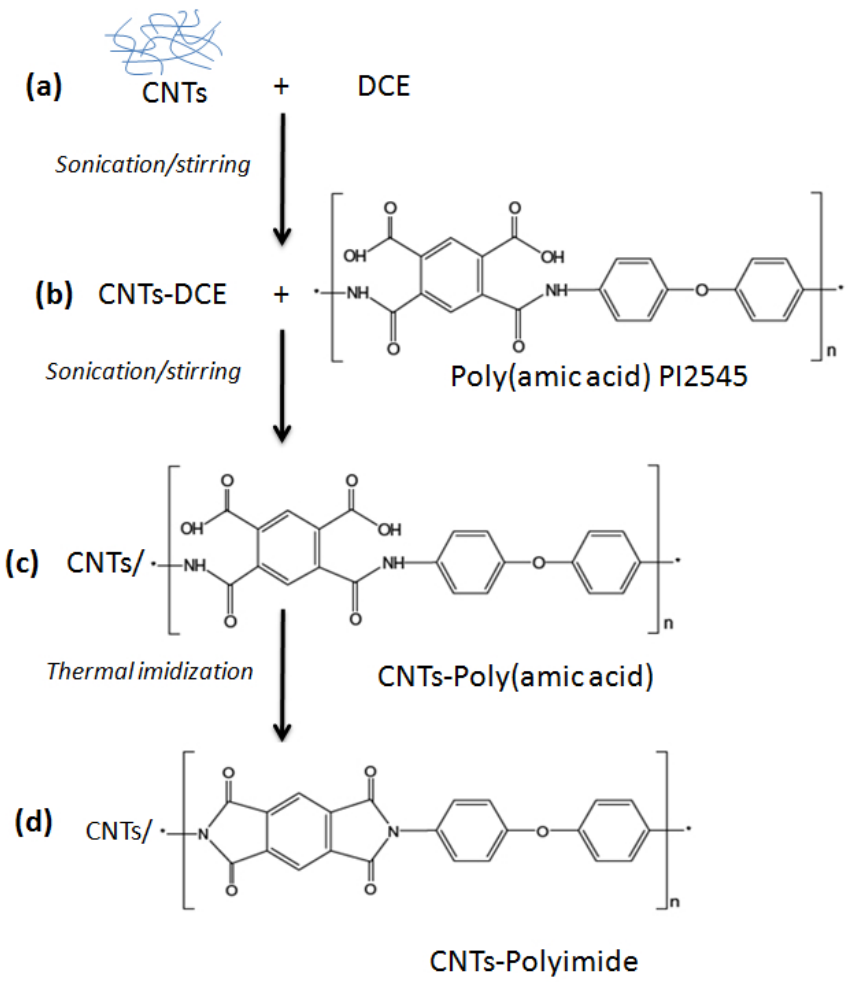

Figure 7.2: *Preparation of CNTs-PI composite via solution mixing processing*

During solution mixing processing, a certain amount of CNTs has been dispersed ultrasonically into dichloroethene (DCE) solvent in order to separate the nanotubes bundles (Figure 7.2 (a)). Once the CNTs have been well separated and dispersed homogeneously into the solvent, the CNTs-DCE suspension has been added slowly to the commercial poly(amic acid) PI 2545 obtained from HD Microsystems and stirred under magnetic stirring overnight (Figure 7.2 (b)). The following imidization process used here is identical to the one used in the in situ polymerisation. The CNTs-poly(amic acid) solution has been spun coated on a 3 in. Si wafer covered with 350 nm thick SiO_2 at 700 rpm for 30 s and 4000 rpm for 1 min. The resulting solution has been cured in an air-circulating oven to obtain solvent-free CNTs-PI film (Figure 7.2 (c)). The curing temperature has been increased from room temperature to $200°$C by a heating rate of $4°$C/min and kept constant at $200°$C for 30 min and slowly cooled down to room temperature. The resulting CNTs-PI film had a thickness of approximately 1.9 μm (Figure 7.2 (d)).

Since the preparation of CNTs-PI via in situ polymerization has been inconclusive, solution mixing processing has been used in this experiment to integrate CNTs into PI. The following section presents the characterisation results of CNTs-PI obtained only from solution mixing.

7.2.2 Characterisation

This section presents the enhancement of the electrical and mechanical properties of the randomly dispersed CNTs-PI composites.

7.2.2.1 Electrical characterisation

The enhancement of the properties has been found to depend strongly on the CNT concentration. A series of CNTs-PI composites with various concentrations of CNTs ranging from 0 to 5 wt% has been prepared using solution mixing method described in Figure 7.2. The electrical conductivities, measured using a two-point probes station, of the CNTs-PI composite as a function of CNTs concentration are shown in figure 7.3.

The conductivity of pristine PI is about $1 \times 10^{-15} S \cdot m^{-1}$. The electrical conductivity is seen to increase by about 12 orders of magnitude as the CNTs concentration in the

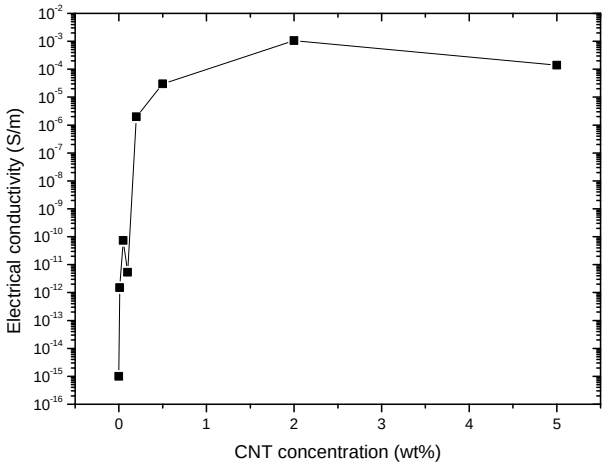

Figure 7.3: *Electrical conductivity of CNTs-PI composite as a function of CNTs concentration*

PI is increased from 0 to 5%. The conductivities show a threshold increase where the electrical conductivities change from $3.83 \cdot 10^{-12}$ to $2.37 \cdot 10^{-6} S \cdot m^{-1}$ between 0.01 and 0.15 wt% of CNT concentration. At loading level above 0.15 wt%, the conductivities increases slowly and reach $4.5 \cdot 10^{-3} S \cdot m^{-1}$ for 5 wt% CNTs. The electrical conductivity of the composite can be considered to follow a percolation theory [241, 242] whereby a critical concentration of CNTs exists at which a conductive path is created in the polymer matrix, increasing conductivity. The conduction inside the composite at the percolation threshold is assumed to occur from electron hopping from one CNT to another if they are close enough to each other or by direct contact at CNTs loading concentration above the percolation threshold.

To determine the critical concentration of CNTs when the electrical nature of the composite switches from insulating to conducting, the electrical conductivity values have been fitted to a power law as a function of the CNT concentration in the PI matrix as shown in Figure 7.4.

The electrical conductivity of the composite increases with the addition of CNTs and can be shown to obey the scaling law, as follows:

$$\sigma = k(\upsilon - \upsilon_c)^t \tag{7.1}$$

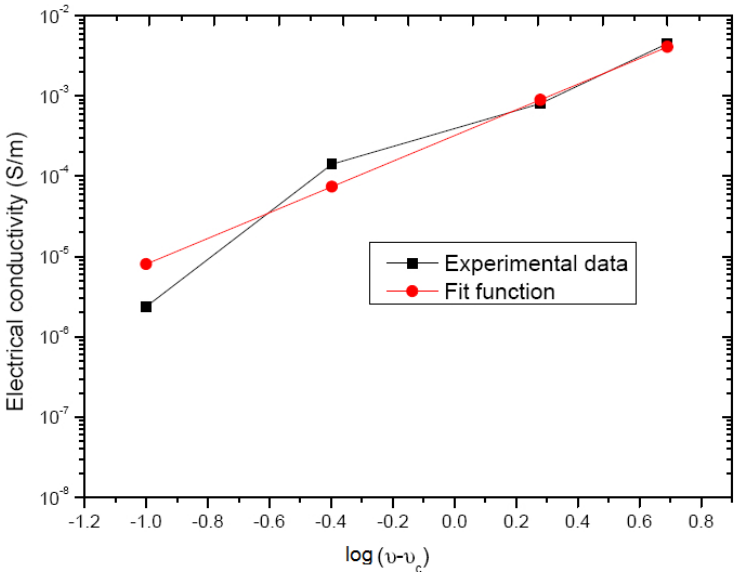

Figure 7.4: *Percolation equation fit to experimental data for the determination of the percolation concentration of CNTs-PI composite*

where υ is the CNTs weight concentration, υ_c is the critical weight concentration corresponding to the percolation and k and t are fitted constant. A best fit to the data resulted in values of $k = 3.2 \cdot 10^{-4} S \cdot m^{-1}$, $t = 1.6$ and $\upsilon_c = 0.15$ wt% (critical concentration value). Theoretically, t is dependent on the dimension of the lattice and the aspect ratio of the filler and reflects the dimensionality of the system, the values 1.3 and 1.94 corresponding to two and three dimensions, respectively [243]. According to Xi *et al*, the value of k should approach the conductivity of CNTs [244].

Other studies on the characterisation of the electrical properties of CNTs-PI have reported similar behaviour where the electrical conductivity of the composite has been found to increase between 7 and 12 orders of magnitude for different amount and types of CNTs integrated to the PI. For instance, Ouaines *et al* [61] reported an increase of electrical conductivity of 12 orders of magnitude by adding 1 wt% of SWNTs into PI, while Jiang *et al* increased the electrical conductivity by more than 11 orders of magnitude from 10^{-15} to 10^{-3} $\Omega.cm^{-1}$ in the range of 0.077 to 0.38 wt% MWNTs [60].

7.2.2.2 Mechanical characterisation

After looking at the electrical properties of the CNTs-PI composite, the following section focuses on the mechanical reinforcement of the composite. The mechanical properties of PI containing different amount of CNTs have been determined using a Tritec 2000 dynamic mechanical analyser (DMA). DMA determines the mechanical properties of the composite giving useful information on the interactions of the polymer chains with the fillers [245], as described in Chapter 3, section 3.4.2.

For mechanical characterisation, $10 \times 5.5 \times 0.25$ mm CNTs-PI samples have been fabricated and tested. Tests have been conducted using a tension clamp, at a frequency of 1 Hz, in a temperature range of $-50°$C to $400°$C and at a heating rate of $4°$C/min. Cyclic stresses have been applied to the sample and its dynamic mechanical response has been recorded as a function of temperature. The influence of the integration of CNTs on the mechanical properties of PI has been evaluated by measurement of the storage modulus (E'), the glass transition temperature T_g of the composite containing different concentration of CNTs.

E' is the storage modulus, which is a measure of stiffness, and E" is loss modulus, which is related to damping or energy dissipation. The ratio of loss to storage modulus is referred as tan delta (tan δ) and represents the measure of the energy dissipation of a material. The maxima peak of the tan δ curve represents the glass transition temperature of the material. Figure 7.5 is a DMA scan of a 1% CNTs-PI composite obtained from Tritec dynamic mechanical analyser. DMA scan plots the storage modulus and the tan δ of the composite as a function of the temperature.

An investigation of the effects of CNT concentration on the storage modulus of the CNTs-PI composites has been done by analysing the storage moduli versus temperature in the range $-50°C/50°C$ for composites with different CNT concentration (0 - 2 wt%) as shown in Figure 7.6.

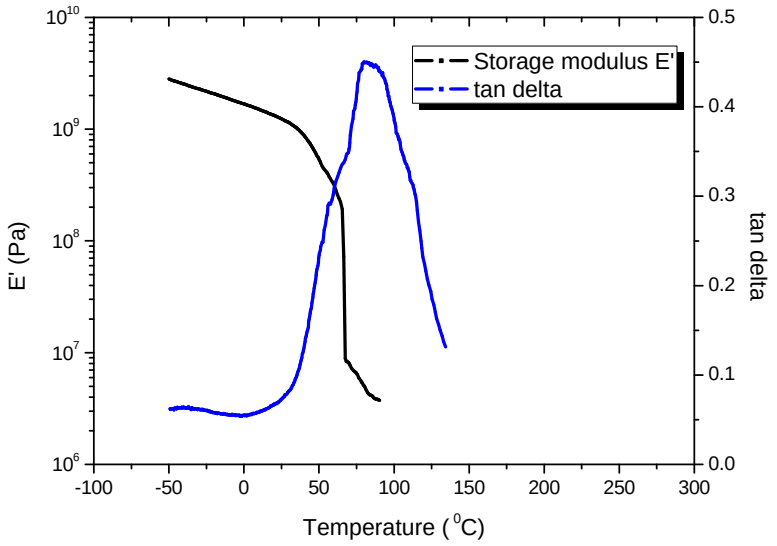

Figure 7.5: *DMA scan of 1 wt% of CNT-PI composite*

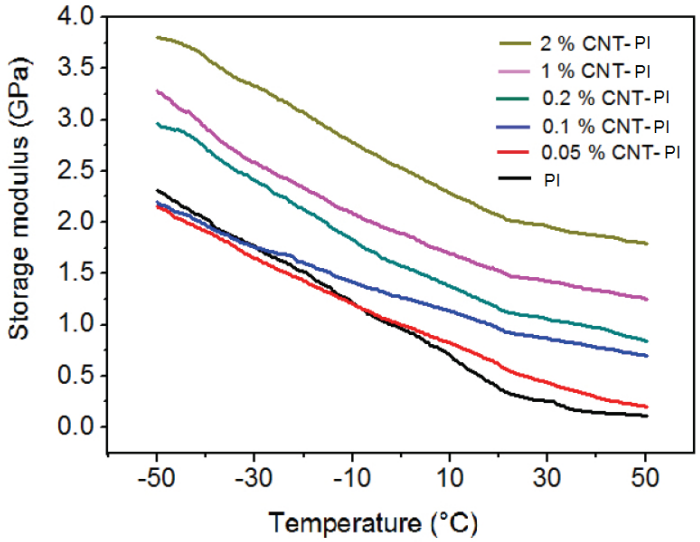

Figure 7.6: *Storage moduli of PI and CNTs-PI composites with different CNTs concentrations as a function of temperature*

From Figure 7.6, it can be seen that as the temperature increases, the storage modulus decreases. This is expected since the increase in temperature results in enhanced molecular motions and, consequently, the material softens. On the other hand, the storage modulus is observed to increase with increasing the CNT concentration from

0 to 2 wt%. At room temperature, the storage modulus of the pure PI is 392 MPa and increases by about 440%, reaching 2.06 GPa at a concentration of 2 wt% CNTs. The increase in storage modulus with increasing CNTs concentration is substantial; it is possible that the CNT dispersion and interfacial bonding with the PI matrix is efficient enough, resulting in an efficient transfer of the excellent mechanical properties of CNTs to the PI matrix.

Figure 7.7 shows the glass transition temperature (T_g) that corresponds to the loss factor (tan δ) peak (see Figure 7.5) for the composite as a function of CNTs concentration. The glass transition temperature (T_g) has been shifted towards higher temperature with the addition of CNTs into the PI matrix. From Figure 7.7, the T_g of PI has been increased from 61.4 to 98.6°C for the composite. The improvement in T_g shows that the CNTs inhibit the onset of the polymer-matrix molecular motions, especially above the percolation threshold, indicating good dispersion and enhanced interfacial interaction between the CNTs and the PI matrix.

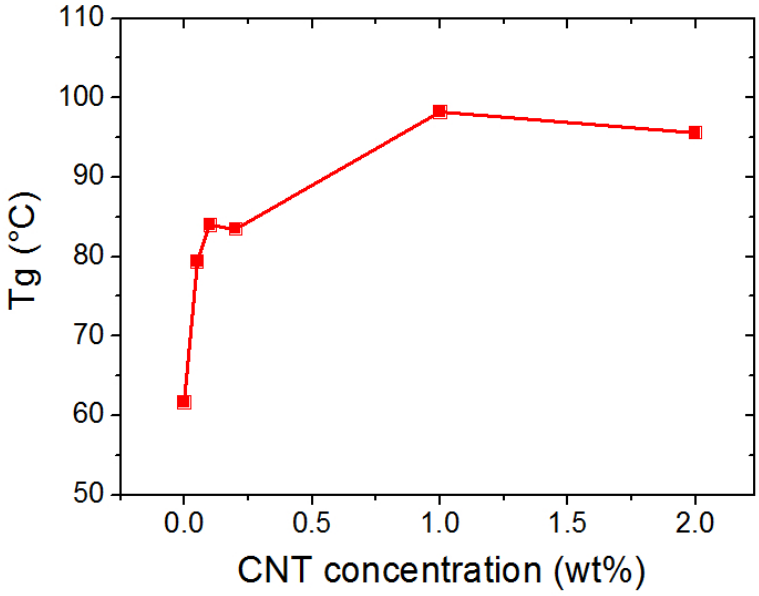

Figure 7.7: *Glass transition temperature (T_g) of CNTs-PI composites as a function of CNT concentration*

7.3 Aligned CNTs-PI composites

This section presents the development of a method to enhance further the electrical properties of the composite. The method consists of applying an AC electric field to the composite in order to induce CNTs alignment into the PI matrix, favouring the electron flow throughout the composite material and preventing CNTs agglomeration.

In Chapter 3, section 3.1, the theory of dielectrophoresis has shown that CNTs experience both dielectrophoretic force and torque in a non-uniform AC electric field that conducts its motion. Although the alignment of CNTs by electric field has been widely reported in solvent solution, the alignment of CNTs into a polymer matrix via dielectrophoresis is a recent practice.

Martin *et al* reported for the first time the formation of a more uniform and aligned network of CNTs into epoxy resin due to the application of an electric field resulting in composite with enhanced electrical properties [65]. Later, the effects of CNTs alignment of the mechanical properties of a high density polyester (HDPE) composite have been investigated [66]. MWNTs were aligned under the presence of an electric field into HDPE. The alignment of MWNTs has shown a significant enhancement of the mechanical properties of the composite resulting in low cost hardness materials for biological applications.

In this experiment, dielectrophoresis (DEP) has been employed to align CNTs inside the PI matrix in order to enhance further the physical properties of the CNTs-PI composites.

7.3.1 Dielectrophoresis (DEP) induced CNTs alignment

The fabrication process flow for the electrodes is illustrated in Figure 7.8 (a). First, a 350 nm thick PECVD SiO_2 layer has been deposited onto a silicon wafer as an insulation layer between the metal electrodes and the wafer. Then, aluminium (Al) electrodes have been fabricated by sputtering a 3 μm thick Al layer and patterned using standard UV lithography and lift-off process as described in Chapter 3, section 3.2. The final structure is presented in Figure 7.8 (b).

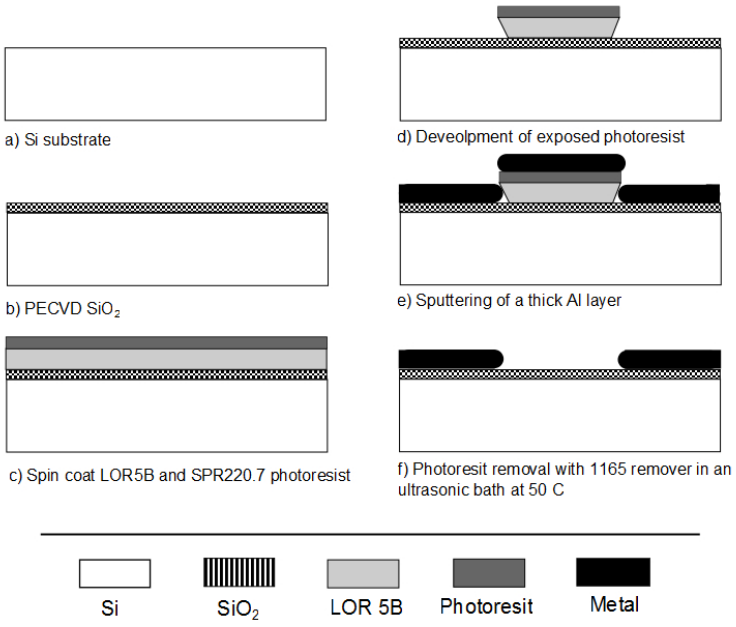

(a) Fabrication process flow

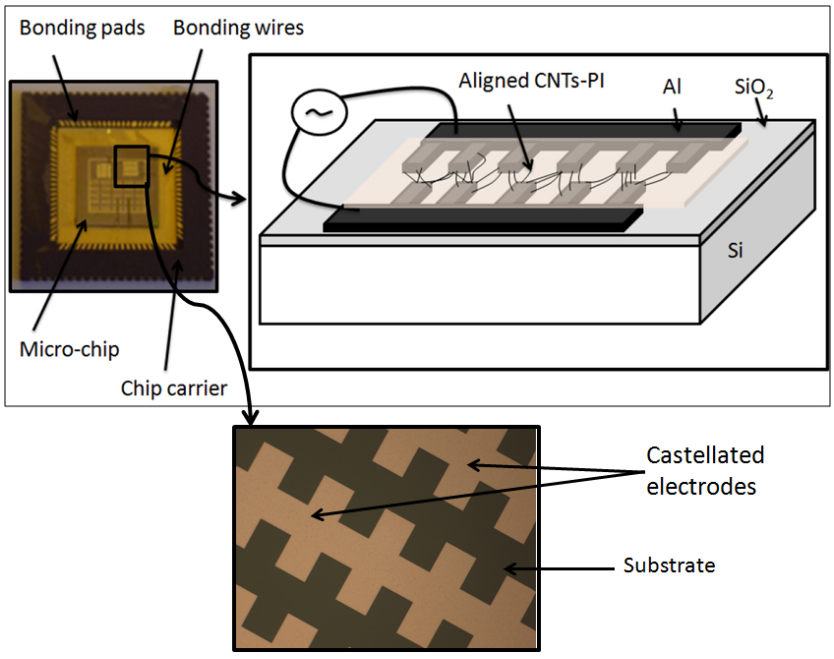

(b) Final device

Figure 7.8: *(a) Schematic of the fabrication process flow and (b) the final structure used for CNTs alignment*

Dielectrophoresis forces have been induced to the CNTs by applying an AC electric field

during the thermal imidization of the CNTs-Poly(amic acid) into CNTs-PI composite. To do so, the as-fabricated Al electrodes have been bonded to a chip carrier before the deposition of the CNTs-PI solution (Figure 7.8 (b)). The processing method used for the preparation of the CNTs-PI solution has been solution mixing processing as shown in Figure 7.2. The AC electric field has been applied at the start of the curing process, when the CNTs are still free to move within the PI. The applied electric field creates dielectrophoresis forces that move and align the CNTs parallel to the electric field lines bridging the Al electrodes. As the temperature increases, the CNTs-Poly(amic acid) imidize into CNTs-PI composite with embedded aligned CNTs within the cured PI matrix as shown in Figure 7.9. It has not been possible to obtain an SEM or optical image of the CNTs alignment, due to charging and the fact that the CNTs are aligned within the PI matrix respectively.

Within the present experiment, an ac electric field of 800 kV.cm^{-1} at a frequency of 1 kHz has been applied during curing in order to create dielectrophoresis forces high enough to induce a movement on the CNTs toward the electrodes.

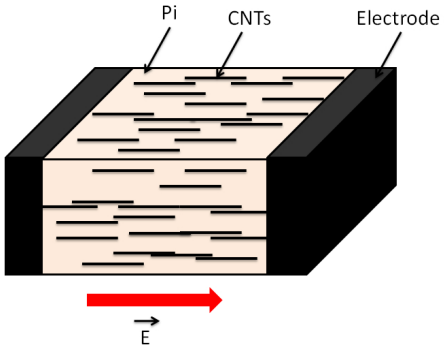

Figure 7.9: *Aligned CNTs in the direction of the electric field*

7.3.2 Dielectrophoresis simulations

As mentioned earlier, the dielectrophoresis response of the CNTs is monitored by the Clausisus-Mossotti factor F_{CM} that defines the magnitude and the sign of the dielectrophoresis forces. In this experiment, the real and imaginary part of the Clausius-Mossotti factor of a SWNTs suspended in PI have been calculated using MATLAB. Here, metallic CNTs will always experience positive dielectrophoresis forces since the permittivity of CNTs, assumed to be $\epsilon_p = 8.8$, is higher than the permittivity

of polyimide $\epsilon_m = 2.8$ and the electrical conductivity of CNTs, $\epsilon_p = 10^8 S \cdot m^{-1}$ is also higher than that of polyimide, $\epsilon_m = 10^{-15} S \cdot m^{-1}$ as shown in Figure 7.10. Theoretical values for the permittivity of metallic and semiconductor CNTs ranging from unity to infinity have been reported [246, 247].

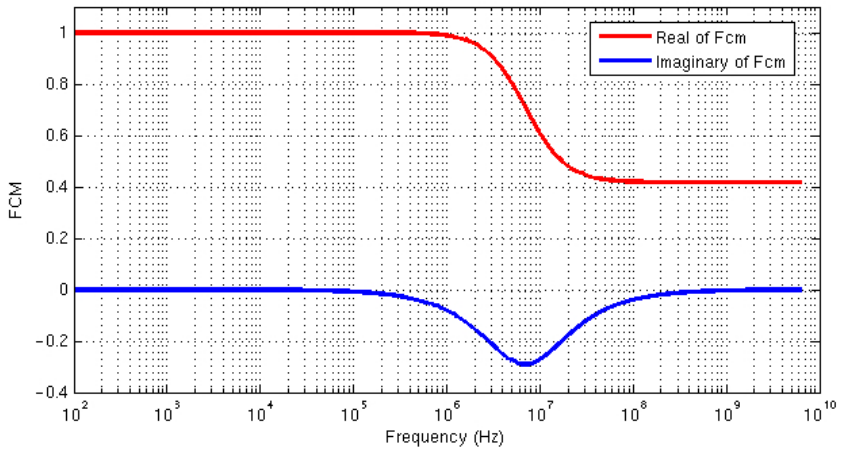

Figure 7.10: *Clausius-Mossotti factor for CNT into PI*

COMSOL simulations of the electric field and dielectrophoresis forces created by applying an external 8 V_{p-p} AC electric field to castellated electrodes are presented in Figure 7.11. From Figure 7.11 (a), the strength of the electric field is maximum in the red regions and minimum in the dark blue regions. The magnitude of the electric field can be seen to be higher at the edges of the electrodes. The electric field between the electrodes effectively drags the SWNTs towards the electrodes. Similarly, the magnitude of the F_{DEP} has been simulated, as shown in Figure 7.11 (b). The strength of the F_{DEP} is defined by the same colour scale, where red regions represent high F_{DEP} and blue regions represent low F_{DEP}. The F_{DEP} appears to be higher in the area between the electrodes, where SWNTs should be attracted.

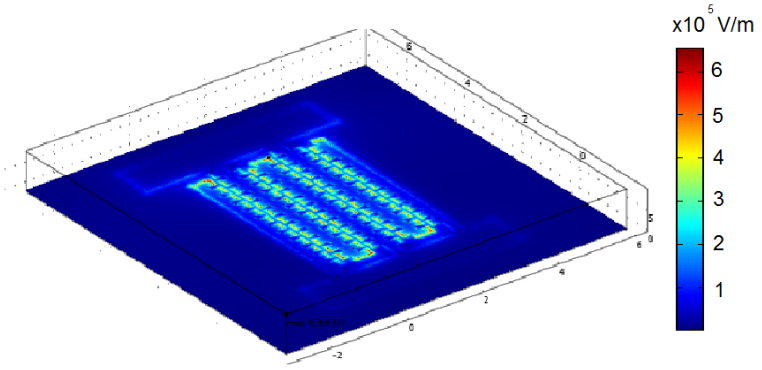

(a) Simualted electric field

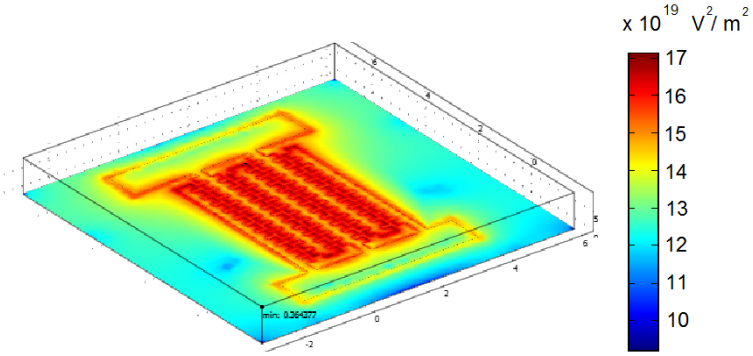

(b) Simulated dielectrophoresis force

Figure 7.11: *COMSOL simulations of the (a) electric field (E) and (b) dielectrophoresis force (F_{DEP}) induced by a 8 V_{p-p} AC electric field applied to castelled electrodes of 10 μm wide separated by a 10 μm gap*

7.3.3 Characterisation

In this section, an AFM characterisation of the CNTs alignment induced by DEP is presented along with the comparison of the electrical conductivities of randomly dispersed and aligned CNTs-PI composites.

7.3.3.1 Surface characterisation using AFM

Figure 7.12 shows AFM images of two samples with 0.1 wt % CNT concentration prepared under (a) no electric field and (b) an AC electric field of 800 kV.cm^{-1} at 1 kHz. It can be seen that the CNTs tend to align in the presence of an AC electric field.

In Figure 7.12 (a), the random dispersion of CNTs without any preferred orientation is observed. On the other hand, in Figure 7.12 (b) where the CNTs-PI composite has been exposed to an external electric field during curing, CNTs chains are observed where most of the CNTs are aligned in the direction parallel to the electric field until bridging the electrode gaps correlating with COMSOL simulations as shown in Figure 7.11.

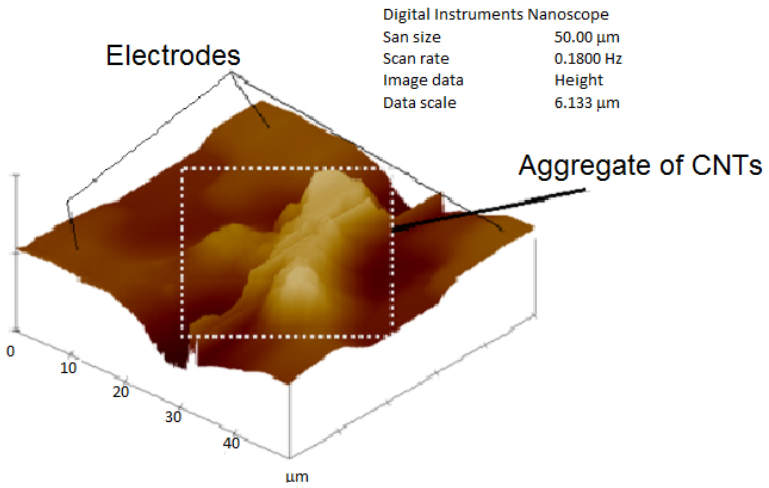

(a) No electric field applied

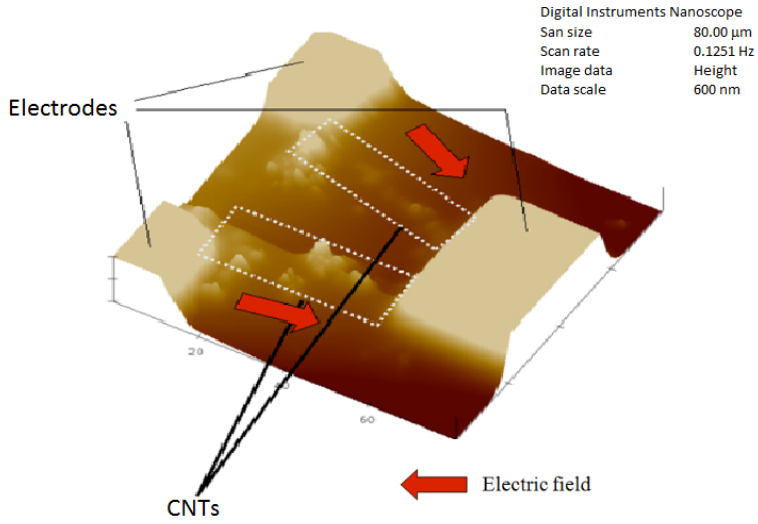

(b) AC electric field of 800 kV/cm at 1 KHz applied

Figure 7.12: *AFM images of CNTs-PI solution subjected to (a) no electric field and (b) an AC electric field of 800 kV/cm at 1 KHz during curing*

Since the CNTs used are both metallic and semiconductor in type, they undergo

different DEP effects. In theory, only metallic CNTs are subjected to DEP forces and therefore attracted between the electrodes. However, there is a possibility for semiconducting CNTs to be tangled within metallic CNTs and be dragged toward the high electric field regions.

7.3.3.2 Electrical conductivity improvements

Figure 7.13 shows the electrical conductivities of a series of randomly dispersed and aligned CNTs-PI with various concentrations of CNTs ranging from 0 to 5 wt% prepared using solution mixing method. The enhancement of the properties has been found to depend strongly on the CNT concentration. Both curves show similar trends where the electrical conductivities increase sharply between 0.02 wt % CNTs and 0.2 wt % CNTs. The electrical conductivities of the randomly dispersed and aligned CNTs-PI composites follow a percolation theory whereby a critical concentration of CNTs exists at which a conductive path is created in the polymer matrix. At concentration above 0.2 wt % CNTs, both composites present electrical conductivity values above the limit ($10^6 S.m^{-1}$) that can be use in electrostatic dissipation (ESD) and electromagnetic interference (EMI)-shielding applications. This value has been chosen as the electrical conductivity threshold for the fabricated composite.

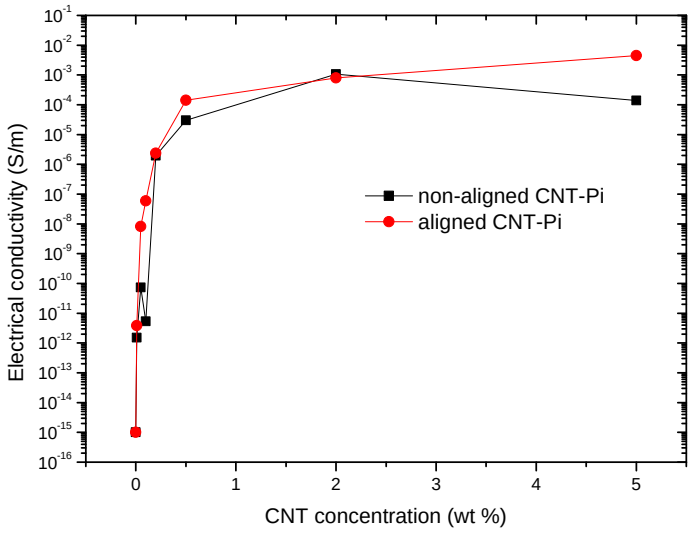

Figure 7.13: *Influence of DEP on the electrical conductivity of the CNTs-PI composites as a function of CNT concentration*

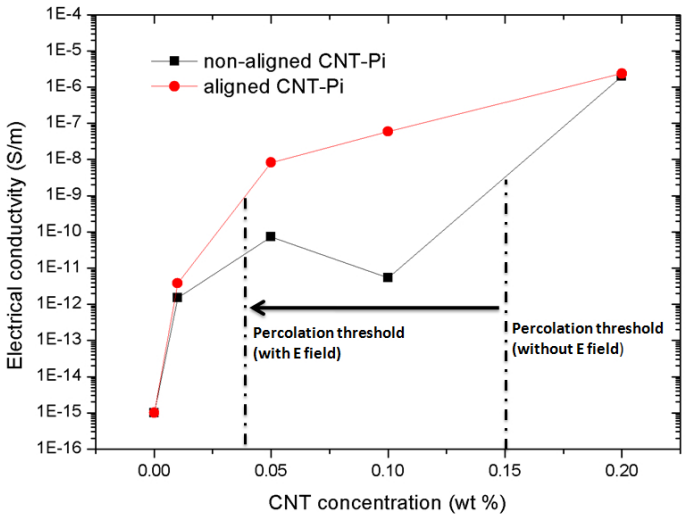

Figure 7.14: *Zoom in the percolation threshold region*

To investigate the possible lowering of the percolation threshold between randomly dispersed and aligned CNTs-PI composites, only the resulting electrical conductivities of the cured CNTs-PI composites (with and without electric field applied) below 0.20 wt% CNT concentration have been of interest as shown in Figure 7.14. At CNT

concentrations below 0.01 wt% CNTs, no significant difference in the increase in the conductivity has been observed with or without electric field. Above 0.036 wt% and below the previously measured percolation threshold (0.15 wt%), the CNTs-PI composite (with field applied) shows much higher electrical conductivities compared to the CNTs-PI composite (with no field applied). For example, at a concentration of 0.05 wt% CNTs, the CNTs-PI composite (with field applied) displays an electrical conductivity value 100 times higher than the CNTs-PI composite (with no field applied). The presence of the electric field during curing of the composite containing CNTs serves to decrease the percolation threshold from 0.15 wt% CNTs to 0.036 wt% CNTs. The large increase in the conductivities and the lowering of the percolation threshold when an electric field is present during curing for the CNTs-PI composite suggests that the CNTs have been aligned to a certain degree within the polymeric network to enable a better conductive pathway through the PI composite, as confirmed by the AFM images in Figure 7.12. The effect of DEP on the electrical conductivity of the composites above the percolation threshold could not be seen in this experiment. It is suggested that at higher CNT concentration, there is a large probability of CNTs contact and agglomeration where the alignment of the tube is not necessary to allow electron flow through the PI matrix.

7.4 Conclusions

This chapter has presented the preparation and the characterisation of high performances properties CNTs-PI composite materials. Two different approaches have been employed to synthesis CNTs-PI composites, in situ polymerisation and solution mixing. The former, has appeared to be unsuccessful whereas the second has led to promising results. Since the preparation of CNTs-PI via in situ polymerization has been inconclusive, solution mixing processing has been used in this experiment to prepare CNTs-PI composite materials.

The electrical and mechanical characterisations of randomly dispersed CNTs into PI via solution mixing have been presented. The electrical and mechanical properties of composites have been seen to improve as a function of the CNT concentration. By adding 5 wt% of CNTs to the PI, the electrical conductivity of the composite has been increased by 12 orders of magnitude. The electrical conductivity has been found to

follow a percolation like power law equation with a percolation threshold of 0.15 wt% CNTs for non-aligned CNTs-PI composite. By integrating 2 wt% CNTs in the PI, the storage modulus of the PI has been improved by about 440% below the glass transition temperature. The T_g of the composite has been increased from 61.4°C to 98.6°C as the CNT concentration increased from 0 to 2 wt%.

In order to improve the electrical properties of the CNTs-PI composites further, DEP has been used to align CNTs inside the PI matrix. One significant finding has been to increase the electrical conductivities and to lower the percolation threshold of the polymer from 0.15 wt% to 0.036 wt% CNT by applying an AC electric field to the PI matrix integrated with CNTs during curing. The large increase in electrical conductivities and the lowering of the percolation threshold when an electric field is present during curing for the CNTs-PI composite suggest that the CNTs have been aligned to a certain degree within the polymeric network to enable a better conductive pathway through the polymer composite. Below the percolation threshold (without field) at 0.15 wt%, the electrical conductivity values of the CNTs-PI composites (with field applied) have been 100 times higher than the electrical conductivity value of the CNTs-PI composites (without field applied). The effect of DEP on the electrical conductivity of the composite above the percolation threshold could not be seen in this experiment. It has been suggested that at higher CNT concentration, there is a large probability of CNTs contact and agglomeration where the alignment of the tube is not necessary to allow electron flow through the polyimide matrix.

The results discussed in this chapter have shown the possibility to develop high performance CNTs-PI composites integrated with extremely low CNT content demonstrating desired electrical and mechanical properties that could be of interest for a wide range of applications from packaging, electrostatic dissipation (ESD) and electromagnetic interference (EMI)-shielding to humidity sensor as presented in the following chapter.

Chapter 8
A resistive CNTs-PI composite humidity sensor

8.1 Introduction

PI, CNTs and CNTs-PI composites have been reported as potential candidates for sensing material layer in humidity sensor applications. Initially, PI has been used for capacitive humidity sensors [75–77]. However, capacitive PI humidity sensors are expensive and require complex measurements methods leading scientists to consider PI as potential resistive humidity sensors [78], which have shown good sensitivity to humidity. Nevertheless, PI resistive humidity sensors experience a non-linear response and have a high humidity level detection limit (≥ 40 %). Therefore, CNTs-PI composites have been regarded recently as a new sensing material in order to overcome the problems encountered by PI resistive humidity sensors [97, 98]. Due to their hollow shape cylinders and their large surface area, CNTs have been reported to be an excellent material for water absorption and therefore humidity sensing applications. CNT network humidity sensors possessing good sensing performances have reported also [80, 81].

In this chapter, randomly dispersed CNTs-PI and aligned CNTs-PI composites have been prepared as presented in Chapter 7 and used as a resistive type humidity sensor.

In section 8.2, the preparation of randomly dispersed and aligned CNTs-PI composite containing different CNT concentrations is presented along with the fabrication process of the sensor devices. High electrical conductivity has been obtained by integrating CNTs into PI composites, resulting in a potential solution to overcome detection problem at very low humidity levels where the resistance of pristine PI is often too high to be measured. In section 8.3, the sensing mechanism of the CNTs-PI film is described.

In section 8.4, the devices performances have been characterised by the sensitivity and the linearity of their change of resistance responses to humidity levels. The alignment

of CNTs has been found to enhance the sensors sensitivity to humidity as well as considerably improve the linearity of the change of resistance in response to humidity leading to more reliable devices.

8.2 Sample preparation

This section presents the synthesis of randomly dispersed and aligned CNTs-PI composite thin films by solution mixing method along with the fabrication process of the sensor devices.

8.2.1 Randomly dispersed CNTs-PI composites

The CNTs used in this experiment (a special polymer grade XD ESD carbon nanotubes obtained from Unidym) have been the same as the ones used in Chapter 7. PI has been synthesised via a commercial poly(amic acid) PI 2545 obtained from HD Microsystems. The method employed to disperse the CNTs within the PI matrix has been the solution mixing technique. The detailed experimental procedure to synthesis CNTs-PI composite is illustrated in Figure 8.1.

Different amounts of CNTs have been dispersed ultrasonically into dichloroethene (DCE) solvent in order to separate the nanotube bundles (Figure 8.1 (a)). Once the CNTs have been well separated and dispersed homogeneously into the solvent, the CNTs-DCE suspension has been added slowly to the commercial poly(amic acid) PI 2545 obtained from HD Microsystems and stirred under magnetic stirring overnight (Figure 8.1 (b)). Then, the poly(amic acid)-CNTs has been imidized to obtain a CNTs-PI layer. To do so, the CNTs-poly(amic acid) solution has been spun coated on a 3 in. Si wafer covered with 350 nm thick SiO_2 at 700 rpm for 30 s and 4000 rpm for 1 min. The resulting solution has been cured in an air-circulating oven to obtain solvent-free CNTs-PI film (Figure 8.1 (c)). The curing temperature has been increased from room temperature to $200°$C by a heating rate of $4°$C/min and kept constant at $200°$C for 30 min and slowly cooled down to room temperature. The resulting CNTs-PI film had a thickness of approximately 1.9 μm (Figure 8.1 (d)).

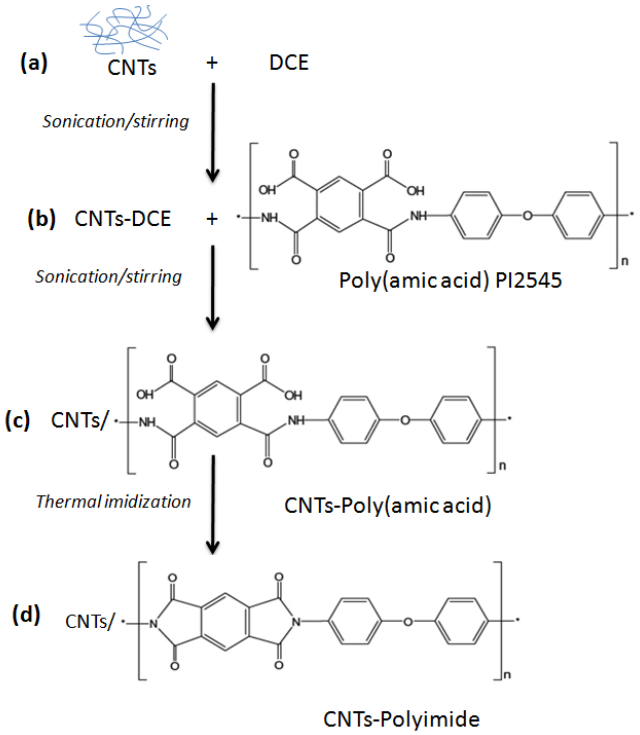

Figure 8.1: *Solution mixing processing synthesis of CNTs-PI composites*

8.2.2 Sensor fabrication

The CNTs-PI humidity sensor consists of a pair of interdigitated Al electrodes patterned on a Si/SiO_2 substrate where the CNTs-PI composite sensing layer synthesised by solution mixing as shown in Figure 8.1 has been spun coated on top. The fabrication process flow is illustrated in Figure 8.2.

First, a 350 nm thick PECVD SiO_2 layer has been deposited onto a silicon wafer as an insulation layer between the metal electrodes and the wafer (Figure 8.2 (a)). Then, Al electrodes have been fabricated by sputtering a 350 nm thick Al layer (Figure 8.2 (b)) and patterned using standard UV photolithography with positive photoresist (Figure 8.2 (c) and (d)) as described in Chapter 3, section 3.2. The exposed Al areas have been etched using an RIE technique in a $SiCl_4/Ar$ plasma (Figure 8.2 (e)) as described in Chapter 3, section 3.3.3. The remaining photoresist has been completely removed in an O_2 plasma after 60 minutes processing (Figure 8.2 (f)). Finally, the CNTs-PI composite has been spin coated on top of the Al electrodes. The final structure is presented in Figure 8.3.

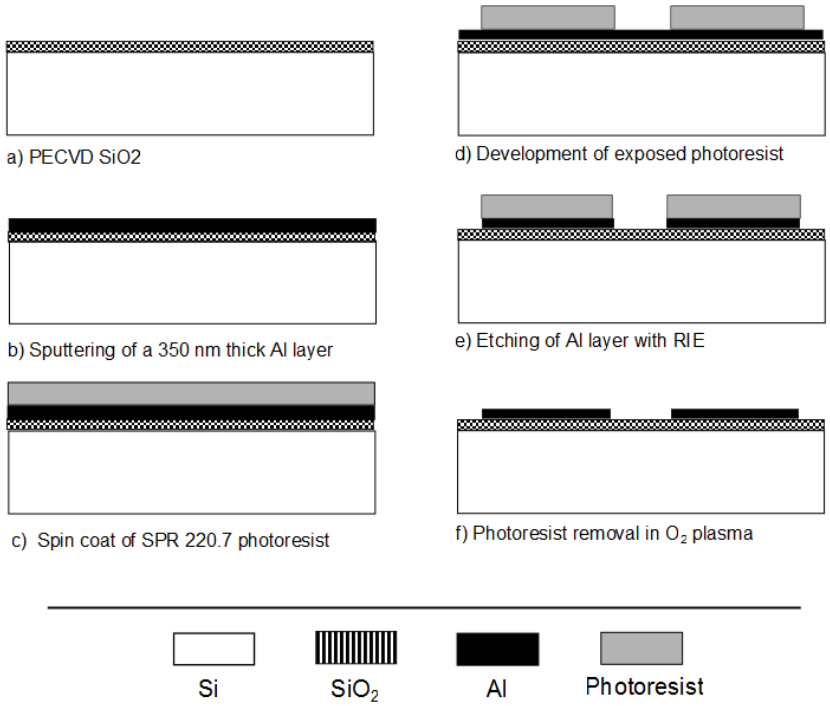

Figure 8.2: *Fabrication process flow of the CNTs-PI resistive humidity sensor*

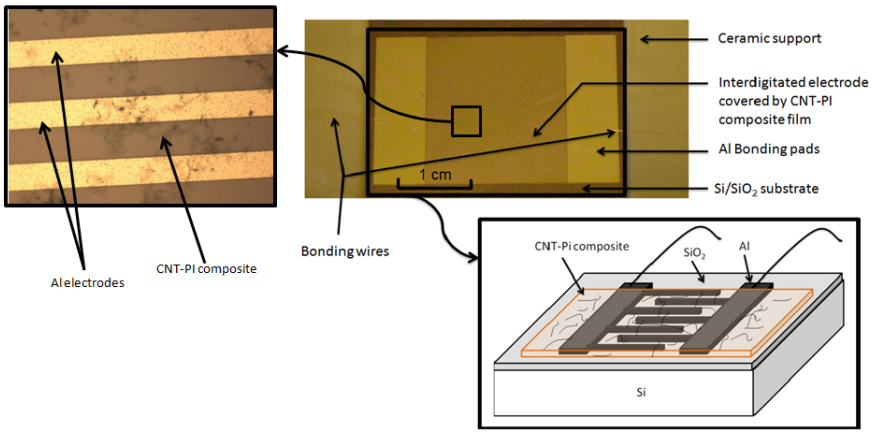

Figure 8.3: *Optical image and schematic of the CNTs-PI resistive humidity sensor*

8.2.3 Aligned CNTs-PI composites

CNTs-polymer composites are used largely as sensor elements for numerous gases and vapour sensors. Therefore, scientists have been devoting much effort to improve

the sensing properties of the devices with various approaches. Recently, oxygen functionalisation of CNTs has been reported to enhance the sensing performance (sensitivity improved by a factor 2 and linearity increased from 0.982 to 0.999 after O_2 plasma treatment) of CNTs-PI composite humidity sensor by increasing the number of functional groups available where water molecules can bond to [97].

The improvement of sensitivity and linearity response due to CNTs alignment into polymer matrix have been reported theoretically [248] and experimentally [249] for strain sensors. In this study, DEP has been used to induce CNTs alignment inside the PI matrix between interdigitated electrodes and is expected to improve the sensing properties of the CNTs-PI composite resistive humidity sensor. This section reports on the COMSOL simulation of the electric field and dielectric forces governing the CNTs movement in the PI matrix and the DEP procedure employed to align CNTs.

8.2.3.1 DEP simulation

Similar to the simulations performed for castellated electrodes presented in the previous chapter, COMSOL simulations of the electric field (E) and dielectrophoresis forces (F_{DEP}) created by applying an external 10 V_{p-p} AC electric field to interdigitated electrodes separated by a 20 μm gap are presented in Figure 8.4 (a) and (b).

The strength of the electric field and the magnitude of the dielectrophoresis force are represented by the same colour scale as in the previous chapters (the high E and F_{DEP} correspond to the red regions and weak E and F_{DEP} to the dark blue regions). The higher electric field regions and dielectrophoresis forces are located between the electrodes dragging the CNTs towards the electrodes. In this experiment, an AC electric field of 10 V_{p-p} at a frequency of 1 MHz has been applied during curing in order to create dielectrophoresis forces high enough to induce a movement of the CNTs toward the electrodes.

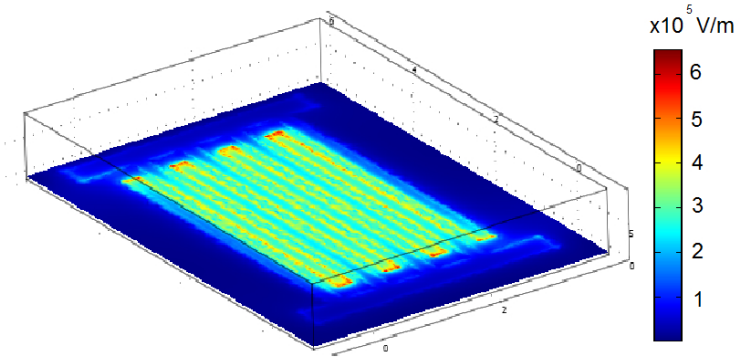

(a) Simulated electric field

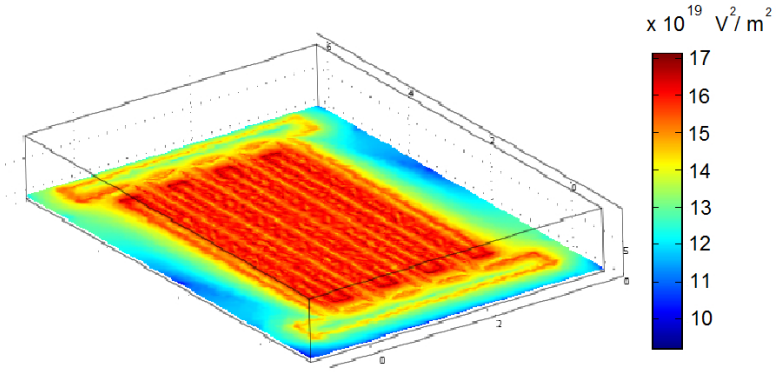

(b) Simulated dielectrophoresis force

Figure 8.4: *COMSOL simulations of the (a) electric field (E) and (b) dielectrophoresis force (F_{DEP}) induced by a 10 V_{p-p} AC electric field applied to interdigitated electrodes of 20 μm wide separated by a 20 μm gap*

8.2.3.2 DEP procedure

The processing method used for the preparation of the CNTs-PI solution has been solution mixing processing as shown in Figure 8.1. Dielectrophoresis has been applied to the interdigitated electrodes to induce CNTs alignment within a PI matrix. To do so, the interdigitated Al electrodes (Figure 8.3) used for the measurement of the variation of the resistances have been bonded before the deposition of the CNTs-PI solution. An AC electric field has been applied at the start of the thermal imidization of the CNT-Poly(amic acid) (when the CNTs are still free to move) between the electrodes creating dielectrophoresis forces that have attracted and aligned the CNTs between

the electrodes. As the temperature increases, the CNTs-Poly(amic acid) imidizes into CNTs-PI composite with embedded aligned CNTs within the cured PI matrix. Figure 8.5 shows (a) an optical image and (b) an AFM scan of 58.76 μm^2 of bundles of CNTs aligned inside the PI matrix between Al electrodes separated by a 20 μm gap.

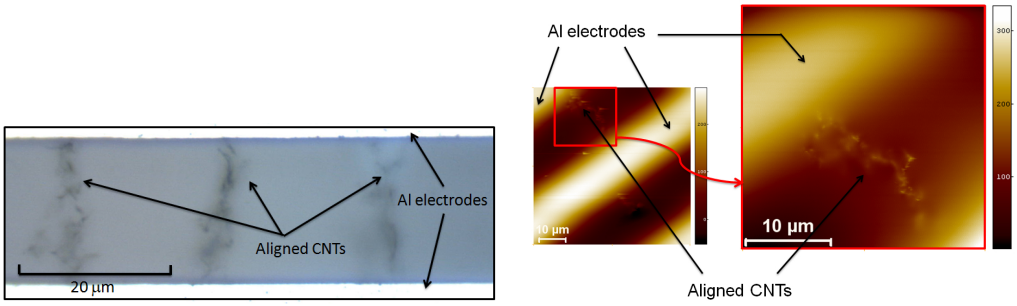

(a) (b)

Figure 8.5: *(a) Optical image and (b) AFM scan of CNTs aligned inside PI between Al electrodes*

From both images, it can be seen that the CNTs tend to align in the direction perpendicular to the electrodes, bridging the electrodes gap.

8.3 Sensing mechanism

In this experiment, the sensing layer of the resistive humidity sensor is made of a CNTs-PI composite film. The resistance of the CNTs-PI composite film depend on the PI resistance, the CNTs resistances, the resistances existing between the CNTs due to the presence of tunnelling effects between the CNTs and the contact resistances at the CNT-CNT interfaces as shown in Figure 8.6.

8.3.1 At low CNT concentration

At low CNT concentration, the CNTs are well separated from each other; therefore the resistance of the composite is dominated by the PI resistance and the resistance existing between the CNTs due to tunnelling effects (Figure 8.6 (a)). In the presence of water, the water molecules are absorbed first at the PI surface and then disseminated across

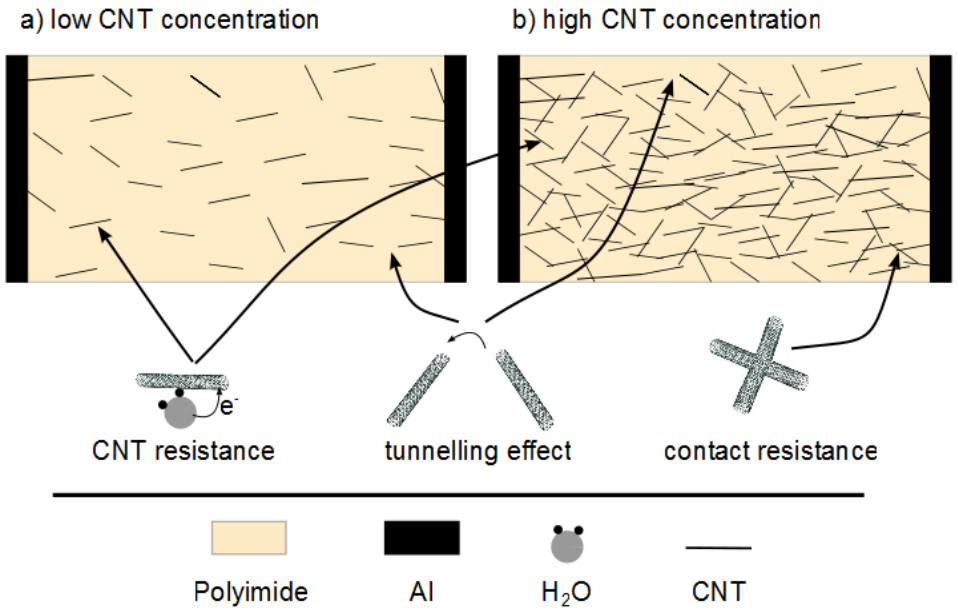

Figure 8.6: *Conductive pathways created by tunnelling effect through CNTs-PI composite (a) at low CNT concentration and (b) at high CNT concentration*

the thickness of the film. There are several sites where the H_2O molecules can bond to the PI chain. According to Melcher *et al* [250], at low humidity level, a chemical bonding occurs between the hydrogen atom of the H_2O molecules and the ether oxygen of the PI chain. While at high humidity levels, the chemical bonding between water and PI is more likely to come from the two hydrogen atoms of the H_2O molecules and two carbonyl oxygen of the carbonyl part of the PI chain. However, an NMR spectroscopy investigation has shown that less than 5 % of H_2O molecules can be bonded to the PI chain from their hydrogen atoms [251]. Therefore, it is more likely that the water absorbed within the PI network remains in free volume increasing the conductivity of the composite film [252]. It is worth noting that the electrical resistivity of PI and water are $1.8.10^7$ and $1.5.10^{18}$ Ω.cm. Consequently, the resistances of the low concentration CNTs-PI composites decrease with the increase of relative humidity (as shown in section 8.4).

8.3.2 At CNT concentration around the percolation threshold

Since the CNTs are dispersed in an insulating PI matrix, at CNT concentration below and around the percolation threshold, the conduction inside the composite is assumed

to occur from electron hopping from one CNT to another. Accordingly, the resistance of the composite is influenced mainly by the PI resistance, the resistance existing between the CNTs due to the tunnelling effect and not so much by the CNTs resistance itself. On the one hand, the absorption of water molecules by the PI chain reduces the composite resistance due to the presence of highly conductive free water in the PI network (see section 8.3.1). On the other hand, in the presence of water, the PI swells increasing the distance between two adjacent CNTs making the electron flow through the composite more difficult and therefore increases the tunnelling resistances [253]. These two opposite trends compensate for each other resulting in a minor change of resistances (as shown in section 8.4).

8.3.3 At high CNT concentration

At high CNT concentration, more CNTs are present inside the PI matrix, and therefore the distance between two adjacent CNTs is smaller so the tunnelling effect on the composite resistance has less influence. In this configuration, as shown in Figure 8.6 (b), the resistance of the composite is dominated by the resistance of the CNT itself and by their contact resistances.

In presence of water, charge transfer occurs between the water molecules and the CNTs. Kong *et al* [254] have studied the change of CNTs electronic properties due to molecular absorption. The electrical properties of CNTs are sensitive to charge transfer and chemical doping effects from the interaction with the absorbed molecules. The absorption of electron donor molecules such as NH_3 or H_2O, or electron acceptor molecules such as NO_2, interact with the CNTs and change the number of charge carriers in the CNTs and therefore, increasing or decreasing the resistance of the CNTs respectively. A more detailed explanation is given by Varghese *et al* [255]. When the CNTs absorb water molecules, a charge transfer occurs between the water molecules and the CNTs. The water molecules donate electrons to the CNTs and therefore reduce the concentration of holes in the CNTs shifting the valence band away from the Fermi level causing an increase of the resistance [256]. As the humidity level increases, more water molecules are absorbed at the CNTs sidewalls, therefore more electrons are transferred, increasing the resistance further (as shown in section 8.4). This is the principle of CNT based resistivity chemical sensors.

At high CNT concentration, the second important component of the composite resistance is the contact resistances at the CNTs interface. In this experiment, a mixture of CNTs has been used as conductive fillers, where CNTs are both semiconducting and metallic in type. Therefore, metal-metal (m-m), semiconducting-semiconducting (s-s) and semiconducting-metal (s-m) CNTs contact junctions can be found within the CNTs network. As explained in Chapter 6, the contact resistances of the CNTs network is due principally to the Schottky barrier at the semiconducting-metal (s-m) CNTs interface [257]. However, it has been reported that the contact resistances at the CNTs interfaces can be negligible compared to the change of resistance due to charge transfer from water molecule to the CNTs [97].

8.4 Characterisation

Humidity testing experiments have been conducted by exposing the CNTs-PI composites to different relative humidity levels using a PROLAN environmental test chamber. The electrical characteristics of randomly dispersed and aligned CNTs-PI composites containing 0.025, 0.05, 0.2 and 1 wt% of CNTs concentrations have been recorded with a Keithley 2400 sourcemeter at different level of humidity. The performances of each device have been determined as a function of the sensitivity and linearity of their responses to different humidity levels.

8.4.1 Resistance of the composite

Figure 8.7 shows the resistance of randomly dispersed and aligned CNTs-PI composites as a function of CNT concentration. The resistance of pristine PI is about 1 GΩ. The resistance has been seen to decrease by 8 orders of magnitude as the CNT concentration in the PI is increased from 0 to 1 wt%. Both curves show similar trends where the resistances show a threshold decrease. The resistance values drop from 1 GΩ to approximately 1 kΩ between 0 and 0.2 wt% of CNT concentration. At loading levels above 0.2 wt%, the resistances decrease slowly and reach 50 Ω for 1 wt% CNTs. The sudden change of resistance between 0 and 0.2 wt% of CNT concentration implies that the resistance of the composite follows a percolation theory whereby a critical concentration of CNTs exists at which a conductive path is created in the

polymer matrix, causing the polymer to change from being an insulator to a conductor. Nevertheless, from Figure 8.7, only two points (0.2 wt% and 1 wt%) have been plotted above the percolation threshold, making difficult the calculation of an accurate percolation threshold. Since the change of resistance as a function of CNT concentration observed in Figure 8.7 correlates with the change of electrical conductivity of the same CNTs-PI films presented in Chapter 7, it has been assumed that the percolation threshold correspond to the same CNT concentration (0.15 wt%). As explained in Chapter 7, the conduction inside the composite at the percolation threshold (0.15 wt%) is assumed to occur from electron hopping from one CNT to another if they are close enough to each other or by direct contact at CNT loading concentration above the percolation threshold.

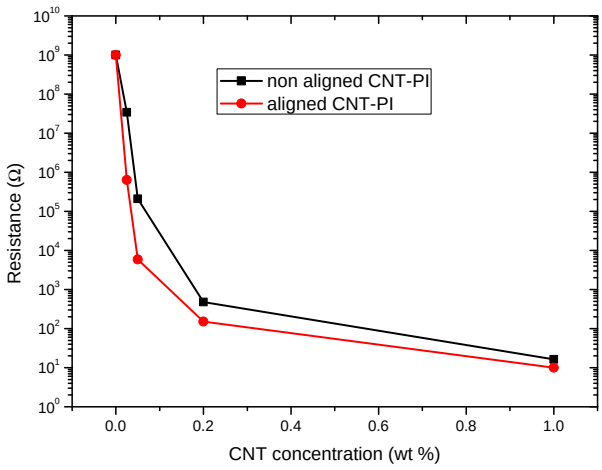

Figure 8.7: *Resistance of CNTs-PI composite as a function of CNT concentration*

Aligned CNTs-PI composites have lower resistances than randomly dispersed CNTs-PI composites. As seen in Chapter 7, the use of DEP has led to the decrease of the percolation threshold from 0.15 wt% CNTs to 0.036 wt% CNTs. The decrease of composites' resistances and the lowering of the percolation threshold when an electric field is present during curing for the CNTs-PI composite suggest that the CNTs have been aligned to a certain degree within the polymeric network to enable a better conductive pathway through the polymer composite. No significant effects of DEP on the electrical conductivity of the composite above the percolation threshold have been observed in the previous chapter where the electrode gap is 1 μm. However, in this experiment, the

resistances of the aligned 0.2 and 1 wt% CNTs-PI composites have been found to be lower compared to randomly dispersed samples. The observed electrical conductivity improvement at CNT concentration above the percolation threshold can be explained by the fact that for larger electrodes gaps (20 μm), the alignments induced by DEP have greater importance, where the probability for randomly dispersed CNTs to bridge the electrodes gaps is lower.

Likewise, the decrease of resistance as a function of CNT concentration could solve potentially the low humidity detection level problem due to the high resistance of pure PI, improving the final performance of the devices.

8.4.2 Response to humidity

8.4.2.1 Randomly dispersed CNTs-PI composites

Figure 8.8 shows the resistances of the (a) 0.025, (b) 0.05, (c) 0.2 and (d) 1 wt% of CNTs-PI devices in response to humidity at 20°C. The initial values of resistances of 0.025, 0.05, 0.2 and 1 wt% of CNTs-PI films correspond to the curves representing the change of resistances as a function of CNT concentration shown in Figure 8.7. The resistances of the composite films are seen to decrease with the addition of CNTs (Figure 8.7).

From Figure 8.8 (a) and (b), the resistances of 0.025 wt% and 0.05 wt% CNTs-PI samples have been seen to decrease slightly with the increase of the relative humidity. As explained in section 8.3, at concentrations below the percolation threshold, the resistance of the composite is dominated by the PI resistance and the resistance existing in between the CNTs due to the tunnelling effect. The results obtained in this experiment are in agreement with previous studies of PI humidity sensors [78, 79] or low concentration CNTs-PI composites where the resistance of the devices decrease with the increase of humidity level [97].

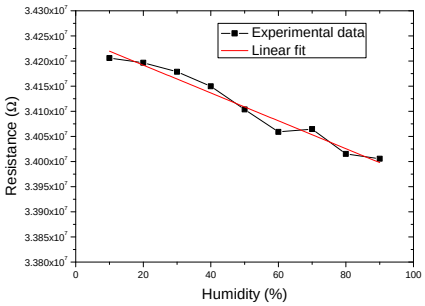

(a) 0.025 wt% CNTs-PI composite

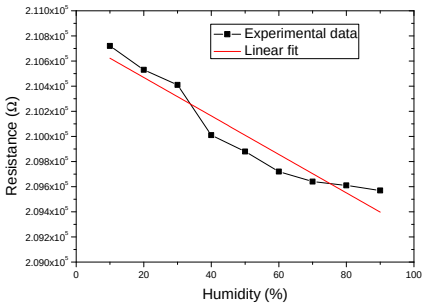

(b) 0.05 wt% CNTs-PI composite

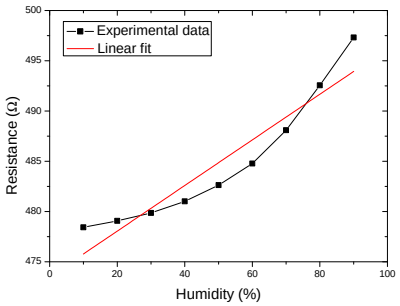

(c) 0.2 wt% CNTs-PI composite

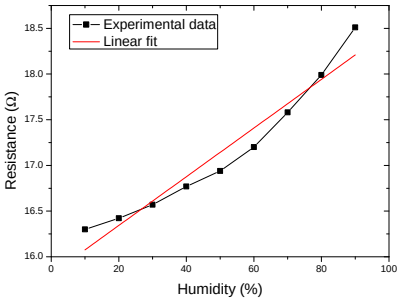

(d) 1 wt% CNTs-PI composite

Figure 8.8: *The change of resistances of randomly dispersed CNTs-PI composite films as a function of humidity levels for (a) 0.025 wt%, (b) 0.05 wt%, (c) 0.2 wt% and (d) 1 wt% CNTs concentration*

On the other hand, at higher CNT concentration, the CNTs-PI composites exhibit another behaviour. Figure 8.8 (c) and (d) show the change in resistance of samples containing 0.2 and 1 wt % of CNTs. Both samples contain a CNT concentration above the percolation threshold where conductive pathways exist within the PI matrix. The resistances 0.2 and 1 wt % of CNTs-PI composites have been observed to increase as the humidity level increases. This is due to the fact that at higher CNT concentration, the change of CNT resistance due to the charge transfer from the H_2O molecules dominates the response of the composite.

In general, the performances of a device are defined by two key performance descriptors that are the sensitivity and the linearity of their responses to different levels of humidity.

The humidity sensitivity (S) of a humidity sensing material is defined as:

$$S = \frac{\Delta R/R_0}{\Delta(\%RH)} \tag{8.1}$$

where $\Delta R = R_i - R_0$, and R_0 is the reference sample resistance. The sensitivity of the different devices calculated from equation 8.1, are listed in Table 8.1.

CNT concentration (wt%)	Sensitivity	Linearity
0.025	0.000073	0.966
0.05	0.000068	0.911
0.2	0.000529	0.883
1	0.001836	0.935

Table 8.1: *Sensitivity and linearity characteristics of the humidity response as a function of CNT concentration of randomly dispersed CNTs-PI composites*

The sensitivity and the linearity of the responses (without taking into account the linearity of 0.025 and 0.05 % due to their negligible variation of resistance) have been found to improve with the increase of the CNT concentration resulting in the 1 wt% CNTs-PI composite devices having the best sensing properties. The 0.025 wt% and 0.05 wt% CNTs-PI samples possess an extremely poor sensitivity of 0.0000797 and 0.0000682 which makes them unsuitable as reliable humidity sensors. The sensitivity of 0.2 wt% and 1 wt% CNT-PI samples have been calculated as 0.000529 and 0.001836 respectively. The resistance of 0.2 wt% CNTs-PI can be seen to increase exponentially as the humidity level increases resulting in a non-linear response (0.883) (Figure 8.8 (c)). On the other hand, 1 wt% CNTs-PI show a better linearity in its change of resistance response (0.935) to humidity levels (Figure 8.8 (d)).

In this experiment, the linearity and the sensitivity of the devices have been improved by increasing the CNT concentration. The results presented differ from a recent study [98] which has identified that the best sensitivity and linearity response is obtained for composite materials containing a CNT concentration around the percolation threshold. This phenomenon has been explained by the fact that a higher number of CNTs inside the PI creates more conductive pathways facilitating the electron flow through the

CNTs-PI composites. The resistance due to the tunnelling effects is then cancelled out or negligible, reducing the variation of resistance of the composite and therefore diminishing the sensitivity of the device.

H_2O molecules are not likely to bond to PI and mainly remain as free water within the polymeric network. Therefore, at low CNT concentration, this results in highly conductive water particles trapped inside the composite film decreasing the composite resistance. In contrast, H_2O molecules bond preferentially to CNTs due to their high specific surface area and large water absorption ability [258] resulting in a charge transfer where water donates electron to the CNTs. The charge transfer changes the electronic properties of the CNT shifting the valence band away from the Fermi level resulting in a large increase of the composite resistance at high CNT concentration. Around the percolation threshold, the decrease of the resistance due to the presence of highly conductive free water molecules and the increase of resistance due to electron transfer from H_2O to the CNTs cancel each other out resulting in the low slope observed in Figure 8.8 (b). As the CNT concentration increases, more surface is available for water molecules to bond to the CNTs sidewalls resulting in more electron transfer to the CNTs and therefore a higher change of resistance, as seen in Figure 8.8 (d).

8.4.2.2 Aligned CNTs-PI composites

In this experiment, DEP has been employed to induce CNTs alignment inside the PI matrix in order to enhance the sensing properties of the CNT-PI resistive humidity sensor. In the same way as for randomly dispersed CNTs-PI composites, the resistances of aligned CNTs-PI composites containing 0.025, 0.05, 0.2 and 1 wt% of CNTs concentrations have been recorded via a Keithley 2400 sourcemeter at different level of humidity and temperature. Figure 8.9 shows the resistances of the (a) 0.025, (b) 0.05, (c) 0.2 and (d) 1 wt% of aligned CNTs-PI devices in response to humidity.

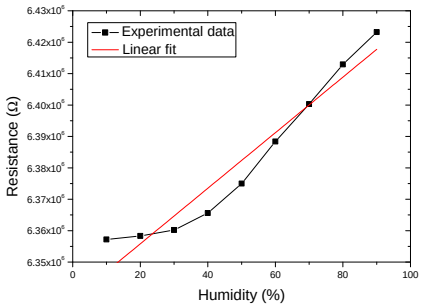

(a) 0.025 wt% aligned CNTs-PI composite

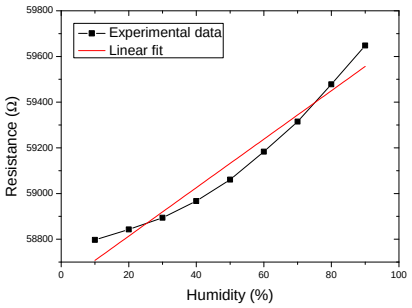

(b) 0.05 wt% aligned CNTs-PI composite

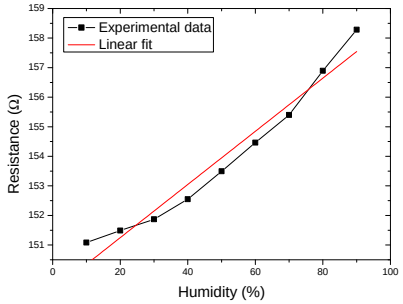

(c) 0.2 wt% aligned CNTs-PI composite

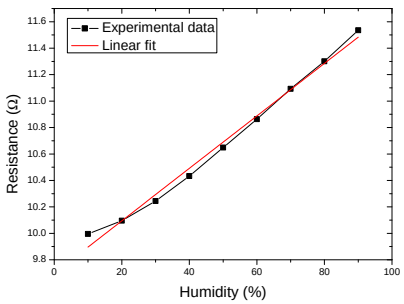

(d) 1 wt% aligned CNTs-PI composite

Figure 8.9: *The change of resistances of aligned CNTs-PI composite films as a function of humidity levels for (a) 0.025 wt%, (b) 0.05 wt%, (c) 0.2 wt% and (d) 1 wt% CNTs*

As explained earlier, in the presence of water, chemical bonding occurs between the H_2O and the CNTs resulting in an electron transfer from the H_2O molecules to the CNTs. This corresponds to a depletion of hole carrier concentration causing an large increase in CNTs resistances resulting in a linear change of resistance response to humidity levels.

While randomly dispersed 0.025 and 0.05 wt% CNTs-PI composites have shown a slight decrease of resistances as the humidity levels increases, the resistances of aligned 0.025 and 0.05 wt% CNTs-PI have been seen to increase with the increase of humidity levels (Figure 8.9 (a) and (b)). The change in behaviour in response to humidity confirms that the DEP has induced a certain alignment of CNTs inside the PI matrix creating new conductive pathways through the polymer composite. The CNTs alignment favours the

electron flow in the direction of the CNTs alignment throughout the composite due to a more homogeneous CNTs network. Therefore, the resistance of the composite has been assessed to be dominated mainly by the CNTs resistance resulting in an improvement of the sensing performance of the devices. The sensing performance improvement has been observed as well for composite films containing higher CNT concentrations (Figure 8.9 (c) and (d)). The sensitivities of randomly dispersed 0.2 and 1 wt% CNTs-PI composites have been found to be 0.000529 and 0.001836, while the sensitivities of aligned 0.2 and 1 wt% CNTs-PI composites have been found to be 0.000681 and 0.002201 respectively (Table 8.2). Therefore, the first consequence of DEP induced CNTs alignment is a significant improvement in the sensitivity of the devices.

In addition, it is noteworthy that the alignment of CNTs inside the PI matrix improves considerably the linearity of the response to humidity. As listed in Table 8.2, the linearity of aligned 0.025, 0.05, 0.2 and 1 wt% CNTs-PI composites varies between 0.931 and 0.990, while the best linearity obtained for randomly dispersed CNTs-PI composites (1 wt% CNT concentration) is 0.935.

	Randomly dispersed CNTs-PI		Aligned CNTs-PI	
CNT concentration (wt%)	Sensitivity	Linearity	Sensitivity	Linearity
0.025	0.000073	-	0.000148	0.931
0.05	0.000068	-	0.000207	0.949
0.2	0.000529	0.883	0.000681	0.955
1	0.001836	0.935	0.002201	0.990

Table 8.2: *Table comparing the sensitivity and linearity characteristics of the humidity response as a function of CNT concentration of randomly dispersed and aligned CNTs-PI composites*

It has been found that the linearity of the change of resistance responses of the composite are a function of the CNT concentration. At low CNT concentration, one can imagine that the CNT network bridging the electrodes is not completely connected where tunnelling effects take place and cause the exponential increase in the resistances, while at higher CNT concentration, the electrons are assumed to flow by direct contact from the different aligned CNTs resulting in a linear change of

resistance responses. Therefore, this observation confirms that the change of resistance in response to humidity is governed by the change of the CNTs' resistances due to charge transfer from the water molecules.

8.5 Comparison with other studies

As mentioned earlier, PI, CNTs and CNTs-PI composite materials have been used as sensing layer in humidity sensors. Table 8.3 compares the sensing properties of the results obtained in this work with other studies on PI, CNTs network and CNTs-PI composites humidity sensors. PI resistive humidity sensors have been reported by [78] showing an excellent sensitivity to humidity. However, PI resistive humidity sensors have shown a non-linear response to humidity and had a not low enough humidity detection level limit (50 %) to be suitable for numerous sensing applications. Therefore, to improve the humidity detection level to below 50 %, CNTs are added to the PI to enhance the electrical conductivity of the composite showing a change of resistance at low humidity level.

The water absorption ability of CNTs have been reported by Liu *et al* [81]. They fabricated a MWNTs network resistive humidity sensor having a sensitivity to humidity of 0.0050 and a linearity correlation of 0.989.

Therefore, the integration of CNTs into PI has led to composite material showing a good compromise between sensitivity, linearity and humidity detection limit [97, 98]. A sensitivity of about 0.002 was reported along with a relatively good linearity in their responses for CNTs-PI composites (Table 8.3). Moreover, an O_2 functionalisation of the CNTs before their integration to the PI has resulted in an enhancement of the sensitivity by a factor two. The sensitivity of O_2 plasma treated CNTs-PI composites has been reported to be 0.0046 which is close to the sensitivity obtained for CNTs network (0.005). In addition, O_2 functionalisation of the CNTs has increased the linearity of the responses to humidity from 0.982 to 0.999.

The randomly dispersed and aligned CNTs-PI composites resistive humidity sensors presented in this experiment have shown sensing performance in the range of results reported by other studies. The principal outcome of this experiment is the significant improvement of the sensitivity and linearity of the sensors' responses due to the

alignment of CNTs within the PI matrix by DEP.

	CNT con.	Sensitivity	Linearity	Detection range
PI [69]	-	0.1833	-	50-90 %
CNTs network [228]	-	0.0050	0.989	25-95 %
CNTs-PI [94]	2.0 wt%	0.0018	0.969	20-90 %
CNTs-PI [95]	0.4 wt%	0.0022	0.982	10-95 %
CNTs-PI functionalised [95]	0.4 wt%	0.0046	0.999	10-95 %
Not aligned CNTs-PI [this work]	1.0 wt%	0.0018	0.935	10-90 %
Aligned CNTs-PI [this work]	1.0 wt%	0.0022	0.990	10-90 %

Table 8.3: *Table comparing the sensing performances of the results obtained in this experiment with other humidity sensors reported in the literature*

8.6 Conclusion

In this chapter, randomly dispersed and aligned CNTs-PI composites films have been prepared and used as a sensing layer in resistive humidity sensors.

The sensing performances of the devices have been seen to depend strongly on the CNTs concentration. The integration of CNTs into the PI matrix has led to a detection of humidity in the range 10-90 %. At low CNT concentration, the CNTs-PI composites have shown poor sensing sensitivity. The poor sensing sensitivity has been explained by the fact that at low CNT concentration, the resistance of the composite is dominated mainly by the PI resistance and the resistance between the CNTs due to tunnelling effects. The absorbed water molecules remain principally in free volume decreasing the resistance of the composite film. At such a concentration and around the percolation threshold, the decrease of the resistance due to the presence of highly conductive free water molecules and the increase of resistance due to the fact that PI swells in the presence of water increasing the distance between adjacent CNTs making the electron flow through the composite more difficult, cancel each other out. As a result, a little change of resistance has been observed leading to poor sensitivity.

At high CNT concentration, more CNTs are present inside the PI matrix, therefore the

distance between two adjacent CNTs is smaller diminishing the influence of the PI resistance and the resistance due to the tunnelling effect on the composite resistance. In this case, the resistance of the composite is dominated by the resistance of the CNT itself and by their contact resistances. In the presence of water, a charge transfer occurs between the water molecules and the CNTs. The water molecules donate electrons to the CNTs and therefore reduce the concentration of holes in the CNTs shifting the valence band away from the Fermi level causing an increase of the resistance. As the humidity level increases, more water molecules are absorbed at the CNTs sidewalls, therefore more electrons are transferred, increasing the resistance further. As a result, a large change of resistance has been observed leading to very good sensitivity.

In the second part of this chapter, DEP has been employed to align CNTs inside the PI matrix. Aligned CNTs-PI composites have shown enhanced sensing performances compared to randomly dispersed CNTs-PI composites. A larger change of resistance in response to humidity levels has been observed with aligned composites resulting in an improvement of the sensitivity of the composite by approximately 20 %. The improvement of the linearity of the responses has been seen for aligned CNTs-PI composites confirming that the change of resistance in response to humidity is governed by the change of the CNTs' resistances due to charge transfer from the water molecules.

Chapter 9
Conclusions and future work

The work presented in this thesis has contributed to the development of thin film material characterisation by providing useful information on the thermal conductivity measurement and the control of the residual stress of thin film materials used commonly in MEMS devices. In addition, the work undertaken in this thesis has developed the use of CNTs in micro-electronics interconnects and as filler reinforcement in composite materials used as sensing layer in resistive humidity sensor applications.

In the first part of this chapter, the results and conclusions obtained from the preceding chapters are summarised. This section begins with the work carried out in contribution to the characterisation of MEMS materials. Subsequently the investigations on the reduction of the contact resistance at the SWNT-metal interface in CNTs interconnects applications are presented. In the last part of this section, the improvement of the electrical and mechanical properties of CNTs-PI composites as a function of CNT concentration and CNT alignment and the use of CNTs-PI composites as sensing layer in resistive humidity sensors are summarised.

In the second part of this chapter, some suggestions on future investigations and work that have arisen from the obtained results are discussed.

9.1 Characterisation of MEMS materials

This section presents the work concentrated on the characterisation of MEMS materials properties. The first step involved the measurement of thermal conductivity of conductive thin film materials. A MEMS device has been designed and fabricated for this purpose. The second step has focused on the development of a method to relieve the residual stress existing in PI cantilever beams built during fabrication processes.

9.1.1 A MEMS for thermal conductivity measurements of conductive thin films

A MEMS device has been developed for the thermal conductivity measurement of ITO, Ti and Al thin films. The design of the MEMS device developed in Chapter 4 consists of a pair of micro-structures; a reference structure and a test structure. From the simulations, the design geometry of the reference and test structures has been optimized to match the several conditions required to lead to the absence of thermal current along the heating stripe of both structures. However, in the test structure there is a beam connected to a heat sink where a thermal current flows. Therefore, the difference obtained by subtracting the heating power of the test and the reference structure has been assumed to be due to the thermal current flowing along the beam towards the heat sink in the test structure and corresponds to the heat dissipation of the metal beam P_B. As a result, only the heat dissipation of the metal beam enters into consideration in the final thermal conductivity calculation.

The thermal conductivity of ITO, Ti and Al thin films have been measured to be 10.2 $W.m^{-1}.K^{-1}$, 16.8 $W.m^{-1}.K^{-1}$ and 200 $W.m^{-1}.K^{-1}$ respectively. Overall, the thermal conductivity values of ITO, Ti and Al thin films have shown good agreement with the thermal conductivity of bulk material. The calculated values in this study are close to but lower than the values of bulk materials as expected. These results demonstrate the capability of the developed MEMS structure for thermal conductivity measurement of conductive thin film.

The main advantage of the MEMS developed is its simplicity and straightforwardness. The measurements can be made in free air and the analysis considers the heat loss due to convection and radiation. Therefore, no extra measurements need to be taken to compensate heat loss which could potentially affect the characteristics of the material being tested or lead to the use of complicated fabrication methods followed by intricate measurements and calculations. However, the limitation of the MEMS device presented lies in the fact that measurement procedure can only work if the beam material is electrically conductive since thermal conductivity is calculated using I-V measurements.

9.1.2 Stress relief in PI cantilevers

The other MEMS materials' property investigated in this thesis has been the residual stress present in Polyimide (PI) micro-cantilever built during fabrication processing. The control of residual stress in thin film material is necessary in device design. The work carried out in Chapter 5 have demonstrated the ability to control the residual stress by using low energy Ar^+ ion bombardment.

Once released, an in-plane extension and a non-linear deflection causing an upward bending of the beam in the z direction has been observed due to the presence of a mean and a stress gradient respectively. Low energy Ar^+ ion bombardment plasma technique has been used as post-fabrication technique to reduce the out of plane deflection of the cantilever beam. The recovery of the out of plane deflection of the cantilever beam has been controlled by both Ar^+ ion energy and bombardment duration. As exposure time and ion energy increase, stress relaxation in the material increases.

Surface and structural characterization of the PI thin film has been carried out by using XPS and FTIR techniques. It has been found that chemical bonds breaking and re-arrangement occur at the surface of the PI film due to low energy Ar^+ ion bombardment. In addition, the interpretation of XPS and FTIR measurements support the recovery of mechanical deflection of the PI cantilever beam exposed to Ar^+ plasma bombardment. The deconvolution of the C 1s, O 1s and N 1s peaks has shown that chemical bonds breaking and re-arrangement after exposure to Ar^+ plasma occurs. The reduction of C=O groups and the increase in C-O and C-N-C groups correlate with the reduction of the mechanical deflection present in the PI cantilever beams. The process of bond re-arrangement and/or the new bond re-arrangement may induce the stress relaxation of the PI cantilevers.

The results discussed in this chapter show that optimization of ion energy and time of ion exposure can lead to stress relaxation of the beam resulting in a straight polymer cantilever beam. The ability of fabricating stress free PI cantilevers offers the possibility for PI to be used in sensing applications. In addition, the low energy Ar^+ ions bombardment plasma technique presented can be used for the optimisation of the design of other polymer (i.e. SU8) suspended structures.

9.2 SWNTs interconnects - Improvement of the contact resistance at the SWNTs-metal interface

SWNTs interconnects have been fabricated in Chapter 6 by aligning SWNTs between metal electrodes using DEP. In particular, attention has been focused to overcome one of the main issue in the fabrication of SWNTs interconnects, namely, the high contact resistance existing at the CNT-metal interface.

The total resistance of a SWNTs interconnects have been analysed by a model representing the different resistance components of the total resistance of the device. The total measured resistance has been defined as the sum of the nanotube resistance, R_{CNT}, and the two contact resistances, R_C, at each SWNT-metal interfaces. Low resistivity SWNTs interconnects have been developed by combining DEP and FIB techniques in order to reduce the R_{CNT} and the two R_C at each SWNT-metal interfaces respectively.

DEP has been employed to align SWNTs between Al and Ti electrodes. The influence of the SWNT concentration, the applied voltage and the frequency on the alignment of SWNTs between Al and Ti electrodes have been investigated with the intention of reducing the resistance of the devices. The lowest resistance has been obtained for the optimum conditions; an AC voltage of 10 V_{p-p} applied for 3 minutes at 1 MHz.

However, the total resistance of the SWNTs interconnect is mainly dominated by the R_C due to the imperfections at the SWNTs-metal junction. Therefore, the major part of the work carried out in this chapter has been aimed to reduce the R_C. The influence of wettability between the SWNTs and the metal (Al and Ti) electrodes and the deposition of Pt contact at the SWNT-metal electrodes interface using FIB on the R_C of SWNTs-metal electrodes have been investigated. Ti-SWNTs-Ti devices have shown a resistance of 83 kΩ/μm which is much lower than the 19 MΩ/μm resistance of the Al-SWNTs-Al devices. Since both metals have similar work functions, the difference in their resistances has been attributed to come from their contact resistance due to different chemical bonding interface between the carbon atoms of the CNTs and the Al and Ti atoms of the metal electrodes. While Al shows a weak bonding to carbon, a strong interaction between Ti and the sp^2 configuration of CNTs exists with strong covalent bonds between the two components.

However, the use of Ti as metal electrode is not enough to achieve low resistivity SWNTs interconnects. Therefore, a technique has been developed to decrease the R_C further. FIB has been employed to improve the contact interface between the CNTs and the metals. One significant finding has been the lowering of the high contact resistances R_C present at the SWNT-metal interface by depositing an additional Pt thin layer on top of the SWNTs-metal electrodes junction. The resistance of Al-SWNTs-Al devices have been reduced from 19 MΩ/μm to 1.8 kΩ/μm, while the resistances of Ti-SWNTs-Ti devices have been reduced from 83 kΩ/μm to 780 Ω/μm respectively. The deposition of Pt contacts by FIB on top of the SWNTs-metal junction has embedded the SWNTs into the metal (Al or Ti) electrodes, limiting the possible separation that can exist when SWNTs are laid on top of the electrodes. The deposition of a top Pt layer creates top and side contacts with the SWNTs, increasing the contact surface area between the SWNTs and the Al and Ti electrodes and therefore decreasing of the resistances of the devices.

9.3 CNTs-PI composite material

The work presented in the last part of this thesis has focused on the preparation of CNTs-PI composites where CNTs have been used as filler reinforcement in order to improve the electrical and mechanical properties of the composite materials. It has been found that the successful transfer of the excellent physical properties of the CNTs to the PI matrix leads to unique composite materials with adjustable properties depending on the concentration of CNTs and the nature of the CNTs alignment inside the PI. The as-prepared CNTs-PI composites have been shown to be an ideal material for electrostatic dissipation or electromagnetic interferences shielding applications. Likewise, in this thesis, the CNTs-PI composites thin films have been used as sensing element and integrated into a resistive humidity sensor that have shown good sensing properties.

9.3.1 Improvement of composite properties

The work presented in Chapter 7 has been focused on the enhancement of the physical properties of the composite by integrating as less CNTs as possible into the PI matrix. Solution mixing processing has been the method employed in this experiment to

prepare CNTs-PI composite materials.

The electrical and mechanical properties of the composites have been seen to improve as a function of the CNT concentration. By adding 5 wt% of CNTs to the PI, the electrical conductivity of the composite has been increased by 12 orders of magnitude. The electrical conductivity has been found to follow a percolation like power law equation with a percolation threshold of 0.15 wt% CNTs for non-aligned CNTs-PI composite. By integrating 2 wt% CNTs in the PI, the storage modulus of the PI has been improved by about 440 % below the glass transition temperature. The T_g of the composite has been increased from 61.4°C to 98.6°C as the CNT concentration increased from 0 to 2 wt%.

Although the integration of CNTs into PI has been drastically shown to improve the electrical and mechanical properties of the composite, DEP has been employed to align CNTs inside the PI matrix in order to improve further the electrical properties of the CNTs-PI composites by lowering the percolation threshold. The alignment of CNTs inside the PI matrix has led to increase the electrical conductivities and to lower the percolation threshold of the polymer from 0.15 wt% to 0.036 wt% CNT. The large increase in electrical conductivities and the lowering of the percolation threshold when an electric field is present during curing for the CNTs-PI composite have suggested that the CNTs have been aligned to a certain degree within the polymeric network to enable a better conductive pathway through the PI composite. Below the percolation threshold (without field) at 0.15 wt%, the electrical conductivity values of the CNTs-PI composites (with field applied) have been 100 times higher than the electrical conductivity value of the CNTs-PI composites (without field applied). The effect of DEP on the electrical conductivity of the composite above the percolation threshold could not be seen in this experiment. It has been suggested that at higher CNT concentration, there is a large probability of CNTs contact and agglomeration where the alignment of the tubes is not necessary to allow electron flow through the polyimide matrix.

The results discussed in this chapter have shown the possibility to develop high performances CNTs-PI composites integrated with extremely low CNT content demonstrating desired electrical and mechanical properties that could be of interest for a wide range of applications from packaging, electrostatic dissipation or electromagnetic interferences shielding applications to resistive humidity sensor as presented in this thesis.

9.3.2 CNTs-PI composites resistive humidity sensor

In Chapter 8, the as prepared CNTs-PI composite materials have been used as sensing layer in a resistive humidity sensor. The fabricated sensor consists of a pair of interdigitated Al electrodes patterned on a Si/SiO_2 substrate where the CNTs-PI composites sensing layer synthesised by solution mixing has been spun coated on top.

Initially, the resistance of CNTs-PI composite materials has been analysed by a model representing all the different resistance components and their influence at different CNT concentration levels. The resistance of the CNTs-PI composite films has been described to depend on the PI resistance, the CNTs resistance, the resistance existing between the CNTs due to the presence of tunnelling effects between the CNTs and the contact resistance at the CNT-CNT interfaces.

The results obtained have shown that the sensing performance of the devices are dependent strongly on the CNT concentration. The integration of CNTs into the PI matrix has led to a larger range of humidity detection of 10-90 % compared to PI itself. At low CNT concentration, the resistance of the composite is governed by the PI resistance. The fact that the absorbed highly conductive water molecules remain principally in free volume inside the PI, decreases the resistance of the composite film. At CNT concentration around the electrical conductivity percolation threshold, the resistance of the composite is dominated mainly by the PI resistance and the tunnelling resistance existing between two adjacent CNTs. Accordingly, the decrease of the PI resistance due to the presence of free water molecules in the PI and the increase of resistance between the tubes due to the fact that PI swells in the presence of water, thus making the tunnelling effect between the CNTs more difficult, cancel each other out. As a result, a little change of resistance has been observed leading to a poor sensitivity about 0.00007.

On the other hand, CNTs-PI composites containing high CNT concentration have shown good sensitivity and linearity in their responses to humidity. At high CNT concentration, more CNTs are present inside the PI matrix; therefore the distance between two adjacent CNTs is smaller diminishing the influence of the PI resistance and the resistance due to the tunnelling effect on the composite resistance. In this case, the resistance of the composite is dominated by the resistance of the CNTs themselves

and by their contact resistances. In the presence of water, a charge transfer occurs between the water molecules and the CNTs. As the humidity level increases, more water molecules are absorbed at the CNTs sidewalls, therefore more electrons are transferred, increasing the resistance further. As a result, a large change of resistance has been observed leading to very good sensitivity. The sensitivity of 0.2 wt% and 1 wt% CNTs-PI composites have been calculated as 0.000529 and 0.001836. A linearity of 0.935 has been obtained for the response of 1 wt% CNTs-PI composites.

Afterwards, DEP has been employed to align CNTs inside the PI matrix and expected to improve the sensing properties of the CNTs-PI composite films given that the change of CNTs resistance dominates the change of resistance of the devices. In fact, as thought probable, aligned CNTs-PI composites have been demonstrated to possess enhanced sensing properties compared to randomly dispersed CNTs-PI composites. A larger change of resistance in response to humidity levels has been observed with aligned CNTs-PI composites resulting in an improvement of 29 and 20% of the sensitivity for the 0.2 wt% and 1 wt% CNTs-PI composites devices respectively. The improvement of the linearity of the responses seen for aligned CNTs-PI composites (0.99 for 1 wt% aligned CNTs-PI composites compared to 0.935 for 1 wt% randomly dispersed CNTs-PI composites) has confirmed that the change of resistance in response to humidity is governed by the change of the CNTs' resistances due to charge transfer from the water molecules.

9.4 Future work

The results presented in this thesis have contributed to the development of thin film material characterisation and have provided new perspectives for the use of CNTs in micro-electronics or composite materials applications. However, further work could be carried out in order to provide a complete characterisation and optimisation of the fabricated devices and composite materials.

9.4.1 Residual stress control

Low energy ion bombardment has been demonstrated to be a suitable post-fabrication method for the relief of the tensile residual stress existing in PI cantilever built during

fabrication process. In this thesis, low energy ion bombardment has been chosen over ion implantation method in order to avoid possible damage caused to the material to be investigated such as heating and partial curing. However, further work could focus on the treatment of the PI before release where more uniform conditions may occur between trials. Similar results would confirm that the stress relaxation is caused by surface effects and not secondary heating.

9.4.2 Low resistivity CNTs interconnects

Further work arises from the investigation of low resistivity SWNTs interconnects. Although the FIB induced Pt deposition at the SWNTs-metal interface method developed in Chapter 6 has been shown to be a promising approach to reduce the high contact resistance of the devices, there are still some challenging process and reliability work that need to be done before SWNT-based devices and interconnects can be integrated into common electronics circuit. Some other issues have to be addressed such as the separation of the CNTs, the quality of the alignment and the purification of the CNTs.

Besides the aforementioned issues related to the CNTs suspension, an improvement of the measurement accuracy could be made by measuring the CNTs resistance using a four point probe measurement technique instead of a two point probe measurement set-up. In a four-point probe measurement, probes resistances and contact resistances of the probes with the electrodes pads are eliminated so that only the bulk resistivity can be obtained.

9.4.3 CNTs-PI composites

In Chapter 7, CNTs-PI composites have been prepared and characterised, showing the impact of the CNT concentration on the electrical and mechanical properties of the composites. However, no work has been carried out on the influence of CNTs on the thermal conductivity of the composite material. Future work should concentrate on measuring the thermal conductivity of the CNTs-PI composites using the MEMS structures presented in Chapter 4. By changing the CNT concentration of the composite, the influence of CNTs on the thermal conductivity of the composite could

be investigated. The main challenge consists on the ability to fabricate a long slab of homogeneous conductive CNTs-PI composite materials integrated in the fabrication the MEMS devices in order to record accurate I-V measurements.

In addition, the final properties of a composite material are strongly dependent on the quality of the dispersion. In particular, a good dispersion increases the interaction surface between the nanotubes and the polymer and limits the CNTs to aggregate with each other. Therefore, future work should concentrate on improving the CNTs suspension and the interfacial bonding between the CNTs and the PI matrix. The preparation of CNTs-PI composite via other synthesis techniques or including functionalisation of the CNTs potentially could lead to composite materials possessing better physical properties.

Appendix A
Fabrication process details

A.1 Tools used for the fabrication

Karl Suss: Photolithography (3-8 inch wafers);

Balzers: metal sputterer;

STS PECVD: plasma enhanced chemical vapour deposition tool used for depositing SiO_2 and Si_3N_4;

STS RIE: reactive ion etching used for metals etching;

STS ICP - RIE: inductively coupled plasma reactive ion etching used for Si etching and argon ion bombardment;

Plasmatherm etcher: SiO_2 etching

Barrel Asher: O_2 plasma used for photoresist removal;

MEMSSTAR: XeF_2 dry chemical etching

A.2 Fabrication processing parameters

	PECVD oxide	PECVD nitride
Pressure (mTorr)	900	900
Gas	N_2 (130 SCCM)	N_2 (1960 SCCM)
	N_2O (13 SCCM)	NH_3 (55 SCCM)
	SiH_4 (10 SCCM)	SiH_4(40 SCCM)
Power (W)	30	20
Temperature (°C)	300 (platen)	300 (platen)
	250 (showerhead)	250 (showerhead)

Table A.1: *PECVD oxide and nitride deposition parameters*

	Etch step	Passivation step
Time (second)	13	7
Pressure (mTorr)	94	94
He flow	40 SCCM, 9.9 Torr	40 SCCM, 9.9 Torr
Gas	SF_6 (130SCCM)	C_4F_8 (143 SCCM)
	O_2 (13 SCCM)	
Power (W)	600 (coil)	600 (coil)
	15 (platen)	0
Temperature (°C)	300	21.4
Etch rate (μm/min)	1.5	0

Table A.2: *Parameters of the DRIE-ICP-RIE process*

SiO_2 etching recipe	
Pressure (mTorr)	72
Gas	CF_4 (60 SCCM)
	H_2 (10 SCCM)
Power (W)	750
Etch rate	33 nm/min

Table A.3: *Parameters of oxide etching recipe using Plasmatherm*

metal etching recipe	
Pressure (mTorr)	100
Gas	$SiCl_4$ (37 SCCM)
	Ar (14.5 SCCM)
Power (W)	60
Etch rate	25 nm/min

Table A.4: *Parameters of metal etching recipe using a RIE system*

Appendix B
Mask design

B.1 Design of the MEMS used for thermal conductivity measurement

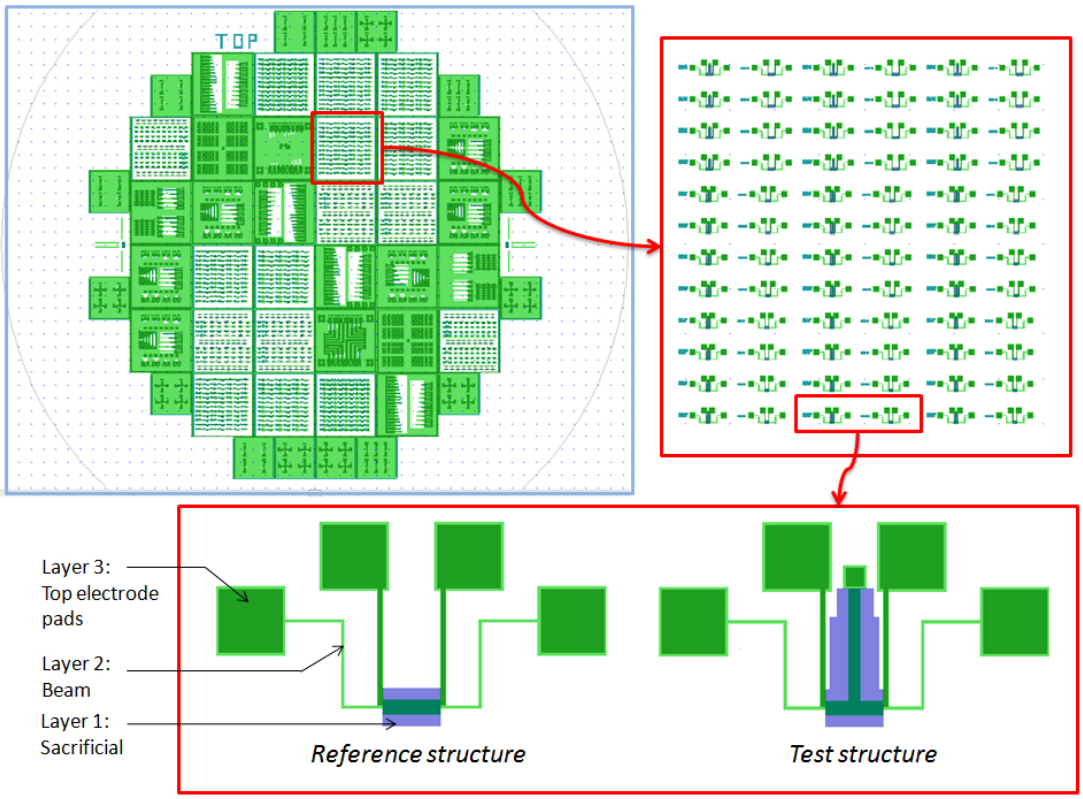

Figure B.1: *Schematic of the design of the three masks used for the fabrication of the MEMS device for the measurement of thermal conductivity of conductive thin films*

B.2 Design of the electrodes used for SWNTs alignment

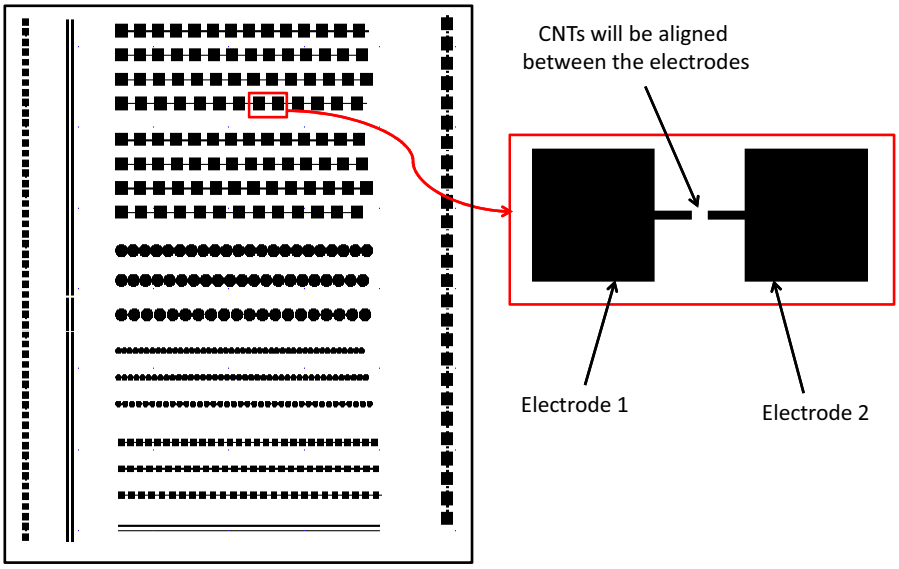

Figure B.2: *Schematic of the design of the mask used for the SWNTs alignment*

Appendix C
Publications

D. Thuau, V. Koutsos and R. Cheung; Electrical and mechanical properties of carbon nanotube-polyimide composites; Journal of Vacuum Science and Technology B: Microelectronics and Nanometer Structures; 27, 3139, 2009

D. Thuau, I. Koymen and R. Cheung; A microstructure for thermal conductivity measurement of conductive thin films; Microelectronic Engineering; 88, 2408, 2011

D. Thuau, V. Koutsos and R. Cheung; Stress relaxation of Polyimide (PI) cantilevers usin low energy ion bombardment; Journal of Micromechanics and Microengineering; under review

D. Thuau, V. Koutsos and R. Cheung; A resistive CNTs-PI composite humidity sensor; to be submitted

References

[1] R. Fenyman, "There is plenty of room at the bottom," in *Presentation at the American Physical Society*, 1959.

[2] H. Nathanson, W. Newell, R. Wickstrom, and J. Davis, J.R., "The resonant gate transistor," *Electron Devices, IEEE Transactions on*, vol. 14, pp. 117 – 133, mar 1967.

[3] K. Peterson, "Silicon as mechanical material," *Proceedings of the IEEE*, vol. 70, p. 420, 1982.

[4] Y. Chen, J. Chen, and S. Lin, "Fracture analysis of thick plasma-enhanced chemical vapor deposited oxide films for improving the structural integrity of power mems," *Journal of Micromechanics and Microengineering*, vol. 12, no. 5, p. 714, 2002.

[5] G. Rebeiz, *RF MEMS: Theory, Design, and Technology*. Gabriel M. Rebeiz, 2003.

[6] J. M. Madou, *Fundamentals of micro fabrication*. CRC Press, 1997.

[7] P. Argyrakis, P. McNabb, A. Snell, and R. Cheung, "Relaxation of process induced surface stress in amorphous silicon carbide thin films using low energy ion bombardment," *Applied Physics Letters*, vol. 89, p. 034101, 2006.

[8] W. Chan, K. Zhao, N. Vo, Y. Ashkenazy, D. Cahill, and R. Averback, "Stress evolution in platinum thin films during low-energy ion irradiation," *Physical review B*, vol. 77, p. 205405, May 2008.

[9] W. Chan and E. Chason, "Stress evolution and defect diffusion in cu during low energy ion irradiation: Experiments and modeling," *Journal of Vacuum Science Technology A: Vacuum, Surfaces, and Films*, vol. 26, pp. 44 –51, Jan. 2008.

[10] S. Keller, D. Haefliger, and A. Boisen, "Fabrication of thin su-8 cantilevers: initial bending, release and time stability," *Journal of Micromechanics and Microengineering*, vol. 20, no. 4, p. 045024, 2010.

[11] D. Sameoto, S.-H. Tsang, I. G. Foulds, S.-W. Lee, and M. Parameswaran, "Control of the out-of-plane curvature in su-8 compliant microstructures by exposure dose and baking times," *Journal of Micromechanics and Microengineering*, vol. 17, no. 5, p. 1093, 2007.

[12] J. Bureau, B. Legrand, D. Collard, and L. Buchaillot, "3d self-assembling of su-8 microstructures on silicon by plasma induced compressive stress," in *Solid-State Sensors, Actuators and Microsystems, 2005. Digest of Technical Papers. TRANSDUCERS '05. The 13th International Conference on*, vol. 1, pp. 19 – 22 Vol. 1, june 2005.

[13] B. J. Bachman and M. J. Vasile, "Ion bombardment of polyimide films," *Journal of Vacuum Science and Technology A*, vol. 7, pp. 2709 – 2716, 1989.

[14] S. Kucheyev, T. Felter, M. Anthamatten, and J. Bradby, "Deformation behavior of ion-irradiated polyimide," *Applied Physics Letters*, vol. 85, p. 733, 2004.

[15] W. Eaton and J. Smith, "Micromachined pressure sensors: review and recent developments," *Smart Materials and Structures*, vol. 6, pp. 530–539, 1997.

[16] M. Asheghi, Y. Leung, S. Wong, and K. Goodson, "Phonon-boundary scattering in thin silicon layers," *Applied Physics Letters*, vol. 71, pp. 1798–1800, 1997.

[17] P. Krulevitch, A. Lee, P. Ramsey, J. Trevino, J. andHamilton, and M. Northrup, "Thin film shape memory alloy microactuators," *Microelectromechanical Systems, Journal of*, vol. 5, pp. 270 –282, Dec. 1996.

[18] O. Korvink, J.; Paul, *MEMS - A Practical Guide to Design, Analysis, and Applications*. William Andrew Publishing/Noyes, 2006.

[19] A. McConnell, S. Uma, and K. Goodson, "Thermal conductivity of doped polysilicon layers," *Microelectromechanical Systems, Journal of*, vol. 10, pp. 360 –369, Sept. 2001.

[20] K. Goodson, M. Flik, L. Su, and D. Antoniadis, "Prediction and measurement of the thermal conductivity of amorphous dielectric layers," *Journal of Heat Transfer*, vol. 116, p. 317, 1994.

[21] A. Jain and K. Goodson, "Measurement of the thermal conductivity and heat capacity of freestanding shape memory thin films using the 3ω method," *Journal of Heat Transfer*, vol. 130, no. 10, p. 102402, 2008.

[22] F. Volklein and H. Balles, "A microstructure for measurement of thermal conductivity of polysilicon thin films," *Microelectromechanical Systems, Journal of*, vol. 1, pp. 193 –196, Dec. 1992.

[23] F. Vflklein and D. Kessler, "Methods for the measurement of thermal conductivity and thermal diffusivity of very thin films and foils," *Measurement*, vol. 5, no. 1, pp. 38 – 45, 1987.

[24] F. Vflklein, "Thermal conductivity and diffusivity of a thin film sio2-si3n4sandwich system," *Thin Solid Films*, vol. 188, no. 1, pp. 27 – 33, 1990.

[25] M. von Arx, O. Paul, and H. Baltes, "Process-dependent thin-film thermal conductivities for thermal cmos mems," *Microelectromechanical Systems, Journal of*, vol. 9, pp. 136 –145, Mar. 2000.

[26] O. Paul, J. Korvink, and H. Baltes, "Determination of the thermal conductivity of cmos ic polysilicon," *Sensors and Actuators A: Physical*, vol. 41, no. 1-3, pp. 161 – 164, 1994. Proceedings of eurosensors VII.

[27] O. Paul and H. Baltes, "Thermal conductivity of cmos materials for the optimization of microsensors," *Journal of Micromechanics and Microengineering*, vol. 3, pp. 110–112, 1993.

[28] G. Xu and Q. Huang, "An online test microstructure for thermal conductivity of surface-micromachined polysilicon thin films," *Sensors Journal, IEEE*, vol. 6, no. 2, pp. 428 – 433, 2006.

[29] S. Iijima, "Synthesis of carbon nanotubes," *Nature*, vol. 354, p. 56, 1991.

[30] N. Hamada, S. Sawada, and A. Oshiyama, "New one-dimensional conductors: Graphitic microtubules," *Phys. Rev. Lett.*, vol. 68, pp. 1579–1581, Mar 1992.

[31] P. McEuen, M. Fuhrer, and H. Park, "Single-walled carbon nanotube electronics," *Transactions on nanotechnology*, vol. 1, p. 78, 2002.

[32] B. Wei, R. Vajtai, and P. Ajayan, "Reliability and current carrying capacity of carbon nanotubes," *Applied Physics Letters*, vol. 79, p. 1396632, 2001.

[33] Z. Chen, J. Appenzeller, Y. M. Lin, J. Sippel-Oakley, A. Rinzler, J. Tang, S. Wind, P. Solomon, and P. Avouris, "An integrated logic circuit assembled on a single carbon nanotube," *Science*, vol. 311, p. 1735, 2006.

[34] P. Avouris, Z. Chen, and V. Perebeinos, "Carbon-based electronics," *Nature Nanotechnology*, vol. 2, p. 605, 2007.

[35] S. Tans, M. Devoret, H. Dai, A. Thess, R. Smalley, L. Geerligs, and C. Dekker, "Individual single-wall carbon nanotubes as quantum wires," *Nature*, vol. 386, p. 474, 1997.

[36] C. White and T. Todorov, "Carbon nanotubes as long ballistic conductors," *Nature*, vol. 393, p. 240, 1998.

[37] J. Kong, E. Yenilmez, T. W. Tombler, W. Kim, H. Dai, R. B. Laughlin, L. Liu, C. S. Jayanthi, and S. Y. Wu, "Quantum interference and ballistic transmission in nanotube electron waveguides," *Phys. Rev. Lett.*, vol. 87, p. 106801, Aug 2001.

[38] A. Naeemi and J. D. Meindl, "Design and performance modeling for single-walled carbon nanotubes as local, semiglobal, and global interconnects in gigascale integrated systems," *Electron Devices, IEEE Transactions on*, vol. 54, pp. 26 –37, jan. 2007.

[39] S. Salahuddin, M. Lundstrom, and S. Datta, "Transport effects on signal propagation in quantum wires," *Electron Devices, IEEE Transactions on*, vol. 52, pp. 1734 – 1742, aug. 2005.

[40] H. J. Li, W. G. Lu, J. J. Li, X. D. Bai, and C. Z. Gu, "Multichannel ballistic transport in multiwall carbon nanotubes," *Phys. Rev. Lett.*, vol. 95, p. 086601, Aug 2005.

[41] M. Nihei, D. Kondo, A. Kawabata, S. Sato, H. Shioya, M. Sakaue, T. Iwai, M. Ohfuti, and Y. Awano, "Low-resistance multi-walled carbon nanotube vias with parallel channel conduction of inner shells [ic interconnect applications],"

in *Interconnect Technology Conference, 2005. Proceedings of the IEEE 2005 International*, pp. 234 – 236, june 2005.

[42] D. Josell, S. Brongersma, and Z. Tokei, "Size-dependent resistivity in nanoscale interconnects," *Annual review of materials research*, vol. 39, p. 231, 2009.

[43] M. S. Dresselhaus and P. Avouris, *Carbon nanotubes: synthesis, structure, properties, and applications*. Springer-Verlag Berlin / Heidelberg, 2001.

[44] C. Berger, Y. Yi, Z. Wang, and W. de Heer, "Multiwalled carbon nanotubes are ballistic conductors at room temperature," *Applied Physics A*, vol. 74, p. 363, 2002.

[45] K. Lozano, "Vapor-grown carbon-fiber composites: Processing and electrostatic dissipative applications," *JOM Journal of the Minerals, Metals and Materials Society*, vol. 52, pp. 34–36, 2000. 10.1007/s11837-000-0196-8.

[46] P. Pftschke, T. Fornes, and D. Paul, "Rheological behavior of multiwalled carbon nanotube/polycarbonate composites," *Polymer*, vol. 43, no. 11, pp. 3247 – 3255, 2002.

[47] C. Zhang, Q. Ni, S. Fu, and K. Kurashiki, "Electromagnetic interference shielding effect of nanocomposites with carbon nanotube and shape memory polymer," *Composites Science and Technology*, vol. 67, no. 14, pp. 2973 – 2980, 2007.

[48] M. H. Al-Saleh and U. Sundararaj, "Electromagnetic interference shielding mechanisms of cnt/polymercomposites," *Carbon*, vol. 47, no. 7, pp. 1738 – 1746, 2009.

[49] J. Coleman, U. Khan, and Y. Gun'ko, "Mechanical reinforcement of polymers using carbon nanotubes," *Advanced Materials*, vol. 18, p. 689, 2006.

[50] J. Coleman, U. Khan, W. Blau, and Y. Gun'ko, "Small but strong: A review of the mechanical properties of carbon nanotube-polymer composites," *Carbon*, vol. 44, no. 9, pp. 1624 – 1652, 2006.

[51] P. Ajayan, L. Schadler, C. Giannaris, and A. Rubio, "Singlewalled carbon nanotube polymer composites, strength and weakness," *Advanced Materials*, vol. 12, p. 750, 2000.

[52] L. Liu and D. Wagner, "Rubbery and glassy epoxy resins reinforced with carbon nanotubes," *Composites Science and Technology*, vol. 65, no. 11-12, pp. 1861 – 1868, 2005.

[53] X.-L. Xie, Y.-W. Mai, and X.-P. Zhou, "Dispersion and alignment of carbon nanotubes in polymer matrix: A review," *Materials Science and Engineering: R: Reports*, vol. 49, no. 4, pp. 89 – 112, 2005.

[54] L. Schadler, S. Giannaris, and P. Ajayan, "Load transfer in carbon nanotube epoxy composites," *Applied Physics Letters*, vol. 73, p. 3842, 1998.

[55] R. Andrews, D. Jacques, D. Qian, and T. Rantell, "Multiwall carbon nanotubes: Synthesis and application," *Accounts of Chemical Research*, vol. 35, no. 12, pp. 1008–1017, 2002. PMID: 12484788.

[56] A. Eitan, K. Jiang, D. Dukes, and L. Andrews, R.and Schadler, "Surface modification of multiwalled carbon nanotubes: Toward the tailoring of the interface in polymer composites," *Chemistry of Materials*, vol. 15, no. 16, pp. 3198–3201, 2003.

[57] S. Banerjee, T. Hemraj-Benny, and S. Wong, "Covalent surface chemistry of single-walled carbon nanotubes," *Advanced Materials*, vol. 17, p. 17, 2005.

[58] M. Theodore, M. Hosur, J. Thomas, and S. Jeelani, "Influence of functionalization on properties of mwcnt-epoxy nanocomposites," *Materials Science and Engineering: A*, vol. 528, no. 3, pp. 1192 – 1200, 2011.

[59] P. Ma, J. Kim, and B. Tang, "Effects of silane functionalization on the properties of carbon nanotube/epoxynanocomposites," *Composites Science and Technology*, vol. 67, no. 14, pp. 2965 – 2972, 2007. Polymer Nanocomposites - Modeling, Mechanical and Functional Properties - Polymer Nanocomposites.

[60] X. Jiang, Y. Bin, and M. Matsuo, "Electrical and mechanical properties of polyimide-carbon nanotubes composites fabricated by in situ polymerization," *Polymer*, vol. 46, no. 18, pp. 7418 – 7424, 2005. Stimuli Responsive Polymers, IUPAC MACRO 2004.

[61] Z. Ounaies, C. Park, K. E. Wise, E. J. Siochi, and J. S. Harrison, "Electrical properties of single wall carbon nanotube reinforced polyimide composites," *Composites Science and Technology*, vol. 63, no. 11, pp. 1637 – 1646, 2003. Modeling and Characterization of Nanostructured Materials.

[62] H. H. So, J. W. Cho, and N. G. Sahoo, "Effect of carbon nanotubes on mechanical and electrical properties of polyimide/carbon nanotubes nanocomposites," *European Polymer Journal*, vol. 43, no. 9, pp. 3750 – 3756, 2007.

[63] H. Cai, F. Yan, and Q. Xue, "Investigation of tribological properties of polyimide/carbon nanotube nanocomposites," *Materials Science and Engineering A*, vol. 364, no. 1-2, pp. 94 – 100, 2004.

[64] B.-K. Zhu, S.-H. Xie, Z.-K. Xu, and Y.-Y. Xu, "Preparation and properties of the polyimide/multi-walled carbon nanotubes (mwnts) nanocomposites," *Composites Science and Technology*, vol. 66, no. 3-4, pp. 548 – 554, 2006.

[65] C. Martin, J. Sandler, A. Windle, M.-K. Schwarz, W. Bauhofer, K. Schulte, and M. Shaffer, "Electric field-induced aligned multi-wall carbon nanotube networks in epoxy composites," *Polymer*, vol. 46, no. 3, pp. 877 – 886, 2005.

[66] M.-W. Wang, T.-C. Hsu, and C.-H. Weng, "Alignment of mwcnts in polymer composites by dielectrophoresis," *The European Physical Journal - Applied Physics*, vol. 42, no. 03, pp. 241–246, 2008.

[67] L. Jiang and S. Spearing, "A reassessment of materials issues in microelectromechanical systems (mems)," *Journal of the Indian Institute of Science*, vol. 83, p. 363, 2007.

[68] Z. Chen and C. Lu, "Humidity sensors: a review of materials and mechanisms," *Sensor letters*, vol. 3, p. 274, 2005.

[69] A. De Queiroz, D. A. Soares, P. Trzesniak, and G. Abraham, "Resistive-type humidity sensors based on complexes," *Journal of Polymer Science Part B: Polymer Physics*, vol. 39, no. 4, pp. 459–469, 2001.

[70] M. Yang, G. Casalbore-Miceli, N. Camaioni, C. Mari, H. Sun, Y. Li, and M. Ling, "Characterization of capacitive humidity sensors based on doped poly(propargyl-alcohol)," *Journal of Applied Electrochemistry*, vol. 30, pp. 753–756, 2000. 10.1023/A:1004031804313.

[71] T. Zhang, X. Tian, B. Xu, W. Dong, L. Sun, S. Xiang, and D. Gao, "A polymer sensitive to humidity and its electrical properties analysis," *Journal of Materials Science Letters*, vol. 19, pp. 1419–1422, 2000. 10.1023/A:1006763103973.

[72] Z. Rittersma, "Recent achievements in miniaturised humidity sensors - a review of transduction techniques," *Sensors and actuators A*, vol. 96, pp. 196–210, 2002.

[73] Z. Chen and C. Lu, "Humidity sensors: a review of materials and mechanisms," *Sensor letters*, vol. 3, pp. 274–295, 2005.

[74] G. Harsaanyi, "Polymer films in sensor applications: a review of present uses and future possibilities," *Sensor Review*, vol. 20, pp. 98–105, 2000.

[75] J. S. Kim, M. J. Lee, M.-S. Kang, K.-P. Yoo, K.-H. Kwon, V. Singh, and N. K. Min, "Fabrication of high-speed polyimide-based humidity sensor using anisotropic and isotropic etching with icp," *Thin Solid Films*, vol. 517, no. 14, pp. 3879 – 3882, 2009. The proceedings of the 1st International Conference on Microelectronics and Plasma Technology (ICMAP 2008).

[76] Y. Kanamoria, E. Itoha, and K. Miyairia, "Improvement of sensitivity and response speed of capacitive type humidity sensor using partially fluorinated polyimide thin film," *Molecular Crystals and Liquid Crystals*, vol. 472, pp. 327–335, 2007.

[77] U. Kang and K. Wise, "A high-speed capacitive humidity sensor with on-chip thermal reset," *IEEE Transactions on Electron Devices*, vol. 47, pp. 702–710, 2000.

[78] M. Packirisamy, I. Stiharu, X. Li, and G. Rinaldi, "A polyimide based resistive humidity sensor," *Sensor Review*, vol. 25, p. 271, 2005.

[79] M. Ueda, K. Nakamura, K. Tanaka, H. Kita, and K. ichi Okamoto, "Water-resistant humidity sensors based on sulfonated polyimides," *Sensors and Actuators B: Chemical*, vol. 127, no. 2, pp. 463 – 470, 2007.

[80] W. F. Jiang, S. H. Xiao, C. Y. Feng, H. Y. Li, and X. J. Li, "Resistive humidity sensitivity of arrayed multi-wall carbon nanotube nests grown on arrayed nanoporous silicon pillars," *Sensors and Actuators B: Chemical*, vol. 125, no. 2, pp. 651 – 655, 2007.

[81] L. Liu, X. Ye, K. Wu, R. Han, Z. Zhou, and T. Cui, "Humidity sensitivity of mwnt networks deposited by dielectrophoresis," *Sensors*, vol. 9, pp. 1714–1721, 2009.

[82] D. Dunson, *Synthesis and characterization of thermosetting polyimide oligomers for microelectronics packaging*. PhD thesis, Virginia Polytechnic Institute and State University, 2000.

[83] A. Ardashnikov, I. Kardash, and A. Pravednikov, "The nature of the equilibrium in the reaction of aromatic anhydrideswith aromatic amines and its role in synthesis of polyimides," *Polymer Science U.S.S.R*, vol. 13, p. 2092, 1971.

[84] M. Koton, V. Kudryavtsev, N. Adrova, K. Kalnin'sh, A. Dubnova, and V. Svetlichnyi, "Investigation of the formation of polyamido-acids," *Polymer Science U.S.S.R*, vol. 16, p. 2411, 1974.

[85] Y. Kato, S. Iba, R. Teramoto, T. Sekitani, T. Someya, H. Kawaguchi, and T. Sakurai, "High mobility of pentacene field-effect transistors with polyimide gate dielectric layers," *Applied Physics Letters*, vol. 84, pp. 3789–3791, 2004.

[86] R. Okuda, K. Miyoshi, N. Arai, and M. Tomikawa, "Polyimide coatings for oled applications," *Journal of Photopolymer Science and Technology*, vol. 17, no. 2, pp. 207–213, 2004.

[87] W. Li, Z. Shen, J. Zheng, and S. Tang, "Ft-ir study of the imidization process of photosensitive polyimide pmda/oda," *Applied Spectroscopy*, vol. 52, pp. 985–989, 1998.

[88] D. W. Van Krevelen, *Properties of Polymers: Their Estimation and Correlation with ChemicalStructure*. Elsevier, 1976.

[89] J. Lai, ed., *Polymers for electronic applications*. CRC Press Inc., 1989.

[90] S. De Souza-Machado, R.and Wu and D. Denton, *Dielectric Properties of Polyimides and Factors Influencing SuchProperties In Polyimides: Fundamentals and Applications*. Dekker, M., 1996.

[91] C. Feger and H. Franke, *Polyimides in High Performance Electronics Packaging and Optoelectronic Applications in Polyimides: Fundamentals and Applications*. Dekker, M., 1996.

[92] R. Tummala, E. Rymaszewski, and A. Klopfenstein, eds., *Microelectronics Packaging Handbook: Semiconductor Packaging, Pt. II (2nd Ed.)*. Chapman and Hall, 1997.

[93] C. Wong, ed., *Polymers for Electronic and Photonic Applications*. Academic Press, 1993.

[94] R. Jensen, J. Cummings, and H. Vora, "Copper/polyimide materials system for high performance packaging," *IEEE Transactions on Components, Hybrids and Manufacturing Technology*, vol. 7, p. 384, 1984.

[95] J. L. Hedrick, H. R. Brown, M. Volksen, W.band Sanchez, C. Plummer, and J. Hilborn, "Low-stress polyimide block copolymers," *Polymer*, vol. 38, no. 3, pp. 605 – 613, 1997.

[96] M. Ree, T. L. Nunes, G. Czornyj, and W. Volksen, "Residual stress behaviour of isomeric pmda-oda polyimides," *Polymer*, vol. 33, no. 6, pp. 1228 – 1236, 1992.

[97] K.-P. Yoo, L.-T. Lim, N.-K. Min, M. J. Lee, C. J. Lee, and C.-W. Park, "Novel resistive-type humidity sensor based on multiwall carbon nanotube/polyimide composite films," *Sensors and Actuators B: Chemical*, vol. 145, no. 1, pp. 120 – 125, 2010.

[98] Q.-Y. Tang, Y. Chan, and K. Zhang, "Fast response resistive humidity sensitivity of polyimide/multiwall carbon nanotube composite films," *Sensors and Actuators B: Chemical*, vol. 152, no. 1, pp. 99 – 106, 2011.

[99] A. Graham, G. Duesberg, W. Hoenlein, F. Kreupl, M. Liebau, R. Martin, B. Rajasekharan, W. Pamler, R. Seidel, W. Steinhoegl, and E. Unger, "How do carbon nanotubes fit into the semiconductor roadmap," *Applied Physics A, Materials science and processing*, vol. 80, p. 1141, 2005.

[100] S. Reich, J. Maultzsch, C. Thomsen, and P. Ordejon, "Tight-binding description of graphene," *Phys. Rev. B*, vol. 66, p. 035412, Jul 2002.

[101] M. Yu, O. Lourie, M. Dyer, K. Moloni, T. Kelley, and R. Ruoff, "Strength and breaking mechanism of multiwalled carbon nanotubes under tensile load," *Science*, vol. 287, p. 637, 2000.

[102] M. Yu, B. Files, S. Arepalli, and R. Ruoff, "Tensile loading of ropes of single wall carbon nanotubes and theirmechanical properties," *Physical review letters*, vol. 84, p. 5552, 2000.

[103] M. Monthioux, P. Serp, E. Flahaut, M. Razafinimanana, C. Laurent, A. Peigney, W. Bacsa, and J. Broto, *Introduction to carbon nanotubes*. Springer Handbook of Nanotechnology, 2007.

[104] T. Ebbesen, H. Lezec, H. Hiura, J. Bennett, H. Ghaemi, and T. Thio, "Electrical conductivity of individual carbon nanotubes," *Nature*, vol. 382, p. 54, 1996.

[105] H. Dai, E. Wong, and C. Lieber, "Probing electrical transport in nanomaterials: Conductivity of individual carbon nanotubes," *Science*, vol. 272, p. 523, 1996.

[106] S. Frank, P. Poncharal, Z. Wang, and W. de Heer, "Carbon nanotube quantum resistors," *Science*, vol. 280, p. 1744, 1998.

[107] P. Avouris, "Carbon nanotube electronics," *Chemical Physics*, vol. 281, no. 2-3, pp. 429 – 445, 2002.

[108] F. Hill, T. Havel, A. Hart, and C. Livermore, "Storing elastic energy in carbon nanotubes," *Journal of Micromechanics and Microengineering*, vol. 19, no. 9, p. 094015, 2009.

[109] F. Hill, T. Havel, and C. Livermore, "Modeling mechanical energy storage in springs based on carbon nanotubes," *Nanotechnology*, vol. 20, no. 25, p. 255704, 2009.

[110] S. Paul and D.-W. Kim, "Preparation and characterization of highly conductive transparent films with single-walled carbon nanotubes for flexible display applications," *Carbon*, vol. 47, no. 10, pp. 2436 – 2441, 2009.

[111] W. Choi, D. Chung, J. Kang, H. Kim, Y. Jin, I. Han, Y. Lee, Y. Jung, N. Lee, G. Park, and J. Kim, "Fully sealed, high-brightness carbon-nanotube field-emission display," *Applied Physics Letters*, vol. 75, p. 125253, 1999.

[112] P. S. Peercy, "The drive to miniaturization," *Nature*, vol. 406, p. 1023, 2000.

[113] A. Javey, J. Guo, Q. Wang, M. Lundstrom, and H. Dai, "Ballistic carbon nanotube field-effect transistors," *Nature*, vol. 424, p. 654, 2003.

[114] F. Kreup, A. Graham, M. Liebau, G. Duesberg, R. Seidel, and E. Unger, "Carbon nanotubes for interconnect applications," in *Electron Devices Meeting, 2004. IEDM Technical Digest. IEEE International*, pp. 683 – 686, 2004.

[115] X. Li, X. Chen, L. Wang, B. Long, M. andZou, and Z. Shuai, "Effect of length and size of heterojunction on the transport properties of carbon-nanotube devices," *Applied Physics Letters*, vol. 91, no. 13, p. 133511, 2007.

[116] G. Close and H. Wong, "Fabrication and characterization of carbon nanotube interconnects," in *Electron Devices Meeting, 2007. IEDM 2007. IEEE International*, pp. 203 –206, 2007.

[117] S. Tans, J. Verschueren, and C. Dekker, "Room temperature transistor based on a single carbon nanotube," *Nature*, vol. 393, p. 49, 1998.

[118] R. Martel, T. Schmidt, H. Shea, T. Hertel, and P. Avouris, "Single- and multi-wall carbon nanotube field-effect transistors," *Applied Physics Letters*, vol. 73, p. 2447, 1998.

[119] A. Bachtold, P. Hadley, T. Nakanishi, and C. Dekker, "Logic circuits with carbon nanotube transistors," *Science*, vol. 294, p. 1317, 2001.

[120] C. Klinke, J. Hannon, A. Afzali, and P. Avouris, "Field-effect transistors assembled from functionalized carbon nanotubes," *Nano Letters*, vol. 6, no. 5, pp. 906–910, 2006.

[121] W. Yu, U. Kim, B. Kang, I. Lee, E. Lee, and Y. Lee, "Adaptive logic circuits with doping-free ambipolar carbon nanotubetransistors," *Nano Letters*, vol. 9, no. 4, pp. 1401–1405, 2009.

[122] M. H. Ben Jamaa, K. Mohanram, and G. De Micheli, "Power consumption of logic circuits in ambipolar carbon nanotubetechnology," in *Proceedings of the Conference on Design, Automation and Test in Europe*, DATE '10, (3001 Leuven, Belgium, Belgium), pp. 303–306, European Design and Automation Association, 2010.

[123] H. Cao, Q. Lu, X. Song, Z. Gan, and S. Liu, "Fabrication and characterization of patterned carbon nanotube flow sensor cell," *Chinese Science Bulletin*, vol. 55, pp. 2579–2583, 2010. 10.1007/s11434-010-3024-8.

[124] E. Snow, F. Perkins, E. Houser, S. Badescu, and T. Reinecke, "Chemical detection with a single-walled carbon nanotube capacitor," *Science*, vol. 307, p. 1942, 2005.

[125] S. Varghese, R. Nair, B. Nair, M. Hanajiri, Y. Yoshida, and S. Kumar, "Sensors based on carbon nanotubes and their applications: A review," *Current Nanoscience*, vol. 6, p. 331, 2010.

[126] M. Martinez, Y. Tseng, N. Ormategui, I. Loinaz, R. Eritja, and J. Bokor, "Label-free dna biosensors based on functionalized carbon nanotube field effect transistors," *Nano Letters*, vol. 9, no. 2, pp. 530–536, 2009.

[127] M. Ahmed, M.and Hossain and E. Tamiya, "Electrochemical biosensors for medical and food applications," *Electroanalysis*, vol. 20, p. 616, 2008.

[128] P. Bondavalli, P. Legagneux, and D. Pribat, "Carbon nanotubes based transistors as gas sensors: State of the art and critical review," *Sensors and Actuators B: Chemical*, vol. 140, no. 1, pp. 304 – 318, 2009.

[129] P. Bondavalli, "Carbon nanotubes based transistors composed of single-walled carbon nanotubes mats as gas sensors: A review," *Comptes Rendus Physique*, vol. 11, no. 5-6, pp. 389 – 396, 2010. Optical properties of nanotubes.

[130] L. Zhao, T. Nakayama, H. Tomimoto, Y. Shingaya, and Q. Huang, "Functionalization of carbon nanotubes with a ph-responsive molecule to produce a ph sensor," *Nanotechnology*, vol. 20, no. 32, p. 325501, 2009.

[131] S. Takeda, M. Nakamura, A. Ishii, A. Subagyo, H. Hosoi, K. Sueoka, and K. Mukasa, "A ph sensor based on electric properties of nanotubes on a glasssubstrate," *Nanoscale Research Letters*, vol. 2, pp. 207–212, 2007. 10.1007/s11671-007-9053-9.

[132] W. Steinhfgl, G. Schindler, G. Steinlesberger, G. Traving, and M. Engelhardt, "Comprehensive study of the resistivity of copper wires with lateral dimensions of 100 nm and smaller," *Journal of Applied Physics*, vol. 97, p. 023706, 2005.

[133] S. M. Rossnagel and T. S. Kuan, "Alteration of cu conductivity in the size effect regime," *J. Vac. Sci. Technol. B*, vol. 22, p. 240, 2004.

[134] C. White and T. Todorov, "Quantum electronics: Nanotubes go ballistic," *Nature*, vol. 411, p. 649, 2001.

[135] H. Cho, K. Koo, P. Kapur, and K. Saraswat, "Performance comparisons between cu, carbon nanotube and optics for future on chip interconnects," *IEEE electron device letters*, vol. 29, p. 122, 2008.

[136] A. Naeemi and J. Meindl, "Carbon nanotube interconnects," in *Proceedings of the 2007 international symposium on Physical design*, ISPD '07, (New York, NY, USA), pp. 77–84, ACM, 2007.

[137] C. Chen, L. Liu, Y. Lu, E. Kong, Y. Zhang, X. Sheng, and H. Ding, "A method for creating reliable and low-resistance contacts between carbon nanotubes and microelectrodes," *Carbon*, vol. 45, no. 2, pp. 436 – 442, 2007.

[138] A. Kane, T. Sheps, V. Branigan, E. andApkarian, M. Cheng, J. Hemminger, S. Hunt, and P. Collins, "Graphitic electrical contacts to metallic single-walled carbon nanotubesusing pt electrodes," *Nano Letters*, vol. 9, no. 10, pp. 3586–3591, 2009. PMID: 19754066.

[139] K. Rykaczewski, M. Henry, S. Kim, A. Fedorov, D. Kulkarni, S. Singamaneni, and V. Tsukruk, "The effect of the geometry and material properties of a carbon jointproduced by electron beam induced deposition on the electrical resistanceof a multiwalled carbon nanotube-to-metal contact interface," *Nanotechnology*, vol. 21, no. 3, p. 035202, 2010.

[140] R. Baughman, A. Zakhidov, and W. de Heer, "Carbon nanotubes-the route toward applications," *science*, vol. 297, p. 787, 2002.

[141] G. Viswanathan, N. Chakrapani, B. Yang, H.and Wei, H. Chung, K. Cho, C. Ryu, and P. Ajayan, "Single-step in situ synthesis of polymer-grafted single-wall nanotube composites," *Journal of the American Chemical Society*, vol. 125, no. 31, pp. 9258–9259, 2003.

[142] S. Qin, D. Qin, W. Ford, D. Resasco, and J. Herrera, "Functionalization of single-walled carbon nanotubes with polystyrene via grafting to and grafting from methods," *Macromolecules*, vol. 37, no. 3, pp. 752–757, 2004.

[143] H. Xia, Q. Wang, and G. Qiu, "Polymer-encapsulated carbon nanotubes prepared through ultrasonically initiated in situ emulsion polymerization," *Chemistry of Materials*, vol. 15, no. 20, pp. 3879–3886, 2003.

[144] Y. Sun, W. Huang, Y. Lin, K. Fu, A. Kitaygorodskiy, L. Riddle, J. Yu, and D. Carroll, "Soluble dendron-functionalized carbon nanotubes: Preparation,characterization, and properties," *Chemistry of Materials*, vol. 13, no. 9, pp. 2864–2869, 2001.

[145] X. Lou, C. Detrembleur, V. Sciannamea, C. Pagnoulle, and R. Jerome, "Grafting of alkoxyamine end-capped (co)polymers onto multi-walled carbon nanotubes," *Polymer*, vol. 45, no. 18, pp. 6097 – 6102, 2004.

[146] F. Gojny, M. Wichmann, B. Fiedler, I. Kinloch, W. Bauhofer, A. Windle, and K. Schulte, "Evaluation and identification of electrical and thermal conductionmechanisms in carbon nanotube/epoxy composites," *Polymer*, vol. 47, no. 6, pp. 2036 – 2045, 2006.

[147] C. Park, Z. Ounaies, K. Watson, R. Crooks, J. Smith, S. Lowther, J. Connell, E. Siochi, J. Harrison, and T. Clair, "Dispersion of single wall carbon nanotubes by in situ polymerizationunder sonication," *Chemical Physics Letters*, vol. 364, no. 3-4, pp. 303 – 308, 2002.

[148] Z. Jia, Z. Wang, C. Xu, J. Liang, B. Wei, D. Wu, and S. Zhu, "Study on poly(methyl methacrylate)/carbon nanotube composites," *Materials Science and Engineering A*, vol. 271, no. 1-2, pp. 395 – 400, 1999.

[149] D. Thuau, V. Koutsos, and R. Cheung, "Electrical and mechanical properties of carbon nanotube-polyimide composites," *Journal of Vacuum Science & Technology B*, vol. 27, pp. 3139–3144, 2009.

[150] Z. Spitalsky, D. Tasis, K. Papagelis, and C. Galiotis, "Carbon nanotube-polymer composites: Chemistry, processing, mechanical and electrical properties," *Progress in Polymer Science*, vol. 35, no. 3, pp. 357 – 401, 2010.

[151] S. Tjong, "Structural and mechanical properties of polymer nanocomposites," *Materials Science and Engineering: R: Reports*, vol. 53, no. 3-4, pp. 73 – 197, 2006.

[152] J. Salvetat, S. Bhattacharyya, and I. R., "Progress on mechanics of carbon nanotubes and derived materials," *Journal of Nanoscience and Nanotechnology*, vol. 6, p. 1857, 2006.

[153] H. Miyagawa, M. Misra, and A. Mohanty, "Mechanical properties of carbon nanotubes and their polymer nanocomposites," *Journal of Nanoscience and Nanotechnology*, vol. 5, p. 1593, 2005.

[154] M. Biercuk, M. Llaguno, M. Radosavljevic, J. Hyun, A. Johnson, and J. Fischer, "Carbon nanotube composites for thermal management," *Applied Physics Letters*, vol. 80, p. 2767, 2002.

[155] J. Hone, M. Llaguno, M. Biercuk, A. Johnson, B. Batlogg, Z. Benes, and J. Fischer, "Thermal properties of carbon nanotubes and nanotube-based materials," *Applied Physics A: Materials Science; Processing*, vol. 74, pp. 339–343, 2002. 10.1007/s003390201277.

[156] J. Coleman, W. Blau, A. Dalton, E. Munoz, S. Collins, B. Kim, J. Razal, M. Selvidge, G. Vieiro, and R. Baughman, "Improving the mechanical properties of single-walled carbon nanotubesheets by intercalation of polymeric adhesives," *Applied Physics Letters*, vol. 82, p. 1682, 2003.

[157] J. Wood, Q. Zhao, M. Frogley, E. Meurs, A. Prins, T. Peijs, and D. Dunstan, D.and Wagner, "Carbon nanotubes: From molecular to macroscopic sensors," *Phys. Rev. B*, vol. 62, pp. 7571–7575, Sep 2000.

[158] M. in het Panhuis, "Carbon nanotubes: enhancing the polymer building blocks for intelligent materials," *J. Mater. Chem.*, vol. 16, pp. 3598–3605, 2006.

[159] K. Lau, H. Cheung, J. Lu, Y. Yin, D. Hui, and H. Li, "Carbon nanotubes for space and bio-engineering applications," *Journal of Computational and Theoretical Nanoscience*, vol. 5, p. 23, 2008.

[160] J. Zou, H. Chen, A. Chunder, Y. Yu, Q. Huo, and L. Zhai, "Preparation of a superhydrophobic and conductive nanocomposite coatingfrom a carbon-nanotube-conjugated block copolymer dispersion," *Advanced Materials*, vol. 20, p. 3337, 2008.

[161] T. Skotheim and J. Reynolds, *Handbook of conductive polymers*. Marcel Dekker, 1998.

[162] P. Chandrasekhar, *Conducting polymers, fundamentals and applications: a practical approach*. Kluwer Academic, 1999.

[163] Y. Liao, C. Zhang, Y. Zhang, J. Strong, V. andTang, X. Li, K. Kalantar-zadeh, E. Hoek, K. Wang, and R. Kaner, "Carbon nanotube/polyaniline composite nanofibers: Facile synthesisand chemosensors," *Nano Letters*, vol. 11, no. 0, pp. 954–959, 2011.

[164] W. Bauhofer and J. Z. Kovacs, "A review and analysis of electrical percolation in carbon nanotubepolymer composites," *Composites Science and Technology*, vol. 69, no. 10, pp. 1486 – 1498, 2009. CNT-NET 07 Special Issue with regular papers.

[165] E. Barrera and K. Lozano, "New technologies, new composites," *JOM Journal of the Minerals, Metals and Materials Society*, vol. 52, pp. 32–32, 2000. 10.1007/s11837-000-0195-9.

[166] H. A. Phol, *Dielectrophoresis*. Cambridge: Cambridge University Press, 1978.

[167] A. Ramos, H. Morgan, N. Green, and A. Castellanos, "Ac electrokinetics: a review of forces in microelectrode structures," *Journal of Physics D: Applied Physics*, vol. 31, no. 18, p. 2338, 1998.

[168] K. J. and C. Han, "Use of dielectrophoresis in the fabrication of an atomic force microscope tip with a carbon nanotube: a numerical analysis," *Nanotechnology*, vol. 16, no. 10, p. 2245, 2005.

[169] A. K. Srivastava, S. J. Jeong, M.-H. Lee, S. H. Lee, S. H. Jeong, and Y. H. Lee, "Dielectrophoresis force driven dynamics of carbon nanotubes in liquid crystal medium," vol. 102, no. 4, p. 043503, 2007.

[170] J. Li, Q. Zhang, Peng, N., and Q. Zhu, "Manipulation of carbon nanotubes using ac dielectrophoresis," *Applied Physics Letters*, vol. 86, no. 15, p. 153116, 2005.

[171] N. Mureau, E. Mendoza, S. Silva, and M. Hoettges, K.and Hughes, "In situ and real time determination of metallic and semiconductingsingle-walled carbon nanotubes in suspension via dielectrophoresis," *Applied Physics Letters*, vol. 88, no. 24, p. 243109, 2006.

[172] N. Peng, Q. Zhang, J. Li, and J. Liu, "Influences of ac electric field on the spatial distribution of carbon nanotubes formed between electrodes," *Journal of Applied Physics*, vol. 100, no. 2, p. 024309, 2006.

[173] Z. Zhang, X. Liu, E. Campbell, and S. Zhang, "Alternating current dielectrophoresis of carbon nanotubes," *Journal of Applied Physics*, vol. 98, no. 5, p. 056103, 2005.

[174] C. Marquardt, S. Blatt, F. Hennrich, H. v. Lohneysen, and R. Krupke, "Probing dielectrophoretic force fields with metallic carbon nanotubes," *Applied Physics Letters*, vol. 89, no. 18, p. 183117, 2006.

[175] T. Jones, *Electromechanics of particles*. Cambridge: Cambridge University Press, 1995.

[176] R. Pethig, Y. Huang, X. Wang, and J. Burt, "Positive and negative dielectrophoretic collection of colloidal particles using interdigitated castellated microelectrodes," *Journal of Physics D: Applied Physics*, vol. 25, p. 881, 1992.

[177] M. King, O. Lomakin, R. Ahmed, and T. Jones, "Size-selective deposition of particles combining liquid and particulate dielectrophoresis," *Journal of Applied Physics*, vol. 97, no. 5, p. 054902, 2005.

[178] S. Auvray, V. Derycke, M. Goffman, A. Filoramo, O. Jost, and J. P. Bourgoin, "Chemical optimization of self-assembled carbon nanotube transistors," *Nano Letters*, vol. 5, no. 3, pp. 451–455, 2005.

[179] H. Dai, "Nanotube growth and characterization," in *Carbon Nanotubes* (M. Dresselhaus, G. Dresselhaus, and P. Avouris, eds.), vol. 80 of *Topics in Applied Physics*, pp. 29–53, Springer Berlin / Heidelberg, 2001. 10.1007/3-540-39947-X_3.

[180] X. Huang, R. Caldwell, L. Huang, S. C. Jun, M. Huang, M. Sfeir, S. O'Brien, and J. Hone, "Controlled placement of individual carbon nanotubes," *Nano Letters*, vol. 5, no. 7, pp. 1515–1518, 2005.

[181] K. Yamamoto, S. Akita, and Y. Nakayama, "Orientation of carbon nanotubes using electrophoresis," *Japanese journal of applied physics*, vol. 35, p. 917, 1996.

[182] K. Yamamoto, S. Akita, and Y. Nakayama, "Orientation and purification of carbon nanotubes using ac electrophoresis," *Journal of Physics D: Applied Physics*, vol. 31, no. 8, p. L34, 1998.

[183] H. Seo, C. Han, D. Choi, K. Kim, and Y. YLee, "Controlled assembly of single swnts bundle using dielectrophoresis," *Microelectronic Engineering*, vol. 81, no. 1, pp. 83 – 89, 2005.

[184] T. Lutz and K. Donovan, "Macroscopic scale separation of metallic and semiconducting nanotubes by dielectrophoresis," *Carbon*, vol. 43, no. 12, pp. 2508 – 2513, 2005.

[185] R. Krupke, F. Hennrich, H. Lohneysen, and M. Kappes, "Separation of metallic from semiconducting single-walled carbon nanotubes," *Science*, vol. 301, p. 344, 2003.

[186] C. Wei, T. Wei, C. Liang, and F. Tai, "The separation of different conducting multi-walled carbon nanotubesby ac dielectrophoresis," *Diamond and Related Materials*, vol. 18, no. 2-3, pp. 332 – 336, 2009. NDNC 2008 Proceedings of the International Conference on New Diamond and Nano Carbons 2008.

[187] R. Krupke, F. Hennrich, H. Weber, D. Beckmann, O. Hampe, S. Malik, M. Kappes, and H. Lfhneysen, "Contacting single bundles of carbon nanotubes with alternating electric fields," *Applied Physics A: Materials Science & Processing*, vol. 76, pp. 397–400, 2003. 10.1007/s00339-002-1592-4.

[188] L. Giannuzzi and F. Stevie, "A review of focused ion beam milling techniques for tem specimen preparation," *Micron*, vol. 30, no. 3, pp. 197 – 204, 1999.

[189] L. R. Harriott, A. Wagner, and F. Fritz, "Integrated circuit repair using focused ion beam milling," *Journal of Vacuum Science & Technology B*, vol. 4, p. 181, 1986.

[190] K. Gamo and S. Namba, "Microfabrication using focused ion beams," *Microelectronic Engineering*, vol. 11, no. 1-4, pp. 403 – 408, 1990.

[191] J. Daniel, D. Moore, and J. Walker, "Focused ion beams and silicon-on-insulator - a novel approach tomems," *Smart Materials and Structures*, vol. 9, no. 3, p. 284, 2000.

[192] D. K. Schroder, *Semiconductor material and device characterisation*. New York: John Wiley & Sons Inc., 1998.

[193] M. Buehler and W. Thurber, "Measurement of the resistivity of a thin square sample with a square four-probe array," *Solid-State Electronics*, vol. 20, no. 5, pp. 403 – 406, 1977.

[194] J. David and M. Buehler, "A numerical analysis of various cross sheet resistor test structures," *Solid-State Electronics*, vol. 20, no. 6, pp. 539 – 543, 1977.

[195] W. Findley, J. Lai, and K. Onaran, *Creep and relaxation of nonlinear materials*. Noth-Holland Pub Co., Amsterdam, 1976.

[196] O. Corbino, "Thermal oscillations in lamps of thin fibers with alternating current flowing through them and the resulting effect on the rectifier as a result of the presence of even-numbered harmonics," *Phys. Z.*, vol. 11, p. 413, 1910.

[197] H. Wang and M. Sen, "Analysis of the 3-omega method for thermal conductivity measurement," *International Journal of Heat and Mass Transfer*, vol. 52, p. 2102, 2009.

[198] L. La Spina, N. Nenadovic, A. van Herwaarden, H. Schellevis, W. Wien, and L. Nanver, "Mems test structure for measuring thermal conductivity of thin films," in *Microelectronic Test Structures, 2006. ICMTS 2006. IEEE International Conference on*, pp. 137 – 142, 2006.

[199] A. Irace and P. Sarro, "Measurement of thermal conductivity and diffusivity of single and multilayer membranes," *Sensors and Actuators A: Physical*, vol. 76, no. 1-3, pp. 323 – 328, 1999.

[200] L. J. van der Pauw, "A method of measuring specific resistivity and hall effect of dics of arbitrary shape," *Philips technical review*, vol. 20, p. 220, 1958.

[201] D. Johnson, N. Hilal, and W. Bowen, *Basic Principles of Atomic Force Microscopy*. Elsevier Ltd, 2009.

[202] R. Howland and L. Benatar, *A Practical Guide to Scanning Probe Microscopy*. Park scientific instruments, 1996.

[203] P. Grundy and G. Jones, *Electron microscopy in the study of materials*. Edward Arnold Publishers Limited, 1976.

[204] B. Stuart, *Modern Infrared Spectroscopy*. John Wiley & Sons Ltd, West Sussex, England, 1996.

[205] J. Moudler, W. Stickle, P. Sobol, and K. Bomben, *Handbook of X-ray photoelectron spectroscopy*. 2nd Edition, ISBN: 0962702625, Perkin Elmer Corporation, Minnesota, 1992.

[206] C. Wagner, W. Riggs, L. Davis, and J. Mulder, *Handbook of X-ray photoelectron spectroscopy,*. 1st Edition, ISBN: 0962702621, Perkin Elmer Corporation, Minnesota, 1979.

[207] J. R. Welty, *Heat transfer engineering*. Wiley, 1978.

[208] M. Kaviany, *Principles of heat transfer*. John Wiley & Sons, Inc., 2001.

[209] A. Geisberger, N. Sarkar, M. Ellis, and G. Skidmore, "Electrothermal properties and modeling of polysilicon microthermal actuators," *Microelectromechanical Systems, Journal of*, vol. 12, no. 4, pp. 513 – 523, 2003.

[210] Q.-A. Huang and N. K. S. Lee, "Analysis and design of polysilicon thermal flexure actuator," *Journal of Micromechanics and Microengineering*, vol. 9, no. 1, p. 64, 1999.

[211] G. Xu and Q.-A. Huang, "On-line extraction for thermal conductivity of surface-micromachined polysilicon thin films," in *Sensors, 2004. Proceedings of IEEE*, pp. 1593 – 1596 vol.3, oct. 2004.

[212] C. O'Mahony, M. Hill, J. P. Hughes, and W. A. Lane, "Titanium as a micromechanical material," *Journal of Micromechanics and Microengineering*, vol. 12, pp. 438–443, 2002.

[213] A. Chebotareva, U. G., T. Kost, S. Jorgensen, and A. Ulyashin, "Ito deposited by pyrosol for photovoltaic applications," *Thin Solid Films*, vol. 515, no. 24, pp. 8505 – 8510, 2007. First International Symposium on Transparent Conducting Oxides.

[214] C. Ywas, *Chemical properties handbook*. McGraw Hill, 1999.

[215] A. Yu, A. Liu, J. Oberhammer, Q. Zhang, and H. Hosseini, "Characterization and optimization of dry releasing for the fabrication of rf mems capacitive switches," *Journal of Micromechanics and Microengineering*, vol. 17, no. 10, p. 2024, 2007.

[216] T. Zhu, P. Argyrakis, E. Mastropaolo, K. Lee, and R. Cheung, "Dry etch release processes for micromachining applications," *Journal of Vacuum Science and Technology B*, vol. 25, p. 2553, 2007.

[217] J. Cooke and G. Hassall, "Low-pressure plasma sources for etching and deposition," *Plasma Sources Science and Technology*, vol. 11, no. 3A, p. A74, 2002.

[218] A. Ektessabi and S. Hakamata, "Xps study of ion beam modified polyimide films," *Thin Solid Films*, vol. 377-378, pp. 621 – 625, 2000.

[219] G. Carter, "Peening in ion-assisted thin-film deposition: a generalized model," *Journal of Physics D: Applied Physics*, vol. 27, no. 5, p. 1046, 1994.

[220] R. Nowak, F. Yoshida, J. Morgiel, and B. Major, "Postdeposition relaxation of internal stress in sputter-grown thin films caused by ion bombardment," *Journal of Applied Physics*, vol. 85, no. 2, pp. 841–852, 1999.

[221] T. J. Kang, J. G. Kim, J. S. Lee, J. H. Lee, J. H. Hahn, H. Y. Lee, and Y. H. Kim, "Low-thermal-budget and selective relaxation of stress gradients in gold micro-cantilever beams using ion implantation," *Journal of Micromechanics and Microengineering*, vol. 15, no. 12, p. 2469, 2005.

[222] N. A. Marks, D. R. McKenzie, and B. A. Pailthorpe, "Molecular-dynamics study of compressive stress generation," *Phys. Rev. B*, vol. 53, pp. 4117–4124, Feb 1996.

[223] M. Koster and H. Urbassek, "Ion peening and stress relaxation induced by low-energy atom bombardmentof covalent solids," *Phys. Rev. B*, vol. 63, p. 224111, May 2001.

[224] T. Bifano, H. Johnson, P. Bierden, and R. Mali, "Elimination of stress-induced curvature in thin-film structures," *Microelectromechanical Systems, Journal of*, vol. 11, pp. 592 – 597, oct 2002.

[225] T. Narushima, A. N. Itakura, T. Kawabe, and M. Kitajima, "Electron-stimulated surface stress relaxation of si," *Applied Physics Letters*, vol. 79, pp. 605 –607, jul 2001.

[226] S. Moon, W. Song, N. Kim, J. Lee, P. Na, S. G. Lee, M. H. Park, J. andJung, H. W. Lee, K. Kang, C. Lee, and J. Kim, "Current-carrying capacity of double-wall carbon nanotubes," *Nanotechnology*, vol. 18, no. 23, p. 235201, 2007.

[227] L. An and C. R. Friedrich, "Measurement of contact resistance of multiwall carbon nanotubes by electrical contact using a focused ion beam," *Nuclear Instruments and Methods in Physics Research Section B: Beam Interactions with Materials and Atoms*, vol. In Press, Corrected Proof, pp. –, 2011.

[228] C. Lu, L. An, Q. Fu, J. Liua, Z. H., and M. J., "Schottky diodes from asymmetric metal-nanotube contacts," *APPLIED PHYSICS LETTERS*, vol. 88, p. 133501, 2006.

[229] Y. Zhang, N. Franklin, R. Chen, and H. Dai, "Metal coating on suspended carbon nanotubes and its implication tometal-tube interaction," *Chemical Physics Letters*, vol. 331, no. 1, pp. 35 – 41, 2000.

[230] R. Martel, V. Derycke, J. Appenzeller, S. Wind, and P. Avouris, "Carbon nanotube field-effect transistors and logic circuits," in *Proceedings of the 39th annual Design Automation Conference*, DAC '02, (New York, NY, USA), pp. 94–98, ACM, 2002.

[231] V. Vitale, A. Curioni, and W. Andreoni, "Metal-carbon nanotube contacts: The link between schottky barrier and chemical bonding," *Journal of the American Chemical Society*, vol. 130, no. 18, pp. 5848–5849, 2008. PMID: 18410108.

[232] T. Meng, C. Wang, and S. Wanga, "First-principles study of contact between ti surface and semiconducting carbon nanotube," *Journal of applied physics*, vol. 102, p. 013709, 2007.

[233] Z. Liu, L. Ci, N. Bajwa, P. Ajayan, and J. Lu, "Benchmarking of metal-to-carbon nanotube side contact resistance," in *Interconnect Technology Conference, 2008. IITC 2008. International*, pp. 144 –146, 2008.

[234] B. Shan and K. Cho, "Ab initio study of schottky barriers at metal-nanotube contacts," *Phys. Rev. B*, vol. 70, p. 233405, Dec 2004.

[235] S. Lim, J. Jang, D. Bae, G. Han, S. Lee, I. Yeo, and Y. Lee, "Contact resistance between metal and carbon nanotube interconnects: Effect of work function and wettability," *Applied Physics Letters*, vol. 95, p. 264103, 2009.

[236] Y. Matsuda, W. Deng, and W. Goddard, "Contact resistance properties between nanotubes and various metals from quantum mechanics," *The Journal of Physical Chemistry C*, vol. 111, no. 29, pp. 11113–11116, 2007.

[237] S. Ke, W. Yang, and H. Baranger, "Nanotube-metal junctions: 2 and 3 terminal electrical transport," *J. Chem. Phys.*, vol. 124, p. 181102, 2006.

[238] C. Lan, P. Srisungsitthisunti, P. Amama, T. Fisher, X. Xu, and R. Reifenberger, "Measurement of metal/carbon nanotube contact resistance by adjustingcontact length using laser ablation," *Nanotechnology*, vol. 19, no. 12, p. 125703, 2008.

[239] F. Wakaya, K. Katayama, and K. Gamo, "Contact resistance of multiwall carbon nanotubes," *Microelectronic Engineering*, vol. 67-68, pp. 853 – 857, 2003. Proceedings of the 28th International Conference on Micro- and Nano-Engineering.

[240] D. Mann, A. Javey, J. Kong, Q. Wang, and H. Dai, "Ballistic transport in metallic nanotubes with reliable pd ohmic contacts," *Nano Letters*, vol. 3, no. 11, pp. 1541–1544, 2003.

[241] I. Balberg, N. Binenbaum, and N. Wagner, "Percolation thresholds in the three-dimensional sticks system," *Phys Rev Lett*, vol. 52, p. 1465, 1984.

[242] I. Balberg, N. Binenbaum, S. Alexander, and N. Wagner, "Excluded volume and its relation to the onset of percolation," *Phys Rev B*, vol. 30, p. 3933, 1984.

[243] D. Stauffer, *Introduction to the percolation theory*. London and Philadelphia, 1985.

[244] Y. Xi, H. Ishikawa, Y. Bin, and M. Matsuo, "Positive temperature coefficient effect of lmwpe-uhmwpe blends filled with short carbon fibers," *Carbon*, vol. 42, no. 8-9, pp. 1699 – 1706, 2004.

[245] H. Watanabe and T. Inoue, "Conformational dynamics of rouse chains during creep/recovery processes:a review," *Journal of Physics: Condensed Matter*, vol. 17, no. 19, p. R607, 2005.

[246] L. X. Benedict, S. G. Louie, and M. L. Cohen, "Static polarizabilities of single-wall carbon nanotubes," *Phys. Rev. B*, vol. 52, pp. 8541–8549, Sep 1995.

[247] J. Ding, X. Yan, and J. Cao, "Analytical relation of band gaps to both chirality and diameter of single-wall carbon nanotubes," *PHYSICAL REVIEW B*, vol. 66, p. 073401, 2002.

[248] T. Theodosiou and D. Saravanos, "Numerical investigation of mechanisms affecting the piezoresistive properties of cnt-doped polymers using multi-scale models," *Composites Science and Technology*, vol. 70, no. 9, pp. 1312 – 1320, 2010.

[249] A. Oliva-Avilis, F. Avilis, and V. Sosa, "Electrical and piezoresistive properties of multi-walled carbon nanotube/polymer composite films aligned by an electric field," *Carbon*, vol. 49, no. 9, pp. 2989 – 2997, 2011.

[250] J. Melcher, Y. Deben, and G. Arlt, "Dielectric effects of moisture in polyimide," *Electrical Insulation, IEEE Transactions on*, vol. 24, pp. 31 –38, feb 1989.

[251] G. Xu, C. Gryte, A. Nowick, S. Li, Y. Pak, and S. Greenbaum, "Dielectric relaxation and deuteron nmr of water in polyimide films," *Journal of Applied Physics*, vol. 66, p. 5290, 1989.

[252] D. Dentona, M. Buncicka, and H. Pranjotoa, "Effects of process history and aging on the properties of polyimide films," *Journal of Materials Research*, vol. 6, p. 2747, 1991.

[253] C. Wei, L. Dai, A. Roy, and T. B. Tolle, "Multifunctional chemical vapor sensors of aligned carbon nanotube and polymer composites," *Journal of the American Chemical Society*, vol. 128, no. 5, pp. 1412–1413, 2006.

[254] J. Kong, N. Franklin, C. Zhou, M. Chapline, S. Peng, K. Cho, and H. Dai, "Nanotube molecular wires as chemical sensors," *Science*, vol. 287, p. 622, 2000.

[255] O. K. Varghese, P. D. Kichambre, D. Gong, K. G. Ong, E. C. Dickey, and C. A. Grimes, "Gas sensing characteristics of multi-wall carbon nanotubes," *Sensors and Actuators B: Chemical*, vol. 81, no. 1, pp. 32 – 41, 2001.

[256] A. Zahab, L. Spina, P. Poncharal, and C. Marlière, "Water-vapor effect on the electrical conductivity of a single-walled carbon nanotube mat," *Phys. Rev. B*, vol. 62, pp. 10000–10003, Oct 2000.

[257] M. Fuhrer, J. Nygard, L. Shih, M. Forero, Y. Yoon, M. Mazzoni, Y. Choi, J. Ihm, S. Louie, A. Zettl, and P. McEuen, "Crossed nanotube junctions," *Science*, vol. 288, pp. 494–497, 2000.

[258] P. Na, H. Kim, H.-M. So, K.-J. Kong, H. Chang, B. Ryu, Y. Choi, J. Lee, B.-K. Kim, J.-J. Kim, and J. Kim, "Investigation of the humidity effect on the electrical properties of single-walled carbon nanotube transistors," *Applied Physics Letters*, vol. 87, p. 093101, 2005.